

# Light Confinement and Nonlinear Light-Matter Interaction in Semiconductor Photonic Crystal Cavities

THÈSE N° 8562 (2018)

PRÉSENTÉE LE 9 MAI 2018

À LA FACULTÉ DES SCIENCES DE BASE  
LABORATOIRE D'OPTOÉLECTRONIQUE QUANTIQUE  
PROGRAMME DOCTORAL EN PHOTONIQUE

ÉCOLE POLYTECHNIQUE FÉDÉRALE DE LAUSANNE

POUR L'OBTENTION DU GRADE DE DOCTEUR ÈS SCIENCES

PAR

Mohamed Sabry Abdel-Aliem MOHAMED

acceptée sur proposition du jury:

Prof. H. P. Herzig, président du jury  
Prof. R. Houdré, directeur de thèse  
Prof. E. Cassan, rapporteur  
Prof. R. Quidant, rapporteur  
Prof. V. Savona, rapporteur



ÉCOLE POLYTECHNIQUE  
FÉDÉRALE DE LAUSANNE

Suisse  
2018



# Abstract

The ability to control and manipulate light is a fundamental aspect that is at the very core of the development of integrated photonic circuits. It is desirable to achieve such control down to a scale that is comparable to or smaller than the wavelength of light, to enable highly efficient interaction with matter, which can eventually go down to single photon levels. Photonic crystals are particularly appealing in that respect, by providing optical bandgaps and facilitating dispersion shaping, through the precise patterning of layers. This is to be accomplished ideally in compact designs that are well-suited for fabrication with current technology and by utilizing material that has the capacity for integration. By exploiting existing light-matter interaction mechanisms, the available toolset for component design can be expanded, allowing to build optical chips with a wide range of functionality.

In the current work, a platform for integrated III-nitride photonic components on silicon is designed and implemented. A refined fabrication process for III-nitride micro- and nanostructures is developed, leading to the realization of suspended optical devices with both high performance and structural stability. Thorough optical and material characterization of the semiconductor layers is conducted to identify potential limitations, particularly with epitaxial GaN on Si technology, with respect to current crystal growth techniques. AlN layers based on a sputter-deposition process are proposed as an alternative for passive optical devices.

Two-dimensional photonic crystals are designed in gallium nitride and aluminum nitride, targeting operational wavelengths in the near-infrared telecom range. Optimized photonic crystal cavities are considered for maximizing light confinement in the semiconductor layers. By utilizing resonance enhancement, second and third harmonic generation are demonstrated in gallium nitride photonic crystal cavities featuring record-high quality factor values. This is achieved through a far-field coupling approach under low-power continuous-wave operation. High conversion efficiencies are attained in gallium nitride, exceeding previous demonstrations in the material. Propagation of the harmonic signals in the semiconductor layer is analyzed using finite-element time-domain modeling for the feasibility of an extraction mechanism.

Moreover, slow light coupled cavity waveguides are developed in a silicon platform, relying on optimized cavity designs that feature wideband operation in the near-infrared telecom range. A record-high value for group-index bandwidth product is achieved in the devices through improved design implementation. An end-fire based Fourier-space imaging technique is applied for the characterization of the optical structures, through which spatially-selective reconstruction of dispersion maps enabled accurate extraction of slow light properties. The influence of finite-size effects on slow light behavior is elucidated by implementing extended cavity chains. Furthermore, light transport regimes across the dispersion band are identified including the transition towards diffusive light transport and subsequent localization. The performance of coupled-cavity waveguides in the presence of disorder is quantified, revealing constraints on slow light transport, considering state-of-the-art fabrication.

**Keywords:** Photonic crystals, optical cavities, light confinement, nonlinear optics, slow light, integrated nanophotonics



# Résumé

La capacité de contrôler et de manipuler la lumière est un aspect fondamental qui est au cœur du développement des circuits intégrés photonique. Il est très désirable d'accomplir un tel contrôle dans des dimensions comparables ou plus petites que la longueur de la lumière afin de rendre possible des interactions très efficaces avec la matière qui peuvent éventuellement aller jusqu'au niveau d'un photon unique. A cet égard, les cristaux photoniques sont particulièrement attractifs car ils permettent la création de bandes interdites optiques et l'ingénierie des propriétés de dispersion par une structuration précise du matériau. Idéalement cela devrait être réalisable avec des structures compactes dont la fabrication est bien adaptée aux technologies actuelles et utilisant des matériaux compatibles. En exploitant les mécanismes d'interaction lumière-matière déjà présents, la boîte à outils disponible pour la conception de composants peut alors être agrandie, rendant possible la fabrication de puces optiques avec une vaste gamme de fonctionnalités.

Dans le travail présenté ici, une plateforme pour des composants photoniques intégrés sur silicium en III-nitride est conçue et mise en œuvre. Un procédé de fabrication pour des composants micro et nano en III-nitride est développé, ce qui mène à la réalisation de structures photonique suspendues avec à la fois de hautes performances et une bonne stabilité structurelle. Une caractérisation optique et matérielle complète des couches semi-conductrices est réalisée afin d'évaluer les limites potentielles. Ces analyses se portent en particulier sur du GaN sur silicium fabriqué par épitaxie telles qu'elles peuvent être obtenues selon les techniques actuelles de croissance cristalline. Des couches d'AlN déposées par pulvérisation cathodique sont proposées comme alternative pour des composants optique passifs.

Des cristaux photoniques en deux dimensions en nitride de gallium et en nitride d'aluminium sont conçues, afin de pouvoir opérer aux longueurs d'onde des télécommunications optiques dans l'infra-rouge proche. Des cavités photoniques optimisées sont considérées pour maximiser le confinement de la lumière dans les couches semi-conductrices. En utilisant un effet d'exaltation dû à la résonance des cavités, la génération de seconde et de troisième harmonique est démontrée avec des cavités optiques dans des cristaux photoniques en GaN, lesquelles présentent des valeurs record de facteur de qualité. Ces résultats sont obtenus avec une approche se basant sur un couplage en champ lointain et un fonctionnement à faible puissance en continu. Des efficacités de conversion élevées sont obtenues dans du GaN, dépassant les résultats précédents obtenus dans ce matériau. La propagation des signaux harmoniques dans la couche semi-conductrice est analysée selon une modélisation par éléments finis dans le domaine temporel, et ce afin d'étudier la faisabilité d'un moyen d'extraction.

De plus, des guides d'ondes en cavité couplées en mode de lumière lente sont développés sur une plateforme en silicium, se basant sur des cavités optimisées démontrant un fonctionnement sur une large bande de longueur d'onde proche de la bande des longueurs d'onde des télécommunications optiques. Une valeur record de produit bande passante index de groupe est obtenue dans ces structures grâce à l'implémentation d'architectures spécifiques. Un dispositif d'imagerie en transformée de Fourier est utilisé pour la caractérisation des structure optiques. Ce dispositif permet la reconstruction des courbes de dispersion avec une résolution spatiale, ce qui permet d'extraire de façon précise les propriétés de la lumière lente. L'influence des effets de dimensions finies sur la lumière lente est élucidée en fabricant des chaînes de cavités étendues. Finalement, des régimes de transport de la lumière sont identifiées dans le diagramme de dispersion, tout en incluant les transitions vers des modes de transport diffusif de la lumière ainsi que sa localisation subséquente. Les performances des guides d'ondes en cavités couplées en présence de désordre sont quantifiées, ce qui révèle les contraintes qui pèsent sur le transport de la lumière lente en considérant l'état de l'art de la fabrication.

**Mots clefs:** Cristaux photoniques, cavités optiques, confinement de la lumière, optique non linéaire, lumière lente, nanophotonique intégrée

# Contents

<b>Abstract</b> .....	<b>i</b>
<b>Résumé</b> .....	<b>iii</b>
<b>1. Introduction</b> .....	<b>1</b>
<b>2. Light Propagation, Confinement, and Interaction in Dielectric Photonic Crystals</b> .....	<b>3</b>
2.1 Principles of Photonic Crystals .....	3
2.1.1 Maxwell's Equations .....	3
2.1.2 Wave Equation in Photonic Crystals.....	4
2.1.3 Photonic Bandgap.....	5
2.1.4 Scaling Properties .....	8
2.2 Light Confinement in Two-Dimensional Photonic Crystals .....	9
2.2.1 Propagating Modes in a Slab.....	9
2.2.2 Light Confinement in Photonic Crystal Cavities .....	10
2.2.3 Multipole Expansion Description for Cavity Mode Analysis .....	13
2.3 Theory of Nonlinear Light-Matter Interaction in Photonic Crystal Cavities.....	14
2.3.1 Classical Theory: The Anharmonic Oscillator.....	15
2.3.2 Quantum Theory .....	17
2.3.3 Theoretical Conversion Efficiency: Coupled Mode Theory Analysis .....	18
<b>3. Fabrication of III-Nitride Planar Photonic Crystals</b> .....	<b>23</b>
3.1 Introduction .....	23
3.2 Process Overview .....	24
3.3 Layer Growth .....	26
3.4 E-beam Lithography .....	28
3.4.1 Overview .....	28
3.4.2 Mask Preparation .....	29
3.4.3 Sample Exposure .....	30
3.4.4 Proximity Effect Correction.....	31
3.5 Mask Transfer .....	33
3.6 III-Nitride Etching .....	34
3.7 Membrane Release .....	36
3.8 Anti-Reflection Coating .....	37
3.9 Summary.....	37

<b>4. Characterization of the III-Nitride on Silicon Platform .....</b>	<b>39</b>
4.1 Introduction .....	39
4.2 Pre-Fabrication Layer Characterization .....	39
4.2.1 Crystallinity.....	39
4.2.2 Surface and Interface Roughness.....	41
4.2.3 Dispersion and Layer Thickness .....	42
4.2.4 Stress in Heteroepitaxial and Sputtered Layers.....	45
4.3 Experimental Setup.....	48
4.3.1 Design and Construction.....	48
4.3.2 Fourier-Space Imaging .....	51
4.3.3 Resonant Scattering Characterization.....	53
4.4 III-Nitride on Si Platform .....	55
4.4.1 Residual Stress.....	55
4.4.2 Platform Design .....	57
4.5 Summary.....	58
<b>5. Frequency Upconversion in Two-Dimensional Gallium Nitride Photonic Crystal Cavities.....</b>	<b>59</b>
5.1 Introduction .....	59
5.2 Comparison of Nonlinearity in III-Nitride Semiconductors .....	60
5.3 Methodology: Cavity Design and Injectors .....	62
5.3.1 Far-field Coupling .....	62
5.3.2 Implemented Designs .....	63
5.4 Experimental Measurements.....	66
5.4.1 Resonant Scattering Characterization.....	66
5.4.2 Nonlinear Frequency Conversion .....	72
5.4.3 Conversion Efficiency and Cavity Enhancement Factors .....	75
5.5 Numerical Modeling of Frequency Conversion in Semiconductor Layers .....	76
5.5.1 Modeling Approach .....	76
5.5.2 Results and Comparison with Experimentation .....	77
5.6 Summary.....	79
<b>6. Wideband Slow Light in Silicon Photonic Crystal Coupled-Cavity Waveguides .....</b>	<b>81</b>
6.1 Introduction .....	81
6.1.1 Brief Overview of Slow Light Schemes .....	81
6.1.2 Implementation of Slow Light in Photonic Crystals .....	82
6.2 Design .....	83



6.2.1	Theoretical Formulation: First Principles Approach .....	83
6.2.2	Cavity Coupling Strength and Implemented Design .....	85
6.2.3	Light Coupling Scheme.....	87
6.3	Experimental Characterization .....	88
6.3.1	Fourier-Space Imaging .....	88
6.3.2	CCW Dispersion .....	89
6.3.3	Length Dependence and Losses .....	93
6.3.4	Discrete State Analysis, Disorder, and Light Localization.....	95
6.4	Structural Characterization .....	100
6.4.1	Buckling-Induced Effects.....	102
6.4.2	Raman Spectroscopy .....	103
6.5	Summary.....	105
<b>7.</b>	<b>Conclusion and Outlook .....</b>	<b>107</b>
	<b>Appendix A: Perturbation Theory Derivation of the Nonlinear Coupling Coefficient .....</b>	<b>111</b>
	<b>Appendix B: Derivation of the Coupled-Cavity Waveguide Dispersion According to the Tight-Binding Model ...</b>	<b>113</b>
	<b>Bibliography .....</b>	<b>117</b>
	<b>Table of Symbols and Acronyms .....</b>	<b>127</b>
	<b>Curriculum Vitae .....</b>	<b>129</b>



# 1. Introduction

Photonic crystals are ubiquitous in nature. They can be found on the exoskeletons of insects, reptile scales, the feathers of common bird species, and even within rock formations in the form of opals. Their appearance is often mistaken for pigmentation, which is another property resulting from light-matter interaction but emerging through a rather different physical mechanism. A photonic crystal (PhC) is a structured medium possessing a pattern that exhibits a certain degree of spatial order which can be anywhere from quasi- to perfectly periodic, such that light with a wavelength on the same length scale can interact with the medium through interference effects. A periodic arrangement of a dielectric medium has the capacity to completely inhibit the propagation of light, as with the simple one-dimensional case of a Bragg mirror, for instance. This effect arises solely from destructive interference of light waves featuring a specific wavelength and polarization. The wavelength range for which light propagation is inhibited is referred to as the optical bandgap and is one of the core concepts behind PhC design.

The field of PhCs was popularized in 1987 after independent work by two pioneering scientists. S. John proposed the formation of pseudogaps in “carefully prepared” dielectric superlattices that exhibit disorder [1], following his work on Anderson localization of photons in disordered media [2]. E. Yablonovitch on the other hand approached the concept of an optical bandgap from a different perspective. His proposal was based on the modification of the density of states to induce electromagnetic gap formation [3], through the introduction of a periodic dielectric medium. This would serve to inhibit spontaneous emission from a lasing system by means of an overlap between photonic and electronic bandgaps. Over the following thirty years, the field of PhCs would grow and diversify to become one of the most researched topics. The impact of PhCs has extended to many fields of science, whether assisting with the exploration of fundamental light-matter coupling [4], elucidating light radiation mechanisms [5], [6], the development of integrated optoelectronic circuits [7], or the investigation of biological systems [8].

A challenging aspect in the study of PhCs since the early days has been the creation of PhC structures for both experimental validation and exploration of novel concepts. This has been primarily limited by the concurrent state of fabrication technology, and indeed, the earliest studies on PhCs were limited to the microwave range, taking advantage of the scalability property of PhCs. The field of PhCs advanced gradually hand in hand with progress in both fabrication technology as well as computational techniques. Optical devices were soon attained in the near-infrared (near-IR) range, and PhCs were seen as primary candidates for silicon integrated photonic circuits. As nanofabrication technology matured, it opened the door towards the exploration of PhCs in various materials including wide bandgap semiconductors, diamond, and various nonlinear material such as  $\text{LiNbO}_3$ .

The prospects of bringing optical technologies to integrated devices relies in great part on the ability to control light in confined geometries in a similar manner to that achieved with charge carriers in semiconductor devices. There are currently very few known physical mechanisms that are capable of controlling light on a wavelength to sub-wavelength scale. PhCs have the advantage of providing various control modalities such as guiding, confinement, and filtering which also happen to be polarization specific. This is in addition to optical effects that require precise dispersion control such as self-collimation and slow light, which can hardly be realized in other platforms. Furthermore, PhCs allow for the employment of transparent dielectric material such as to minimize losses. They can also host layers or nanostructures that can assist with achieving specific optical functionality, such as gain media. Some of the potential applications include frequency conversion [9], optical switching [10], and optical memories [11] for example.

The following thesis explores applications of enhanced light confinement by two-dimensional PhC lattices in semiconductor layers, those of which target integrated photonic circuits. We make use of the light confinement

capacity of photonic crystal cavities to demonstrate exceptional performance in both wide bandgap and Si platforms. Wide bandgap semiconductors, namely GaN and AlN, are investigated due to their intrinsic optical properties (besides other exceptional mechanical and electronic properties) that contribute to an ideal platform for realizing integrated photonic components, with linear and nonlinear functionality. Wide bandgap semiconductors are regarded as potential candidates for next generation integrated optical chips. Si on the other hand is ideally suited for investigating novel phenomena and exploring the experimental limits in PhC design, since the platform is fully mature on both the material and fabrication side.

The beginning of the thesis presents a theoretical introduction to the fundamentals of photonic crystals, with a focus on planar two-dimensional geometries which are later implemented. The different aspects related to the design and confinement of light are detailed, and the basic theory behind nonlinear light-matter interaction is consequently laid out.

The second chapter details the fabrication process of photonic crystals in III-nitride layers on Si wafers. The process development and fabrication were carried out at the Institute of Physics and the Center of MicroNanoTechnology at EPFL. The produced optical micro- and nanostructures have yielded record performance values, for both waveguides and photonic crystals.

The third chapter is dedicated to the characterization of III-nitride layers and the fabricated devices. This includes various layer properties such as crystallinity, stress, and surface roughness. A presentation of the designed and constructed visible/ near-IR Fourier-imaging setup is also provided. The implementation of the integrated III-nitride platform design is then detailed, including stress mitigation schemes for lattice-mismatched III-nitride on Si semiconductor layers. The growth of GaN layers was carried out by J.-F. Carlin through a collaboration with the group of Prof. N. Grandjean (EPFL).

In the fourth chapter, the design and experimental characterization of high-Q GaN PhC cavities is presented, which is targeted towards intrinsic nonlinear frequency conversion. Through resonant enhancement, record-high harmonic generation efficiency in GaN is achieved, and third harmonic generation in GaN was further obtained for the first time under continuous-wave operation in the material (the latter result was concurrent with that of the “Quantum dot & photonic nanostructures” group at the University of Paris-Sud). Optimized cavity design values were provided by M. Minkov through a collaboration with the group of Prof. V. Savona (EPFL), and the final experiments were carried out in collaboration with Prof. M. Galli, Prof. D. Gerace, and A. Simbula (University of Pavia).

The fifth chapter presents a demonstration of optimized Si PhC coupled cavity waveguides, which were able to achieve record-high group-index bandwidth product values. Through Fourier-space imaging, the characteristics of slow light propagation in the slow light waveguides are identified, and the influence of disorder on the device performance is elucidated. Theoretical designs were developed by M. Minkov and Prof. V. Savona [12]. The devices were fabricated at the Cornell Nanoscale Science and Technology Facility by Y. Lai through a collaboration with the group of Prof. A. Badolato (formerly at the University of Rochester).

The following sections begin by providing a formulation for electromagnetic mode analysis in PhCs that is conventionally utilized, working up from Maxwell’s equations. The fundamental concepts of PhCs are introduced such as bandgap formation, lattice geometries, and the creation of defects. Light localization behavior in PhC cavities is then described including the multipole expansion approach. Following that, nonlinear light-matter interaction in dielectric media is described *ab initio*, from the perspective of both classical and quantum theories. Finally, nonlinear light-matter interaction mediated by PhC cavities is analyzed through coupled-mode theory.

## 2. Light Propagation, Confinement, and Interaction in Dielectric Photonic Crystals

### 2.1 Principles of Photonic Crystals

#### 2.1.1 Maxwell's Equations

Light propagation in a medium can be described by Maxwell's equations, which consider the electric and magnetic fields that derive from the potentials, under a selected gauge. In the time domain, they are expressed as follows:

Faraday's law:

$$\nabla \times \mathbf{E} = -\partial_t \mathbf{B} \quad (2.1.1)$$

Gauss' law:

$$\nabla \cdot \mathbf{D} = \rho_{free} \quad (2.1.2)$$

Ampère's law:

$$\nabla \times \mathbf{H} = \partial_t \mathbf{D} + \mathbf{J} \quad (2.1.3)$$

Gauss' law for magnetism:

$$\nabla \cdot \mathbf{B} = 0 \quad (2.1.4)$$

where  $\mathbf{E}$  is the electric field,  $\mathbf{H}$  is the magnetic field,  $\mathbf{D}$  is the electric displacement,  $\mathbf{B}$  is the magnetic induction,  $\rho_{free}$  is the free charge density, and  $\mathbf{J}$  is the current density of free carriers. The time and frequency dependence of each field are linked via a Fourier transform relation. For the electric field for instance, it is given by:

$$\mathcal{E}(\omega) = \int_{-\infty}^{\infty} \mathbf{E}(t) e^{i\omega t} dt \quad (2.1.5)$$

The field script symbol  $\mathcal{E}$  indicates frequency rather than time dependence.

Inside a medium, the macroscopic Maxwell's equations account for interaction with bound/ free charges and currents in matter using terms that are spatially averaged over multiple atoms or molecules. The physical quantities are linked by the following relations:

$$\mathbf{D} = \varepsilon \mathbf{E} = \varepsilon_0 \mathbf{E} + \mathbf{P} = \varepsilon_0 \varepsilon_r \mathbf{E} \quad (2.1.6)$$

$$\mathbf{B} = \mu \mathbf{H} = \mu_0 \mathbf{H} + \mu_0 \mathbf{M} = \mu_0 \mu_r \mathbf{H} \quad (2.1.7)$$

$$\mathbf{J} = \sigma \mathbf{E} \quad (2.1.8)$$

where  $\mathbf{P}$  is the polarization,  $\mathbf{M}$  is the magnetization,  $\varepsilon$  is the material permittivity,  $\mu$  is the magnetic permeability, and  $\sigma$  is the material conductivity.  $\varepsilon_r$  and  $\mu_r$  are the relative permittivity and permeability respectively, while,  $\varepsilon_0$  and  $\mu_0$  are the permittivity of free space and the magnetic permeability of vacuum respectively.

The total polarization is defined as:

$$\mathbf{P} = \frac{\sum_n \mathbf{p}}{V} \quad (2.1.9)$$

where the summation is carried out over the number of dipoles  $n$ , and  $V$  is the volume of the medium. The polarization charge  $\rho_{polarization}$  and the total charge  $\rho_{total}$  can be obtained through:

$$\nabla \cdot \mathbf{P} = -\rho_{polarization} \quad (2.1.10)$$

$$\nabla \cdot \mathbf{E} = \frac{\rho_{total}}{\varepsilon_0} \quad (2.1.11)$$

### 2.1.2 Wave Equation in Photonic Crystals

The general wave equation can be derived by applying the curl operator to Faraday's law and substituting with Ampère's law, to obtain the following expression for non-magnetic media ( $\mu_r = 1$ ):

$$\nabla(\nabla \cdot \mathbf{E}) - \Delta \mathbf{E} = -\mu_0 \partial_t (\partial_t \mathbf{D} + \mathbf{J}) \quad (2.1.12)$$

A homogeneous medium is assumed ( $\nabla \varepsilon = 0$ ), such that the  $\nabla \cdot \mathbf{E}$  term equates to 0. Assuming further that the medium is uncharged ( $\sigma = 0$ ), the wave equation simplifies to:

$$\Delta \mathbf{E} = \mu_0 \varepsilon \partial_t^2 \mathbf{E} \quad (2.1.13)$$

and in the frequency domain:

$$\Delta \mathcal{E} = -\mu_0 \varepsilon \omega^2 \mathcal{E} = -\varepsilon_r \left(\frac{\omega}{c}\right)^2 \mathcal{E} \quad (2.1.14)$$

The above is the basis of the formulation of the eigenvalue problem, used to for the computation of electromagnetic modes in a PhC medium. The wave equation in its generalized form is often expressed in terms of the magnetic field, which is commonly referred to as the "master equation":

$$\nabla \times (\epsilon_r^{-1} \nabla \times \mathcal{H}) = \left(\frac{\omega}{c}\right)^2 \mathcal{H} \quad (2.1.15)$$

$$\hat{\Theta} \mathcal{H} = \left(\frac{\omega}{c}\right)^2 \mathcal{H} \quad (2.1.16)$$

where the operator  $\hat{\Theta} = \nabla \times (\epsilon_r^{-1} \nabla \times$ .

The eigenvalues and corresponding eigenvectors (eigenmodes) of the photonic crystal can be retrieved through matrix diagonalization. The eigenmodes of the system form an orthogonal basis, and the eigenvalues are real due to the Hermiticity of the operator. The mode structure then goes in accordance with the variational method [13], i.e. the minimization of energy principle.

Photonic crystals feature discrete translational symmetry. This is common to any unperturbed PhC lattice, where a repeating unit cell can be defined. As a consequence, the Bloch-Floquet theorem can be applied, which states that the solution to the wave equation for a mode can be expressed as a plane wave multiplied by a periodic function with the same periodicity as the lattice:

$$\mathcal{H}(\mathbf{r}) = e^{i\mathbf{k}_{Bloch}\mathbf{r}} u(\mathbf{r}) \quad (2.1.17)$$

where  $\mathbf{k}_{Bloch}$  is the Bloch wave vector and  $u(\mathbf{r})$  is the aforementioned periodic function.

In reciprocal space, a Brillouin zone can be defined in terms of the reciprocal lattice vectors  $\frac{2\pi}{\Lambda_i}$ , which are linked to the periodicity directions in real space, of length  $\Lambda_i$ . Conservation of momentum implies that any momentum offset by a multiple of the reciprocal lattice vectors yields an equivalent point on the dispersion surface, that is to say  $\omega(\mathbf{k}) = \omega\left(\mathbf{k} + m \frac{2\pi}{\Lambda_i}\right)$ , where  $m$  is an integer.

### 2.1.3 Photonic Bandgap

The formation of a photonic bandgap in a structured medium such as a photonic crystal comes by due to electromagnetic interference. Considering the simplest case of a one-dimensional Bragg mirror comprising layers of periodically alternating permittivity with a period equal to  $\Lambda$ , a monochromatic plane wave travelling at normal incidence undergoes maximal reflection when the condition for destructive interference is met, according to Bragg's law:

$$2\Lambda \cos \vartheta = m\lambda \quad (2.1.18)$$

where  $\vartheta$  is the angle of incidence, and  $m$  is an integer.

The interference is determined by the wavelength of light relative to the periodicity of the dielectric stack. The higher the permittivity contrast  $\Delta\epsilon$  between the layers, the stronger the reflectivity that is achieved. Now considering a waveguiding slab that supports a single optical mode, the dispersion response is expected to be linear as displayed in Fig. 2.1.1. If the refractive index were to be gradually perturbed as to introduce a periodic spatial modulation to the structure (similar to that of a Bragg mirror), a Brillouin zone boundary would form, enabling the folding of modes by integer multiples of the reciprocal lattice vector. This allows the forward and backward modes to couple, resulting in the breaking of the degeneracy through state splitting. A frequency band emerges where the propagation of light is inhibited along all directions. It is referred to as the optical bandgap. As the refractive index contrast between the low-index and high-index layers is increased, the coupling between the modes strengthens, which eventually gives

a wider bandgap through a larger splitting of the states. Additionally, towards the edge of the Brillouin zone, the dispersion of light is no longer linear but acquires a parabolic shape that strongly modifies the group velocity in the medium.

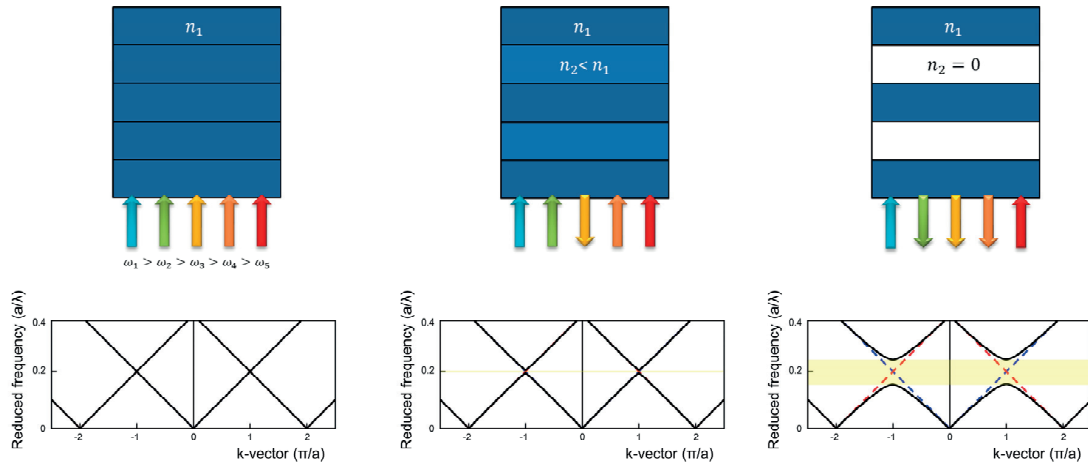


Fig. 2.1.1 Schematic diagram illustrating bandgap opening in the bandstructure of a one-dimensional photonic crystal, as the permittivity contrast between the layers is gradually increased.

Transitioning towards a two-dimensional photonic crystal, the same principle applies but with consideration to the complexity introduced by the additional dimension. Different periodic arrangements can be realized in two dimensions among which the square, triangular (also referred to as hexagonal), honeycomb, and kagome lattices are commonly used for photonic crystal applications. Each lattice can be defined by a primitive unit cell in real space comprising a set of basis vectors. The period of the PhC lattice is referred to as the lattice constant ( $a$ ). In reciprocal space, the transformed basis vectors provide for the construction of the Wigner-Seitz cell (the reader may refer to standard solid state physics textbooks for details [14]) to obtain the reduced Brillouin zone. It features the high symmetry points of the lattice, along which the dispersion curve can be traced to identify bandgap formation since band opening occurs typically near the edges, as shown in Fig. 2.1.2 for a triangular hole-based lattice. A density of states computation can absolutely confirm the presence of the bandgap as it considers all existing states in the entire Brillouin zone. Wave propagation in the two-dimensional lattice is then fully described by the dispersion surface.

The waveguiding mechanism in a PhC slab structure relies primarily on the PhC bandgap for lateral confinement, while vertical confinement must be fulfilled by total internal reflection, which dictates that the substrate and superstrate be of lower refractive index. A two-dimensional PhC lattice implemented in slab geometry differs from an infinite structure due to the existence of a radiative light cone through which light can escape from the structure. For ideal confinement of modes, their  $k$ -vector values should neither lie within the radiative cone nor couple to equifrequency modes in the continuum. Fig. 2.1.2 displays the light cone boundary marked on the bandstructure of a triangular lattice AlN hole-based PhC slab. The lower frequency band (below the bandgap) is found to be completely confined within the structure across the entire Brillouin zone boundary. This energy band is commonly labelled the “dielectric band”, in reference to the region where the mode energy is concentrated, in line with the variational principle mentioned earlier. On the other hand, mode energy of the upper band (above the bandgap) is found to concentrate more inside the PhC holes, in comparison to the dielectric band, and through a similar argument, the band is consequently labelled the “air band”. The upper band can be seen to overlap with the light cone towards higher frequencies when it takes on specific  $k$ -vector values. Such partially confined modes of a PhC slab are referred to as lossy modes.



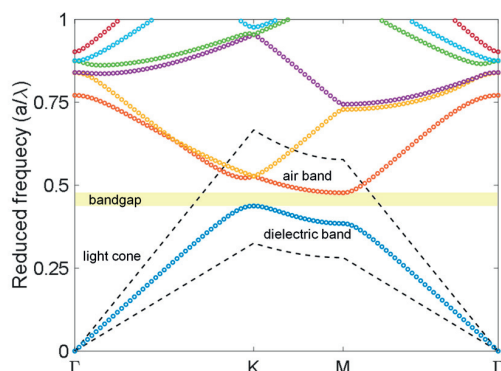


Fig. 2.1.2 Dispersion band diagram of a triangular lattice slab PhC in AlN (radius-to-lattice constant ratio of 0.35), computed using guided-mode expansion for transverse electric polarization. The dashed black line encloses the confined modes of the slab, and the upper boundary marks the light cone of the air cladding. The optical bandgap is highlighted in yellow.

Different lattice geometries of two-dimensional PhCs exhibit a varying optical response to light polarization. For ideal analysis of polarization, one must consider a lattice that is infinitely extended along the vertical homogeneous direction. With regard to finite slab geometries, only quasi transverse electric (TE)/transverse magnetic (TM) modes can be defined, which are often referred to as TE/TM directly. Implemented PhC lattices can be either hole based or pillar based, where the two implementations differ by the exchange of the permittivity between the dielectric and air regions for a given pattern. A square lattice comprising dielectric pillars of high refractive index surrounded by air favors the formation of TM bandgaps. To the contrary, the inverted hole-based lattice favors the formation of TE bandgaps instead. This relates to the connectivity of high-permittivity regions along the field orientation. A compromise between the two cases is provided by a triangular lattice of air-holes in a high refractive index medium since it is naturally a hole-based lattice and furthermore resembles a pillar-based lattice when the filling factor (ratio of the hole area to the PhC unit cell area) is sufficiently high. It is therefore capable of producing a complete bandgap for both TE and TM polarizations, which justifies its common use. The honeycomb lattice also features overlapping TE and TM bandgaps, however, its unit cell size which is significantly larger than that of a triangular lattice is deterrent for light confinement applications.

An optical bandgap map traces the evolution of the bandgap of a PhC lattice with the variation of the PhC hole radius relative to the lattice constant. It is presented in Fig. 2.1.3 considering wide bandgap semiconductor, for hole-based two-dimensional PhC lattices, which can be implemented in a slab geometry. The optical bandgaps were computed using guided-mode expansion (GME) [15] for two semiconductor layer types: GaN ( $n=2.31$  at  $\lambda=1550$  nm) and AlN\* ( $n=2.05$  at  $\lambda=1550$  nm). Bandgap maps for Si are thoroughly discussed in literature [16] and are therefore omitted. A hole-based square PhC lattice does not present any significant bandgap for either TE or TM polarizations in both GaN and AlN, up to the limit of the PhC hole overlap, i.e.  $r/a=0.5$ , where  $r$  is the PhC hole radius. This is also the case for the hole-based honeycomb lattice in AlN. As seen in Fig. 2.1.3, the units are normalized by the lattice constant, given the spatial scalability property of the electromagnetic eigenvalue equation. A measure of the bandgap size can be computed through the ratio of the bandgap extent relative to the mid-gap frequency. The general trend when increasing the slab thickness, given all other parameter being constant, is the pulling of modes from the continuum to the slab. A similar effect can be seen when the radius of the PhC holes is reduced relative to the lattice constant, besides altering the bandgap size and frequency. A common tuning method for red-shifting the bandstructure of a PhC is by gradually reducing the native hole size.

\* The refractive index of the computed structures corresponds to sputtered AlN layers.

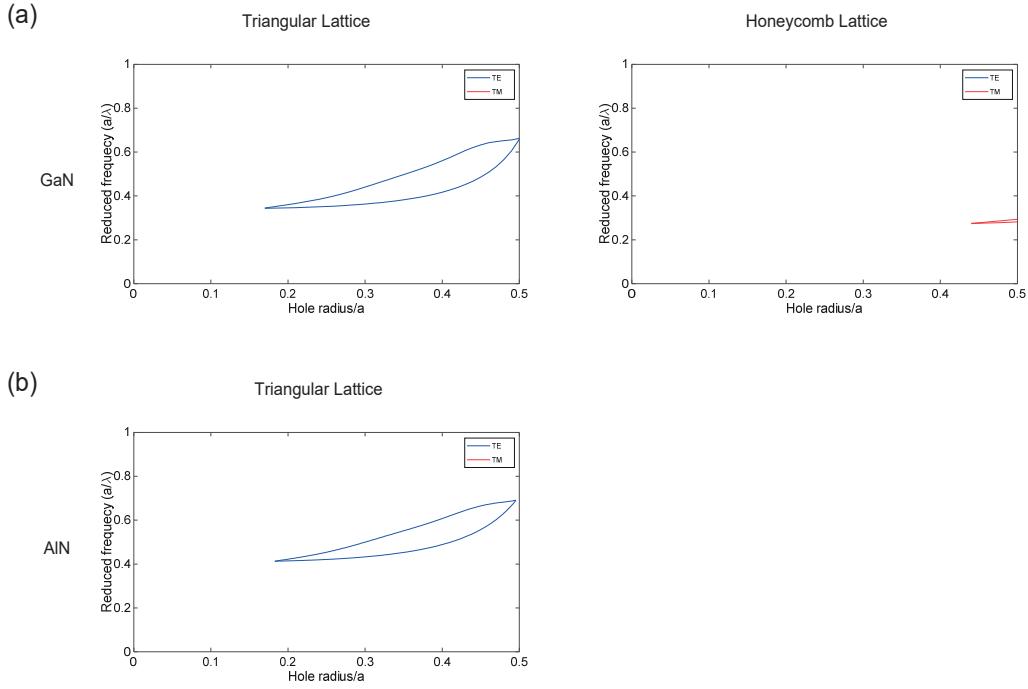


Fig. 2.1.3 Optical bandgap maps for GaN and AlN two-dimensional hole-based PhC lattices in a slab geometry. The calculations were performed using guided-mode expansion for a slab thickness of 350 nm.

With wide bandgap semiconductors such as AlN, the optical bandgaps that are created in two-dimensional slabs are found to be significantly smaller in comparison with Si, as a consequence of the reduction in the index contrast. Taking the case of a triangular hole lattice for instance, A high-energy TM bandgap is naturally present in Si for hole radius-to-lattice constant ratios in excess of 0.35 [16]. The situation is different in AlN, since a full TM bandgap does not form at all. This remains true when the PhC hole size is swept up to the limit of hole overlap, after which the PhC lattice transforms into a pillar-type honeycomb geometry.

When working with quasi-TE polarization, the most suitable lattice geometry is the triangular, hole-based lattice for several reasons. First and foremost is the confinement due to the size and location of the bandgap. A quasi-TE bandgap is present in a frequency range that can be well confined in a slab geometry and exhibits considerable bandwidth, offering freedom in design. The repeating PhC unit cell has an area of  $\frac{3a^2}{2\sqrt{3}}$ , which is amongst the smallest attainable values for PhCs. An advantage is that defect states can be consequently realized with reduced volumes, which is essential towards light-matter enhancement effects. As for quasi-TM operation, the honeycomb lattice is the only option in a hole-based geometry for GaN, presenting a bandgap near  $a/\lambda=0.28$ . A similar TM bandgap does not open in AlN however, and a pillar-based approach must be followed in two-dimensional PhCs.

### 2.1.4 Scaling Properties

A particular advantage of PhC systems pertains to their scalability property which derive from the electromagnetic wave equation. This applies to both to the length dimension and to the permittivity value of the medium. Taking for instance a PhC lattice where equation (2.1.15) describes the allowed eigenmodes, if the spatial scale were to be expanded by a factor of  $b$ , the wave equation would transform to the following expression under change of variables ( $\mathbf{r}' = b\mathbf{r}$  and  $\nabla' = \nabla/b$ ):

$$\nabla' \times \left( \frac{1}{\varepsilon_r(\mathbf{r}'/b)} \nabla' \times \mathcal{H}(\mathbf{r}'/b) \right) = \left( \frac{(\frac{\omega}{b})^2}{c^2} \right) \mathcal{H}(\mathbf{r}'/b) \quad (2.1.19)$$

It can thus be seen that the solution should be identical apart from the scaling factor applied to the frequency and modes: the eigenfrequencies are divided by a factor of  $b$ , and the eigenmodes are spatially extended by the same factor. Similar analysis applies to the permittivity. By applying a multiplication factor of  $d$  to the permittivity distribution, the following expression is obtained:

$$\nabla \times \left( \frac{1}{\varepsilon_r(\mathbf{r})} \nabla \times \mathcal{H}(\mathbf{r}) \right) = \left( \frac{d\omega^2}{c^2} \right) \mathcal{H}(\mathbf{r}) \quad (2.1.20)$$

It can be deduced from the above equation that there is no spatial variation in the eigenmodes of the transformed system, while the eigenfrequencies are multiplied by a factor of  $d^{1/2}$ . In practice, such scaling is not straightforward to implement, even in semiconductors layers which can be readily doped to alter their intrinsic permittivity, since most PhC designs rely on a strong refractive index contrast against a surrounding air medium.

## 2.2 Light Confinement in Two-Dimensional Photonic Crystals

One of the important features of PhC systems is the ability to control the flow of light on a scale that is comparable to the wavelength. We restrict the following discussion to two-dimensional PhCs to maintain clarity, bearing in mind that the same principles apply to lower/higher dimensionality, with certain considerations. To begin with, a PhC lattice must be introduced in a medium such that an optical bandgap is created, which by definition, covers all  $k$ -vectors in the reduced Brillouin zone. It is not necessary that the bandgap be complete however. The bandgap should target the specific polarization of light over a defined frequency band, and should eventually cover the  $k$ -vector span of the mode. The spatial dependence of the optical potential can be shaped by locally modifying the permittivity, which essentially leads to the creation of states in those altered regions that would otherwise be prohibited. This will be detailed in the following sections with regard to one and zero-dimensional defects. A linear defect serves to guide light along a single spatial direction, and the  $k$ -vector therefore takes on a discrete value. A point defect on the other hand localizes light around a point. Since light of a given wavelength resists localization in space beyond a certain limit, it consequently exhibits a spread in momentum that is inversely proportional to the spatial extent of the mode.

### 2.2.1 Propagating Modes in a Slab

A linear waveguide can be created in a PhC lattice by modifying the dielectric permittivity periodically along the direction of a lattice basis vector, in such a way that the inherent discrete translational symmetry of the PhC lattice remains preserved along a single direction. This is typically the effective propagation direction of the confined mode. If the change in permittivity is on the scale of the unit cell of the lattice, the defect is referred to as a line defect. Alternatively, linear waveguides may still be realized but with a longer-scale periodicity (relative to the PhC lattice) through the evanescent coupling of individual defects. They are referred to as coupled-cavity waveguides, and they will be treated further in chapter 6.

The common implementation of waveguides in a triangular PhC lattice, is through the removal of a row of holes along the  $\Gamma K$  direction, as displayed in Fig. 2.2.1(a). The two supported modes are TE-polarized, and their non-trivial dispersion behavior originates from hybridization between index-guided and gap-guided modes of the defect [16],

which has been thoroughly exploited for band engineering. The modes can be distinguished by the symmetry of the electric field with respect to the axis of the defect line ( $\sigma^{xz}$  plane), as either even or odd as displayed in Fig. 2.2.1(b). The even mode can be interfaced easily via wire waveguides. The relatively higher group velocity ( $v_g = \frac{d\omega}{dk}$ ) away from the band edge additionally improves the mode matching conditions. Towards lower frequencies, the mode transitions along the dispersion curve to the region below the light line, as the in-plane k-vector assumes a higher value. Radiative losses are greatly reduced, and disorder-induced scattering primarily dictates the propagation loss figure, assuming sufficient in-plane confinement.

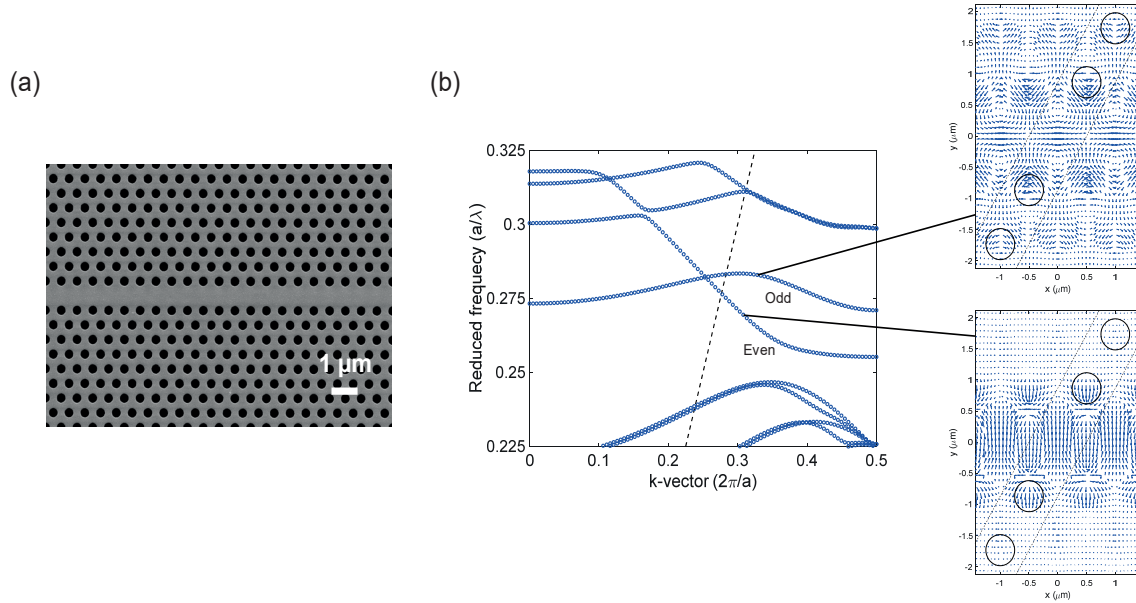


Fig. 2.2.1 Scanning electron micrograph displaying a line-defect (W1) waveguide in a triangular lattice PhC. (b) Simulated bandstructure of a W1 waveguide in Si using guided-mode expansion. The even and odd modes are labelled on the bandstructure, and their respective mode-field distribution (E-field vector) is shown in the inset to the right. The light cone is indicated by the dashed black line.

Towards the band edge, the curvature of the energy band induces what is referred to as “slow light” behavior, where the group velocity of light is greatly reduced. Theoretically, the slow-down factor of light in a W1 waveguide tends to infinity towards the band edge. The behavior of light in that regime has been the subject of intense study, as it approaches localization and is prone to disorder.

### 2.2.2 Light Confinement in Photonic Crystal Cavities

In analogy to electronic systems, a point defect may be introduced to a PhC lattice possessing an optical bandgap such that a defect state is formed in the otherwise unoccupied frequency range of the bandgap. This is physically achieved by disrupting the translational symmetry of the lattice through a local modification of the effective refractive index. A structural change can be imparted in the form of a displacement of a hole or pillar, or by modifying their size or shape. Alternatively, the permittivity value of the lattice can be locally altered towards the same purpose. This leads to light being essentially “trapped” at the defect site due to the surrounding optical potential of the bandgap.

A defect state can either be pulled from the upper air band or pushed from the lower dielectric band in a similar manner to electronic donor and acceptor states, respectively, present in an electronic bandgap. A donor state is a result of a net positive variation of the permittivity, which reduces the eigenfrequency, while the opposite is true for

an acceptor state, in accordance with perturbation theory. The mode profile of a defect state tends to retain the same mode symmetry character, i.e. multipole order, as that of the band from which the state originates.

A point defect that is introduced to a PhC lattice functions to confine light, both spatially and temporally, and is referred to as a PhC cavity. Multiple modes can be supported by a single defect depending on its geometry. Modes are ranked in ascending order beginning from the ground state. It is typically the case that the higher the order of the mode, and its frequency thereof, the greater the number of nodal lines appearing in the spatial mode profile. Perturbation theory confirms that with the introduction of nodal lines, the consequential higher energy concentration in the surrounding low-permittivity regions does indeed raise the frequency. The mode profile can be analyzed through the multipole expansion technique detailed in section 2.2.3, which is a similar approach for assessing the formation and hybridization of molecular orbitals.

### 2.2.2.1 Cavity Designs

There are several common cavity geometries that have been implemented in two-dimensional PhCs. The majority discussed here relate to the triangular lattice for reasons pertaining primarily to the bandgap, as mentioned earlier. Cavities can be classified as either point-defect or line-defect based.

Point-defect cavities offer the smallest possible modal volumes for a given lattice geometry, with examples such as the H0 (point-shift) cavity [17] based on the translation of PhC holes around a central node, or the H1 cavity [18] based on the elimination of a single PhC hole, as shown in Fig. 2.2.2. Line-defect cavities, as the name implies, necessitate the elimination of multiple holes along a single line of the PhC lattice, thus forming a Fabry-Perot type cavity. Due to the delocalization of the mode profile, this class of cavities can offer higher Q-factors than their point-defect counterparts. When the number of  $n$  removed holes is limited, the terminated cavity is referred to as an L( $n$ ) cavity. The number of eliminated holes is usually odd to support a fundamental mode of even parity, with the most common implementation being the L3 cavity [19] as it offers a good balance between modal volume and Q-factor.

A cavity may also be realized by removing an entire row of holes, thus forming a W1 waveguide, and subsequently modifying the hole size or translation around a central point to form a point defect. This is referred to as a width-modulated cavity [20], [21] (as displayed in Fig. 2.2.2d). Another cavity implementation that is adopted from electronic systems also utilizes a W1 waveguide geometry. There, the lattice periodicity is expanded relative to the native lattice within an intermediate region that extends perpendicular to the W1 waveguide axis, in a way to form a “potential well”. It is referred to as a heterostructure cavity [22], and more specifically in Fig. 2.2.2e, a double-heterostructure cavity. Multi-heterostructure designs possessing graded potential confinement have also been explored [23].

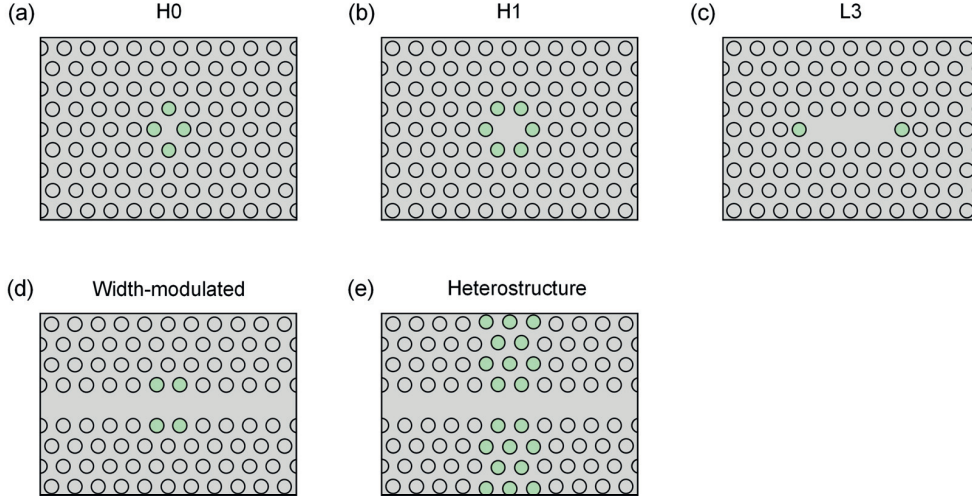


Fig. 2.2.2 Schematic diagrams of commonly implemented PhC cavity designs in two-dimensional triangular lattices. PhC holes that are modified in size or position are indicated in green.

Another notable class of cavities which is rather based on a one-dimensional structure is the nanobeam design. It has been widely adopted due to the high attainable theoretical Q-factors. The cavity relies on strong confinement by total internal reflection along two dimensions. The cavity volumes are also amongst the lowest across all PhCs. Various defect designs have been implemented in nanobeams, and they often utilize the same layout: a central region of modified or eliminated PhC holes, followed by tapered PhC holes, which are finally enclosed by a high-reflecting set of PhC holes [24], [25].

### 2.2.2.2 Figure-of-merit

A standard figure-of-merit of an optical cavity describes its ability to retain photons relative to its physical size. This is formulated by two parameters: the quality (Q)-factor and the modal volume (V). There are other factors that may be accounted for, such as the radiation pattern for instance, which affects coupling to particular radiative modes. Another characteristic that depends more on the application at hand is the overlap factor of the mode energy with the dielectric or the ambient medium.

The Q-factor of a cavity is a measure of its temporal light confinement capacity. In other words, it indicates how long a photon, whose frequency is centered on the resonance frequency of the cavity, can be retained relative to its optical cycle. The frequency equivalence of the Q-factor definition is the ratio of center frequency to the linewidth of the resonance, assuming exponential energy decay from the cavity. The aforementioned Q-factor definitions are summarized by the following equations:

$$Q = \omega_0 \frac{E_{\text{stored}}}{P_{\text{dissipated}}} = \frac{\omega_0 \tau_{\text{cavity}}}{2} \quad (2.2.1)$$

$$Q = \frac{\omega_0}{\delta\omega} \quad (2.2.2)$$

The modal volume of a cavity on the other hand provides a measure of the spatial extent of the resonant electromagnetic mode that is confined at the PhC defect site. The importance of quantifying modal volumes of microcavities relates to the various enhancement mechanisms that scale directly with it, such as the Purcell factor [26] or strong coupling in applications of cavity quantum electrodynamics [27].

The modal volume may consequently follow different formulations according to the application. One of the widely adopted and earliest definitions is the following [28]:

$$V_{effective} = \frac{\int_{-\infty}^{\infty} \epsilon(\mathbf{r}) |\mathbf{E}(\mathbf{r})|^2 d^3\mathbf{r}}{\max[\epsilon(\mathbf{r}) |\mathbf{E}(\mathbf{r})|^2]} \quad (2.2.3)$$

Here, the normalization factor of the field integral is considered to be the peak permittivity-intensity product, which requires caution should the cavity mode exhibit sharp spatial transitions.

Concerning mode normalization, there is an important point to consider which pertains to leaky PhC cavities. Taking slab PhC cavities for instance, as they are in most cases open and lossy systems, the confined cavity modes are considered to be quasi-bound states. This implies that standard mode volume definitions will exhibit divergence. With high-Q cavities however, it is often sufficient to impose a cut-off volume to avoid that problem. In other cases, the mode volume may be estimated according to the normalization in [29], which proposes the incorporation of an additional border integral in the modal volume equation that should reach convergence within a reasonable computational volume for the cavity.

Another modal volume definition that may be used, which is also useful for the quantification of light localization volumes, is that based on the concept of the inverse participation ratio [30], [31]:

$$V_{effective} = \frac{[\int_{-\infty}^{\infty} \epsilon(\mathbf{r}) |\mathbf{E}(\mathbf{r})|^2 d^3\mathbf{r}]^2}{\int_{-\infty}^{\infty} [\epsilon(\mathbf{r}) |\mathbf{E}(\mathbf{r})|^2]^2 d^3\mathbf{r}} \quad (2.2.4)$$

The following table lists a brief comparison between the typical modal volumes obtained in common PhC cavity geometries:

Table 2.2.1 The computed modal volumes of common PhC cavities, obtained through finite-element modeling simulations.

Cavity	Equation (2.2.3) Definition $(\lambda/n)^3$	Equation (2.2.4) Definition $(\lambda/n)^3$
<b>H0</b>	0.42	2.13
<b>L3</b>	0.71	2.90
<b>Width-modulated</b>	1.34	6.02
<b>Heterostructure</b>	1.58	6.07

### 2.2.3 Multipole Expansion Description for Cavity Mode Analysis

Similar to molecular structure in nature, PhC cavities can be classified into point groups according to the symmetry relations that their design satisfies. For example, the majority of cavities implemented in a triangular lattice have either point group  $C_{2v}$  or  $C_{6v}$  symmetry. Molecular orbitals need not satisfy the symmetry operations of the molecule's point group. Each orbital obeys a set of symmetry operations that determines its character classification. A point group can support orbitals falling within a discrete set of predetermined characters as dictated by its symmetry, which are typically enumerated in a character table [32]. This includes state degeneracy as well. An identical analysis can be applied to the modes of a PhC cavity, which can likewise be classified according to their character. From that, one can determine whether Neumann or Dirichlet boundary conditions apply at the symmetry planes.

An interesting aspect following from the symmetry analysis of cavity modes is the emergence of their intrinsic radiative nature. Each cavity mode can be decomposed into a sum of radiating multipole moments (monopole, dipole, quadrupole, etc.) carrying varying weight coefficients, in what is referred to as a multipole expansion. It is described by the following equation [33]:

$$E_z(r, \varphi) = \sum_{m=-\infty}^{\infty} a_m \frac{e^{im\varphi}}{\sqrt{2\pi}} H_m^{(1)} \quad (2.2.5)$$

where the multipole moment  $a_m \propto \Delta\varepsilon$  and  $H_m$  is the complex Bessel function.

By virtue of the variational principle, the lowest order modes of a cavity feature a reduced number of nodes, i.e. fewer angular oscillations, and therefore by energy composition are found to consist primarily of the lowest-order components of the multipole expansion. The fundamental mode typically holds more than 50% of its energy capacity in either the monopole or dipole term (depending on its symmetry).

Optimization schemes for cavity Q-factors in photonic crystal slabs, in essence, target two aspects: the first relies on inducing gradual modifications in the angular distribution of the radiative profile such that the overlap with the light cone is minimized. It is often the case that the rise in Q-factor is at the expense of mode delocalization. While, the second aspect is based on inducing destructive interference amongst the radiating multipole moments. The latter is referred to as multipole cancellation and is usually the more effective method especially when applied to the lowest order multipole moments.

Theoretically speaking, any variation in the defect permittivity of the PhC cavity will affect all orders of the multipole moments, which is at the origin of the complexity in finding an optimal permittivity distribution analytically. Inverse computational approaches have been sought towards this end [34], [35]. However, the location of the permittivity modification within the defect will tend to specifically influence one or more multipole moments over the remaining set. A scheme has been recently proposed, which relies on the inverse-Fourier transform of the leaky components to pinpoint the lattice sites which contribute mostly to the radiative losses. When the permittivity was modified in Si iteratively at the respective positions, a Q-factor beyond  $5 \times 10^6$  was attained [36].

For the work carried out in this thesis, we rely on an automated optimization algorithm implemented by M. Minkov, which takes on a rather semi-heuristic approach [37]. The algorithm utilizes the guided-mode expansion technique for PhC eigenmode computation and further makes use of the Matlab genetic optimization toolbox for the optimization procedure of the figure-of-merit. For each of the common PhC designs in a triangular lattice, a set of PhC holes is identified which contribute the most towards the improvement of the Q-factor values. A first approach is to target PhC holes featuring the highest overlap with the field intensity of the respective modes. The holes can be either translated or modified in size. PhC hole translation tends to be more precisely determined in nanofabrication and is usually preferred. The  $n$  parameters applied for the optimization of a cavity design thus translate to an optimization problem in an  $n$ -dimensional Hilbert space. A genetic optimization algorithm that utilizes a relatively quick and accurate solver, such as with the guided-mode expansion technique, is well-suited to find the global maximum in such a problem.

### 2.3 Theory of Nonlinear Light-Matter Interaction in Photonic Crystal Cavities

Nonlinear optical effects are seldom observed in nature around us due to the high field strengths that are necessary to generate them, in addition to the minute response that is consequently produced. It was through the advancement of high-intensity, coherent radiation (and detectors alongside) that the field of nonlinear optics started



to grow. A common misconception has been that nonlinear effects in matter could only be brought about with either high-power or pulsed radiation. The employment of optical microcavities has been revolutionary in that respect, whereby through their field enhancement capacity, the power requirements for observing nonlinear effects was essentially reduced by a few orders of magnitude. It opened the door to the development of chip-scale nonlinear devices.

A nonlinear optical effect occurs when an interaction between an electromagnetic field and matter alters the optical response of a material in a reversible manner, where the induced polarization of the medium commonly deviates from a linear dependence with the field, albeit not a requirement\*. The interest in the study of nonlinear optics arises—in part—from the inherent nature of light, through which photon-photon interactions in vacuum are prohibited. An atomic system possessing a suitable electronic configuration can respond to light in a manner where two or more incident photons can undergo a correlated interaction through a single parametric or non-parametric process. Such process is mediated by a higher-order susceptibility contribution, which effectively enables an electromagnetic field to impact another electromagnetic field (interference effects aside), thus bringing about indirect photon-photon interactions. Some of the nonlinear optical effects include: self-/cross-phase modulation, harmonic generation, parametric down-conversion, and multi-photon absorption.

The initial state of an atomic system transitions to a virtual state during a nonlinear process, occurring on a time scale  $\Delta t < \frac{1}{2} \frac{\hbar}{\Delta E}$  in accordance with the uncertainty principle, since the virtual state is forbidden. Considering the energy of a visible-range photon for instance ( $\approx 2$  eV), one finds  $\Delta t$  to be on the order of  $10^{-16}$  seconds, making it one of the fastest occurring physical processes, which is why a nonlinear response is often deemed instantaneous.

### 2.3.1 Classical Theory: The Anharmonic Oscillator

At the origin of the nonlinear interaction is the polarization response of material, that is to say, the displacement of the electron cloud in response to an applied electric field. It can be understood in classical theory by considering the simple harmonic oscillator model of an electron bound to an atom, i.e. the Lorentz model. Under the application of a perturbing optical field, the electron will undergo acceleration such that it follows the oscillation of the driving field. Since the electron lies in a potential well that can be approximated to be parabolic under weak perturbation, the resulting restoring force is linear. The electron therefore oscillates at the same frequency of the perturbing field. In the presence of damping, the oscillation frequency is not pure, but rather exhibits a spread around the center frequency that is inversely proportional to the decay time. If the applied field were to be made more intense, the parabolic potential argument would no longer be valid. The potential well in that case can be described by higher-order polynomial terms and may as well be asymmetric. As a result, the restoring force will lose its linear profile, and the electron will exhibit anharmonic oscillation, which essentially is a collection of oscillating frequency components.

Since the quantitative measure of the polarization of a material is the sum of the constituent dipoles, the electron displacement analysis carries on to the susceptibility. The susceptibility can be decomposed into a linear response, i.e.  $\chi^{(1)}$ , and a higher order response  $\chi^{(i>1)}$ , whose components can be derived from the Lorentz model through perturbation analysis [38], [39]:

\*A nonlinear effect such as the electro-optic (Pockels) effect for instance, which modifies the local refractive index, exhibits a linear response with the incident field.

$$X^{(2)} = A \frac{Nq^3}{\epsilon_0 m^2} \frac{1}{[\omega_0^2 - (\omega_a + \omega_b)^2 - 2i(\omega_a + \omega_b)\gamma](\omega_0^2 - \omega_a^2 - 2i\omega_a\gamma)(\omega_0^2 - \omega_b^2 - 2i\omega_b\gamma)} \quad (2.3.1)$$

where  $A$  is the nonlinear strength,  $N$  is the atomic density,  $q$  is the electron charge,  $m$  is the electron mass,  $\omega_0$  is the intrinsic oscillation frequency of the electron,  $\omega_a$  and  $\omega_b$  are the incoming field frequencies, and  $\gamma$  is the damping constant.

The polarization is then expressed as a power series expansion in terms of the electric field:

$$\mathbf{P} = \epsilon_0 \sum_{i \geq 1} \chi^{(i)} \mathbf{E}^i \quad (2.3.2)$$

The higher-order susceptibilities ( $i > 1$ ) in a nonlinear material are described by a rank  $i + 1$  tensor, where  $i$  is the order of the susceptibility. The lowest-order nonlinearity is provided by the second-order polarization, which can be

expressed in terms of the nonlinear coefficients  $d_{ijk} = \frac{\chi_{ijk}^{(2)}}{2}$  as [40]:

$$P_i^{(2)} = \frac{\epsilon_0}{2^{n-1}} \sum_{\mathcal{P}(\omega_a, \omega_b)} \sum_{jk} d_{ijk}(\omega_c; \omega_a, \omega_b) E_{j, \omega_a} E_{k, \omega_b} \quad (2.3.3)$$

where  $\omega_c = \omega_a + \omega_b$ ,  $n$  is the total number of incident fields ( $n = 2$  in this case),  $\mathcal{P}(\omega_a, \omega_b)$  is the number of distinct permutations of the incoming fields, and  $i/j/k$  are cartesian coordinate indices.

The complexity of the susceptibility tensor is often reduced by the various symmetries that apply, whether they relate to the interchangeability of the electromagnetic fields (intrinsic or full permutation symmetry), the higher-order dispersion properties of the medium (Kleinman symmetry), or the inherent symmetry of the medium (Neumann's principle) [40]. Each crystal class will feature the same set of non-zero components that specify the material polarization response to the polarization of the incident fields. Taking for instance the case of wurtzite III-nitride semiconductors, their crystal structure belongs to point group  $C_{6v}$ , according to Schoenflies notation. The components of the second-order polarization can be analyzed to be:

$$\begin{bmatrix} P_x^{(2)} \\ P_y^{(2)} \\ P_z^{(2)} \end{bmatrix} = \epsilon_0 \begin{bmatrix} 0 & 0 & 0 & 0 & d_{15} & 0 \\ 0 & 0 & 0 & d_{15} & 0 & 0 \\ d_{31} & d_{31} & d_{33} & 0 & 0 & 0 \end{bmatrix} \begin{bmatrix} E_{x, \omega}^2 \\ E_{y, \omega}^2 \\ E_{z, \omega}^2 \\ 2E_{y, \omega} E_{z, \omega} \\ 2E_{x, \omega} E_{z, \omega} \\ 2E_{x, \omega} E_{y, \omega} \end{bmatrix} \quad (2.3.4)$$

Here, the nonlinear coefficients are expressed in contracted notation given that permutation symmetry holds. This compresses the final two indices of the susceptibility  $\chi_{ijk}$ , and similarly the nonlinear coefficient  $d_{ijk}$ , according to the following:

$$jk = \begin{bmatrix} 11 & 12 & 13 \\ 21 & 22 & 23 \\ 31 & 32 & 33 \end{bmatrix} = \begin{bmatrix} 1 & 6 & 5 \\ 6 & 2 & 4 \\ 5 & 4 & 3 \end{bmatrix} \quad (2.3.5)$$

Kleinman symmetry applies when operating far off resonance such that the dispersion of the susceptibility can be neglected. Along with the Neumann's principle which utilizes crystal symmetry, they bring the number of unique coefficients to a minimum, here to only three independent elements. For each specific crystal class, there are components within the nonlinear susceptibility which are typically dominant. In the case of wurtzite III-nitrides, the strongest contribution comes from the  $\chi_{333}^{(2)}$  component followed by  $\chi_{311}^{(2)}$  [40]. It is well known that centrosymmetric material lack even-order susceptibility due dipole cancellations that arise from their symmetry. This does not hold however should the symmetry be broken, e.g. at interfaces, and centrosymmetric media such as Si can as a result generate second-order nonlinearity.

### 2.3.2 Quantum Theory

The nonlinear optical response can be alternatively calculated through a quantum-mechanical approach, which does provide an accurate prediction for the magnitudes and symmetries of the nonlinearities. The derivation, in a similar manner to classical theory, relies on perturbation theory beginning with the time-dependent Schrödinger equation of an atomic wavefunction:

$$i\hbar \frac{\partial \psi}{\partial t} = (\hat{H}_0 + \hat{V}(t))\psi \quad (2.3.6)$$

The interaction Hamiltonian  $\hat{V}(t)$ , comprising the dipole moment operator, is introduced to the total Hamiltonian  $\hat{H} = \hat{H}_0 + \lambda \hat{V}(t)$  in a perturbative approach using the strength parameter  $\lambda$ . A wavefunction solution can be found as a power series, where the perturbation orders satisfy:  $i\hbar \frac{\partial \psi^{(i)}}{\partial t} = \hat{H}_0 \psi^{(i)} + \hat{V}(t) \psi^{(i-1)}$  for  $i \geq 1$ . The wavefunction is expressed as an expansion in terms of an orthonormal basis set:  $\psi^{(i)}(\mathbf{r}, t) = \sum_n a_n^{(i)}(t) u_n(\mathbf{r}) e^{-i\omega_n t}$ , where  $u_n$  is the spatial wavefunction satisfying the time-independent Schrödinger equation,  $n$  is the eigenstate index, and  $a_n^{(i)}$  is the time-dependent probability amplitude of occupying the eigenstate  $n$ , under the  $i^{th}$  order of the perturbation.

After computing the higher-order corrections to the probability amplitudes  $a_n^{(i)}$ , the expectation value of the dipole moment of a given order can be obtained through:  $\langle \mathbf{d} \rangle = \langle \psi | \hat{\boldsymbol{\mu}} | \psi \rangle$  where  $\hat{\boldsymbol{\mu}} = -q\hat{\mathbf{r}}$  is the dipole moment operator. The polarization is then retrieved by accounting for the atomic density ( $N$ ):  $\mathbf{P}^{(i)} = N \langle \mathbf{d}^i \rangle$ . For a thorough derivation of the nonlinear susceptibilities, the reader is referred to [38], [39], where the second-order susceptibility is computed to be:

$$X_{ijk}^{(2)}(\omega_c; \omega_a, \omega_b) = \frac{N}{\epsilon_0 \hbar^2} \mathcal{P} \left( \sum_{n,o} \frac{\mu_{mo}^i \mu_{on}^j \mu_{nm}^k}{(\omega_{om} - \omega_c)(\omega_{nm} - \omega_a)} + \frac{\mu_{on}^i \mu_{mo}^j \mu_{nm}^k}{(\omega_{om}^* + \omega_b)(\omega_{nm} - \omega_a)} + \frac{\mu_{nm}^i \mu_{on}^j \mu_{mo}^k}{(\omega_{om}^* + \omega_b)(\omega_{nm}^* + \omega_c)} \right) \quad (2.3.7)$$

Here,  $\{m, n, o\}$  are the state indices, and a summation is performed over all existing states through indices  $n$  and  $o$ .  $\mathcal{P}$  represents the permutation over the participating fields  $\omega_a$ ,  $\omega_b$ , and  $\omega_c = \omega_a + \omega_b$ . The above expression demonstrates how the second-order nonlinearity scales with the transition dipole moments between the states in addition to the atomic density. Also, the susceptibility can peak significantly if resonance can be attained, which

requires the existence of more than one resonant state in the system. Higher order susceptibilities are derived in a similar manner, accounting for an additional field contribution with every step in the order of the nonlinearity.

The density matrix formalism is typically used to compute the nonlinear susceptibility of atomic ensembles. It offers the advantage of accounting for broadening effects in atomic resonances in contrast to the previous analysis, where each state was considered to be a delta function in the spectrum. A system is described by a density matrix  $\rho_{nm}$ , which carries information on the occupation probability of the eigenstates and the coherence between them, and state decay is accounted for through a phenomenological damping rate  $\gamma_{nm}$ . For computing the nonlinear susceptibility, a similar perturbation approach to the one used with the atomic wavefunction is followed but applied to the density matrix equation of motion:  $\dot{\rho}_{nm} = \frac{-i}{\hbar} [\hat{H}, \hat{\rho}]_{nm} - \gamma_{nm}(\rho_{nm} - \rho_{nm, equilibrium})$ . A detailed derivation can be found in [38], [41]. The outcome bears close resemblance to the atomic wavefunction approach. The contribution towards the susceptibility originates from the transition dipole moments and frequencies, but also the dipole dephasing rates introduced by the damping terms. Furthermore, an additional term appears in the susceptibility which accounts for the population of the states. It is noteworthy that the dipole dephasing is the only contribution towards the susceptibility that is not an inherent property of the material, but rather depends on the environment.

### 2.3.3 Theoretical Conversion Efficiency: Coupled Mode Theory Analysis

In order to clarify the nonlinear light-matter interaction picture in a PhC defect cavity, where the input light becomes localized, it is necessary to comprehend the traditional nonlinear frequency conversion process of light which involves propagating light beams. The latter makes use of a highly-nonlinear bulk crystal that is placed in the optical path of a pump laser beam. The crystal is oriented in such a way to optimize the susceptibility tensor components relative to the optical fields, whilst simultaneously minimizing the phase mismatch between the fundamental signal and the generated harmonic, according to the implemented phase-matching scheme. In a co-propagating configuration of the interacting light frequencies, phase matching is an essential requirement that ensures net energy transfer from the induced polarization in the material to the generated harmonic wave.

Considering the case of second-harmonic generation, conversion from the fundamental to the harmonic signal occurs with increasing efficiency, given by the quadratic dependence of the second-harmonic intensity on the propagation length [40]. This occurs up to a coherence length  $l_{coherence} = \frac{\pi}{\Delta k}$ , which is specified by the phase mismatch  $\Delta k = k_{2\omega} - 2k_{\omega} = n(2\omega) - n(\omega)$ , beyond which the conversion efficiency drops as the second-order polarization becomes out of phase with the generated harmonic signal, and back-conversion to the fundamental frequency takes place.

The efficiency of a nonlinear frequency conversion process is specified by the ratio of the power of the generated signal relative to the pump power. With SHG for instance in the undepleted pump regime (i.e. the pump intensity is assumed to be constant as a function of propagation length), the conversion efficiency ( $\eta_{SHG}$ ) for a fixed propagation length  $l$  is given by:

$$\eta_{SHG} = \frac{P_{SHG}}{P_{pump}} = \frac{I_{SHG}}{I_{pump}} = \frac{1}{\epsilon_0 c^3} \frac{(\omega_{pump} \chi^{(2)} l)^2}{n_{\lambda_{pump}}^2 n_{\lambda_{SHG}}} \left( \frac{\sin \Delta k l}{\Delta k l} \right)^2 \quad (2.3.8)$$

Moving onto a PhC cavity geometry, an enhancement factor in the nonlinear process emerges from the spatial confinement and temporal build-up of light, which collectively result in higher field strength per unit length within the modal volume. The dependence of this factor on the cavity parameters can be derived from the nonlinear coupling term that relates the fundamental and harmonic signals, through coupled mode theory analysis. Such treatment is not restricted to PhC cavities but rather applies broadly to optical cavities that feature a combination

of optical nonlinearity and one or more states that are resonant with the participating optical fields. The following description is based on the coupled-mode theory framework presented in [42] and the analysis carried out in [43], [44].

The time dependence of a resonant mode is given by:

$$\dot{a}_n = (i\omega_n - \tau_n^{-1})a_n \quad (2.3.9)$$

where  $\omega_n$  is the harmonic frequency of the mode and  $|a_n|^2$  gives the total mode energy. The decay rate of the mode  $\tau_n^{-1} = \tau_{n,loss}^{-1} + \tau_{n,coupling}^{-1}$  accounts for both the rate of intrinsic losses  $\tau_{n,loss}^{-1}$  and energy decay  $\tau_{n,coupling}^{-1}$  through the coupling port. It can be similarly formulated through the Q-factors as  $Q_n^{-1} = Q_{n,loss}^{-1} + Q_{n,coupling}^{-1}$ . Under weak coupling ( $\omega_n \tau_n \gg 1$ ), the time evolution of the fundamental mode can be expressed as:

$$\dot{a}_0 = \left(i\omega_0 - \frac{\omega_0}{2Q_0}\right)a_0 + \sqrt{2\tau_{0,coupling}^{-1}}s_{0+} \quad (2.3.10)$$

The total incoming (+) and outgoing (-) power through the coupling port  $s_{n\pm}$  can be obtained through  $|s_{n\pm}|^2$ , and these quantities are linked by the following expression:

$$s_{0-} = -Cs_{0+} + \sqrt{2\tau_{0,coupling}^{-1}}a_0 \quad (2.3.11)$$

The first term of the equation expresses the direct scattering pathway through scattering matrix C which takes the form of a diagonal matrix [43].

Now, in the presence of a second resonant mode  $a_1$  that matches the condition:  $\omega_1 = 2\omega_0$ , the two states are linked in a nonlinear medium through a second-order nonlinearity by a nonlinear coupling term  $\beta_{\chi^{(2)}}$ , with either a second harmonic generation (SHG) or parametric down-conversion (PDC) process. This gives the following coupled-mode equations under the rotating-wave approximation:

$$\dot{a}_0 = \left(i\omega_0 - \frac{\omega_0}{2Q_0}\right)a_0 + \sqrt{2\tau_{0,coupling}^{-1}}s_{0+} - i\omega_0\beta_{\chi^{(2)},PDC}a_1a_0^* \quad (2.3.12)$$

$$\dot{a}_1 = \left(i\omega_1 - \frac{\omega_1}{2Q_1}\right)a_1 + \sqrt{2\tau_{1,coupling}^{-1}}s_{1+} - i\omega_1\beta_{\chi^{(2)},SHG}a_0^2 \quad (2.3.13)$$

It should be noted that the coupling terms are linked through conservation of energy by [44]:

$$\omega_0\beta_{\chi^{(2)},PDC} = \omega_1\beta_{\chi^{(2)},SHG}^* \quad (2.3.14)$$

Fig. 2.3.1 displays a schematic diagram of the coupled-mode model of a dual-resonance configuration, comprising a second-order nonlinearity.

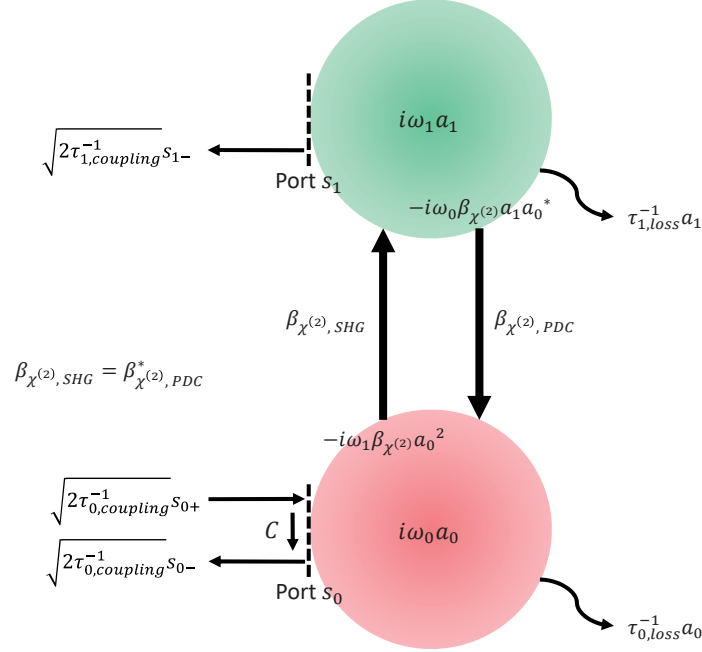


Fig. 2.3.1 Schematic diagram of the coupled theory model applied to a system exhibiting  $\chi^{(2)}$  nonlinearity, presenting second harmonic generation (SHG) and parametric down-conversion (PDC).

Since there is no direct coupling to the amplitude  $a_1$ , the port  $s_{1+}$  is equated to zero. The nonlinear coupling coefficients can then be deduced to be (a detailed derivation can be found in Appendix A):

$$\beta_{\chi^{(2)},PDC} = \frac{1}{4} \frac{\int_{-\infty}^{\infty} \sum_{ijk} \epsilon_0 \chi_{ijk}^{(2)} (E_{0i}^* E_{1j} E_{0k} + E_{0i} E_{0j}^* E_{1k}) d^3 \mathbf{r}}{(\int_{-\infty}^{\infty} \epsilon |\mathbf{E}_0|^2 d^3 \mathbf{r}) (\int_{-\infty}^{\infty} \epsilon |\mathbf{E}_1|^2 d^3 \mathbf{r})^{\frac{1}{2}}} \quad (2.3.15)$$

$$\beta_{\chi^{(2)},SHG} = \frac{1}{4} \frac{\int_{-\infty}^{\infty} \sum_{ijk} \epsilon_0 \chi_{ijk}^{(2)} E_{1i} E_{0j} E_{0k} d^3 \mathbf{r}}{(\int_{-\infty}^{\infty} \epsilon |\mathbf{E}_0|^2 d^3 \mathbf{r}) (\int_{-\infty}^{\infty} \epsilon |\mathbf{E}_1|^2 d^3 \mathbf{r})^{\frac{1}{2}}} \quad (2.3.16)$$

It becomes clear that the nonlinear process scales directly with the nonlinear susceptibility  $\chi_{ijk}^{(2)}$ , as well as with a factor  $(\int_{-\infty}^{\infty} \epsilon |\mathbf{E}_n|^2 d^3 \mathbf{r})^{-\frac{1}{2}}$  that is representative of the inverse square-root mode volume ( $V$ ) of each participating field in the process. The nonlinear coupling coefficients can be expressed in terms of the modal volumes ( $V_i$ ) as:

$$\beta_{\chi^{(2)},PDC} = \frac{1}{4} \frac{\int_{-\infty}^{\infty} \sum_{ijk} \varepsilon_0 \chi_{ijk}^{(2)} (E_{0i}^* E_{1j} E_{0k}^* + E_{0i}^* E_{0j}^* E_{1k}) d^3 \mathbf{r}}{\left(V_0 V_1^{\frac{1}{2}}\right) (\max[\varepsilon(\mathbf{r}) |E_0|^2]) (\sqrt{\max[\varepsilon(\mathbf{r}) |E_1|^2]})} \quad (2.3.17)$$

$$\beta_{\chi^{(2)},SHG} = \frac{1}{4} \frac{\int_{-\infty}^{\infty} \sum_{ijk} \varepsilon_0 \chi_{ijk}^{(2)} E_{1i}^* E_{0j} E_{0k} d^3 \mathbf{r}}{\left(V_0 V_1^{\frac{1}{2}}\right) (\max[\varepsilon(\mathbf{r}) |E_0|^2]) (\sqrt{\max[\varepsilon(\mathbf{r}) |E_1|^2]})} \quad (2.3.18)$$

The normalized conversion efficiency of second harmonic generation process is constant in the non-depletion regime and can be computed through:

$$\begin{aligned} \eta_{SHG} &= \frac{P_{\omega_1}}{P_{\omega_0}^2} = \frac{|s_{1-}|^2}{|s_{0+}|^4} = 128 \frac{Q_0^4 Q_1^2 |\beta_{\chi^{(2)}}|^2}{\tau_{0,coupling}^2 \tau_{1,coupling} \omega_0^3 \omega_1} \\ &= 32 \frac{(\eta_0 Q_0)^2 \eta_1 Q_1 |\beta_{\chi^{(2)}}|^2}{\omega_0} \end{aligned} \quad (2.3.19)$$

Here, we define the external coupling efficiency to a cavity mode  $\omega_n$  through the coupling port by:

$$\eta_n = \tau_n / \tau_{n,coupling} \quad (2.3.20)$$

The full enhancement factor of the nonlinear process arising from the cavity is now evident. First, there is the Q-factor contribution providing the resonant enhancement, which scales as  $Q^{(i)}$  for  $i$  participating resonant fields in  $i^{th}$  order process. Then there is the external coupling efficiency  $\eta$ , which gives a similar scaling behavior with respect to each of the participating fields. Moreover, the  $|\beta_{\chi^{(2)}}|^2$  factor provides an inverse mode volume scaling for each field. Assuming that all participating modes in the process have identical mode volumes, i.e.  $V_0 = V_1 = V$ , the nonlinear overlap factor in the numerator will approximately reduce the final mode volume scaling of the second-order process efficiency to  $V^{-1}$ . Thus, the efficiency of the process in total will be proportional to  $\frac{(\eta_0 Q_0)^2 \eta_1 Q_1}{V}$ . In the case of a singly resonant process at  $\omega_0$ , the analysis of absolute conversion efficiency becomes non-trivial due to the lack of a truly confined mode at the second harmonic frequency. A PhC lattice may still support one or more guided modes at  $\omega_1$  that have low photon lifetimes such that  $\frac{\tau_1}{\tau_0} \ll 1$ . The nonlinear process retains the scaling factor at the fundamental frequency:  $(\eta_0 Q_0)^2 |\beta_{\chi^{(2)}}|^2$ , and in the limit that  $V_1 \gg V_0$ , the inverse volume scaling in the  $|\beta_{\chi^{(2)}}|^2$  factor will lose its dependence on  $V_0$ . It should be noted that the dependence of the efficiency of a singly-resonant second order process on  $V_0$  has not been experimentally confirmed yet, with various scaling factors being proposed [45], [46].





# 3. Fabrication of III-Nitride Planar Photonic Crystals

## 3.1 Introduction

The general strategy for the fabrication of photonic crystals is primarily dictated by the geometry of the conceived design and the imperfection tolerances associated with the wavelength of operation. Two-dimensional slab structures have been and still are the most popular implementation of PhCs, motivated on one hand by the desire for on-chip integration, especially with the prevalence of the semiconductor industry. On the other hand, the existing state of fabrication technology provides for relative ease of fabrication using planar layers. More complex PhC geometries are desirable, yet their realization faces persisting technical challenges, those of which set a boundary on the permissible scale and extent of the manipulation of matter. This has been a major obstacle for instance in the progress of three-dimensional PhCs, in the quest for ultimate control over light.

The top-down fabrication approach, adopted from integrated-circuit processing, is well established and widely employed, mainly for its reliability and efficiency. A layer of interest may be patterned through a sequence of lithography and etching steps. Alternatively, material can be deposited after carrying out lithography, e.g. by an evaporation and lift-off procedure. For obtaining the finest possible patterning resolution in PhCs, either electron-beam (e-beam) lithography or focused-ion-beam (FIB) milling can be employed. The former is more time efficient and avoids layer damage, while the latter is advantageous when material etching with standard techniques is problematic. Both tools are comparable in terms of resolution, as they can go down to a limit in the range of 1 to 5 nm. This is already very close to atomic-scale lithography. Since FIB milling relies on a physical sputtering mechanism, direct patterning of layers may not produce the same sidewall quality as compared to a plasma etching process that is often performed after e-beam lithography, since it utilizes reactive chemical species. Photonic crystal fabrication by conformal growth has also been shown to be an effective way to circumvent etching material in target semiconductor layers [47].

With regard to three-dimensional photonic crystals, bottom-up approaches have been mainly utilized [48], relying on self-assembly. Yet, such techniques suffer from limited control over lattice features and design parameters. In addition, structural defects that are usually generated may destroy the functionality of the device. Other fabrication attempts involve micromanipulation [49] and holographic lithography [50], [51], with the latter being more suited for structures operating at longer wavelengths due to its resolution. Current integrated circuit fabrication techniques employing layer-by-layer processing are not well-adapted for quick and reliable fabrication of three-dimensional photonic crystal structures. Nevertheless, there have been several demonstrations using top-down fabrication strategy [52], [53]. In a more exciting approach, three-dimensional semiconductor photonic crystals were obtained through template-directed epitaxial growth, producing functional active devices [54].

Processing of wide bandgap semiconductors such as AlN, GaN, and SiC is perceived as being challenging due to their intrinsically high bond strength. While that provides for many of the outstanding properties that these materials exhibit, it often presents difficulty in terms of material etching. Plasma-based etching [55] and wet chemical etching techniques [56] have been developed, offering varying extents of roughness and anisotropy. Another commonly encountered challenge is the membraning of the semiconductor layers for the purpose of achieving maximum optical confinement within a photonic crystal slab. Wide bandgap semiconductors are typically prepared by

heteroepitaxial vapor growth on host substrates, whether through molecular beam epitaxy (MBE) or metalorganic chemical vapor deposition (MOCVD). Undercut etching of substrates such as sapphire, SiC, or GaN is a particularly challenging task. Nonconventional techniques like photo-electrochemical etching can be carried out on SiC or GaN substrates [56], and it has been successfully utilized for suspending AlN photonic crystals on SiC [57]. This process relies on sacrificial layers that are introduced during growth [58]. Several research groups have also resorted to alternative approaches such as layer transfer [59], adopted from the fabrication of GaN HEMT devices [60], to overcome this issue. The layer transfer technique presents the possibility for integration with silicon technology [61], as the growth substrate can be eliminated entirely after relocating the layer of interest to a host substrate.

The fabrication process described in this chapter is tailored towards the fabrication of integrated optical components in III-nitride layers that are grown on Si. While heteroepitaxial growth on Si(111) wafers does not provide layers of superior crystalline quality, it is a suitable platform as proof-of-concept for the integration capability of wide bandgap semiconductors. The fabrication process was developed throughout 2014, based on standard semiconductor micro- and nanofabrication techniques, and assisted in part by previous III-nitride fabrication trials reported in literature. The processing steps and sequence were designed to minimize the impact of fabrication imperfection on the performance of PhCs, within the capacity of the available tools. Micro- and nanostructures of high quality and stability have been realized using the reported process, achieving state-of-the-art performance values for GaN optical devices.

## 3.2 Process Overview

A short summary of the fabrication process will be initially provided before discussing the details of important fabrication steps, each in their respective section. The fabrication process, displayed in Fig. 3.2.1, commences with the growth of III-nitride layers<sup>\*,†</sup>, primarily using internal facilities at EPFL. The layers used for principle investigations into wide bandgap material were prepared using MOCVD, and it will therefore be elaborated on in section 3.3. It should be noted that from this point onwards, the fabrication will refer to GaN layers epitaxially grown on Si(111), for the sake of clarity. Similar considerations apply to AlN layers for the majority of the fabrication steps, unless where explicitly noted.

Following layer growth, the wafers are stored in an enclosed nitrogen atmosphere to prevent adsorption and incorporation of oxygen in GaN [62], as well as potential surface oxidation [63]. The wafers then undergo thorough characterization as outlined in section 4.2, mostly through non-invasive measurements including X-ray diffraction and optical techniques to determine crystal quality, the optical response, layer dimensions, and some additional physical properties. This helps identify whether the wafer fits the fabrication criteria, and furthermore, it determines the target regions of the wafer for patterning. Once complete, the wafer in-hand undergoes thorough cleaning using a sequence of: acetone immersion in an ultrasonic bath, followed by isopropanol (IPA) rinsing, then blow-drying using a nitrogen gun. A SiO<sub>2</sub> layer is then deposited on the surface afterwards using plasma-enhanced chemical vapor deposition (PECVD) at a rate of 0.9 nm/s, which acts as a hard mask for subsequent etching of the III-nitride layer. The thickness of the III-nitride layer (200–350 nm) to be etched determines the required thickness of the SiO<sub>2</sub> film, the latter typically being between 75 nm and 100 nm.

\* MOCVD layers were prepared by J. F. Carlin, while MBE layers were prepared by D. Martin and S. Tamariz from the Laboratory of Advanced Semiconductors for Photonics and Electronics (LASPE).

† Sputtered AlN layers were prepared either internally at the Center of MicroNanoTechnology (CMI), using the Pfeiffer Spider 600 magnetron sputtering system, or obtained from Evatec AG.

### 3. Fabrication of III-Nitride Planar Photonic Crystals

Sample preparation for the lithography process comes next, beginning with a two-minute heating of the wafer at 180°C to ensure that the surface is free of condensation. Adhesion primers are not added to the wafer surface before spin coating. The wafer is left to cool down to room temperature before initiating the spin coating of ZEP-520A resist. ZEP is a positive-tone resist that is suitable for electron-beam writing. It has been selected primarily for its capacity to obtain high resolution patterns, in addition to its etch resistivity and exposure sensitivity. For a SiO<sub>2</sub> layer that is approximately 100 nm thick, a 310 nm layer of ZEP is required. The spin coating step is done using an automated recipe at a spin speed of 6000 rpm for a 60 s duration, preceded by a 5 s pre-spin step at 500 rpm to initially spread the resist evenly across the sample. If a resist thickness below 250 nm is needed, ZEP should be diluted to a 50% solution using anisole beforehand (o-Dichlorobenzene also functions as a thinner). The wafer is then immediately baked for 3 minutes at 180°C, then left to cool down. The spin coating procedure should be carried out shortly before the exposure to ensure that the resist retains its stability and performance.

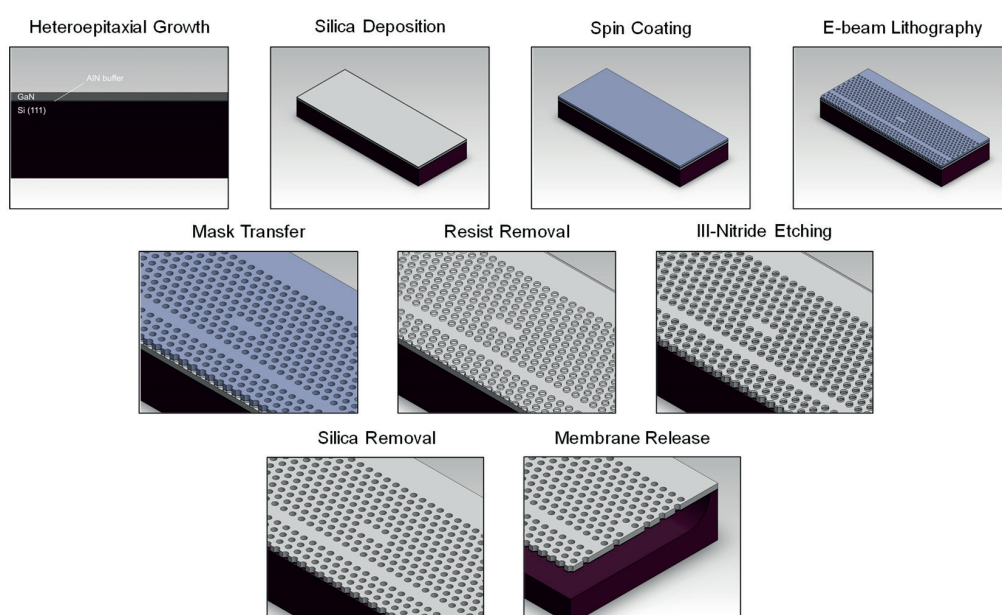


Fig. 3.2.1 Schematic diagram illustrating the steps of the fabrication process of III-nitride PhCs on Si.

The lithography is then carried out using e-beam patterning to obtain the nm-scale features required for photonic crystals. The Vistec EBPG5000 e-beam lithography tool was used throughout all the exposures, providing a beam energy of 100 keV. The beam size and current was adjusted in accordance with the pattern to optimize both feature resolution and writing time. While deep UV photo-lithography may offer an alternative to e-beam writing and has been demonstrated to achieve high quality factor photonic crystals in the near-IR range [64], the process is limited in terms of critical dimension and is still in the development stages. Furthermore, mask creation can be costly and does not offer the versatility needed to freely alter the lithography pattern compared to vector scanning in e-beam writing.

After e-beam exposure, the wafer was developed manually by a process of immersion and agitation in a solution of n-amyl acetate for 1 minute, followed by immersion in solution of methyl isobutyl ketone (MIBK) and IPA (mixing ratio of 90:10 respectively) for 1 minute. The former immersion functions as the ZEP developer, while the latter serves to halt the development. The wafer is finally rinsed with IPA before blow drying using a nitrogen gun. At this stage, the wafer is examined using an optical microscope to ensure that the pattern has been cleared. For dimensions below the diffraction limit of light, scanning electron microscope (SEM) examination can be done under low acceleration voltage (near 0.7 kV), preferably on disposable or dedicated features within the pattern.

The wafer then undergoes an SiO<sub>2</sub> etch process to transfer the ZEP mask. This is performed using inductively-coupled plasma reactive ion etching (ICP-RIE). Since most of the processing machines are mainly compatible with 4-inch wafer processing, 2-inch wafers as well as wafer chips require that they be attached to a carrier wafer. This is done using either kapton tape or thermoplastic mounting. The bottom surface of the wafer or chip must not be contaminated beforehand to ensure optimal thermal transport to the carrier wafer, which is temperature controlled. A gas mixture of CHF<sub>3</sub> and SF<sub>6</sub> is used for the plasma etching process. Once complete, the ZEP resist is removed by immersion in acetone in a low-power ultrasonic bath (for approximately 5 minutes), followed by IPA rinsing and nitrogen drying. A one-minute O<sub>2</sub> plasma ashing of the resist (80 W) may be performed afterwards if ZEP traces remain.

The wafer at this stage has the lithography pattern embedded in the hard SiO<sub>2</sub> mask which is ready for transfer to the III-nitride layer. The wafer will have to be attached in a similar manner to a carrier wafer for the next step. ICP-RIE etching of the wafer is performed using chlorine-based chemistry in a controlled manner to effectively etch the GaN layer and achieve vertical and smooth side walls. The SiO<sub>2</sub> thickness is chosen such that with the selectivity of the etch recipe, a layer of SiO<sub>2</sub> at least 20 nm thick remains to protect the GaN surface underneath. Once complete, cleaving of the wafer is done using a semi-automatic cleaving tool. It helps obtain cleave marking accuracy better than 25 μm if appropriate calibration is done. Cleaving accuracy down to 10 μm has been achieved with the tool, although with medium-to-low reproducibility. Breaking of the sample chips can be either done on the tool or manually. The SiO<sub>2</sub> layer is retained throughout the cleaving to ensure proper protection of the GaN surface. Since wafer debris is generated in the process, a through solvent cleaning in an ultrasonic bath is to be conducted afterwards in a similar manner to that done with the initial wafer cleaning.

Next, the remaining SiO<sub>2</sub> layer is removed. It is dissolved by immersing the sample in 40% HF for 5 minutes. This guarantees that the silica layer is entirely removed, along with surface contaminants. Additionally, the HF treatment helps eliminate the native oxide (Ga<sub>2</sub>O<sub>3</sub>) [65] and reduce the surface oxygen concentration on the GaN layer [66]. The immersion is followed by multiple rinsing cycles in deionized water until the HF is completely diluted and the pH returns to neutral. Appropriate safety precautions for HF handling and disposal should be taken while carrying out this step. Following the rinse cycles, the sample is immersed in IPA then nitrogen dried. In the case that suspended membranes are present on the sample at this stage (if membrane release is done beforehand), then supercritical drying of the sample with CO<sub>2</sub> is to be carried out instead after the immersion. This step is mandatory to protect delicate features that can be affected by tension.

The final step of the fabrication process involves releasing the III-nitride layer to form a suspended membrane. A delicate vapor-phase etching process has been selected for this step using XeF<sub>2</sub> gas, which is compatible with both GaN and AlN. The etch process is highly Si-selective and therefore leaves the III-nitride layer in an unaltered state. No further cleaning of the sample is necessary, unless debris from the etch chamber is transferred onto the sample surface. In that case solvent cleaning and the aforementioned supercritical drying should be performed.

### 3.3 Layer Growth

Several methods exist for the vapor-phase growth of epitaxial layers, including MBE, MOCVD, and hydride vapor-phase epitaxy (HVPE). MOCVD was the primary method employed for the growth of III-nitride layers and will therefore be detailed in this section. MOCVD, otherwise known as metalorganic vapor-phase epitaxy (MOVPE), is a vapor-phase technique that enables the growth of crystalline layers by making use of high-purity metalorganic precursor molecules, hydride molecules, and a carrier gas medium to initiate a chemical reaction at the host surface, which triggers growth. MOCVD growth, in contrast to MBE, takes place under thermal equilibrium conditions on the heated sample surface, which is temperature controlled and can go as high as approximately 1500°C. This growth technique is particularly popular in the semiconductor industry for its ability to achieve high growth rates.

### 3. Fabrication of III-Nitride Planar Photonic Crystals

A simplified diagram of the growth process of GaN is displayed in Fig. 3.3.1. The precursor gases, trimethylgallium (TMGa) and  $\text{NH}_3$  in the case of GaN growth, are injected into the low-pressure growth chamber where their volatile molecules are transported by the carrier gas, e.g.  $\text{H}_2$ , closer to the surface of the substrate. During its path, TMGa may decompose into dimethylgallium, monomethylgallium, or gallium [67]. These various organometallic molecules form complexes with  $\text{NH}_3$ , which dissociate at the host wafer surface. The complexes can undergo methyl elimination once the free energy activation barrier is overcome [68], and the growth elements are adsorbed at the growth interface where they contribute to the crystal growth. Methane is formed in the process. Elements may also adsorb to the growth surface through sequential decomposition route. According to the kinetics at the growth interface, elements undergo surface diffusion and can also desorb from the surface back to the ambient atmosphere. Crystal growth initially occurs around the nucleation seeds which induce island formation. These islands progressively grow and coalesce until step growth dominates.

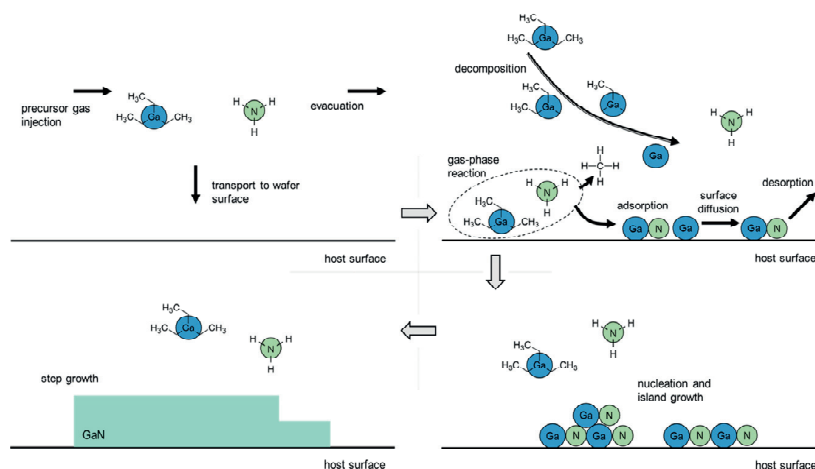


Fig. 3.3.1 Illustration of epitaxial semiconductor growth process by metalorganic chemical vapor deposition. The growth steps progress in the sequence indicated by the arrows.

The growth of GaN on Si requires the use of Si(111) wafers, which are commercially readily available, in order to provide a similar crystallographic basis on the surface upon which c-axis growth of hexagonal III-nitrides can be performed. The successful growth of GaN on Si has been enabled by the use of an AlN buffer between the two layers [69]. AlN has a relatively small lattice mismatch with GaN in comparison to Si. Furthermore, the AlN buffer prevents induced etching of the Si surface by Ga as well as the formation of Ga-Si eutectic [70]. GaN that is grown directly on Si(111) is N-polar and exhibits a rough surface, while that grown on an AlN buffer is Ga-polar [71].

The growth of III-nitride layers was carried out in an Aixtron AIX200 RF-S horizontal reactor by J.-F. Carlin. The Si wafer is first heated above  $1000^\circ\text{C}$  in a  $\text{H}_2$  ambient for a duration of one minute as a standard cleaning step to eliminate contamination on the surface. Next, the growth of the AlN buffer layer is initiated at a temperature of  $1070^\circ\text{C}$  using trimethylaluminum and  $\text{NH}_3$  precursors, and  $\text{N}_2$  as a carrier gas. The nucleation mechanism takes place as described earlier, and AlN grows at a rate of  $1.4 \text{ \AA/s}$ . The buffer layer is grown to a thickness of typically 40 nm and higher to avoid Ga-Si eutectic formation. When transitioning to GaN growth, the temperature is reduced to  $1000^\circ\text{C}$ . The gas precursors are switched to TMGa and  $\text{NH}_3$ , and  $\text{H}_2$  is used as the carrier gas with addition of  $\text{N}_2$ . This gives a growth rate of  $2.8 \text{ \AA/s}$ , twice that of AlN, which is maintained until the target thickness is reached. An in-situ reflectometry measurement is done in real time to probe the growth rate and thickness of the layers with nm accuracy. The resulting GaN layer is c-axis oriented and metal-polar Ga-face.

The primary impurity that is incorporated in the III-nitride layers is oxygen, as it cannot be entirely eliminated from the precursor gases, notably the presence of  $\text{H}_2\text{O}$  impurity in ammonia [72]. The concentration of oxygen in the

layers can range between  $10^{16}$ – $10^{17}$   $\text{cm}^{-3}$ , and it results in absorption just under the bandgap in both GaN and AlN [73]. During lattice-mismatched growth, plenty of defects are created which can reach densities in excess of  $10^{10}$   $\text{cm}^{-3}$ , especially in the AlN nucleation layer [74]. They include misfit, edge, threading, and screw dislocations. This is evident from the rocking-curve measurements presented in section 4.2.1.

## 3.4 E-beam Lithography

### 3.4.1 Overview

Amongst the existing nanofabrication toolset, e-beam lithography is currently the tool of choice for fabricating features with nm-scale critical dimensions. In comparison with other fabrication techniques, it strikes a good balance between accuracy, precision, time requirement, and degree of complexity. The patterning mechanism makes use of a high-energy electron beam that can induce changes in the molecular structure of a resist material, commonly a polymer, whether by molecular chain scission (typically positive resist) or cross-linking (typically negative resist) when the exposure dose surpasses a threshold value. The resist is then developed by a chemical solution that dissolves chains of a specific molecular weight distribution or terminations. The e-beam lithography process utilizes a top-down fabrication approach which relies on mask creation followed by either material etching or deposition. It may be the case that the material to be patterned also functions as a resist, e.g. SU8, and thereby a chemical development step would be sufficient.

A standard e-beam lithography tool, as displayed in Fig. 3.4.1 (a), consists of an electron source (referred to as an electron gun) which generates electrons by either thermal or field emission (or a combination of both) in an ultra-high vacuum atmosphere. After an electron extraction unit, a gun alignment module comprising a set of coils adjusts the shift and tilt of the e-beam relative to the electron column axis. This is followed by a series of electromagnetic lenses that focus and adjust the e-beam size, as well as a blanking unit that serves to temporarily and rapidly switch on/off the e-beam in between the vector scan steps. Towards the lower end of the column, a focusing lens and a series of deflectors for the main field and the subfield are present, which are usually composed of a combination of magnetic and electrostatic lenses for long and short-range deflection, respectively [75]. At the final stage of the column are the fine focusing lenses and the stigmation control system.

Electron beams that are generated using a dedicated e-beam system—rather than a scanning electron microscope comprising a writing module—have an energy near 100 keV and upwards. The necessity to accelerate electrons to such high energy serves primarily to reduce the minimum attainable focal spot size, thereby increasing the writing resolution. When electrons are incident on a material at high energy, both elastic and inelastic scattering processes take place upon collision. X-rays are also generated in the process due to the deceleration of electrons, and depending on the material composition, cathodoluminescence may also be generated. Forward scattering occurs as the electron beam traverses the material, i.e. low-angle diffusion of electrons takes place as a result of Coulomb interactions with the electron cloud of the atoms. Secondary electrons are also generated when inelastic collisions occur, and their lower energy compared to the beam implies that they follow random walks in the material. Additionally, some electrons are backscattered when they collide elastically with the atomic nuclei, and their direction of travel is reversed. The interactions collectively cause the electron beam to diverge, and the beam cross-section increases in diameter with penetration depth. This is illustrated in Fig. 3.4.1 (b), which shows a Monte Carlo simulation of a 5 nm-diameter e-beam possessing an energy of 10, 30, and 100 keV incident upon a 350 nm layer of GaN on a Si substrate. The 30 keV beam energy is currently the highest magnitude offered by common scanning electron microscope (SEM) tools. From the comparison of the different beam energies in the figure, it is apparent how a higher acceleration voltage can maintain the beam size as a function of distance travelled to achieve an even exposure over the focal volume.

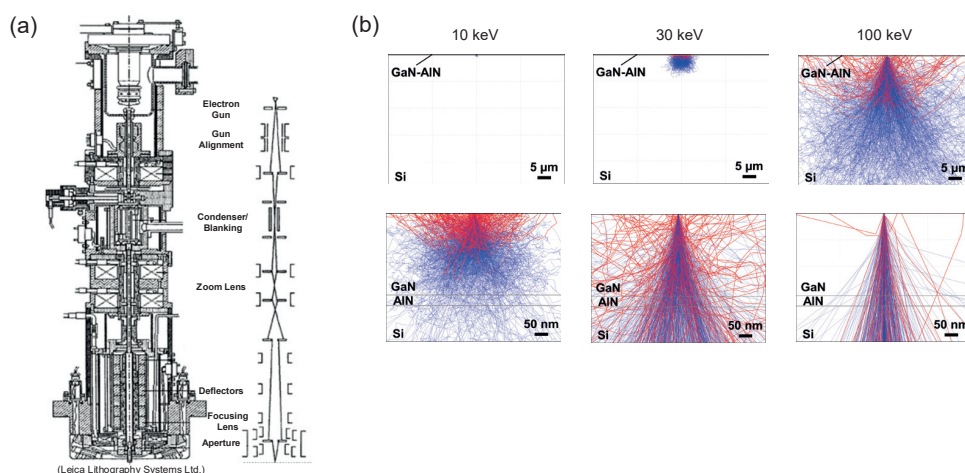


Fig. 3.4.1 (a) Cross-sectional view of a Vistec VB6 e-beam tool displayed on the left side, and a simplified diagram of the beam path is illustrated adjacent to it (right side). (b) Monte Carlo simulation of a 5 nm-diameter electron-beam trajectory of 10, 30, and 100 keV energy upon impinging on a 350 nm GaN-AIN layer on a Si substrate. The top row displays the layer cross-section for a depth of  $\approx 50 \mu\text{m}$  to compare the penetration of the e-beam. While, the bottom row displays a depth of  $\approx 500 \text{ nm}$  to compare the beam blur. The trajectory of forward and secondary-scattered electrons is shown in blue, and that of back-scattered electrons is shown in red.

As mentioned earlier, e-beam writing was performed using a Vistec EBP5000 tool. The thermal field-emission gun was operated at a beam energy of 100 keV, with a fixed aperture of  $300 \mu\text{m}$ . The exposure frequency can go up to 50 MHz, and the minimum attainable feature size is approximately 5 nm. For aligned exposure, i.e. with pattern overlay, placement accuracy is approximately 20 nm.

### 3.4.2 Mask Preparation

There are several approaches for the preparation of e-beam masks. A common method relies on the use of dedicated CAD layout-making tools such as CleWin or Tanner L-Edit, where patterns are graphically constructed layer by layer. An alternative approach, which is more practical for well-defined patterns such as PhCs is to generate the mask by directly coding it. Some CAD tools offer their custom scripting language, however, a commonly acknowledged programming language for layout design is the Caltech intermediate format (CIF) [76], which enables a hierarchy-based creation of patterns. Predefined geometric entities such as circles exist to assist with the coding. The advantage of this approach is that it enables the automation of mask generation for a given application, with flexible control over design tweaking.

Once a mask is generated as a CIF file, it can be imported to a layout editing tool and converted to a standard GDSII file format, which is common for mask layouts. The latter file contains all information about the pattern including the selected manufacturing grid size and the details of each constituent layer of the pattern. A fracturing procedure is then carried out using dedicated software, here GenlSys Layout Beamer, which primarily serves—as the procedure label implies—to break down the pattern into polygons and convert them into smaller and less complex shapes that can be easily swept by an e-beam scan. In this step, technically speaking, the writing grid is confirmed, the pattern is segmented into writing fields, and the sub-fields are defined. It is important to check that the writing field boundaries fall on non-critical regions of the pattern, as to minimize the impact of potential stitching errors that may occur during stage translation between fields of the pattern. By enforcing floating instead of fixed fields, they can be distributed in such a way that individual PhCs can be entirely contained within a single writing field. The final file

format required by the e-beam control software is the GPF format, which the e-beam software can then convert into the interfacing signals for the hardware controller.

As an example, the fracturing of a PhC hole is analyzed. When using a curved fracturing routine, shown in Fig. 3.4.2 (a), the displayed circular geometry is subdivided into a square region and a set of polygons to cover the area of the PhC hole, within the accuracy of the writing grid, here 1 nm. The advantage of curved fracturing when compared to standard trapezoidal fracturing is that it optimizes fracturing of curved geometries relative to the grid in a way that minimizes distortions that may introduce symmetry-breaking. This is particularly important for the exposure of periodic structures such as PhCs. During writing, the e-beam travels randomly across the fractured sub-fields. Fracturing can be further improved by using sequential fracturing, in combination with bulk-sleeve writing as shown in Fig. 3.4.2 (b). The non-critical inner circular core (bulk) of the PhC hole is fractured separate to the border (sleeve), and the former can be done with any course fracturing technique such as curved fracturing to retain symmetry. The outer fine region (sleeve) of the PhC hole, which has a ring shape, is then written in a circular sequential manner along several loops, thus maximizing the homogeneity of the exposure around the edges. In Fig. 3.4.2 (b), the sleeve was selected to be 20 nm thick to allow for an overlap with the bulk pattern. The bulk pattern can be written with a larger sized beam as long as the exposure overlap is retained and proximity effects are accounted for.

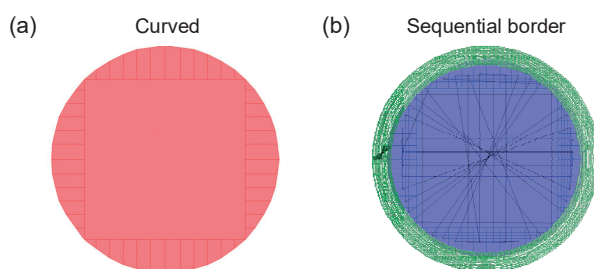


*Fig. 3.4.2 Comparison of the fracturing of a PhC hole of diameter =235 nm using (a) curved and (b) combination of curved and sequential routines. Bulk-sleeve writing was utilized in for the sequential fracturing pattern, using a 20 nm thick border (sleeve).*

#### 3.4.3 Sample Exposure

The wafer/ chip is mounted on the e-beam holder, aligned in such a way to have the cleaving axis of the semiconductor crystal perpendicular to the x-axis of the tool. Fine rotation alignment is done on an alignment microscope, where also the surface height can be measured and adjusted (in the case of a sample chip) to the writing height of the e-beam. The pin push-back mounting mechanism used with wafers helps align their surface by default to the beam focus. Wafers exhibiting significant bowing, beyond 100  $\mu\text{m}$ , may fail to be exposed correctly across the entire wafer, as the defocusing of the electron beam can only be corrected within a limited height range. Adjustments, if needed, have to be otherwise done mechanically. At this point, reference measurements are made relative to distinct markers on the e-beam holder, using the Faraday cup for example, in order to define the relative position of the pattern. This is particularly important for alignment exposures. Before transferring the e-beam holder to the stage, it is left in a temperature-controlled transfer window until its temperature equilibrates. This helps reduced thermally induced drifting during the writing process.

For the exposure, the dose delivered to the resist can be calculated according to the following equation:



$$Dose = \frac{10^3 \cdot I_{beam}}{f_{beam} \Delta x^2} \quad (3.4.1)$$

where  $I_{beam}$  is the beam current,  $f_{beam}$  is the exposure frequency, and  $\Delta x$  is the beam step size. The computed dose is given in  $\mu\text{C}/\text{cm}^2$  for standard units. The dose for ZEP resist was determined through a series of dose tests, which were conducted in conjunction with proximity effect correction calibration, discussed in the next section. Small variations in the dose, on the order of 10–15  $\mu\text{C}/\text{cm}^2$ , were found between the different beam sizes that were used.

For the writing of the PhC patterns, the lowest configured e-beam current of 100 pA is specifically selected, which gives the smallest e-beam size, with a full width at half maximum (FWHM) diameter of 42 Å. A minimum grid size of 1 nm is used for the pattern, corresponding to the minimum beam step size of the tool. This was to ensure the highest possible mask sidewall smoothness for PhCs. The effect of the beam step size on the patterning of a PhC hole is displayed in Fig. 3.4.3 for 1, 2, and 5 nm grids, relative to a hole 235 nm in diameter. The 5 nm step exposure is shown here to clearly display the beam placement of a 5 nm-diameter e-beam on the hole pattern. When comparing the two practical implementations using the 1 and 2 nm beam stepping, one finds that the 2 nm stepping already produces a significant roughness in the exposure pattern. Once exposed and developed, the introduced disorder propagates with the fabrication process and only increases in magnitude on average.

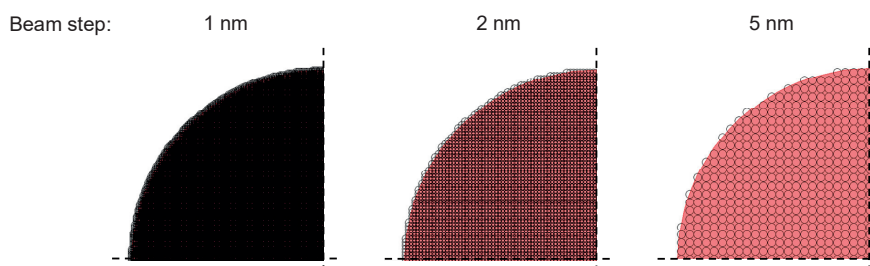


Fig. 3.4.3 Schematic of the electron beam placement on a fraction of a PhC hole, featuring a diameter of 235 nm, for 1, 2, and 5 nm beam stepping considering an e-beam diameter (FWHM) of 5 nm.

For writing larger features such as waveguides, a more suitable beam of 11.5 nm diameter (15 nA current) is selected, in conjunction with a 10 nm pattern grid. This resolution fits well with regular and suspended waveguides, the latter which contain nanotethers. Non-critical features such as trenches and alignment markers are patterned using the coarser beams, which can go up to 100 nm in diameter. The size selection depends on the proximity of the features to the primary pattern.

#### 3.4.4 Proximity Effect Correction

As seen earlier, an electron beam with an energy of 100 keV does not strictly maintain a forward trajectory inside the sample (refer to Fig. 3.4.1 (b)) compared to its prior path in vacuum, due to various interactions with the constituent atoms, which induce elastic and inelastic scattering events. For a 100 keV e-beam, the simulated mean penetration depth was found to be approximately 37  $\mu\text{m}$ . While backscattered and secondary electrons do not travel as deep into the material, they can however reach regions far beyond the focal volume, going laterally as far as tens of microns away from the focal spot. If these electrons happen to arrive at the resist again with an energy that is sufficient to expose it, then they contribute to what is called the proximity effect. This issue becomes more prominent the larger and denser the patterns are. The extent of the proximity effect in commonly used semiconductors like Si can go up to a length of approximately 30  $\mu\text{m}$ .

An effective solution to the proximity effect is to consider electron scattering behavior in advance and adjust the pattern dose accordingly, in what is called the proximity effect correction (PEC). The e-beam is accounted for by a

multi-Gaussian distribution consisting of a short-range beam broadening contribution and another longer-range contribution from backscattering. They are summed up by the standard deviations of the forward scattering parameter ( $\alpha$ ) and the backscattering parameter ( $\beta$ ). The point spread function (PSF) of the corrected beam as a function of its radius ( $r$ ) is then given by the following equation [77]:

$$PSF(r) = \frac{1}{1 + \eta} \left( \frac{1}{\pi\alpha^2} e^{-\left(\frac{r}{\alpha}\right)^2} + \frac{\eta}{\pi\beta^2} e^{-\left(\frac{r}{\beta}\right)^2} \right) \quad (3.4.2)$$

Here,  $\eta$  is the ratio of energy of the backscattering relative to the forward scattering, quantified by the  $\beta$  and  $\alpha$  Gaussian distributions.

Here, the  $\alpha$ -parameter was assumed to have the same distribution as the e-beam PSF, i.e. the divergence of the beam can be neglected relative to its size within the thickness of the e-beam resist layer. The  $\beta$ -parameter on the other hand was considered to be 33  $\mu\text{m}$  for the III-nitride on Si layers, the same value reported for pure Si wafers. This was confirmed by Monte Carlo electron scattering simulations. A dose test on the layers of interest was carried out to retrieve both the  $\eta$ -parameter and the base dose ( $D_{\text{base}}$ ) to be used. The dose test pattern was generated as described in [78]. A 310 nm ZEP layer (spun on 100 nm  $\text{SiO}_2$ , using a 350 nm GaN on Si wafer) was exposed with a checkerboard pattern, which was surrounded by a set of concentric square frames of constant pitch. The pitch was altered between patterns such that the effective pattern density ( $\zeta$ ) can be varied from 0% to 100%.  $D_{\text{base}}$  and  $\eta$  were swept within the range of expected values. The  $\alpha$  and  $\beta$  values were fixed, as described earlier. The quality of the exposure was determined by examining the edges and overlap of the pattern features. For a pattern of uniform density and a given  $\eta$ -parameter, the applied dose can be estimated to be:

$$Dose(\zeta) = D_{\text{base}} \frac{1 + \eta}{1 + 2\eta\zeta} \quad (3.4.3)$$

This expression allows for the retrieval of the  $D_{\text{base}}$ , which is the dose applied to a pattern density of 50% and does not necessitate compensation. The optimal exposure parameters were found to be  $D_{\text{base}}=170 \mu\text{C}/\text{cm}^2$  and  $\eta=0.4$ , for which the pattern is displayed in Fig. 3.4.4 (a). An example of the implementation of PEC is shown in Fig. 3.4.4 (b), where a triangular lattice PhC with lattice constant of 470 nm extends 50  $\mu\text{m}$  in length along each axis and is surrounded by etch trenches at a distance of 75  $\mu\text{m}$  from the center. The figure displays the compensation factor that is applied to the base dose across the PhC field. Since the central portion of the PhC receives the largest flux of backscattered electrons, it therefore requires a lower exposure dose compared to the extremities.

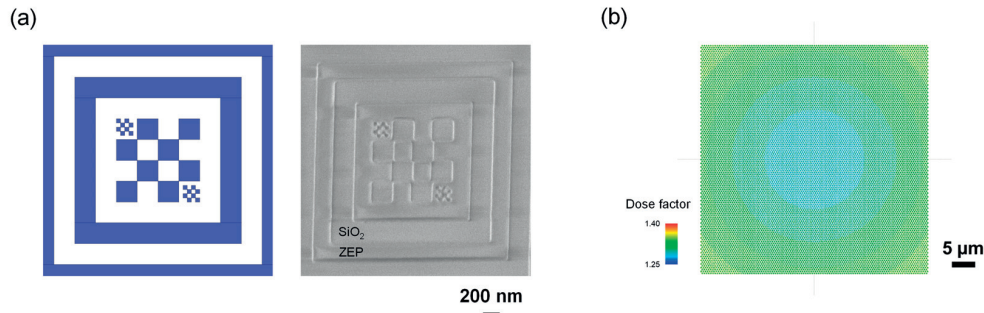


Fig. 3.4.4 (a) Dose test pattern in ZEP for a base dose of  $170 \mu\text{C}/\text{cm}^2$  and  $\eta=0.4$ , at a pattern density of 50% using a beam diameter of 4.2 nm. (b) Proximity effect correction applied to a PhC field ( $a=470 \text{ nm}$ ) surrounded by trenches at a distance of  $75 \mu\text{m}$ . The dose correction factor is color-coded.

### 3.5 Mask Transfer

The mask transfer process involves the etching of the SiO<sub>2</sub> layer using the patterned ZEP as the mask. It is desirable to minimize any deviation from the initial e-beam writing, and to avoid slanting of the mask sidewalls to prevent bowing effects in subsequent III-nitride etching [79]. The etch process of SiO<sub>2</sub> must be highly anisotropic to accomplish these requirements. An etch process is implemented based on ICP-RIE (refer to section 3.6 for more details on the ICP-RIE process), which uses a gas mixture of CHF<sub>3</sub> and SF<sub>6</sub>, at a mixing ratio of 5:1 respectively. High density plasma is produced using an ICP power of 950 W, and the chamber pressure is set to 2 Pa. Helium backside cooling maintains the wafer temperature at 10°C during the process. An etch rate of 1 nm/s is obtained for SiO<sub>2</sub> PECVD layers, and the selectivity in comparison with ZEP is 1:2. Fig. 3.5.1 displays patterns of the ZEP mask after carrying out SiO<sub>2</sub> etching, along with the resulting hard mask after the removal of the ZEP layer. When selecting the ZEP thickness, one should account for the additional SiO<sub>2</sub> etch time needed to clear small features such as PhC holes. A ZEP spacing layer should remain at the end of the etch process to prevent the adhesion of the plasma-exposed ZEP to the surface of SiO<sub>2</sub>.

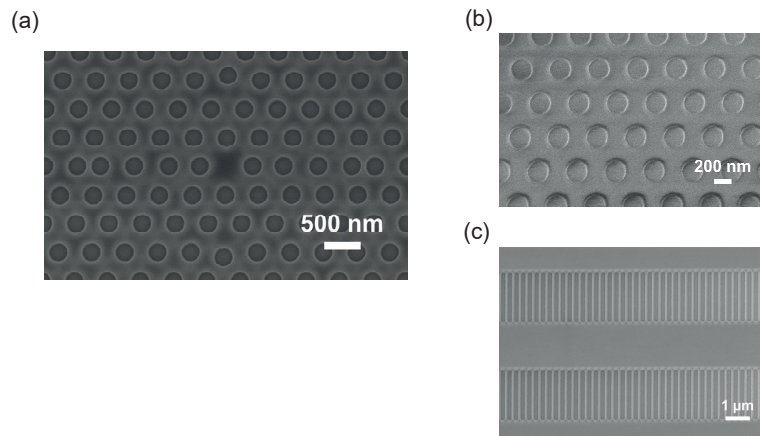


Fig. 3.5.1 (a) ZEP mask pattern after carrying out SiO<sub>2</sub> etching, displaying an optimized H<sub>0</sub> cavity. The patterned SiO<sub>2</sub> mask before GaN etching is shown for (b) a PhC lattice and (c) a subwavelength waveguide.

In the case of cooling failure during the etching, a ragged texture forms on the surface of the ZEP layer. It can be easily identified using bright-field microscopy as shown in Fig. 3.5.2 (a). If the heating is excessive, ZEP is partially baked and cracks appear in the film, displayed in Fig. 3.5.2 (b). They are visible under dark-field illumination with a

microscope. In the case of ZEP adhering to  $\text{SiO}_2$  due to etch overheating, the sample is immersed in a solution of N-methyl-2-pyrrolidone (NMP) at  $80^\circ\text{C}$  for 1 hour. The standard ZEP removal process (outlined earlier) is then carried out afterwards. Care should be taken when handling NMP due to its high toxicity.

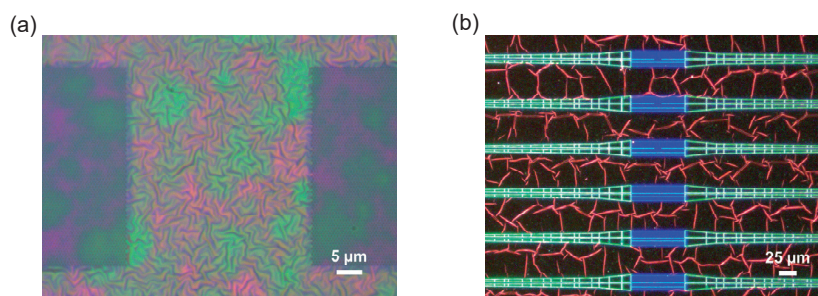


Fig. 3.5.2 (a) Bright-field microscopy image of a ZEP layer on  $\text{SiO}_2$ , deposited on a GaN layer, after inadequate cooling during plasma etching of  $\text{SiO}_2$ . (b) Dark-field microscopy image of a burnt ZEP layer after an immersion process in acetone to remove it. Patches of ZEP remain attached between the waveguides and over the fine lithographic features.

## 3.6 III-Nitride Etching

The etching of the III-nitride layer is one of the most critical steps in the fabrication process. The quality of the etching directly impacts the performance of the photonic crystals in many aspects, including the spectral response and the light attenuation figure. Roughness of PhC sidewalls for instance introduces a loss channel through which light can scatter out of the system, and moreover, the roughness adds to the degree of disorder in the PhC lattice design. Meanwhile, non-vertical PhC sidewalls break the vertical symmetry of the PhC slab, resulting in TE-TM mode mixing [80]. There should be a clear distinction between fabrication imperfections that are carried on from previous steps, i.e. mask quality, and the imperfections that solely emerge from the etching process. The primary attributes of the etching that serve as assessment criteria for the quality of the process are the smoothness of the sidewalls, sidewall verticality, and conformity to the mask dimensions. Other factors to consider include: induced surface damage due to ion bombardment, ion implantation, and the generation of adhering films or contaminating particulates on the surface via etch byproducts.

The desired etch geometry for two-dimensional PhCs can be provided mainly by dry etching techniques, as opposed to wet etching. The former can offer highly anisotropic etching such that the required sidewall verticality can be achieved. Dry etching takes advantage of the acceleration of ions/ atoms to arrive at the sample surface with high energy to assist in the dissociation of the constituent material. The dissociation can be done either purely physically, as with ion-beam etching, or chemically, by adding reactive species. Effective etching techniques rely on both mechanisms, generating the reactive species (ions and free radicals) via plasma ignition of the etchant gases, and then accelerating them towards the sample. In the etching process, reactive species reach the surface with high energy where they are adsorbed and break the material bonds to dissociate the atoms. Volatile byproducts are generated, which are then transported away from the surface in accordance with their vapor pressure.

We specifically utilize ICP-RIE for our application. An ICP-RIE system, as presented in Fig. 3.6.1, consists of an etch chamber operating under low pressure and served by gas inlets. Coils around the top of the chamber generate the plasma via electromagnetic induction when fed by an RF generator, operating typically at 13.56 MHz. A second RF generator that is connected between the top and bottom electrodes (combined with a blocking capacitor) applies a net voltage bias, vertically across the chamber, to accelerate ions towards the chuck that clamps the wafer. Temperature control is maintained through helium backside cooling of the wafer. The presented ICP-RIE

### 3. Fabrication of III-Nitride Planar Photonic Crystals

configuration, with separate RF controls for the ICP generator and the RIE electrode bias, is particularly advantageous as it allows for the decoupling of the control over plasma density and ion energy.

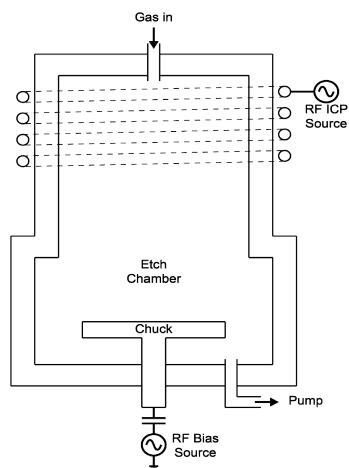


Fig. 3.6.1 Illustration of an ICP-RIE etcher, employed for the etching of III-nitride layers on Si layers.

An etch recipe was developed for III-nitrides which relies on the use of a low-density plasma that is biased with a voltage of 250 V. Due to the high bond strength of GaN and AlN, a physical contribution to the bond breaking is necessary for the etch process. Anisotropy is prioritized over the etch rate to achieve the smoothest possible sidewalls. The gas mixture consists primarily of  $\text{Cl}_2$ , with the addition of  $\text{N}_2$  as a carrier gas at a mixing ratio of 3:1. Chlorine dissociates upon plasma formation to create  $\text{Cl}^+$  ions, the main chemically reactive species in the process. These ions are accelerated in the chamber towards the III-nitride surface, and once adsorbed, they react to form volatile compounds:  $\text{GaCl}_2$  and  $\text{GaCl}_3$  in the case of GaN and  $\text{AlCl}_3$  with AlN [79]. The etch chamber maintains a pressure of 1 Pa such that the boiling/ sublimation temperature of these compounds is surpassed. They become volatile and are carried away with the gas outflow.

Tracking of the etch process can be carried out through several approaches, whether using in-situ reflectance, plasma spectrometry, or ion-mass spectrometry. A laser reflectance measurement was used here for its simplicity in addition to its location specificity, which cannot be attained by the other two listed techniques. Etch tracking patterns are embedded in the lithography mask, such that a defined area of the III-nitride layer is exposed. Knowing the optical composition and properties of the layer, the laser reflectance as a function of the III-nitride layer thickness can be calculated. This can be compared in real-time to the in-situ reflectance curve to retrieve the etch rate and layer thickness, down to nm accuracy. A calibration procedure is carried out to determine the aspect ratio dependency since narrower features such as PhC holes will exhibit a slower etch rate. This effect comes into play starting with feature sizes  $\approx 50 \mu\text{m}$  and smaller, and it becomes more significant as the aspect ratio of the etching increases. For instance, the etch rate of PhC holes that are 250 nm in diameter and require an etch aspect ratio of approximately 3:2 is 35% lower than bulk. An etch tracking acquisition using a HeNe laser source ( $\lambda=632.8 \text{ nm}$ ), and the theoretical reflectance curve are displayed in Fig. 3.6.2, for a GaN on Si layers consisting of a buffer AlN layer.

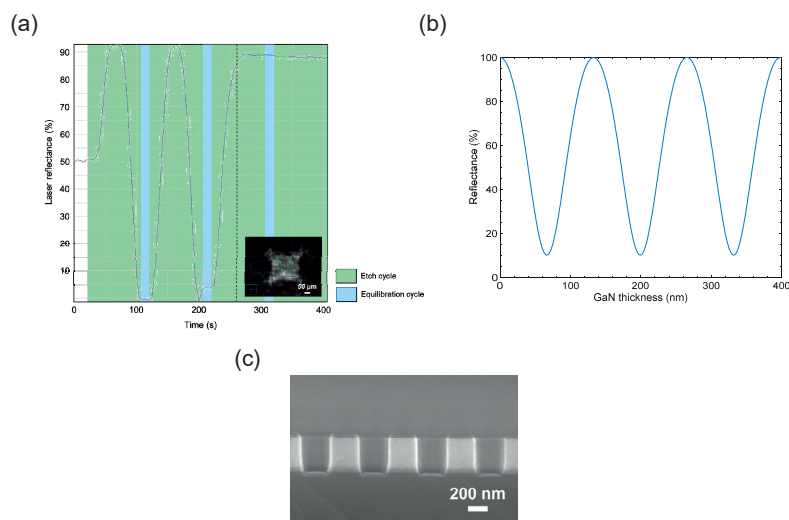


Fig. 3.6.2 (a) In-situ laser reflectance signal as a function of time acquired during the ICP etching of a GaN sample. The displayed signal was retrieved from the center of the etch tracking window displayed in the inset. The plasma etch cycles are highlighted in green, while the equilibration cycles are highlighted in blue. The dashed black line marks the time when the AlN buffer layer is reached. (b) Theoretically computed reflectance from a GaN on Si layer at normal incidence as a function of GaN thickness. (c) Cross-sectional SEM micrograph of a GaN PhC on Si after ICP etching of GaN.

The developed etch recipe resulted in a GaN etch rate of 1.5 nm/s. The etch process was divided into multiple etch cycles that do not exceed 90 s each, over the etch thickness of the layer. Plasma acceleration was halted in between the etch cycles to help equilibrate any wafer overheating and to clear etch byproducts. The point where the Si layer is reached within the tracked region can be clearly seen in Fig. 3.6.2 (a). When etching GaN layers on Si, prepared by MOCVD, the kink in the curve signals that the AlN interface has been reached. The etch rate of AlN is slower by a factor of approximately two, for the same process parameters. Highly vertical sidewalls have been achieved in GaN, measured on average to be better than 89°. The buffer AlN layer however does not feature the same verticality since the etching of AlN is not ion-assisted in nature [81], and the etch parameters specific to GaN thereby do not provide the same anisotropy. For the etching of pure AlN layers,  $\text{BCl}_3$  is added to the gas mixture, and the plasma density is doubled. The etching process is halted as soon as the Si layer is reached in the PhCs, in order to prevent bowing [79]. The etch rate selectivity of GaN to  $\text{SiO}_2$  was measured to be 7:1, while the selectivity of AlN to  $\text{SiO}_2$  was 4.5:1.

### 3.7 Membrane Release

The suspension of the III-nitride membrane comes as the final step of the fabrication process. Any cleaning step should preferably be done beforehand to avoid dealing with potential stiction effects when using liquid solvents. Otherwise, critical-point drying should be carried out. Since the III-nitride layer is exposed at this point, plasma etching is avoided to prevent any damage. Isotropic chemical etching is needed to produce the necessary undercut to eliminate the Si entirely underneath the waveguiding structures. A vapor-phase etching technique is utilized here, which relies solely on  $\text{XeF}_2$  gas.

The Si etching process of the sample is performed in a custom tool which contains a pressure controlled etch chamber.  $\text{XeF}_2$  gas, produced through low-pressure sublimation of  $\text{XeF}_2$  crystals, is first prepared in an expansion chamber and brought to a pressure of 40 Pa. The  $\text{XeF}_2$  gas is then transferred to the etch chamber, where the etch process is initiated.  $\text{XeF}_2$  adsorbs to the exposed Si surface, where F radicals dissociate and react with Si [81], gradually etching it away. The reaction goes according to the following chemical equation:



The gas remains in the etch chamber for a 30 second duration of an etch pulse, after which the etch chamber is evacuated and etch byproducts are removed. The etching of Si halts for that duration. Since the etching is characteristically isotropic, the etch depth can be obtained by measuring the retreat length of the underlying Si along an edge of the pattern. This is done optically in real-time through a window port on the top of the etch chamber. The effective etch rate of Si is 11 nm/s, which necessitates 6 etch cycles to reach an etch depth of approximately 2  $\mu$ m. This distance is sufficient for optical structures operating near  $\lambda=1550$  nm, and it may be reduced for shorter-wavelength devices. The etch depth should be limited to the nominal design value to avoid excessive stress release, which may otherwise result in membrane cracking and collapse.

### 3.8 Anti-Reflection Coating

Reflection of light occurs at the interface between media possessing differing refractive index, as described by the Fresnel equations. When considering end-fire coupling, the facets of a sample surrounded by air act as partially reflecting mirrors, and the two ends are sufficient to form a Fabry-Perot cavity that can sustain modes. Its effect is manifested in the observation of amplitude oscillations in the transmission spectrum of a waveguide that runs between the two facets.

To suppress these oscillations, a dielectric anti-reflection film can be deposited on the chip facet. The standard approach, targeting a single design wavelength, makes use of a layer of  $\lambda/4$  effective length which functions to create a destructive interference condition for the two waves reflecting from the air-coating and coating-material interface. Considering normal incidence, the refractive index of the anti-reflection coating is computed using the refractive indices of the surrounding layers:  $n_{coating} = \sqrt{n_{air}n_{material}}$ . For guided modes, the effective index in the material is considered instead. The thickness is then given by:  $d_{coating} = \frac{\lambda}{4}n_{coating}$ . A single-layer anti-reflection coating suitable for GaN devices that operate at  $\lambda=1550$  nm should have a refractive index of 1.52 and thickness of 255 nm. This was implemented by depositing a SiO<sub>2</sub>-TiO<sub>2</sub> layer (9.5% TiO<sub>2</sub> by composition) using e-beam evaporation.

### 3.9 Summary

The growth and fabrication of III-nitride layers on Si substrates has been detailed for the implemented layers. Epitaxial growth was primarily carried out using MOCVD for the GaN on Si(111) layers. A fabrication process has been developed and tweaked to yield micro- and nanostructures of superior quality, suitable for GaN and AlN. This was accomplished through a refined e-beam lithography process taking the tool to its limits, in combination with highly-controlled etching of the III-nitride layers. The resulting devices feature high stability and minimal damage from the fabrication run as will be detailed in the next chapter.





# 4. Characterization of the III-Nitride on Silicon Platform

## 4.1 Introduction

III-nitrides such as GaN and AlN offer a particularly appealing platform for integrated optoelectronic devices, owing to a unique combination of optical, electrical, and mechanical properties. These semiconductors feature a direct electronic bandgap, large exciton binding energy, and a wide transparency window which has promoted their use for various active optoelectronic devices, notably light-emitting devices such as lasers and LEDs. GaN is an ideal material for optical structures since its dispersion throughout the near-IR to visible range offers a good balance between optical confinement ( $n=2.3-2.4$ ) and transparency (absorption edge in the near ultraviolet range). By realizing high-quality III-nitride layers on Si, the platform can foresee wide adoption for a broad range of applications.

The quality of semiconductor layers is key to the performance of optical devices. Optical characteristics of a specific material are not preserved, but can rather be influenced by variations in its composition, physical properties, or surface structure and chemistry. This consideration begins from the growth phase all through the different fabrication stages. The inclusion of impurities for instance can introduce absorption lines, and through the Kramers-Kronig relation, one finds that the dispersion is consequently modified. The electronic bandgap and permittivity can also be altered through straining of the layers, which is yet another example of how fabrication control may impact the optical properties. A thorough characterization therefore allows to closely match the experimental response of optical devices to theoretical designs. PhCs are primarily targeted in this thesis, and their bandgap properties along with the dispersion rely primarily on the permittivity of the material.

In this chapter, characterization of III-nitride layers is conducted to identify both material and optical properties. This served to probe layer quality following growth and adapt the design and fabrication accordingly. The experimental setup which was designed and constructed for device characterization is presented, and the utilized experimental techniques are detailed. Finally, the III-nitride on Si platform is discussed in terms of design, stress mitigation, and optical characteristics.

## 4.2 Pre-Fabrication Layer Characterization

### 4.2.1 Crystallinity

Crystal quality of semiconductor layers can vary vastly from that of an ideal crystal lattice according to the growth technique and conditions that are utilized. Concerning optical applications, it is desirable to characterize the crystal structure of a layer for several reasons. First, knowledge of the crystal quality conveys information on dipole orientation, allowing one to accurately predict light-matter interaction, especially when dealing with nonlinear processes. Another motivation is the identification of potential loss mechanisms, whether they are scattering or absorption-induced in nature, those of which emerge from embedded defects and impurities. The presence of dislocations for instance has been linked to excessive scattering losses in GaN waveguides [82]. Furthermore, photoelastic effects have a direct impact on the refractive index of the semiconductor, and they can be also computed through strain analysis of the crystal.

The primary technique used to measure crystal quality of the prepared semiconductor layers is X-ray diffraction, where the principle of operation is based on Bragg's diffraction law. An area of the sample is illuminated with a monochromatic X-ray beam, using a four-crystal X-ray diffractometer, incident at a specific angle relative to the crystallographic orientation of a semiconductor sample. By measuring the signal that is diffracted from the atomic lattice planes, information on the composition and underlying order of the lattice can be retrieved. A rocking curve measurement offers a useful measure of crystal quality by quantifying the degree of orientation of a layer along a specific crystallographic axis. With wurtzite III-nitrides, the rocking curve is measured with respect to the c-axis, that is along the growth direction. The (0002) rocking curve measurement performed on a GaN layer, grown on Si(111) by MOCVD, is displayed in Fig. 4.2.1. Two diffracted lines can be seen, one belonging to the GaN lattice, centered at  $17.28^\circ$ , in addition to another from the AlN (buffer layer) lattice at  $17.96^\circ$ . The GaN layer has a characteristic FWHM of 1500 arcsec. This figure is relatively large when compared to epitaxial GaN growth on sapphire or SiC, where GaN layers of comparable thickness have a FWHM below 1000 arcsec. For GaN layers grown on SiC, the FWHM value can go down to 200 arcsec for a thickness greater than  $2\ \mu\text{m}$  [83]. The reduced crystallinity is a direct consequence of non-lattice matched growth using Si. This is apparent in the figure when observing the diffraction line of the intermediate AlN buffer layer. It is directly grown on Si and has a FWHM of 5450 arcsec. It is noteworthy that these values are at the lower end of the mean values obtained for regular MOCVD growth runs.

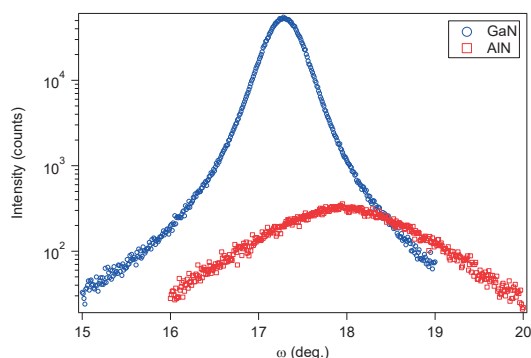


Fig. 4.2.1 X-ray diffraction rocking curve measurement\* of a GaN layer grown by MOCVD on Si(111) with an intermediate AlN buffer.

X-ray diffraction measurements were additionally carried out on sputtered AlN layers to investigate their crystal quality when sputtered on Si(111) wafers. A similar (0002) rocking curve measurement for AlN indicated a FWHM in the range of 1980–2200 arcsec. This range is close to the values obtained for AlN layers grown by MBE<sup>†</sup> on Si(111) and MOCVD GaN on Si(111). Sputtered AlN layers undergo columnar growth, and as a result, they are highly c-axis oriented despite the non-epitaxial growth technique that is employed. The orientation of the AlN columns however does exhibit random rotation, which was elucidated by a (302) scan, and an average twist angle of  $1.02^\circ$  was measured. A  $2\theta$ - $\omega$  scan further revealed that other crystal phases are present in the layer including Al (220) and Al (311), which is expected with sputtered layers [84]. Based on a model-based fit, the density of the layer was deduced to be  $3.26\ \text{g/cm}^3$ , the same value that is obtained with epitaxial AlN. This indicates a high degree of packing and that the layer, by composition, is void-free.

\* The XRD measurement was performed by J.-F. Carlin.

† The FWHM of AlN layers grown by MBE on Si(111) was measured to be 2160 arcsec. Growth and measurements were carried out by D. Martin. Higher quality layers were obtained at a later point in time by S. Tamariz, yet the thickness of the growth was limited due to residual stress.

### 4.2.2 Surface and Interface Roughness

The quality of a layer's surface is paramount to the optical performance in terms of losses. Higher roughness translates to stronger scattering at interfaces, which can be assessed through Rayleigh scattering theory. The scaling factor of the scattered intensity with wavelength is  $\lambda^{-4}$  [85]. This implies that if losses in a system are scattering-limited, improving on the surface roughness can significantly expand the operational range, should the material remain optically transparent. Epitaxial wafers are known to produce surfaces of high level of smoothness, down to atomic height.

The surface and interface quality of the III-nitride layers were characterized using different techniques to assess their features. First, the surface was measured using atomic force microscopy (AFM). Fig. 4.2.2 displays the AFM surface map for an MOCVD GaN on Si(111) wafer, acquired before processing. The root-mean-square (RMS) roughness is found to fluctuate around a value of 2 nm across the wafer. One of the striking features is the lack of a flat surface topology over large surface areas (beyond ten microns). This can be clearly seen in Fig. 4.2.2 (a), where the peak-valley separation exceeds 20 nm. Elevated clusters that are approximately 5-10  $\mu\text{m}$  in diameter are present over the entire surface. They can indeed be identified through bright-field microscopy by their varying coloration.

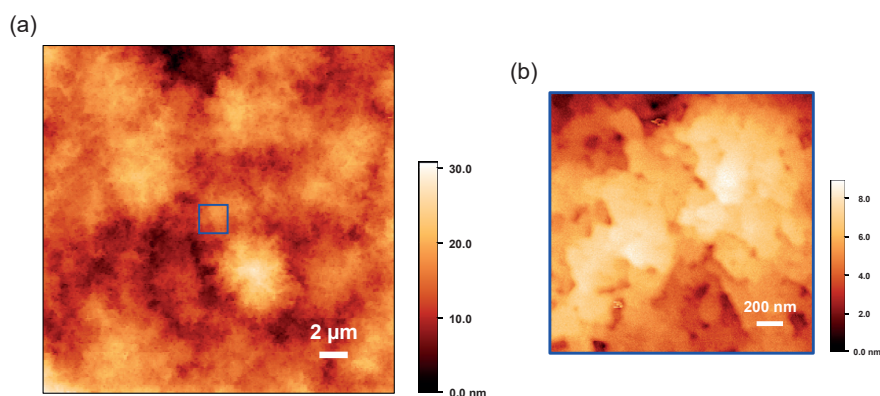


Fig. 4.2.2 (a) AFM scan of a 350 nm thick GaN layer on Si(111), and (b) a close-up view of the center as marked in (a).

To complement the AFM measurements, confocal microscopy and SEM were both employed to retrieve information on the quality of the interfaces. This was particularly aimed at probing the interface between the GaN and AlN buffer layer. As seen with the X-ray diffraction measurements, the AlN buffer layer exhibits poor crystal quality and is not expected to reach a step growth regime for the target thickness value that is below 50 nm; a rough interface is created as a result. This was indeed confirmed with the aid of confocal microscopy, through which the interface topology was measured by taking advantage of the transparency of the III-nitride layer in the visible range. The topology reconstruction displayed in Fig. 4.2.3 (a) indicates an RMS roughness value of 7 nm for the GaN-AlN interface. The elevated clusters seen in the III-nitride layers through AFM measurements also appear in the confocal reconstruction, since the thickness fluctuation represents a variation of the optical path length. The interface roughness on the other hand has a much shorter lateral length scale and can therefore be distinguished. An SEM cross-section micrograph of the layer in Fig. 4.2.3 (b) confirms the validity of the confocal microscopy reconstruction. The roughness of the GaN-AlN interface is clearly visible with the same peak-to-peak magnitude. Absorption losses have been already attributed to the AlN buffer layer [86], but so far the associated scattering loss has not been quantified.

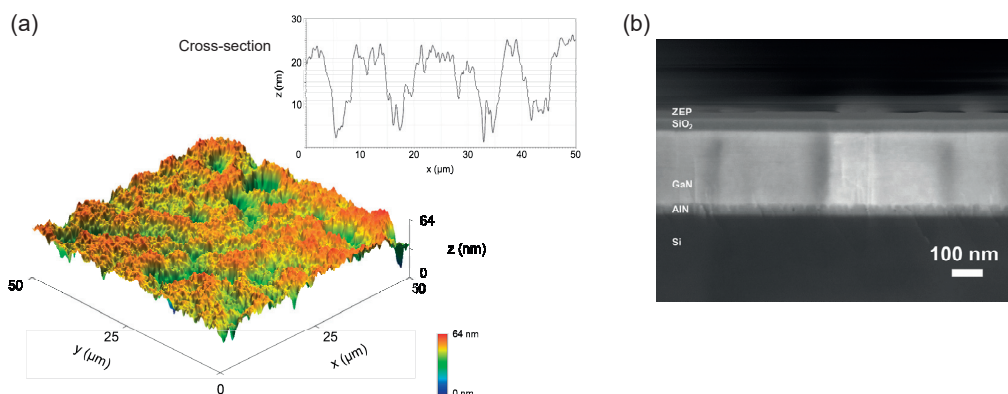


Fig. 4.2.3 (a) Confocal microscopy surface reconstruction of a GaN on Si wafer displaying the Al-GaN interface roughness. The surface profile along the x-axis is shown in the inset. (b) Cross-sectional SEM micrograph of a GaN on AlN wafer, with SiO<sub>2</sub> and ZEP resist deposited on the surface.

Another layer of interest is the sputtered AlN on Si, the surface quality of which is strongly dependent on the tweaking of the sputtering parameters. High quality layers have been reported in literature for AlN through the sputter deposition method, reaching roughness values below 1 nm [87]. AFM measurements were conducted on the sputtered AlN layers\*, and Fig. 4.2.4 displays the profile of a layer approximately 185 nm in thickness. The observed grainy texture is characteristic of AlN sputter deposition, and it outlines the individual c-axis oriented crystallite columns in this layer. The crystallite diameter is measured to be approximately 35 nm on average. As for the surface roughness, the extracted mean RMS value is 2.2 nm, which was not found to vary across the wafer. Furthermore, the topology of the surface was measured to be flat over extended regions beyond 100 μm in length.

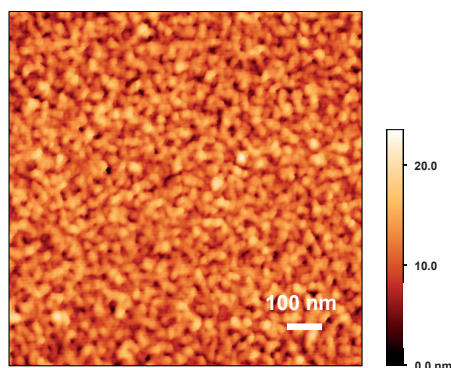


Fig. 4.2.4 AFM scan of a 200 nm thick sputtered AlN layer on Si(111).

### 4.2.3 Dispersion and Layer Thickness

Ellipsometry is an optical, non-invasive technique that enables the measurement of thin film properties such as thickness and permittivity by analyzing the change in the polarization state of light upon reflection from the sample surface, at oblique incidence. A goniometer controls the illumination angle of the light source, such that a linearly polarized beam is incident on the layer near its Brewster angle, to enhance the sensitivity of the measurement [88]. The polarization of light is modified upon reflection, transforming into a polarization ellipse. Through polarization-controlled excitation and detection, with the analyzer being fixed at 45°, the complex reflection can be retrieved, and is given by the following equation:

\* The sputtered AlN layers for the measurements were provided by Evatec AG.

$$R = \frac{R_p}{R_s} = \tan \Psi e^{i\Delta} \quad (4.2.1)$$

where  $R_p$  and  $R_s$  refer to the complex reflection of the p- and s-polarized light components respectively.  $\Psi$  and  $\Delta$  are the amplitude and phase parameters, respectively, describing the polarization ellipse. They are related to the rotation angle  $\theta$  of the ellipse around the origin and  $\varepsilon$ , the inverse tangent of the ratio between the minor and major axis lengths of the ellipse (as shown in Fig. 4.2.5), through the following equations:

$$\begin{aligned} \sin 2\varepsilon &= \sin 2\Psi \sin \Delta \\ \tan 2\theta &= \tan 2\Psi \cos \Delta \end{aligned}$$

In other words,  $\tan \Psi$  indicates the inclination of the ellipse, while  $\cos \Delta$  indicates its eccentricity.

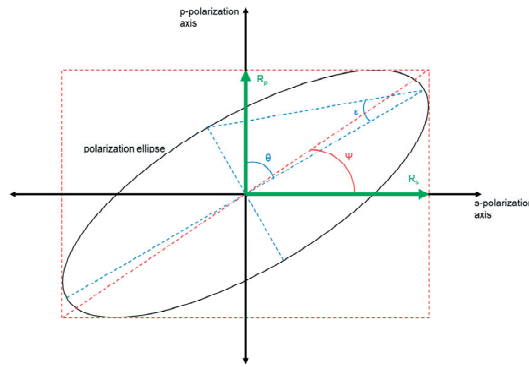


Fig. 4.2.5 Plot of the polarization ellipse at the detection plane, considering reflection off the sample surface at oblique incidence. The ellipse parameters  $\Psi$ ,  $\varepsilon$ , and  $\theta$  as well as the reflection vectors along the polarization axes  $R_s$  and  $R_p$  are indicated.

The ellipsometry measurement was carried out on the semiconductor wafers directly after growth. The goniometer angle was adjusted to the respective Brewster's angle of the layer ( $67^\circ$  for GaN and  $65^\circ$  for AlN). A Xe lamp source with a focal spot size of  $400 \mu\text{m}$  illuminated the sample, and reflection from the surface was measured across a wavelength range of  $190 \text{ nm}$  to  $1.7 \mu\text{m}$  using grating spectrograph acquisition.

Ellipsometry necessitates the use of a thin film model that is representative of the layer stack being measured, in order to fit the acquired spectrum and subsequently extract the optical properties of the unknown layer. An anisotropic two-resonance Sellmeier model is introduced for GaN and AlN, according to the following equation:

$$n(\lambda) = \sqrt{A + \frac{B \cdot \lambda^2}{\lambda^2 - C^2} + \frac{D \cdot \lambda^2}{\lambda^2 - E^2}} \quad (4.2.2)$$

Here, A through E are fitting constants of the model. The C-parameter was set to the exciton energy of the semiconductor, while the E-parameter was bound to the wavelength range of higher energy band transitions, in a similar approach to [89]. While for the Si substrate, pre-acquired refractive index measurement values were utilized. The nominal thickness values obtained through MOCVD in-situ reflectometry measurements were used as a starting point for regression fitting, which was carried out using the Levenberg-Marquardt method. The measured refractive index curves for MOCVD GaN and sputtered AlN layers are displayed in Fig. 4.2.6.

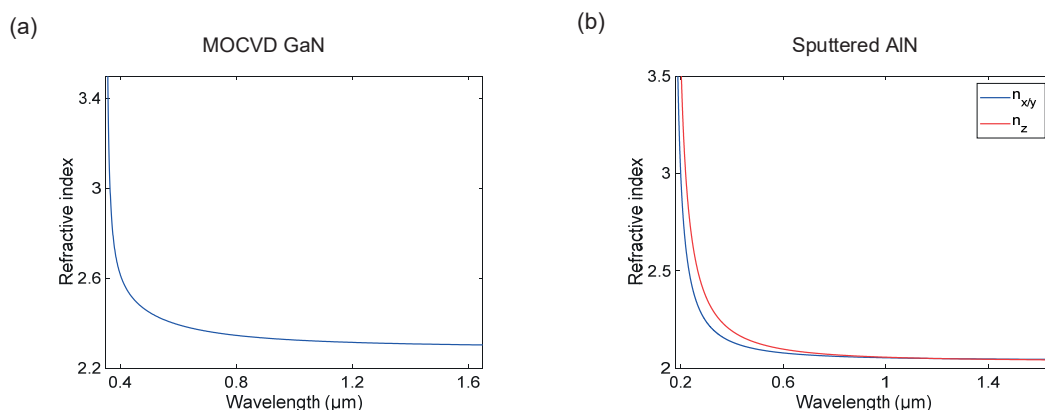


Fig. 4.2.6 Refractive index of (a) MOCVD GaN and (b) sputtered AlN obtained through ellipsometry measurements.

The ellipsometric model for GaN failed to distinguish the birefringence of the layer, and an average refractive index was extracted. This can be attributed to the quality of the interfaces of the layer. The refractive index at the wavelengths of interest, namely  $\lambda = 1550$  nm and  $\lambda = 1300$  nm, was measured to be  $n = 2.306$  and  $n = 2.312$  respectively. As for the sputtered AlN layer, both the ordinary (perpendicular to the  $c$ -axis) and extraordinary (parallel to the  $c$ -axis) components of the refractive index were obtained. Birefringence was found to be minimal in the near-IR range. For the ordinary ray, the refractive index at  $\lambda = 1550$  nm and  $\lambda = 1300$  nm was measured to be  $n = 2.046$  and  $n = 2.049$  respectively. While the refractive index of the extraordinary ray differed by less than 0.01% in that wavelength range, birefringence in AlN however did peak near the bandgap energy, just at the edge of the experimental acquisition range.

The ellipsometry measurement was performed pointwise, spatially along the primary axes of the semiconductor wafer to measure the homogeneity of the growth. Fig. 4.2.7 (a) displays the profile measured for a MOCVD-grown GaN layer on a 2-inch wafer. According to the profile, the thickness was found to vary by approximately 1 nm/mm within the central 20 mm diameter of the wafer. The thickness then sharply drops beyond 15 mm from the center. It should be noted that the measured thickness is an averaged value of the layer topography within the probe area. The GaN thickness profile was accounted for when positioning the pattern during the exposure, to have the layer centered around the nominal thickness design value. Sputtered AlN layers on the other hand maintained a flat surface, with the average thickness varying by less than 1 nm over a 40 mm diameter on a 6-inch wafer.

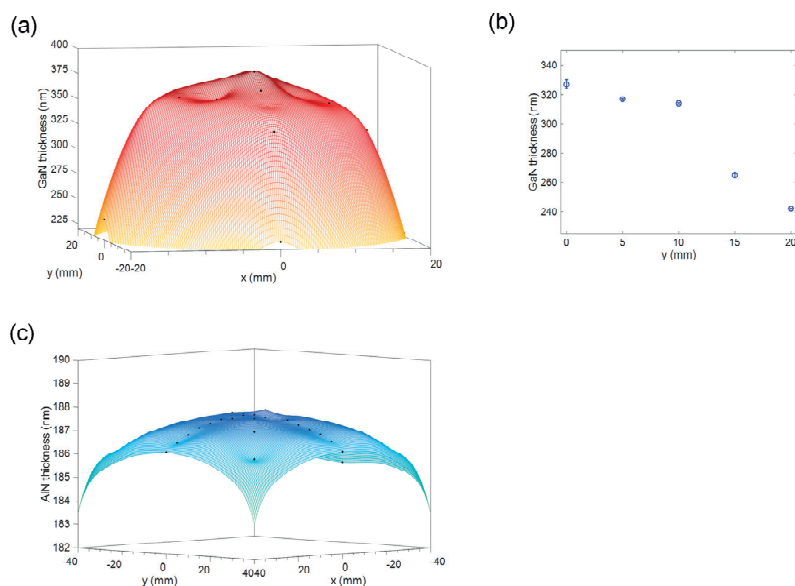


Fig. 4.2.7 (a) GaN layer thickness profile obtained through ellipsometry, for growth on a 2-inch Si wafer (target thickness=330 nm). The interpolated surface is displayed for the ellipsometry data points plotted in black. (b) Layer thickness measurement of a similarly grown GaN layer on Si (target thickness=312 nm) using SEM along a vertical cross-section of a 2-inch wafer. (c) Layer thickness profile of a sputtered AlN layer, measured using ellipsometry. All data point positions are relative to the center of the wafer.

#### 4.2.4 Stress in Heteroepitaxial and Sputtered Layers

III-nitride layers that are prepared using epitaxial growth techniques, e.g. MOCVD or MBE, have characteristically high stress values when grown on Si wafers. There are two primary factors that contribute to the presence of stress in the epilayers. The first is the fact that lattice mismatched growth of III-nitrides on Si naturally results in a strained layer through a pseudomorphic growth regime. Both GaN and AlN have lower in-plane lattice constant values compared to Si, as listed in Table 4.2.1, leading to tensile strain in the III-nitride layers. When growing GaN on Si with an intermediate AlN buffer layer, the expected strain is mostly mitigated through the introduction of misfit and edge dislocations in the AlN layer beyond the critical thickness. This allows for gradual strain relaxation.

The second contribution of stress which is of higher impact pertains to the thermal expansion coefficients of the different materials. The elevated growth temperatures of epitaxy, which can exceed 1000°C with MOCVD, amplify the extent of this effect. Since the thermal expansion coefficients of GaN and AlN are higher in comparison to Si (refer to Table 4.2.1), tensile stress builds in the III-nitride epilayer when the wafer temperature is brought down to room temperature after growth, while compressive stress forms in Si near the interface. The restoring force induces concave bowing of the wafer [90]. The desired thickness of the III-nitride layers for optical applications (typically below 500 nm) is too thin to allow for the introduction of intermediate strain-compensation layers. The stress profile is not uniform along the growth direction, but a stress gradient forms during growth due to the slight difference in the in-plane lattice constant between AlN and GaN. GaN will be more compressively strained near the AlN-GaN interface, and this compressive strain profile will relax with the growth height.

#### 4. Characterization of the III-Nitride on Silicon Platform

Table 4.2.1 List of parameters related to the mechanical and thermal properties of Si, GaN, and AlN.

Material	Si		GaN		AlN	
	<b>Lattice Constant a (Å)</b>		<b>Lattice Constant a (Å)</b>	<b>Lattice Constant c (Å)</b>	<b>Lattice Constant a (Å)</b>	<b>Lattice Constant c (Å)</b>
	5.4309 [91]		3.1890 [92]	5.1864 [92]	3.1106 [93]	4.9795 [93]
	<b>Thermal Expansion Coefficient <math>\Delta a/a</math> at 298 K (K<sup>-1</sup>)</b>		<b>Thermal Expansion Coefficient <math>\Delta a/a</math> at 298 K (K<sup>-1</sup>)</b>		<b>Thermal Expansion Coefficient <math>\Delta a/a</math> at 298 K (K<sup>-1</sup>)</b>	
	2.59·10 <sup>-6</sup> [94]		3.43·10 <sup>-6</sup> [95]		4.35·10 <sup>-6</sup> [95]	
	<b>Phonon Mode</b>	<b>Energy (cm<sup>-1</sup>) [96]</b>	<b>Phonon Mode</b>	<b>Energy (cm<sup>-1</sup>) [97]</b>	<b>Phonon Mode</b>	<b>Energy (cm<sup>-1</sup>) [98]</b>
	LO	520.2	E <sub>2</sub> <sup>high</sup>	567.6	E <sub>2</sub> <sup>high</sup>	653.7
			E <sub>2</sub> <sup>low</sup>	144.0	E <sub>2</sub> <sup>low</sup>	244.8
			A <sub>1</sub> (TO)	531.8	A <sub>1</sub> (TO)	607.3
			E <sub>1</sub> (TO)	558.8	E <sub>1</sub> (TO)	666.8
			A <sub>1</sub> (LO)	734.0	A <sub>1</sub> (LO)	895.5
			E <sub>1</sub> (LO)	741.0	E <sub>1</sub> (LO)	908.7
	<b>Phonon Pressure Coefficient <math> \tilde{\alpha} </math> (cm<sup>-1</sup>GPa<sup>-1</sup>)</b>		<b>Phonon Pressure Coefficient <math> \tilde{\alpha} </math> (cm<sup>-1</sup>GPa<sup>-1</sup>)</b>		<b>Phonon Pressure Coefficient <math> \tilde{\alpha} </math> (cm<sup>-1</sup>GPa<sup>-1</sup>)</b>	
	1.07 [99]		1.215 [100]		1.87 [98]	

A considerable advantage of Raman spectroscopy is the ability to measure mechanical properties of materials at the micrometer scale, both non-invasively and with chemical bond specificity. When a photon undergoes an inelastic scattering process with a molecule, it loses or gains energy, shifting its frequency in what is labelled as a Raman scattering process. The photon is blue-shifted in an anti-Stokes Raman scattering event and red-shifted in a Stokes event. Raman scattering can be generated due to the presence of vibrational and rotational transitions in matter, which are determined by selection rules that emerge out of the bonding structure of the constituent atoms. Therefore, a Raman spectrum reveals the unique spectral signature of matter which identifies its chemical composition. Raman spectroscopy can further relay quantitative information on disorder and the stress state within a sample, since these properties directly impact the phonon modes.

The characterization of semiconductor crystals was performed using two commercial micro-Raman spectroscopy systems: the LabRAM HR and the Renishaw inVia Raman systems. They both comprise a microscopy unit with



#### 4. Characterization of the III-Nitride on Silicon Platform

confocal detection capability. Laser excitation and Raman scattered light travel through the same microscope objective in a reflection configuration. Solid-state lasers provide several excitation lines, of which the  $\lambda=488$  nm (diode-pumped laser) and  $\lambda=532$  nm (frequency-doubled Nd:YAG laser) wavelengths were used. An edge filter suppresses the excitation laser frequency on the collection line. Detection was performed using a monochromator system comprising a variable grating:  $600\text{ mm}^{-1}$ ,  $1800\text{ mm}^{-1}$  and  $2400\text{ mm}^{-1}$ . Calibration was carried out using the spectral lines of a Hg-Ar lamp. A motorized stage allowed for fine positioning and translation of the sample with sub- $\mu\text{m}$  precision, enabling spatial mapping acquisitions.

Measurements were conducted on the semiconductor layers before and after carrying out fabrication processing to determine the residual stress values. Spontaneous Raman scattering was collected in backscattering geometry, and mode selection was achieved through polarization control of incident and detected light. Considering the zone-center optical phonon modes and accounting for wurtzite structure III-nitrides in accordance with group theory, the Raman-active modes are the  $A_1$ ,  $E_1$ ,  $E_2^{\text{low}}$ , and  $E_2^{\text{high}}$  modes [101]. In line with the selection rules using TE excitation on c-axis grown layers, the visible phonon lines are the  $A_1$  (LO),  $E_2^{\text{low}}$ , and  $E_2^{\text{high}}$  modes. It should be noted that other phonon lines may appear in the spectrum due to polarization distortion or disorder in the crystal. The primary observable phonon lines in Si, GaN, and AlN can be found in Table 4.2.1.

The  $E_2^{\text{high}}$  phonon line is found to possess the largest scattering cross-section in III-nitrides, and thereby is primarily used for indirect stress measurements. Under the influence of stress, the vibrational energy of the phonon mode is altered. It drops in magnitude in the case of tensile stress, and vice versa. We rely on the phonon pressure coefficients and deformation potentials that are reported in literature to help deduce the stress and strain values, respectively, based on the shift of the Raman resonance from its unperturbed value. The use of elevated excitation laser powers may result in local heating which in turn red-shifts the Raman resonance [102]. Power dependence checks are conducted to ensure that the observed Raman line is not influenced by the probe. Fig. 4.2.8 displays the Raman scattering spectrum that was acquired from c-axis grown GaN and sputtered AlN wafers. Despite the use of confocal detection, scattered light from the Si substrate is captured in the spectrum and dominates the weaker intensities emerging from the thin membranes. The  $E_2^{\text{high}}$  phonon is seen to have the largest amplitude in GaN and AlN. The AlN  $E_2^{\text{high}}$  mode appears in the GaN spectrum, originating from the AlN buffer layer, and exhibits a broad profile (FWHM  $\approx 8\text{ cm}^{-1}$ ) due to the expected degree of disorder. The Raman intensity captured from the PhC is larger by a factor of approximately 20 compared to that from bulk (under identical excitation and collection conditions) due to the enhanced scattering provided by the PhC structure.

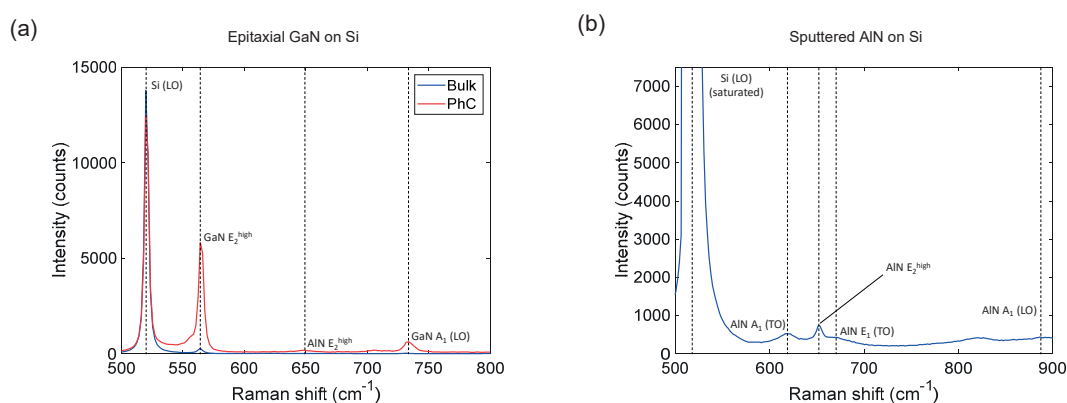


Fig. 4.2.8 (a) Raman spectrum of an epitaxial GaN on Si layer (330 nm in thickness), captured on bulk and photonic crystal patterned regions of the wafer. (b) Raman spectrum of a sputtered AlN on Si wafer.

The GaN  $E_2^{\text{high}}$  phonon mode is measured to be at  $563.8\text{ cm}^{-1}$  in the bulk region of the MOCVD-grown wafer and  $564.4\text{ cm}^{-1}$  in the patterned PhC region. In comparison to the unperturbed  $E_2^{\text{high}}$  phonon energy of  $567.6\text{ cm}^{-1}$  (refer

to Table 4.2.1), the entire layer is under tensile stress, which is computed to be 1.57 GPa and 1.33 GPa ( $\pm 0.04$  GPa) in the bulk and PhC regions, respectively. The lower tensile stress present in the PhC is a consequence of suspension of the PhC membrane, which releases some of the stress in the material. However, as the PhC is still physically bound to the bulk GaN layer, it remains under net tensile stress. The tensile stress values in MOCVD-grown GaN layers was found to be in the range of 1.4–1.6 GPa. These values were measured for GaN layers of thickness ranging from 300 nm to 350 nm. Analysis of strain behavior in fabricated III-nitride layers is presented in section 4.4.1.

Sputtered AlN wafers on Si(111) substrates were also investigated for built-in stress. As displayed in Fig. 4.2.8(b), the  $E_2^{\text{high}}$  phonon line is located at  $652.7 \text{ cm}^{-1}$ , to be compared to an unperturbed value of  $653.7 \text{ cm}^{-1}$  (refer to Table 4.2.1). Similar to the GaN layers, the AlN layer is under tensile stress. However, the magnitude of the stress is much lower at a value of 0.27 GPa, for an AlN layer thickness of 185 nm. With thicker AlN layers (up to 300 nm), the tensile stress value was measured to be marginally higher and did not exceed 0.3 GPa. In comparison, AlN layers that were grown by MBE on Si exhibited tensile stress exceeding 3 GPa. The lower stress values in sputtered AlN layers are expected, due to the columnar growth of the layers which reduces the overall in-plane stress contribution arising from the difference in thermal expansion coefficients between AlN and Si.

### 4.3 Experimental Setup

#### 4.3.1 Design and Construction

The design and construction of the optical setup was carried out during the course of this thesis, building on the pre-existing setup. The initial configuration [103] was constructed to allow for sample characterization of near-IR photonic structures using end-fire excitation and detection. A dedicated near-IR line was used for both real-space and Fourier-space imaging, and a standard imaging path additionally allowed for viewing samples under visible-range illumination. The functionality of the setup was to be expanded, to enable the following:

- Far-field polarization-resolved excitation and detection in the near-IR wavelength range
- Precision sample translation control, below 2 nm
- End-fire polarimetry in the near-IR wavelength range
- Characterization of photonic structures in the visible wavelength range, including Fourier-space imaging and transmission measurements
- Polarization-resolved far-field excitation in the visible wavelength range
- Single-photon detection and imaging in the visible wavelength range

A schematic diagram of the implemented experimental setup is displayed in Fig. 4.3.1. The setup can be divided into three distinct sections: a sample mounting and end-fire coupling section, a near-IR wavelength range section, and a visible wavelength range section.

#### 4. Characterization of the III-Nitride on Silicon Platform

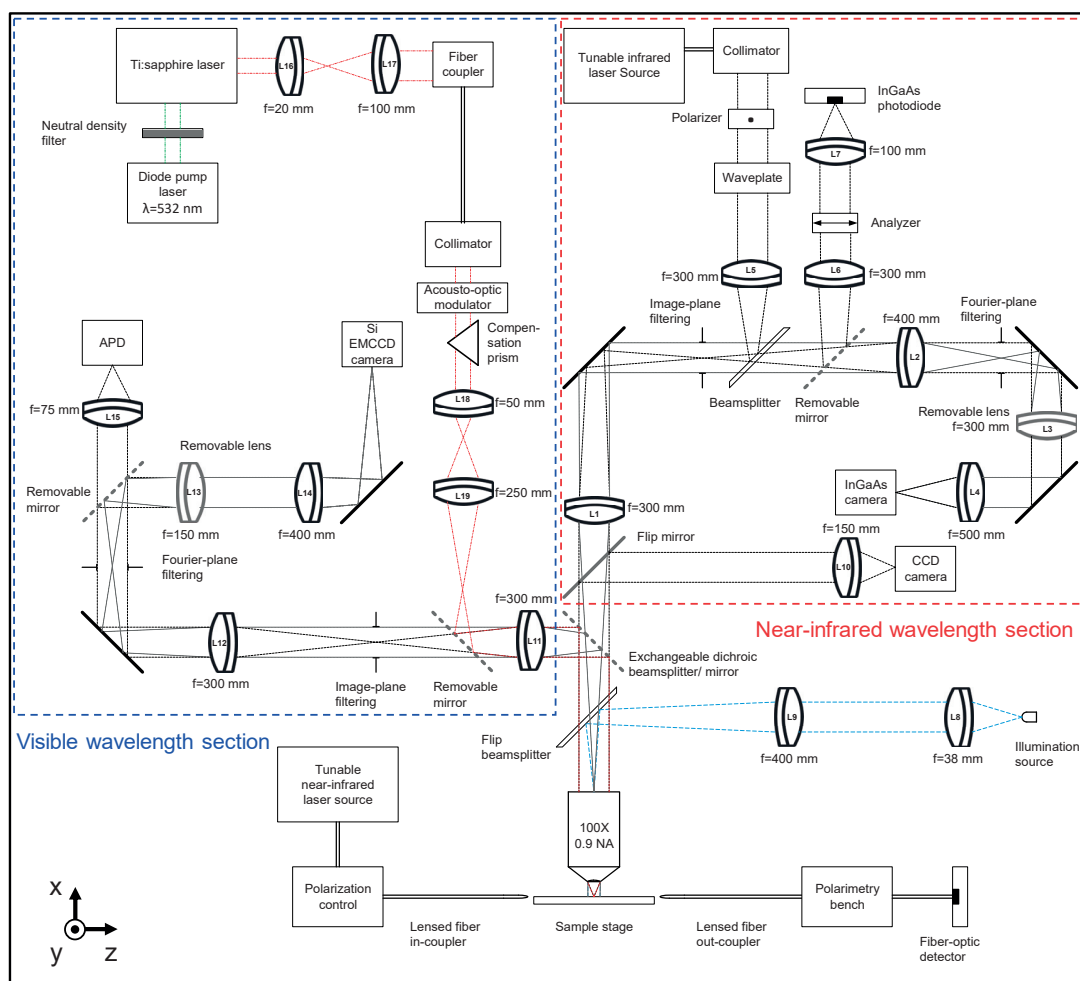


Fig. 4.3.1 Schematic diagram of the experimental setup. Removable components are displayed in gray.

Beginning with the sample-mounting and end-fire coupling section, a sample stage was designed and constructed to incorporate a piezo-translation positioner (PI Nanocube P-611.3S), enabling three-axis sample positioning with 1 nm resolution and 100  $\mu\text{m}$  travel in closed-loop mode. A custom-built sample holder allows for further control over the pitch, yaw and rotation. The piezo stage is mounted on long-range micrometer translators covering a range of 20, 12.7, and 25 mm along each of the x, y, and z axis respectively (axis reference in Fig. 4.3.1). Tapered and lensed single-mode polarization maintaining fibers interface the sample facet. Excitation and detection fibers are selected according to the wavelength range of operation. The light source is generated by a tunable external cavity diode laser (Yensita Optics Tunics system) for operation in the near-IR range (around  $\lambda=1300$  or  $\lambda=1550$  nm). The laser source may otherwise be fiber coupled from a free-space tunable Ti:sapphire or green diode-pumped solid-state laser for visible-range excitation. A polarization control unit comprising a  $\lambda/4 - \lambda/2 - \lambda/4$  waveplate configuration enables precise adjustment of the excitation beam for end-fire coupling in the near-IR range. A polarimetry bench is installed on the detection side, consisting of a configurable polarization selection unit. The detection of the end-fire transmission signal is finally carried out using a fiber-coupled photodiode detector.

The sample is viewed using a standard microscopy imaging configuration. The system comprises an infinity-corrected microscope objective that is mounted on a translating kinematic mount, followed by an imaging achromatic lens and

a visible-range camera for quick sample viewing. A light-emitting diode source, combined with a lens pair provide homogeneous epi-illumination over the field-of-view.

Moving onto the near-IR wavelength range section, the imaging path (refer to Fig. 4.3.1) consists of a set of three achromatic lenses that magnify and project the microscope objective's image plane onto an InGaAs camera (Xenics XEVA-423). Intermediate image and Fourier planes are created along the beam path to allow for light filtering using metallic masks. Placement of an additional lens (lens "L3" on the near-IR line in Fig. 4.3.1) at the end of the line transforms the detection plane at the InGaAs camera to the Fourier plane. An auxiliary section to the imaging path enables resonant scattering characterization (details in section 4.3.3) and contains both the near-IR free-space excitation and detection lines. The excitation line hosts a source, which can be either a near-IR LED or a parabolic mirror collimator for fiber-coupled lasers. It is followed by a polarizer (to maintain a polarization ratio above 1000:1) and a  $\lambda/2$  waveplate for polarization rotation. The excitation beam is introduced to the primary near-IR line through a beamsplitter cube. On the free-space detection line, an analyzer filters the light polarization before it reaches the photodiode detector at the end of the path. Light is directed towards the free-space detection line from the primary near-IR line by mounting a removable mirror, in the case of a weak-scattering signal. Otherwise, a beamsplitter is used, which additionally allows for simultaneous sample imaging. In circumstances where the scattered signal cannot be distinguished from the background, mode-locked detection is employed, and the excitation beam is directly modulated at source.

The final section of the optical setup groups the visible wavelength range optics. The setup is designed to operate both the visible and near-IR lines simultaneously and with high efficiency, using the same microscope objective. A dichroic mirror, installed just after the microscope objective, reflects visible light and transmits near-IR light at over 98% and 96% respectively. A standard visible-range imaging line is installed, in a similar manner to the near-IR line, enabling real and Fourier-space imaging by exchanging a single lens. Light filtering can likewise be applied in the image and Fourier planes using metallic masks. The focal length of the mounted lenses is adapted for the size and pixel density of the EMCCD (Andor iXon Ultra 897 EXF) to achieve sampling beyond the Nyquist rate, when assessing the Rayleigh limit under a numerical aperture of 0.9 and near the center wavelength of operation ( $\lambda=530$  nm). The detector quantum efficiency exceeds 50% in the wavelength range of 375 to 880 nm and is capable of single photon detection in electron multiplication mode. A single-channel APD detector is installed for quantitative and high-speed detection. An excitation laser can be introduced to the primary line through a beamsplitter cube. The laser source is a Ti:sapphire laser that is tunable over  $\lambda=690-1100$  nm and pumped by a solid-state laser ( $\lambda=532$  nm). The Ti:sapphire laser power can reach up to 200 mW. An acousto-optic modulator in combination with a dispersion compensating prism are used to modulate the excitation beam before going through beam-expansion optics and towards the primary beam path. Images of the constructed setup are displayed in Fig. 4.3.2.

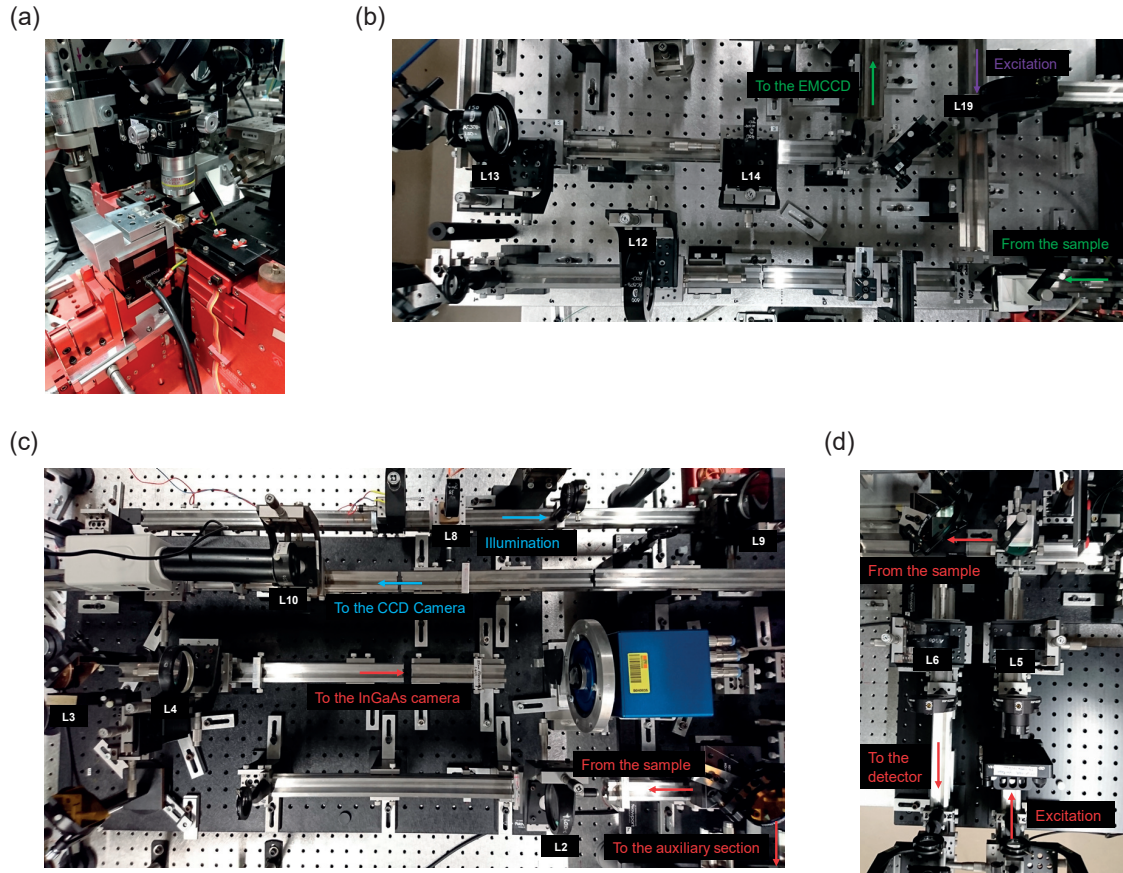


Fig. 4.3.2 Images of the (a) sample stage, (b) the visible wavelength range section, and the near-IR wavelength range section comprising (c) the primary and (d) auxiliary (resonant scattering characterization) lines.

### 4.3.2 Fourier-Space Imaging

The characterization of optical structures often necessitates the observation of momentum space to retrieve information related to the propagative, dispersive, and radiative behavior of light upon interaction with the medium. A simple and common way to do that is by transforming the optical field from real-space to  $k$ -space using the optical Fourier-transform feature of an, ideally, aberration-free lens in what is known as Fourier-space or far-field imaging. The advantage of carrying out the process optically, as opposed to numerically, besides speed is preserving interference effects. If it were to be done numerically, this would require capturing the phase information fully and accounting for it in the calculations. The Fourier-plane forms at the back-focal plane of an infinity-corrected microscope objective, and therefore, the imaging technique can be implemented with relative ease in any standard imaging setup by adding a few lenses.

The Fourier-space imaging approach described in this section relies on the acquisition of the Fourier plane from a sample as a function of wavelength such as to be able to fully reconstruct the dispersion map of light in a specific medium [104]. The sample is typically excited in an end-fire coupling configuration, which delivers light to the optical structures of interest, e.g. PhCs, via waveguides that extend from one facet of the chip to the other. Let's assume the sample features a slab geometry that supports one or more optical modes. The optical structures embedded in the slab may be naturally radiative, and in that case the emitted light is collected directly for imaging using the setup described in section 4.3.1. As a consequence of momentum conservation at the sample-air interface, where air is the ambient medium, the wave vector of light along the propagation direction ( $\beta$ ) inside the slab can be related to

the radiation angle ( $\phi$ ) through  $\beta = k_z = k \cos \phi$ , where  $k = n \frac{2\pi}{\lambda}$  is the magnitude of the wave vector in the surrounding medium of refractive index  $n$ . Therefore, a particular magnitude of the wave vector along the propagation direction in the slab is mapped onto a distinct radiative angle, which can then be reconstructed in the momentum plane in far-field. An illustration of the principle of imaging is shown in Fig. 4.3.3. All radiating modes within the collection aperture of the microscope objective (represented by a thin lens in the figure) should be visible on the Fourier plane. In the case that an optical mode lies underneath the light line and is confined to the layer, an artificial probe must be introduced to extract light out of the system, while minimally perturbing the optical mode [105]. The probe can be a simple grating that imparts momentum onto light such that the mode diffracts at specific angles according to the grating period, as specified by the following equation:

$$k_{\text{diffracted}} = k_{\text{medium}} + m \frac{2\pi}{\Lambda} \quad (4.3.1)$$

Here,  $\Lambda$  is the grating period and  $m$  is the diffraction order. This approach can be also implemented should the radiative angle of a mode lie outside the collection aperture of the microscope objective. It is often the case with fabricated micro- and nanostructures that the defects introduced during fabrication are periodic, and as a result, may form a natural grating that scatters light out, providing the functionality of a probe grating.

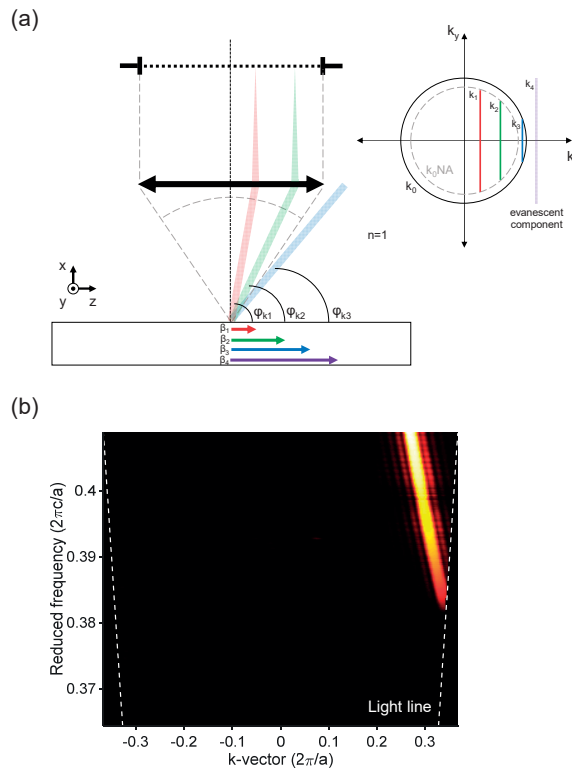


Fig. 4.3.3 (a) Illustration depicting the concept of operation of Fourier-space imaging. (b) Dispersion acquisition of the forward-propagating mode of a GaN W1 waveguide ( $a=605$  nm), operating near  $\lambda=1550$  nm. The light line is indicated by the dashed white line.

The dispersion relation  $\omega(k)$  provides a complete characterization of wave behavior in a dispersive medium. To retrieve it, the frequency dependence of the wave vector in the optical structure is analyzed by scanning the output frequency of the tunable laser over a specified range, while accumulating a Fourier-plane stack. During the process,

the collected set of Fourier planes is acquired in a sequential manner, at the desired spectral resolution specified by the scan. To reconstruct a dispersion map section, i.e.  $\omega$  vs.  $k$ , the acquired two-dimensional Fourier plane at each frequency is projected along a single axis in momentum-space. Each resulting one-dimensional array is associated with a single excitation frequency. By successively stringing the array output of each frequency within the excitation range, the complete dispersion response of the device is obtained with respect to the selected momentum axis.

Fourier-space imaging is a vital tool for the characterization of PhCs, since the purpose of PhCs is to fundamentally modify the dispersive response of material. Retrieval of the dispersion relation allows one to verify that the fabricated device conforms to the computed bandstructure. Radiation losses in PhC waveguides and cavities can be quantitatively analyzed through the leaky components in far-field. When analyzing a waveguiding structure, forward and backward modes can be clearly distinguished in  $k$ -space since they are mirrored about the  $k=0$  axis. Their relative intensities give insight into scattering and reflection processes that induce cross-coupling, with scattering analysis being particularly useful for assessing disorder.

The momentum spread of a dispersion line in  $k$ -space is a useful quantity as it allows to estimate loss in an optical waveguide. This is assuming that the resolution in  $k$ -space ( $\Delta k_{limit}$ ) is smaller than the loss-induced broadening. It should be noted that any momentum line is naturally broadened by the sample size. The broadening equates to the convolution in  $k$ -space of the original momentum line with a sinc function that corresponds to the cut-off window [103]. The other contribution towards broadening comes from losses in the system. Considering the case of a lossy propagating wave, its exponential decay as a function of distance described by an attenuation coefficient ( $\alpha$ ) corresponds to a Lorentzian function in  $k$ -space, whose linewidth scales directly with  $\alpha$  [106].

Under the discretized acquisition,  $\Delta k_{limit}$  is linked to real-space through a Fourier-pair conjugate relation:

$$N\Delta x_{limit}\Delta k_{limit} = 2\pi \quad (4.3.2)$$

where  $N$  is the number of units (pixels) and  $\Delta x_{limit}$  is the resolution in real space.

At a fixed optical resolution ( $\Delta x_{limit} = const.$ ),  $\Delta k$  is dictated by the sampling range in real space ( $N\Delta x_{limit}$ ). In practice, this quantity is either determined by a finite sample size or a limited field-of-view. For sufficiently large structures, the latter sets the limit. This is also often the case, given that real-space filters are used to crop the region of interest within the field of view. The camera pixel pitch ( $30 \mu\text{m}$ ) in combination with the magnification of the lens system on the near-IR line, providing a field-of-view of  $250 \mu\text{m}$ , is capable of resolving  $\Delta k_{x,y} = 0.05 \mu\text{m}^{-1}$  at  $\lambda=1550$ . The Rayleigh criterion specifies an angular resolution of  $\theta = \frac{1.22\lambda}{d}$ , where  $d$  is the diameter of the aperture. A cropped field-of-view below  $\approx 24 \mu\text{m}$  in diameter will therefore deteriorate the  $k$ -space resolution beyond the aforementioned value which is set by the acquisition system. Hence, the employed spatial filters are  $25 \mu\text{m}$  or larger in diameter.

An advantage of Fourier-space imaging compared to other characterization techniques is the ability to directly extract the dispersion relation of optical structures, and with spatial selectivity. The group velocity of light can be subsequently computed with high accuracy, as will be presented in section 6.3.2. Moreover, light propagation regimes can be identified with high clarity, including the onset of light localization [107]. Many reports in literature rely solely on transmission measurements and spectral interferometry [108], [109] for dispersion analysis. This can be misleading as the transmission often includes effects from other waveguiding elements and interfaces besides the PhCs. Moreover, the response is averaged over the entire device and excludes local effects.

#### 4.3.3 Resonant Scattering Characterization

It is often necessary to characterize PhC cavities, to identify the quality of fabrication and the epitaxial layer. Doing so through end-fire coupling can be time-consuming, primarily when switching from one device to another. The

resonant scattering technique offers a quick characterization approach for PhC cavities, where the Q-factor and coupling efficiency of the PhC cavities can be directly measured through free-space excitation and detection without necessitating coupling waveguides.

A simplified schematic of the experimental configuration is shown in Fig. 4.3.4. The PhC cavity axis is mounted and oriented at 45° relative to a vertical polarizer. This enables the excitation of in-plane field components ( $E_x$  and  $E_y$ ) of the cavity modes, under free-space illumination. The back-scattered/ reflected signal is then filtered in cross polarization by a horizontal analyzer. By carefully adjusting the coupling, the resonantly-scattered signal of the cavity mode is maximized over the background from the PhC lattice to produce a symmetric Lorentzian line shape.

The spectral intensity profile of the Fano resonance can be described by the following equation [110], [111]:

$$I(\omega) = A + B \frac{\left[ C + 2 \frac{(\omega - \omega_0)}{\Gamma} \right]^2}{1 + \left[ 2 \frac{(\omega - \omega_0)}{\Gamma} \right]^2} \quad (4.3.3)$$

Here,  $\omega_0$  and  $\Gamma$  are the center frequency and mode linewidth respectively. A and B are constants, while C is the Fano parameter which gives the ratio between the resonant and non-resonant (background) contribution of the scattering process. The C-parameter consequently expresses the asymmetry of the resonance, which can depend strongly on the excitation geometry. When both the resonant scattering and background amplitudes are comparable, the magnitude of C is nearly equal to 1, and the equation gives a Fano line shape. For a dominant resonant scattering contribution however, the magnitude of C is  $\gg 1$ , and the equation gives a Lorentzian line shape.

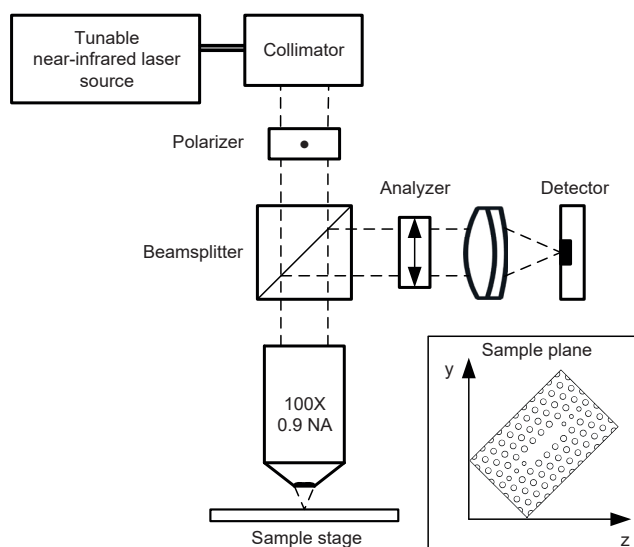


Fig. 4.3.4 Schematic diagram of a standard resonant scattering characterization configuration. The inset displays the orientation of the PhC cavity at the sample plane, relative to the polarizer that is oriented along the y-axis.

The calibration procedure involves evaluating the power impinging on the cavity in parallel-polarization (analyzer relative to the polarizer) after replacing the sample with a mirror. The ratio of the resonantly scattered light intensity to the measured total incident intensity indicates the fraction of light that couples into the cavity and allows one to obtain the coupling efficiency. It should be noted that this efficiency scales with the overlap of the excitation beam and the cavity mode and will therefore vary with the polarization, size, and shape of the excitation beam. Resonant scattering characterization of GaN cavities is presented in section 5.4.1.



An advantage of resonant scattering is the ability to extract the unloaded Q-factor of cavities in a rapid manner. In comparison to evanescent coupling via waveguides, the only loss channel of the cavity is through coupling to radiative modes, so there is no need for the identification of the coupling regime to obtain the intrinsic cavity Q-factors. However, free-space characterization does present difficulties in terms of matching the excitation beam to the profile and parity of the cavity mode. Moreover, in the case of high-Q cavities, the scattered signal from cavities can be extremely weak, since the cavity design is optimized to inhibit radiative coupling.

## 4.4 III-Nitride on Si Platform

### 4.4.1 Residual Stress

As seen earlier in section 4.2.4, stress in III-nitride layers on Si can reach values exceeding 1 GPa. The stress, being tensile in nature, triggers crack formation and growth. This impedes the fabrication of functional micro- and nanoscale devices, especially if the III-nitride layer is to be suspended. Fig. 4.4.1 displays a fabricated GaN on Si sample after membrane release. The sample contains PhCs that are interfaced by wire waveguides in an end-fire coupling configuration. Micro-cracks appear in all suspended microstructures, particularly near edges, where they form and preferentially propagate along the crystallographic axes. Since GaN has a lower refractive index compared to Si, wire waveguides must be suspended and supported by tethers along the entire length of the chip. The weak joints of the nanotethers (100–200 nm in width) are the most vulnerable to stress. They often break off entirely, and if they do remain intact, cracks that form at the tether-waveguide interface (shown in Fig. 4.4.1 (b)) were found to significantly enhance scattering losses from the wire waveguides. This is likely to be the reason behind the low reported loss values in literature [112], [113]. A consequence of tether breakage is the in-plane bending of wire waveguides (for wire width < 1  $\mu\text{m}$ ) and potential wire curling near terminations, which impedes coupling. It is noteworthy that the structures do not remain stable, and micro-cracks continue to grow with time.

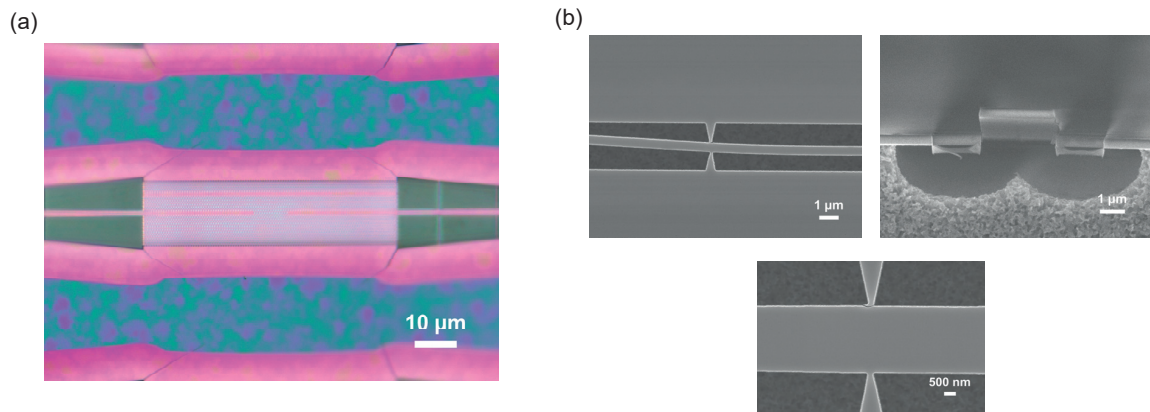


Fig. 4.4.1 (a) Bright-field microscopy image of an initial PhC platform implementation in GaN on Si layers, where cracking is induced in the bulk particularly near sharp edges of the pattern. (b) SEM micrographs displaying in-plane bending of GaN wire waveguides, curling of wire waveguides near the facet, and cracking of support nanotethers at the tether-waveguide interface.

The behavior of stress in the III-nitride layers is elucidated through micro-Raman spectroscopy mapping of the fabricated structures. Before vapor-phase etching of Si, GaN layers are under a tensile stress of approximately 1.5 GPa, as measured directly on GaN wafers after growth. Once the Si is isotropically etched underneath the patterned regions (etch depth=2–3  $\mu\text{m}$ ), the detached GaN layer will immediately have the tendency to relax by compressing in order to retain its natural lattice spacing. This can be deduced from Fig. 4.4.2 (a) and (d), which show the Raman shift of the  $E_2$  phonon line along a vertical cross-section of a suspended GaN wire waveguide and PhC respectively. The phonon energy in the PhC membrane increases by almost  $1\text{ cm}^{-1}$ , amounting to 0.41 GPa of

#### 4. Characterization of the III-Nitride on Silicon Platform

released tensile stress. The induced compression of the suspended membrane in conjunction with the tensile stress in the surrounding intact regions is resolved through crack formation to ease stress release, which can be clearly seen near the lower left edge of the PhC. A corresponding reduction in the tensile stress is measured at the proximity of the micro-crack (at position  $\approx -25 \mu\text{m}$ ) in Fig. 4.4.2 (d). The release of tensile stress in the wire waveguide is almost double in comparison with the PhC due to its reduced dimensions and attachment mechanism. The Raman line scan in Fig. 4.4.2 (a) runs across the suspension tether. The lowest tensile stress points are at the tether sites, clearly indicated by the peaks in the Raman shift, due to their capacity to deform. Since the tethers are surrounded on both sides by layers with high tensile stress, they are vulnerable to cracking and breakage should the stress limit be exceeded. This geometry for suspension is therefore not ideal for high-stress layers.

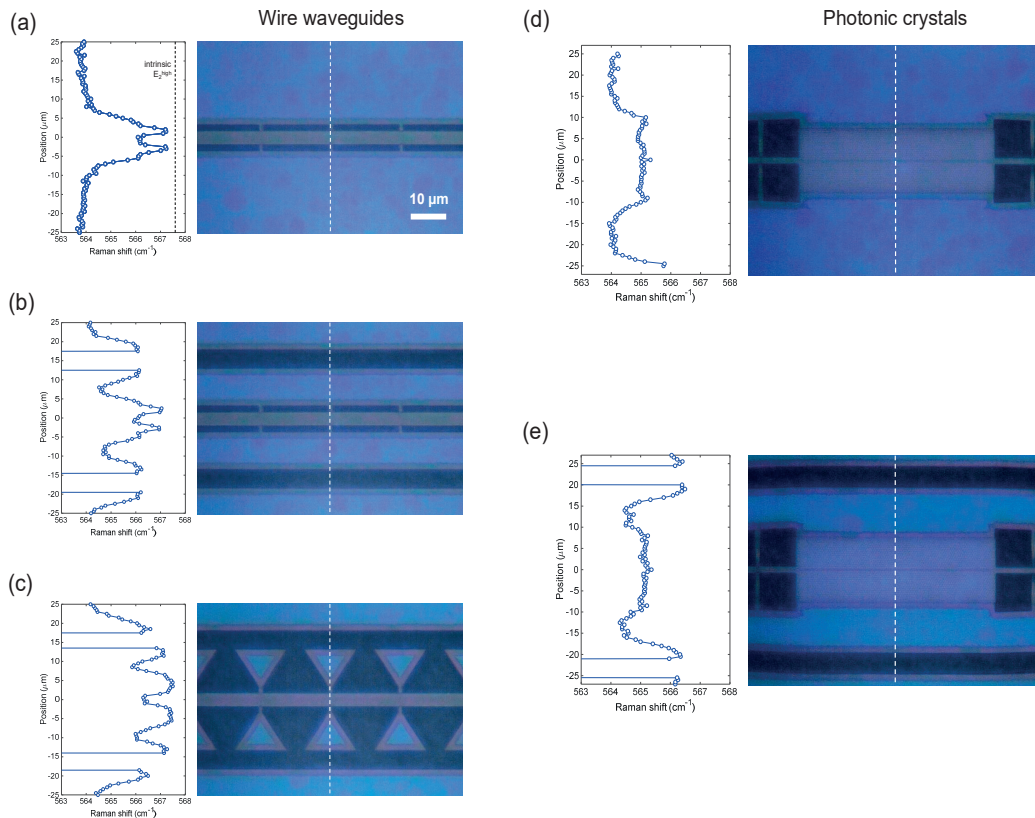


Fig. 4.4.2 Micro-Raman maps of the GaN  $E_2^{\text{high}}$  phonon line performed on a suspended (a) regular waveguide, (b) isolated waveguide, (c) pillar supported waveguide, (d) regular PhC, and (e) isolated PhC, along the vertical direction as indicated in the corresponding bright-field microscopy images by the dashed white line. All images share the same scale bar as indicated in (a).

To mitigate stress-induced effects, the patterned photonic structures were isolated from the bulk layer to allow the III-nitride layer to extend/ contract. This lead to partial stress relaxation, and cracks previously seen near the edges were greatly reduced in number and extent. This is displayed in Fig. 4.4.2 (a)–(c), where linear Raman scans of the GaN  $E_2^{\text{high}}$  phonon line were successively performed on regular waveguides, isolated waveguide, and pillar-supported waveguides. The effect of isolation is evident. The phonon line transitions from a value below  $564 \text{ cm}^{-1}$  to one above  $566 \text{ cm}^{-1}$  near the suspended edges in Fig. 4.4.2 (b). By gradually isolating the waveguides from the bulk, the overall tensile load on the suspended structure drops. When pillars are added at the end of the support tethers Fig. 4.4.2 (c), the stress is seen to become more level on the side of the pillar. The pre-existing tensile load that the tethers had to endure is reduced, and both tether breakage and cracking are circumvented. The tensile stress however cannot be entirely eliminated from the photonic structures since the intact GaN regions remain

anchored to the substrate, straining the membrane. To mitigate stress further in the waveguides, engineered nanotethers must be introduced, which have the capacity to release stress via in-plane deformation (similar to those implemented with Si in section 6.4).

#### 4.4.2 Platform Design

The design of the III-nitride on Si platform for end-fire coupling revolves around photonic crystal structures that are positioned at the center of the chip. Modified W1 waveguides run through the PhC lattice, which is approximately 100–150 lattice units in length and 50–100 units in width. Photonic crystal cavities embedded in the lattice can be coupled to evanescently through the W1 waveguides. The W1 waveguides are width-tuned to shift their dispersion response, such that the resonant cavity frequency overlaps the fast-light region where light propagation in the waveguide is not hindered.

At their termination, PhCs are interfaced by adiabatically tapered wire waveguides where they meet the W1 waveguides. The wire waveguides are fully suspended from facet-to-facet, by means of nanotethers attached to support pillars. The III-nitride thickness ensures single mode operation at  $\lambda=1550$  nm, however, multiple TE and TM modes may be sustained according to the waveguide width. The PhC is physically supported by an isolated ridge for stability, while the wire waveguides utilize triangular pillars to mitigate stress. For coupling to a tapered and lensed optical fiber ( $1/e^2$  spot size =  $2.5 \mu\text{m}$  at  $\lambda=1550$  nm), the wire waveguide at the facet is either cleaved as is or adiabatically tapered to form a nanowire coupler as displayed in Fig. 4.4.3 (c). The dimensions of a cleaved wire waveguide are designed to provide maximal matching with the fiber spot size. Adiabatically-tapered wires were found to improve light coupling, achieving coupling losses better than 2 dB. However, since cleaving must be done within  $15 \mu\text{m}$  from the nanowire coupler tip for optimal coupling, the reproducibility of devices was low with the employed semi-automatic cleaving tool. The components of the fabricated GaN photonic crystal platform are displayed in Fig. 4.4.3.

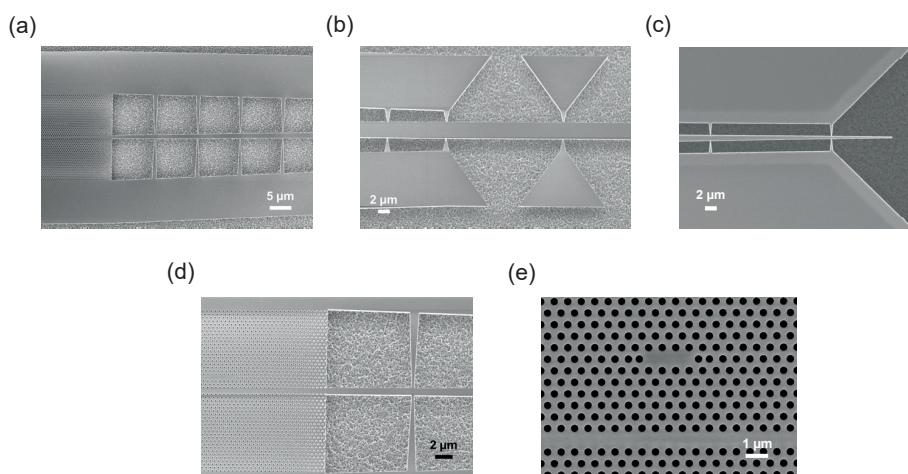


*Fig. 4.4.3 SEM micrographs of the GaN on Si PhC platform. (a) A PhC coupled to a suspended wire waveguide, which is tapered toward the interface with the PhC W1 waveguide. (b) Suspended wire waveguides supported by nanotethers, which connect them to support pillars. (c) Adiabatically-tapered wire waveguide near the facet of the optical chip forming a nanowire coupler. (d) A close-up view of the PhC-wire waveguide interface. Light entering the W1 waveguide is evanescently coupled to the incorporated L3 cavity. (e) Top view of a W1 waveguide at coupling distance to an L3 cavity.*

Initial optical characterization of the GaN photonic structures has revealed the lowest loss values in suspended GaN waveguides to date. The propagation loss in the pillar-supported waveguides was measured to be  $3.7 \text{ dBmm}^{-1}$  through direct transmission measurements in 3 mm long wire waveguides. This is to be compared to loss values in

the range of  $10\text{--}12\text{ dBmm}^{-1}$  in previous reports [112], [113]. The spectral response however remained plagued by distributed Bragg-reflection from the periodic tethers, which was addressed in later designs through an aperiodic tether spacing distribution. The primary contribution towards the measured losses was scattering, which amounted to  $7.3\times 10^{-2}$  dB per tether pair, neglecting absorption losses over the propagation distance in GaN. Other scattering loss contributions originate from the GaN-AlN interface roughness that is inherent to the MOCVD growth. The sidewall roughness contribution was greatly reduced by optimizing the e-beam lithography resolution near the edges of the pattern and through the implementation of a refined etch recipe.

### 4.5 Summary

Characterization of GaN and AlN layers, prepared by MOCVD and sputter deposition respectively, was conducted to obtain their structural and optical properties. GaN layers were found to exhibit high interface roughness at the AlN-GaN interface in addition to an uneven surface topography, both of which contributed to scattering and non-trivial transmission properties in optical devices. Sputtered AlN on the other hand featured surface roughness a few angstroms higher than the epitaxial layers, yet with the characteristic grainy texture. The constituent crystallites in the AlN layer were measured to be highly c-axis oriented, but exhibited a random twist around the c-axis. Raman spectroscopy revealed tensile stress in both GaN and AlN layers, exceeding 1.4 GPa in the former and below 0.3 GPa in the latter.

The experimental setup and characterization techniques were presented. The design of the III-nitride on Si platform was elaborated and shown to mitigate the residual tensile stress in semiconductor layers. The platform was successfully fabricated in GaN, producing structures of high stability compared to previous implementations. Record-high transmission values were obtained for the fully suspended GaN waveguides, reducing losses by more than  $6\text{ dBmm}^{-1}$  in comparison to reported values.

# 5. Frequency Upconversion in Two-Dimensional Gallium Nitride Photonic Crystal Cavities

## 5.1 Introduction

Progress in integrated optics requires the employment of advanced light control modalities on a chip which can be implemented both with a reasonable footprint as well as have potential for integration. These modalities include but are not limited to: routing of light signals, signal modulation, frequency conversion, and imparting phase delay. Through nonlinear light-matter interaction, such control schemes become feasible. Optical nonlinearities in condensed matter systems have long been considered to be a perturbative effect, and a standard approach towards intentionally generating them has been to rely on intense optical fields provided by pulsed lasers, which can typically reach fluence values up to  $\sim 100 \text{ J/cm}^2$ . With regard to integrated systems, a more efficient and compact alternative is needed, which would be capable of reaching nonlinear operation regimes under low photon flux and preferably enable continuous-wave operation. Thereby, adaptable material, a suitable platform, and a light-field enhancement mechanism are necessary towards realizing such a solution.

Beginning with the platform, III-nitride semiconductors have been selected for this study due to their wide electronic bandgap, which offers a broad transparency window, combined with low linear absorption losses in the wavelength range of operation (here in the near-IR telecom range) such that losses do not impose restrictions on a given application. Moreover, nonlinear absorption losses are relatively low, as to not simultaneously hamper an occurring nonlinear process. By examining commonly used semiconductors such as Si and GaAs, they are found to inherently suffer from undesirable effects such as thermal instability (leading to hysteresis), peak-dragging, and linewidth broadening [114]–[116]. These effects are induced by two-photon absorption and free-carrier absorption, which accompany any nonlinear process that is triggered by high-field strength. Despite its drawbacks, silicon is currently the material-of-choice for integrated optics due to ease of integration, with the established Si semiconductor electronics industry, as it enables the introduction of the technology at low cost. We have selected wide bandgap material grown on Si(111) to demonstrate the capacity of the platform for integration with Si. This can be brought about with the more common Si(100) in practice through future advances in growth techniques [117]. Currently, the flip-chip bonding approach is most suited for incorporating III-V semiconductors with Si(100) fabrication.

III-nitrides in their non-centrosymmetric wurtzite crystal structure possess a strong second-order susceptibility [118], [119], unlike Si, which must resort to symmetry-breaking at the surface [120], straining [121], plasma activation [122], [123], or the application of intense fields [124] to induce second-order nonlinear effects. This gives III-nitrides a significant advantage beyond achieving higher efficiency in nonlinear processes, being the freedom of design implementation. This becomes particularly important when scaling down device dimensions. Beyond the utilization of intrinsic material nonlinearity, III-nitrides can additionally function as an ideal host material for highly nonlinear material that can benefit from its transparency range, including polymers [125] or transition-metal dichalcogenides [126] for instance.

As for light-field enhancement, we rely on two-dimensional slab photonic crystals to confine light to wavelength-scale volumes, or smaller, in high-Q defect cavities. While a slab geometry suffers inherent radiative light-cone losses, they are most suited for integration, and radiative losses can be mitigated through design optimization. PhC cavities have the advantage of the ability to enhance optical fields without incurring significant attenuation, in comparison to competing approaches that rely solely on plasmonic enhancement for example. An essential requirement with the PhC approach is that the absorption losses at the pump wavelength be sufficiently low relative to leakage losses, e.g. light-cone radiation, from the PhC slab such as not to degrade the cooperativity factor [127] of the cavity. This condition can be essentially met with several wide bandgap semiconductors.

In this chapter, GaN slab PhC cavities on Si are presented which operate in the telecom range, with designs that are optimized for both light confinement and far-field coupling. Characterization of fabricated cavities reveals record-high Q-factors for GaN, which has enabled enhanced second harmonic generation (SHG) and third harmonic generation (THG) by means of resonant far-field excitation. The highest conversion efficiency of SHG in GaN to date is achieved under continuous-wave operation. Factors contributing to the observed enhancement in nonlinear conversion are highlighted within the context of PhC design.

## 5.2 Comparison of Nonlinearity in III-Nitride Semiconductors

A wide range of nonlinear effects are displayed by hexagonal lattice polytypes of wide bandgap semiconductors which include GaN and AlN. This is due to their non-vanishing second-order susceptibility by virtue of their non-centrosymmetric crystal structure. The wurtzite crystal lattice of GaN is displayed in Fig. 5.2.1, which possesses  $C_{6v}$  point-group symmetry, following the Schoenflies notation. Based on symmetry considerations [40], the non-zero contributions towards second-order susceptibility are the  $\chi^{(2)}_{113}$ ,  $\chi^{(2)}_{223}$ ,  $\chi^{(2)}_{311}$ ,  $\chi^{(2)}_{322}$ , and  $\chi^{(2)}_{333}$  components and their respective permutations, while the remaining components vanish. With regard to the third-order susceptibility, the most prominent contribution comes from  $\chi^{(3)}_{1111}$  and  $\chi^{(3)}_{2222}$ . Consequently, the generation and observation of nonlinear processes are constrained by geometric considerations for a non-distorted crystal lattice.

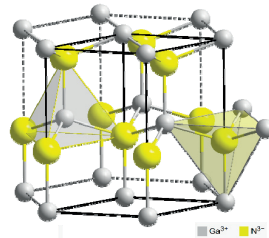


Fig. 5.2.1 Crystal lattice of wurtzite-symmetry GaN.

The feasibility of generating  $\chi^{(2)}$  and  $\chi^{(3)}$  processes has been sought in wide bandgap material through many studies on their susceptibility [118], [128], [129], dating back more than 40 years. Table 5.2.1 summarizes the linear and nonlinear parameters of the GaN and AlN susceptibility as reported in literature. First-principles many-body calculations of GaN monolayer susceptibility have shown that the second-order susceptibility has a spectral response that is strongly affected by excitonic effects, and high  $\chi^{(2)}$  values have been predicted that are on the order of 10 pm/V. Experimental values in bulk GaN on the other hand are lower by approximately a factor of two (refer to Table 5.2.1).  $\chi^{(2)}_{333}$  is the strongest second-order component in GaN ( $\sim 7$  pm/V), yet utilizing it requires all-TM operation in c-axis monocrystalline layers.  $\chi^{(2)}_{311}$  is therefore the alternative component to be used in the presence of TE modes, but at the expense of a factor of two reduction in the nonlinear susceptibility. The second-order susceptibility of AlN is comparable in terms of  $\chi^{(2)}_{333}$ , however, the  $\chi^{(2)}_{311}$  component has been measured to be below

## 5. Frequency Upconversion in Two-Dimensional Gallium Nitride Photonic Crystal Cavities

1 pm/V [130], [131]. The third-order nonlinearity on the other hand has been less thoroughly characterized, in part due to the complexity of extracting single susceptibility parameters from the number of different nonlinear processes that are simultaneously generated. They include but are not limited to third harmonic generation, two-photon absorption, and self-phase modulation.

*Table 5.2.1 Experimental refractive index and nonlinear susceptibility values reported in literature for wurtzite GaN, wurtzite AlN, and sputtered AlN. Components of the susceptibility tensor which are unspecified in the table were not identified by the respective publications.*

	GaN, wurtzite	AlN, wurtzite	AlN, sputtered
<b>Refractive index</b>	2.32 (ordinary) at $\lambda=1550$ nm [132]	2.12 (ordinary) at $\lambda=1550$ nm [133]	2.08 (ordinary) at $\lambda=1550$ nm [134]
<b><math>\chi^{(2)}</math></b>	$\chi^{(2)}_{311} \approx 2 - 5$ pm/V, $\chi^{(2)}_{333} \approx -7 - 4$ pm/V at $\lambda=1064$ nm [118]  $\chi^{(2)}_{311}/2=2.5$ pm/V, $\chi^{(2)}_{333}/2=-3.8$ pm/V at $\lambda=1064$ nm [119]	$\chi^{(2)}_{333}/2=18.5 \times 10^{-9}$ esu (=7.75 pm/V), $\chi^{(2)}_{311}/2 \leq 0.04 \chi^{(2)}_{333}/2$ near $\lambda=1064$ nm [129]	$\chi^{(2)}/2 \approx 5 \times 10^{-9}$ esu (=2.09 pm/V) near $\lambda=400$ nm [135]  $\chi^{(2)}_{311}/2=0.2$ pm/V, $\chi^{(2)}_{333}/2=8$ pm/V at $\lambda=1064$ nm [130]  $\chi^{(2)}_{311}/2=0.04$ pm/V, $\chi^{(2)}_{333}/2=4$ pm/V at $\lambda=1064$ nm [131]
<b><math>\chi^{(3)}</math></b>	$\approx 10^{-9}$ esu (= $1.7 \times 10^{-17}$ m <sup>2</sup> /V <sup>2</sup> ) at $\lambda=353$ nm [136]  $\chi^{(3)}_{xxxx}=2.7 \times 10^{-11}$ esu (= $3.8 \times 10^{-19}$ m <sup>2</sup> /V <sup>2</sup> ) at $\lambda=365$ nm [137]		
<b><math>\chi^{(3)}</math>, two-photon absorption</b>	$\approx 15$ cm/GW at $\lambda=400$ nm [138]  9 cm/GW at $\lambda=530$ nm [128]  0.65 cm/GW at $\lambda=730$ nm, [139]	$\approx 13$ cm/GW at $\lambda=355$ nm [140]	
<b><math>\chi^{(3)}</math>, nonlinear refractive index</b>	$\approx 2 \times 10^{-12}$ cm <sup>2</sup> /W at $\lambda=370$ nm [138]  $2.5 \times 10^{-14}$ cm <sup>2</sup> /W at $\lambda=530$ nm [128]  $2.5 \times 10^{-14}$ cm <sup>2</sup> /W at $\lambda=724$ nm [139]	$-1.91 \times 10^{-13}$ cm <sup>2</sup> /W at $\lambda=355$ nm, $1.79 \times 10^{-13}$ cm <sup>2</sup> /W at $\lambda=532$ nm, $1.61 \times 10^{-12}$ cm <sup>2</sup> /W at $\lambda=1064$ nm [129]	

### 5.3 Methodology: Cavity Design and Injectors

Through the use of optical cavities, light-matter interaction within a specified volume can be strengthened for the purpose of amplifying the relatively small intrinsic nonlinear coefficients in many condensed-matter systems. The enhancement in a cavity is two-fold: spatial through modal confinement and temporal through the Q-factor of the cavity. Both lead to optical energy build-up per unit volume of the material in the regions overlapping with the resonant mode. An intensity build-up factor of  $Q/V$  at the fundamental frequency therefore leads to an enhancement factor proportional to  $(Q/V)^n$  at the harmonic frequency, for the case of frequency upconversion with  $n$  interacting fields in an  $n^{\text{th}}$ -order nonlinear process. The nonlinear material overlap must be additionally accounted for. Furthermore, the efficiency of the nonlinear process can be improved or deteriorated depending on the fraction of the power of the source that can be delivered to the resonant mode, i.e. the coupling efficiency ( $\eta$ ). A similar argument for the enhancement of the fundamental excitation frequency leads to the reformulation of the aforementioned enhancement factor to be proportional to  $(\eta Q/V)^n$  for the nonlinear process.

#### 5.3.1 Far-field Coupling

Achieving optimal coupling to the resonant mode of a cavity is critical to maximizing the enhancement factor of the nonlinear process. Far-field coupling is particularly appealing since it enables access to the cavity mode through free-space, lifting restrictions on the required separation length, apart from coherence length considerations for certain applications. The complexity of the coupling scheme is reduced in comparison to techniques based on evanescent field coupling, e.g. tapered fiber coupling for instance. With far-field coupling, fine positioning control of the excitation beam relative to the cavity is still necessary for the optimization of the coupled power.

To be able to efficiently excite the resonant mode of a cavity in far-field, it is imperative that there be an overlap between the radiative components of the cavity mode and excitation beam. Such overlap is not straight-forward to bring about with slab PhC cavities, since ideally for a high Q-factor systems, radiative leakage channels are minimized. By observing the far-field pattern of an optimized L3 cavity for instance, the radiative energy is found to be negligible at  $k=0$  and concentrated near the circumference of the light cone, since the reduction of cavity radiation relies on the cancellation of lowest-order multipole moments of the mode [33]. This impedes to a great extent any sort of coupling to a focused Gaussian beam.

An effective solution to this problem is to make use of band folding techniques in PhCs as proposed in [141], [142]. The essence of this approach is superimposing an artificial grating onto the native PhC lattice such that light scattering occurs in a controlled manner that follows the PhC symmetry. The introduction of a spatial periodicity of  $2a$  to the lattice for instance functions to fold the  $k$ -vector components that exist near the Brillouin zone edge to the  $\Gamma$ -point in reciprocal space, thereby increasing the optical energy density within the excitation aperture, and ergo, the overlap with the excitation beam. This is shown in Fig. 5.3.1, where the far-field pattern of an optimized L3 cavity is plotted before and after the introduction of an out-coupler grating.



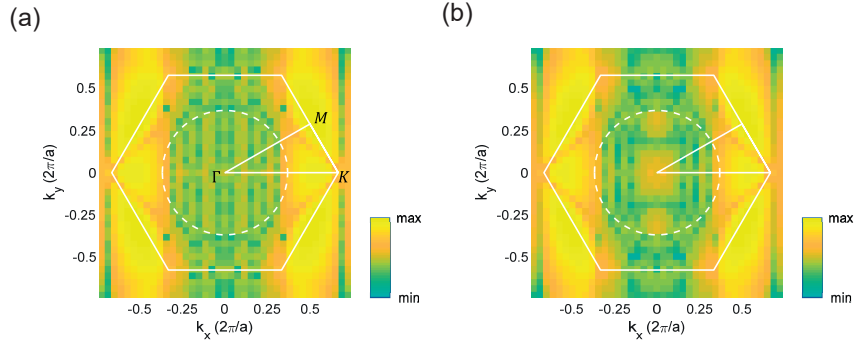


Fig. 5.3.1 Simulated reciprocal space map of the fundamental cavity mode of an optimized L3 cavity (a) before and (b) after the introduction of a double-period lattice grating. The high-symmetry points of the PhC lattice and the reduced Brillouin zone are indicated, along with the radiative light cone (dashed line).

This technique is particularly advantageous due to its robustness to disorder and its ability to shape the far-field pattern to a near-Gaussian distribution in PhC cavities that possess matching mode parity. This allows for attaining coupling efficiencies values beyond 50% in common cavity designs, e.g. L3 cavity. It should be noted that this is achievable without significantly disturbing the spatial profile of the cavity mode. However, a direct intuitive consequence of band-folding in PhC slabs is the reduction of the cavity mode Q-factor, in correspondence with the power that is transferred to radiative modes. The coupling efficiency can be approximated through the variation of the cavity Q-factor  $\eta \sim \left(1 - \frac{Q_{folded}}{Q_{intrinsic}}\right)$ , since the Q-factor gives a direct quantification of the radiative losses. It may however be misleading in practice should the extracted radiation not be contained within the excitation aperture.

The effective experimental coupling efficiency ( $\eta_{exp}$ ) between the excitation beam and the cavity mode can be computed by considering the overlap between the two modes, while accounting for the numerical aperture of the optical system. As the Fourier transform from real-space to k-space is unitary, following Parseval's theorem, the modal overlap can be computed in k-space between the excitation beam and the cavity mode.  $\eta_{exp}$  then goes according to the following expression:

$$\eta_{exp} = \frac{\left| \iint_{-k_0 NA}^{k_0 NA} \hat{\mathbf{E}}_{cavity\ mode} \cdot \hat{\mathbf{E}}_{Gaussian} dk_x dk_y \right|^2}{\iint_{-\infty}^{\infty} |\hat{\mathbf{E}}_{cavity\ mode}|^2 dk_x dk_y \iint_{-\infty}^{\infty} |\hat{\mathbf{E}}_{Gaussian}|^2 dk_x dk_y} \quad (5.3.1)$$

### 5.3.2 Implemented Designs

Two cavity designs were considered for light confinement in a two-dimensional, triangular PhC lattice: the L3 cavity, based on three missing holes [19], and the H0 (point-shift) cavity, which displays the lowest modal volume amongst planar, two-dimensional PhC cavities [17]. To enable Q-factor optimization through the manipulation of out-of-plane radiative losses, the first three side holes of the L3 cavity were modified both in size and position, while with the H0 cavity, the first five side holes and two vertical holes were adjusted only in position. A schematic of each of the optimized cavity designs is displayed in Fig. 5.3.2, along with the field profile of the fundamental cavity mode. The modified horizontal and vertical holes of the PhC cavity are labeled  $h_i$  and  $v_j$  respectively, enumerated from inside out, for which the employed parameters are summarized in Table 5.3.1.

Design wavelengths in the telecom range, at  $\lambda=1300$  nm and  $\lambda=1550$  nm, were targeted for each cavity by scaling the lattice constant ( $a=470$  nm and  $570$  nm respectively) while maintaining a lattice-constant to hole-radius ratio of 4:1, for a fixed slab thickness of 350 nm. An automated optimization algorithm based on guided-mode expansion was utilized to sweep parameter space within specified constraints for the highest attainable Q-factors, which was

## 5. Frequency Upconversion in Two-Dimensional Gallium Nitride Photonic Crystal Cavities

carried out by M. Minkov [37]. The optimization runs yielded cavities with a theoretical Q-factor of  $1.1 \times 10^5$  for both L3 and H0 cavities resonant near  $\lambda=1300$  nm, while Q-factors of  $2.2 \times 10^5$  and  $1.2 \times 10^5$  were obtained for L3 and H0 cavities respectively, resonant near  $\lambda=1550$  nm. The higher Q-factors obtained at  $\lambda=1550$  nm were in part due to the chosen slab thickness, which was kept constant for both design wavelengths to integrate the cavities on the same chip. Simulations using finite-difference time domain (FDTD) and finite-element method (FEM) solvers confirmed the computed profiles and Q-factors of the cavity modes.

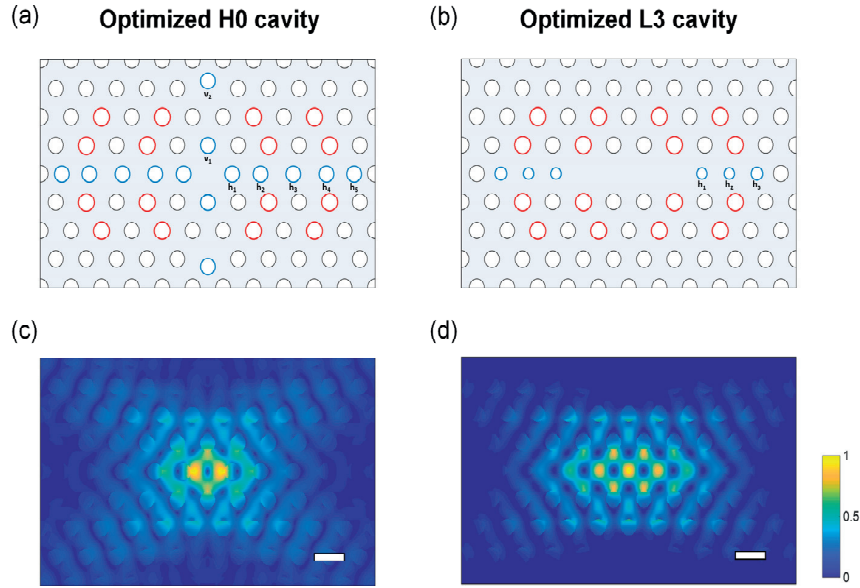


Fig. 5.3.2 Schematic illustration of the (a) H0 and (b) L3 cavity designs, showing the modified PhC holes in blue and the injector holes in red, and the fundamental cavity mode electric-field norm is displayed in (c) and (d) respectively. The bar corresponds to the PhC lattice constant length.

Table 5.3.1 Design parameters of the optimized L3 and H0 PhC cavities, resonant near  $\lambda=1300$  nm and  $\lambda=1550$  nm. The translation along the x-axis ( $\Delta x$ ) and y-axis ( $\Delta y$ ), as well as the change in hole radius ( $\Delta r$ ) are indicated relative to the PhC lattice constant ( $a$ ).

	$\lambda = 1300$ nm		$\lambda = 1550$ nm	
	L3 cavity	H0 cavity	L3 cavity	H0 cavity
$\Delta x_{h1}/a$	0.3482	0.3	0.3999	0.3000
$\Delta x_{h2}/a$	0.2476	0.2293	0.3029	0.2327
$\Delta x_{h3}/a$	0.0573	0.2801	0.2109	0.3085
$\Delta x_{h4}/a$		0.3		0.4000
$\Delta x_{h5}/a$		0		0.3087
$\Delta y_{v1}/a$		-0.0074		0.0043
$\Delta y_{v2}/a$		0.15		0.2325
$\Delta r_{h1}/a$	-0.098		-0.1000	
$\Delta r_{h2}/a$	-0.0882		-0.0979	
$\Delta r_{h3}/a$	-0.0927		-0.0505	

Further modification of the PhC lattice served to enhance coupling to the fundamental cavity mode through band folding, as detailed earlier. The PhC holes surrounding the cavity as shown in Fig. 5.3.2 earlier, referred to as “injectors”, were increased in radius relative to the native PhC holes such that a two-fold periodicity ( $2a$ ) is imposed on the lattice. The resultant far-field emission pattern ( $|E|^2$ ) of the H0 and L3 cavities is displayed in Fig. 5.3.3 for an injector-hole radius incrementation ( $\Delta r_i$ ) of 0, 5 and 10 nm.

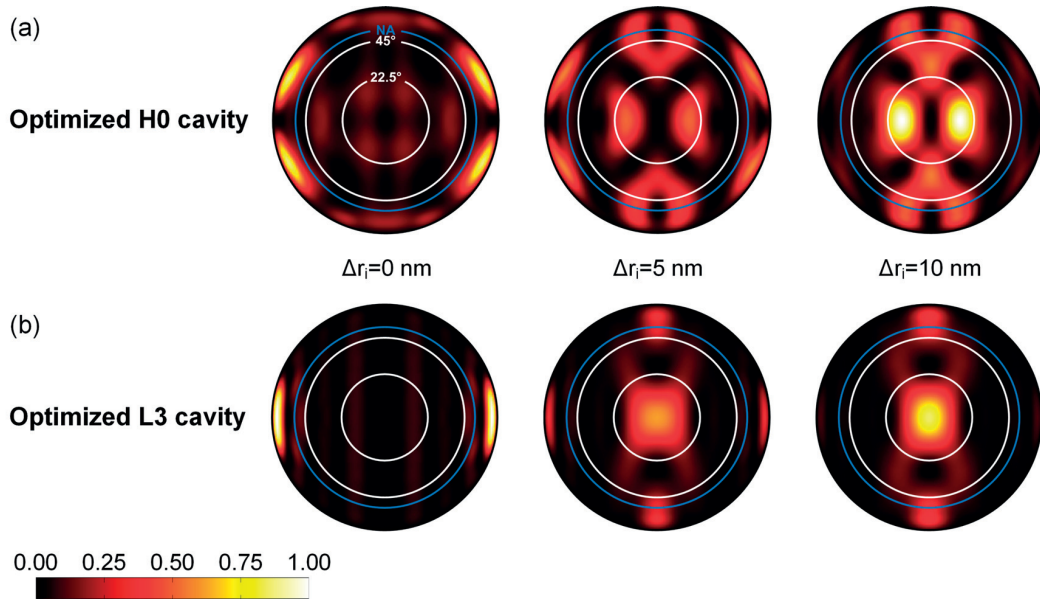


Fig. 5.3.3 Evolution of the far-field normalized electric-field intensity profile for the fundamental mode of the (a) H0 and (b) L3 cavities as a function of injector size for  $\Delta r_i = 0, 5,$  and  $10$  nm. From inside out, the circles correspond to emission angles of  $22.5^\circ,$   $45^\circ,$  and a numerical aperture (NA) =  $0.8$ .

Upon the introduction of the injector-hole perturbation to the lattice, the band folding effect is manifested in directional emission near the  $\Gamma$  point in  $k$ -space for the fundamental mode of both cavity designs. Contrary to the near-Gaussian distribution of the far-field pattern of the L3 cavity, two lobes appear around the center of reciprocal space for the H0 cavity, arising from the odd parity of the fundamental mode. Cavity simulations based on GME and FDTD modeling were used to compute the cavity Q-factor and external coupling efficiency respectively, both of which are plotted in Fig. 5.3.4 as a function of  $\Delta r_i$  for cavities resonant near  $\lambda = 1550$  nm. The external coupling efficiency was calculated by accounting for the channeling of the far-field emission of the fundamental cavity mode into the numerical aperture (NA) of the employed microscope objective (NA =  $0.8$ ). The polarization properties of the excitation beam and modal overlap with the fundamental cavity mode can further reduce the effective coupling.

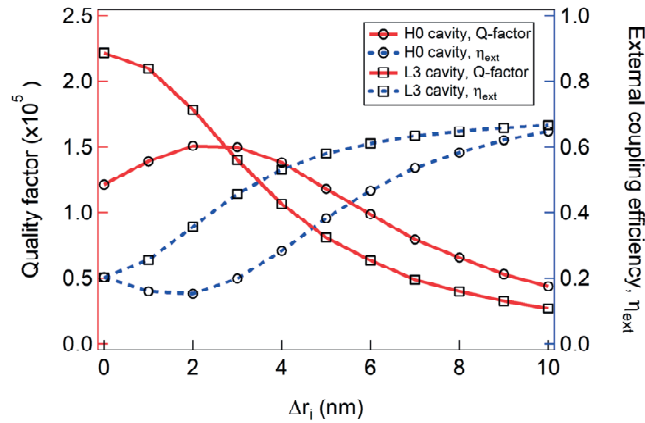


Fig. 5.3.4 Dependence of the theoretical Q-factor and external coupling efficiency (computed for  $NA=0.8$ ) on the injector hole radius, for the fundamental mode of the H0 and L3 cavities, which are resonant near  $\lambda=1550$  nm.

Three injector sizes were selected for fabrication with each cavity to cover an effective coupling efficiency ( $\eta$ ) range from approximately 2% to 20%. The injector hole radius variation values were  $\Delta r_i=[3, 5, 8]$  nm for the L3 cavity and  $\Delta r_i=[5, 7, 10]$  nm for the H0 cavity. The PhC cell was chosen to be 65a by 39v3a units in size, with the cavity residing at the center. The sample design accounted for lithographic tuning of the PhC-hole radius around the nominal optimization values to target the design wavelength. Fracturing of the lithographic mask pattern was performed with a 1 nm resolution, corresponding to the minimum translation for electron-beam writing.

The GaN layers that were used were obtained through heteroepitaxial growth by metalorganic chemical vapor deposition on a Si(111) wafer. A nucleation layer consisting of 40 nm of AlN was first deposited, followed by 310 nm of GaN. The grown layers are gallium-face and c-axis oriented, characterized by a (0002) rocking curve FWHM of 1500 arcsec. Pre-fabrication wafer characterization and fabrication of PhCs was carried out as detailed in earlier sections. SEM micrographs of the fabricated H0 and L3 cavities are displayed in Fig. 5.3.5.

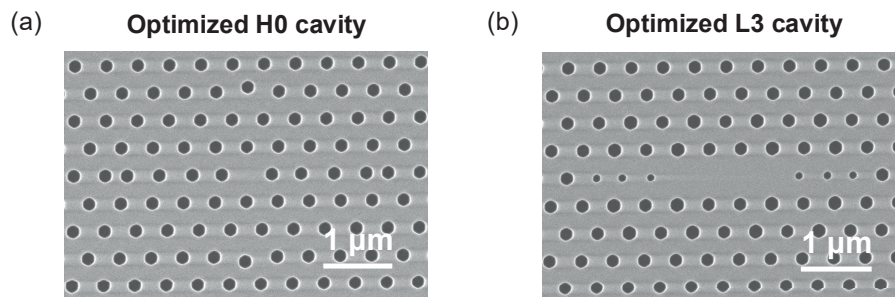


Fig. 5.3.5 SEM micrographs of a fabricated GaN (a) H0 cavity and (b) L3 cavity with embedded injectors.

## 5.4 Experimental Measurements

### 5.4.1 Resonant Scattering Characterization

#### 5.4.1.1 Experimental Procedure

Resonant scattering was employed for the characterization of the fabricated PhC cavities. The advantage of this technique is that it allows for measuring cavity Q-factors without introducing additional coupling channels [143], thus directly extracting the unloaded values (refer to section 4.3.3 for a sketch of the experimental setup and a

summary of the measurement technique). The scattering spectrum of each cavity was initially measured by utilizing a broadband excitation source in combination with a spectrometer (150 lines/mm grating) at the detection end, to help identify cavity modes and their respective resonance frequencies. The cavity axis was oriented at  $45^\circ$  relative to the polarization axis of the near-IR source to allow for the excitation of all radiative quasi-TE modes.

For measuring the cavity Q-factors, the excitation source was subsequently switched to a tunable laser to run fine spectral scans around the resonance frequency of the modes of interest. Coupling to the cavity was optimized via three-axis piezo-translation of the sample stage, which controlled sample translation down to 1 nm resolution, such that the resonantly scattered signal was maximized. The excitation beam was initially loosely focused on the cavity, then gradually adjusted to control the coupling efficiency and Fano interference [111]. The background scattered signal was suppressed by varying the axial position of the cavity relative to the excitation beam. At the optimal position for coupling to the fundamental cavity mode, the excitation beam was in the range of 1–3  $\mu\text{m}$  in diameter.

The coupling efficiency was then measured by first assessing the power incident on the PhC cavity. A metallic mirror with high reflectivity (>95%) was placed at the focal plane of the microscope objective, and the spectrum near the fundamental mode was captured in parallel polarization (analyzer relative to the polarizer) to get a measure of the incident intensity, then in cross polarization to subtract the background. The resonant scattering spectrum of the PhC cavity was subsequently acquired and normalized by the reference power measurement to obtain the coupling efficiency. The directionality of the emission into full space from the slab was accounted for by a factor of two.

The broadband resonance scattering spectrum which was captured for an L3 and an H0 cavity is displayed in Fig. 5.4.1, along with the corresponding FDTD-computed spatial profiles of the resonant modes. It should be noted that the excitation here was provided by a broadband light-emitting diode (LED) source rather than a laser scan which is typically used for the characterization of individual resonances.

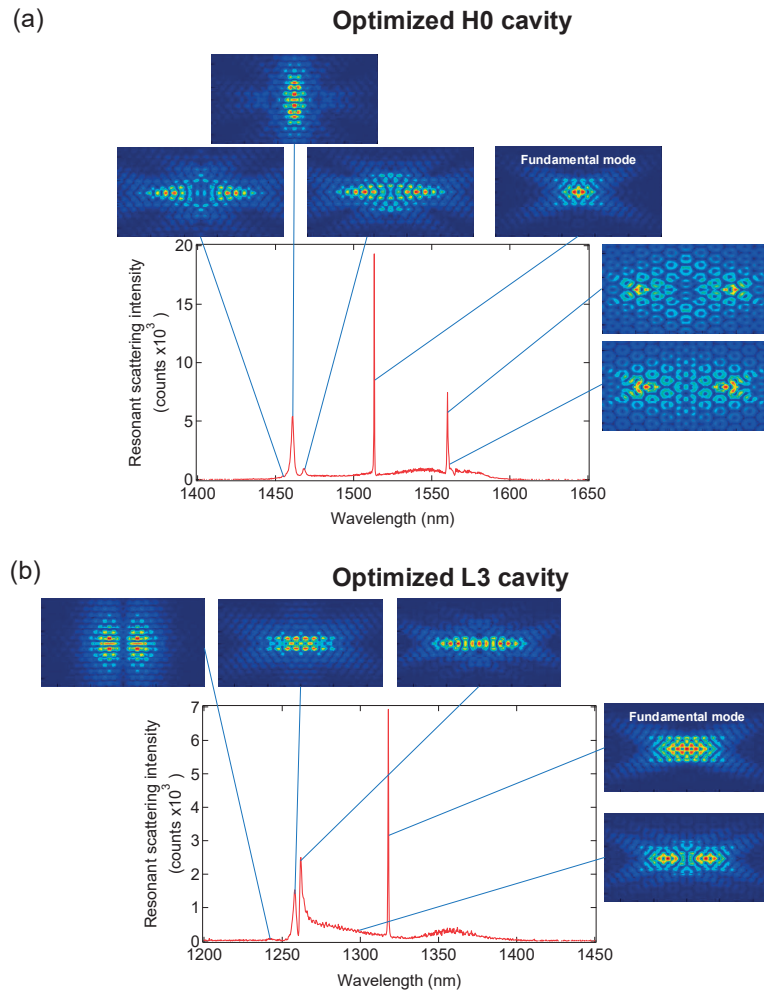


Fig. 5.4.1 The acquired resonant scattering spectrum of (a) an optimized H0 cavity and (b) an optimized L3 cavity under broadband excitation. The electric-field norm of the FDTD computed modes of each cavity is shown, and their respective resonance frequencies are marked on the spectrum.

The strongest scattering signal seen in the spectrum in Fig. 5.4.1 emanates from the fundamental cavity mode, as the excitation beam geometry and polarization with respect to that particular mode are experimentally optimal. The fundamental mode can further be distinguished by its linewidth, which is expected to be the narrowest amongst the resonant states. The signal scattered from higher-order modes goes according to the coupling strength with the Gaussian excitation beam. By observing the spatial profiles of the FDTD-simulated modes in Fig. 5.4.1, one can see clearly that modes exhibiting poor spatial overlap with the excitation spot, e.g. their maximal antinodes are located far off the cavity center, feature low-intensity peaks and may even be indistinguishable from the background. The overall features of the cavity spectrum were reproduced by all measured cavities, with some minor variations in the relative intensity of the modes between measurements, due to slight changes in excitation, cavity orientation, and possibly also due to disorder which impacts the radiative profile of modes.

Measurements that were carried out on a sequence of lithographically-tuned cavities confirmed the controlled tuning dependence. Fig. 5.4.2 shows the measured resonance wavelength for a set of H0 cavities resonant near 1550 nm. As per design, the lithographic tuning ensured that the 10 fabricated cavity groups possessed a sequential increase in the native PhC hole radius, in 2 nm increments. The resonance wavelength dependence of the fabricated

cavities was measured to be -2.3 nm wavelength shift per nm increase in hole radius. Fluctuations in the value of the resonance wavelength amongst identical cavities reached a standard deviation of up to 5.2 nm. This is primarily due to the layer topography, which exhibits a spatial variation in the thickness of GaN and AlN, and the inhomogeneity of the AlN-GaN interface as detailed in section 4.2.2. A comparable statistical distribution of the resonance frequencies of GaN cavities has been reported earlier [144], where GaN wafers of similar growth conditions have been used. Fluctuations however were solely attributed to disorder in the report without considerations for the layer properties.

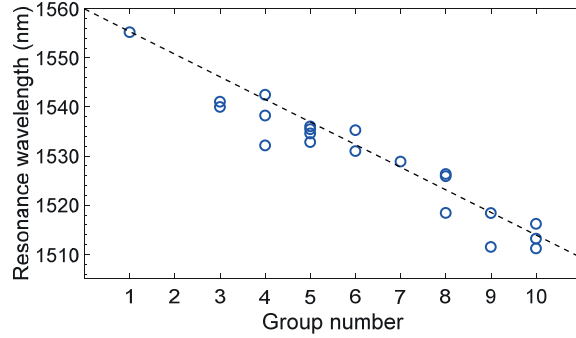


Fig. 5.4.2 Resonance wavelength of the H0 cavity fundamental mode as a function of lithographic tuning group number, where the native PhC hole radius is increased in 2 nm increments. The shown cavities feature an injector of size  $\Delta r_1 = 7$  nm.

5.4.1.2 Analysis of the Experimental Q-factors and Coupling Efficiency

The contributions towards the measured Q-factor of a given cavity can be expressed using the following expression:

$$\langle \frac{1}{Q_{total}} \rangle = \frac{1}{Q_{intrinsic}} + \frac{1}{Q_{absorption}} + \langle \frac{1}{Q_{scattering}} \rangle \tag{5.4.1}$$

where  $\langle Q_{total} \rangle$  is the average measured *unloaded* Q-factor.  $Q_{intrinsic}$  represents the cavity’s natural lifetime, i.e. the theoretically computed value as per design for an unperturbed structure (determined mostly by radiative loss in PhC slab geometry), while  $Q_{absorption}$  and  $Q_{scattering}$  account for the two distinct loss channels through which light can escape the cavity.  $\langle Q_{scattering} \rangle$  represents scattering losses due to surface roughness and medium inhomogeneities, in addition to PhC disorder, where the Q-factor can be expressed as an ensemble average value of the disorder-specific distribution [145]. On the other hand, the primary contribution towards  $Q_{absorption}$  comes from the linear material absorption loss of GaN. In the near-IR range linear absorption losses are relatively low and can reach values down to  $0.65 \text{ dBcm}^{-1}$  (equivalent to  $0.15 \text{ cm}^{-1}$ ) near  $\lambda=1500$  nm, as measured in wurtzite GaN epilayers [146]. This attenuation figure translates to  $Q_{absorption} \approx 0.6 \times 10^6$ . Compared to typical  $Q_{intrinsic}$  that is on the order of  $10^5$ , it allows for  $Q_{total}$  to be on the same order of  $10^5$ , should  $Q_{scattering}$  be negligible.  $Q_{scattering}$  however has a sizable contribution in III-nitride PhCs, which emerges from fabrication imperfections and the quality of epilayers, especially when grown on lattice mismatched substrates. Additional absorption may be present depending on the free carrier concentration, which rises monotonically with increasing wavelength of light in the near-IR range [147]. The presence of impurities and surface contaminants may further introduce absorption lines throughout the spectrum.

Over the investigated range of cavities, the average cavity Q-factor values of each injector-size group was measured to be above  $2.7 \times 10^4$  near the design wavelength of 1550 nm, for both L3 and H0 cavity designs. Fig. 5.4.3 displays the measured Q-factor values for a series of H0 cavities resonant near  $\lambda=1550$  nm. A gradual rise in the measured Q-factors is seen with the reduction of the injector size. Towards higher theoretical Q-factor values however, the

deviation of the measured Q-factors becomes more pronounced, which hints at the presence of a capping loss mechanism.

The Q-factor values of their 1300 nm counterparts were found to be lower on average, by a factor of approximately 2.5. Since the theoretical Q-factors of the optimized cavities at both wavelengths are comparable, being on the order of  $10^5$ , it can be inferred that a wavelength-dependent loss mechanism is dominating, setting the upper limit on light confinement. Based on free-carrier considerations, as discussed earlier, light absorption in this range is expected to have the opposite dependence—to what is observed experimentally—as a function of wavelength, which points to scattering and disorder as the primary loss channels.

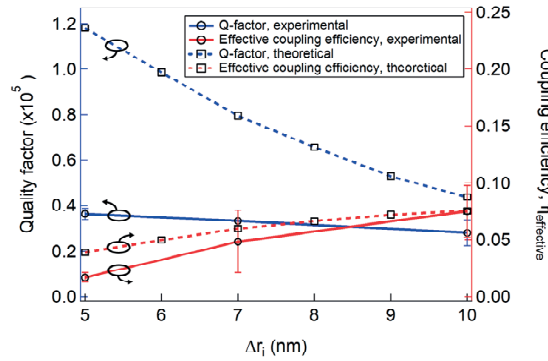


Fig. 5.4.3 Experimentally acquired Q-factor and effective coupling efficiency ( $NA=0.8$ ) for a series of optimized H0 cavities with injector hole radius  $\Delta r_i=5, 7,$  and  $10$  nm, plotted alongside the computed theoretical values.

Indeed, through an assessment of Rayleigh scattering, which has a wavelength dependence that is  $\propto \lambda^{-4}$ , one retrieves a scattering ratio between  $\lambda=1300$  nm and  $\lambda=1550$  nm of 2:1. At the origin of the scattering losses, besides membrane surface roughness and PhC sidewall roughness, is the AlN-GaN interface inhomogeneity [148] (shown in section 4.2.2 to exhibit RMS fluctuation of up to 7 nm), in addition to defects that are abundant near interfaces, which act as scattering centers [149]. In comparison, one retrieves a scattering ratio of 1.4:1 based on PhC lattice disorder models, which propose that disorder-induced loss scales with the magnitude squared of fluctuation along a single spatial dimension [150].

Analysis of the average experimental Q-factor values obtained with the optimized L3 cavities, resonant near  $\lambda=1300$  nm and  $\lambda=1550$  nm, confirms that scattering contributions (including disorder) are primarily present. This is assuming constant material absorption loss across the near-IR range. The plot in Fig. 5.4.4 displays the unloaded experimental Q-factor dependence on  $Q_{absorption}$  and  $Q_{scattering}$ , for a fixed  $Q_{intrinsic}=8 \times 10^4$ . The measured average experimental Q-factor values (at  $\lambda=1300$  nm and  $\lambda=1550$  nm) are indicated by iso-Q-factor lines (solid and dashed black lines respectively). A near-vertical transition on the plot is expected between these iso- $Q_{total}$  lines of  $\lambda=1300$  nm and  $\lambda=1550$  due to the near-constant absorption dependence of GaN in that range. The difference in scattering losses between the aforementioned wavelengths should not exceed an order of magnitude for Rayleigh and disorder-induced scattering combined. To remain consistent with this estimated value, the variation of the measured  $Q_{total}$  between the wavelengths dictates that  $Q_{absorption}$  must be greater than  $10^5$ . It can be inferred that for the highest absorption loss scenario ( $Q_{absorption} \approx 10^5$ ),  $Q_{scattering}$  will still set the upper limit on the experimental  $Q_{total}$  at  $\lambda=1300$  nm. Meanwhile at  $\lambda=1550$  nm, scattering losses will be comparable to absorption. This argument is further strengthened by the fact that the experimentally compared cavities originate from an identical fabrication batch and the same wafer, and thus, layer properties and fabrication induced roughness should be nearly identical.

Earlier analysis of disorder in L3 GaN cavities [144] considered fluctuation of PhC hole radius and position with a standard deviation of 5 nm, the value of which is inferior on average to what is achievable in practice, yet an



additional loss channel besides disorder was still necessary to simulate experimental Q-factors averaging  $\sim 1.4 \times 10^4$  near  $\lambda=1300$  nm. This further confirms that scattering losses are dominantly present. In order to unravel the exact contribution of each loss channel in GaN, elaborate characterization of all loss contributions is necessary as performed in Si PhCs [151].

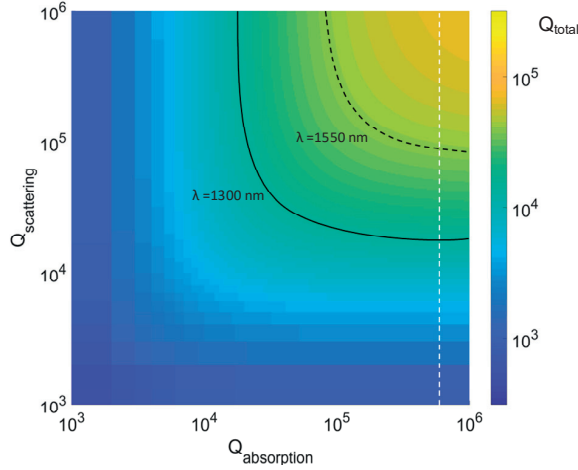


Fig. 5.4.4 Computed  $Q_{total}$  plot as a function of  $Q_{absorption}$  and  $Q_{scattering}$  for a fixed value of  $Q_{intrinsic}=0.8 \times 10^5$ . Iso- $Q_{total}$  lines are shown in solid and dashed black, representing the measured average Q-factor values at  $\lambda=1300$  nm and  $\lambda=1550$  nm respectively for the selected  $Q_{intrinsic}$  value. The dashed white line marks the  $Q_{absorption}=0.6 \times 10^6$  limit, which corresponds to the lowest reported absorption loss in GaN [146].

Despite the limitations set by losses, record Q-factors for GaN cavities were still achieved reaching as high as  $4.1 \times 10^4$  and  $4.4 \times 10^4$  with the optimized L3 and H0 cavities respectively, resonant near  $\lambda=1550$  nm. The linewidth of the latter is displayed in Fig. 5.4.5. It is noteworthy that both cavities exhibited intermediate-sized injectors ( $\Delta r_i=5$  nm and  $\Delta r_i=7$  nm respectively) and a theoretical Q-factor  $\approx 8.0 \times 10^4$ . Near  $\lambda=1300$  nm, record Q-factors were similarly achieved in optimized L3 cavities that featured injectors, with measured values up to  $3.7 \times 10^4$ .

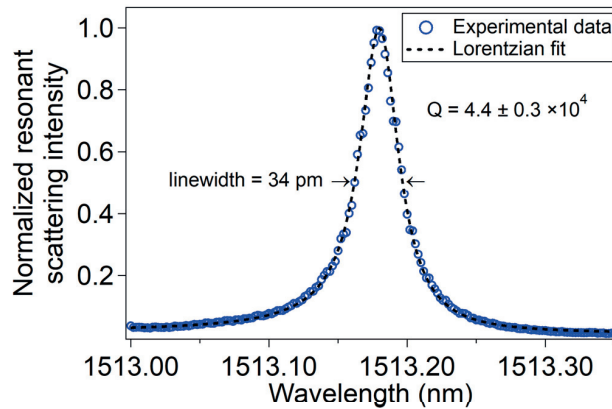


Fig. 5.4.5 Resonant scattering spectrum of the fundamental mode of an optimized H0 cavity, resonant near  $\lambda=1513$  nm. The cavity has a characteristic linewidth of 34 pm, corresponding to a Q-factor of  $4.4 \times 10^4$ .

An estimate of the effective coupling efficiency ( $\eta_{eff}$ ) to the fundamental cavity mode was obtained through resonant scattering. At  $\lambda=1550$  nm,  $\eta_{eff}$  values for L3 cavities ranged between 3% and 19% over the fabricated range of injector sizes. While with the H0 cavities in comparison,  $\eta_{eff}$  values ranged between 2% and 10%. Some cavities possessing

strong disorder deviated from this range. The experimental  $\eta_{\text{eff}}$  values for a series of H0 cavities of varying injector sizes (resonant near  $\lambda=1550$  nm) are shown in Fig. 5.4.3 (presented earlier). The plot additionally displays the theoretically-computed values for comparison. The theoretical  $\eta_{\text{eff}}$  was calculated considering equation (5.3.1), by making use of the mode profiles of the cavity mode and the excitation beam that were obtained through the numerical simulations. The mode profile of a y-polarized Gaussian beam at the focus of an NA=0.8 objective was simulated using FDTD to accurately reproduce the experimental excitation. A fairly good agreement is found with the experimental values, with some minor disparity due to varying spatial overlap of the modes, possible distortion of the excitation beam during measurements, and the disorder present in cavities which can alter the radiative profile.

#### 5.4.2 Nonlinear Frequency Conversion

Frequency upconversion was investigated in the fabricated samples using near-IR, tunable continuous-wave laser sources (operating in the  $\lambda=1300$  and  $\lambda=1550$  windows), which did not exceed 40 mW at the source output. The sample was irradiated with a linearly polarized beam, oriented such that the electric field is perpendicular to the horizontal axis of the PhC cavity (refer to Fig. 5.3.2). The collimated laser beam was tightly focused at the sample plane by a microscope objective (50x, 0.8 NA) to match the cavity mode size. Coupling to the cavity was optimized through fine translation of the sample in the transverse plane and axial direction using a piezo stage, in a similar manner to the resonant scattering measurement, but optimizing the nonlinear conversion process. The upconverted signal was collected through the same objective and redirected for detection by a dichroic mirror. Axial translation of the sample affected simultaneously both the excitation beam position and the collection plane, which meant that the ideal coupling position did not necessarily correspond to the position of maximal harmonic signal detection.

Second harmonic generation from the PhC cavities was directly evident when excited on resonance, through a relatively strong emission pattern with distinct features, emerging from the cavity center. SHG emission observed at the sample plane is displayed in Fig. 5.4.6, from optimized L3 and an H0 cavities, resonantly excited at  $\lambda=1545$  nm and  $\lambda=1513$  nm respectively. The z-component of the second-order polarization is shown in the inset for comparison. It was computed by considering the electric field of the fundamental mode, using the following expression:

$$P_z^{(2\omega)} = \frac{\epsilon_0}{2} \left( \chi_{zxx}^{(2)} E_x^{(\omega)^2} + \chi_{zyy}^{(2)} E_y^{(\omega)^2} + \chi_{zzz}^{(2)} E_z^{(\omega)^2} \right) \quad (5.4.2)$$

where  $|\chi_{zxx}^{(2)}| = |\chi_{zyy}^{(2)}| = 0.5|\chi_{zzz}^{(2)}|$ . As mentioned earlier, the dominant components of the second-order susceptibility tensor of wurtzite GaN are  $\chi_{zzz}^{(2)}$  followed by  $\chi_{zxx/zyy}^{(2)}$  and  $\chi_{xxz/yyz}^{(2)}$  (and their respective permutations) [40]. As the GaN layer is c-axis oriented, only  $\chi_{zxx/zyy}^{(2)}$  can be exploited with the quasi transverse electric nature of the fundamental cavity mode. The spatial profile of the induced polarization consequently follows that of the resonant fundamental mode.

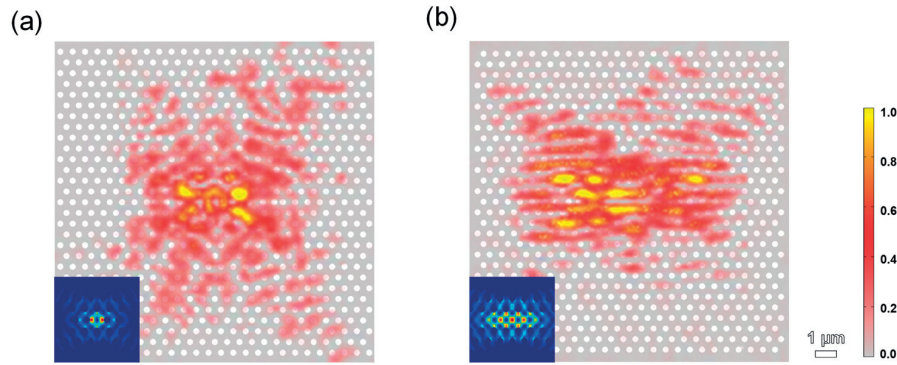


Fig. 5.4.6 SHG spatial emission profile of an optimized (a) H0 cavity and (b) L3 cavity under resonant excitation, overlaid on a schematic of their respective PhC lattice. The normalized SHG intensity is displayed in false color, and the computed z-component of the second-order polarization ( $|P_z^{(2\omega)}|$ ) that is generated by the resonant mode is shown in the inset.

It is evident in Fig. 5.4.6 however that the imaged SHG emission pattern does not directly map the cavity mode. This is in part due to the transparency of the GaN layer, which is multi-modal at the harmonic wavelength, combined with the symmetry of the  $\chi^{(2)}$  tensor. The generated harmonic originating from the bulk nonlinearity is propagative and appears to be strongly scattered upon interaction with the PhC lattice. The characteristic extended parallel lines at the vicinity of the cavity which were previously reported in SHG experiments are present in both cavities [152], along with the cross-shaped pattern, where the second harmonic traverses the lattice along the  $\Gamma K$  direction. With the H0 cavity, a ring appears at the center, overlapping with the position of the first set of holes surrounding the polarization hotspots. Modeling of SHG emission by FDTD (detailed in section 5.5) has confirmed guided propagation of the SHG signal in the GaN slab between PhC holes, primarily along the diagonal directions. It is noteworthy that the PhC lattice does not exhibit any bandgap at the SHG wavelength, and consequently, light confinement that may lead to doubly-resonant enhancement effects is not expected.

The nature of the second harmonic process was verified through power dependence measurements. A Si photodetector was placed at the output port, behind an optical filter that suppressed the source laser wavelength. No power was measured from the PhC cavities off-resonance across the spectrum under the highest incident power of 6 mW. The collected SHG power was subsequently measured directly under resonant excitation and is shown in Fig. 5.4.7(b) as a function of the power coupled into the L3 cavity. The displayed cavity exhibits a coupling efficiency of 13% and a Q-factor of  $3.3 \times 10^4$ . A fit to the data gives a slope of 2.0, confirming the expected quadratic power dependence. The characteristic Lorentzian-squared spectral profile of SHG was captured and is displayed in Fig. 5.4.7(a), alongside the resonant scattering spectrum for comparison.

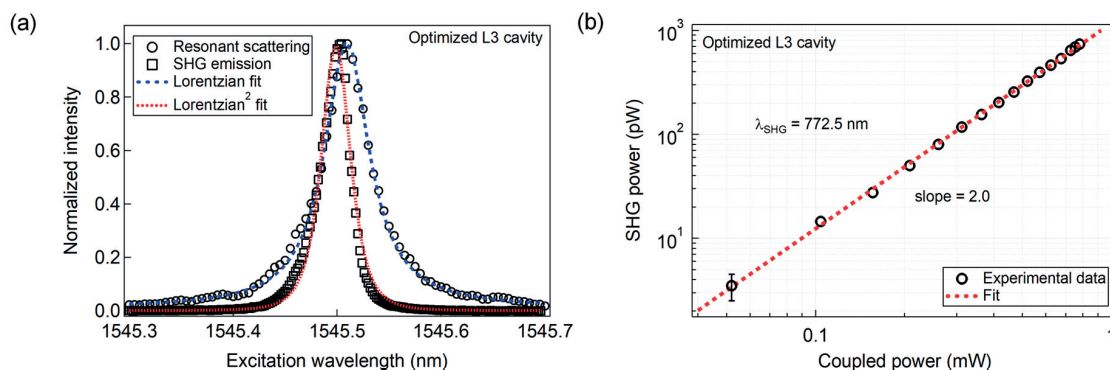


Fig. 5.4.7 (a) Normalized resonant scattering and SHG intensity collected from an optimized L3 cavity as a function of the excitation laser wavelength around resonance ( $\lambda=1545 \text{ nm}$ ). (b) Evolution of the collected SHG power with the power coupled into the optimized L3 cavity.

THG was further detected under continuous-wave resonant excitation, with an expected weaker intensity in accordance with third-order nonlinear susceptibility. The emission was fiber-coupled at the output port to a single-mode fiber and delivered to a monochromator (600 lines/mm grating) where the intensity count was monitored with a cooled Si detector. The spectrum was acquired and is displayed in Fig. 5.4.8(a). SHG and THG peaks are seen at 772.5 nm and 515 nm respectively, both below the GaN bandgap (3.4 eV).

The ratio between the second and third harmonic intensities was found to be sensitive to the working distance of the objective during the measurement, as the radiation patterns of the two harmonic signals differ significantly. The displayed spectrum has been captured under optimal THG collection. The plot in Fig. 5.4.8(b) shows the growth ratio of THG intensity relative to SHG as a function of input power. An exponential ratio of 1.4 is observed, slightly off the expected 3:2 ratio. Under an incident power of 4.4 mW, THG power was estimated to be on the order of 100 fW based on calibrated power conversion. Amongst the relevant tensor elements of GaN with regard to the cavity mode and crystallographic orientation, the ones with the principle contribution are  $\chi_{xxxx}^{(3)}$  and  $\chi_{yyyy}^{(3)}$ . They are followed by  $\chi_{xxyy}^{(3)}$  and  $\chi_{yyxx}^{(3)}$ , which are one-third the value and contribute to partial mixing of the field components. The generated third-order polarization pattern should therefore be relatively identical to the resonant cavity mode, raised to the third power.

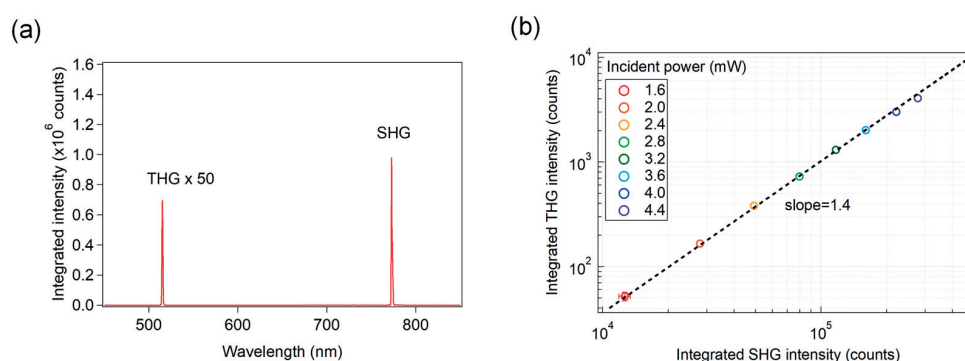


Fig. 5.4.8 (a) Nonlinear upconversion emission spectrum from an optimized L3 cavity under resonant excitation at  $\lambda=1545 \text{ nm}$ , displaying SHG and THG lines at 772.5 nm and 515 nm, respectively. (b) Evolution of the collected SHG and THG intensities from the optimized L3 cavity as a function of incident power.

### 5.4.3 Conversion Efficiency and Cavity Enhancement Factors

As outlined in section 2.3, nonlinear processes in a PhC cavity benefit from an enhancement factor that emerges from its capacity to confine light. The conversion efficiency was investigated in the cavities under optimal excitation conditions to compare the performance of the two cavity designs and identify the experimental limits. Under the highest excitation power from the near-IR laser source, the collected SHG power from the previously characterized L3 cavity reached a value of 0.74 nW on resonance, for effectively 0.78 mW of power coupled into the cavity. By accounting for SHG emission into full-space (multiplication factor of two), this equates to a normalized conversion efficiency ( $P_{SHG}/P_{coupled}^2$ ) of  $2.4 \times 10^{-3} \text{ W}^{-1}$ . Since the collection of the SHG signal is limited by the numerical aperture of the objective (NA=0.8), and the propagating portion of the generated harmonic is unaccounted for, this value here represents a lower bound on the efficiency of the SHG process. At  $\lambda=1309 \text{ nm}$ , similar SHG power was obtained with a resonant L3 cavity, reaching up to 0.20 nW for 0.43 mW of coupled power, achieving a conversion efficiency of  $2.2 \times 10^{-3} \text{ W}^{-1}$ . By that, performance scalability in the telecom window was confirmed.

In comparison to L3 cavities, SHG collected from H0 cavities did not reach the same power levels. The highest measured SHG power was 0.13 nW for a cavity resonant at  $\lambda=1513 \text{ nm}$ . Similar analysis—accounting for 0.63 mW of coupled power—indicates a conversion efficiency of  $0.65 \times 10^{-3} \text{ W}^{-1}$ . The weaker SHG emission observed with H0 cavities relative to L3 cavities of the comparable Q-factor can be attributed to the inferior coupling arising from the reduced overlap between the Gaussian excitation beam and the odd-parity mode of the H0 cavity. This can be resolved through the introduction of injector designs with odd symmetry to better match the Gaussian beam profile.

Overall, the achieved conversion efficiency values in the GaN L3 and H0 cavities on this platform were found to exceed previous experimental reports of SHG in GaN, including a PhC cavity by more than two orders of magnitude [153], as well as reports of SHG in microring [154] and microdisk [155] resonator platforms. Table 5.4.1 summarizes the highest demonstrated conversion efficiency values for SHG in GaN under continuous-wave operation. Depending on the material, the conversion efficiency may often be capped by residual absorption losses in the layer, which prevent the nonlinear process from reaching the critical power where maximal conversion can be attained. A compelling aspect here is that no saturation effects [46] for the SHG process have been observed for the aforementioned magnitude of injected power.

Table 5.4.1 Comparison between SHG normalized conversion efficiency in GaN under continuous-wave excitation across different platforms.

GaN Platform	Operational Wavelength (nm)	Normalized Conversion Efficiency ( $\text{W}^{-1}$ )	Phase Matching Scheme
Microring [154]	1550	$0.3 \times 10^{-3}$	modal
Microdisk [155]	1550	$2 \times 10^{-3}$	modal
PhC [153]	1550	$3.5 \times 10^{-6}$	
PhC (this work)	1300, 1550	$2.2 \times 10^{-3}, 2.4 \times 10^{-3}$	

The volume dependence of the nonlinear conversion process was assessed through a comparison between the two cavity designs. By computing the modal volume of the L3 and H0 cavities according to equation (2.2.3), one finds a normalized value of  $1.04 \left(\frac{\lambda}{n}\right)^3$  and  $0.44 \left(\frac{\lambda}{n}\right)^3$  respectively, giving a ratio of 2.4:1 between them. According to the overall nonlinear conversion enhancement effect for a singly-resonant second-order process (refer to section 2.3.3), the  $V^{-2}$  scaling implies an additional factor of 5.8 enhancement in SHG for H0 cavities over L3 cavities. The volume

dependency however is approximately balanced when further considering the nonlinear material overlap (assuming the field resides primarily in the dielectric) through the introduction of a  $V^2$  factor.

For cavities with the highest conversion efficiency,  $\eta_{\text{eff}}$  was measured to be twice as high for L3 cavities ( $\Delta r_i=5$  nm) compared to H0 cavities ( $\Delta r_i=7$  nm). Given that the theoretical and experimental average Q-factors of both aforementioned cavities were comparable, the resulting enhancement factor ratio between H0 and L3 cavities can be deduced to be  $\frac{(\eta_{\text{eff,L3}}Q_{\text{L3}})^2}{(\eta_{\text{eff,H0}}Q_{\text{H0}})^2} \approx 4$ . This ratio has been indeed observed throughout the measurements. With regard to the L3 cavity featuring the highest conversion efficiency ( $Q = 3.3 \times 10^4$  and  $\eta_{\text{eff}}=13\%$ ), the experimental resonance enhancement factor per modal volume was computed to be  $\frac{(\eta_{\text{eff}}Q)^2}{V} = 1.8 \times 10^7 \left(\frac{\lambda}{n}\right)^{-3}$ . The magnitude of this enhancement figure is behind the ability to generate nonlinear processes under low-power continuous-wave excitation. The crucial role of the designed injectors is to raise  $\eta$  without significant reduction of the experimental Q-factor, thus boosting the conversion efficiency. This figure can still be increased by more than two orders of magnitude for the current cavity design by improving on the fabricated cavity Q-factors and the excitation beam overlap.

## 5.5 Numerical Modeling of Frequency Conversion in Semiconductor Layers

To better understand the behavior of the frequency upconversion process, numerical tools primarily based on FDTD were put to use to simulate the PhC cavities. Since the experimental setup employed here does not offer near-field characterization, we rely on FDTD calculations to retrieve the emission profile of the generated harmonic signals. The use of such simulation tools is not only limited to pre-fabrication design validation, but they become indispensable when experimental observational tools fall short of the detection limit with regard to the anticipated physical response. Through FDTD simulations, the propagative behavior of the harmonic signals, namely SHG and THG, within the transparent wide bandgap semiconductor layers is unveiled. Furthermore, quantitative estimates of the power distribution are obtained for the harmonic signal, assisting with the design of harmonic extractors. Considering reciprocity, such a system may as well be suited for photon-pair generation via parametric down-conversion, enhanced by the cavity resonance.

### 5.5.1 Modeling Approach

The primary purpose of the initial model is to accurately reproduce the emission profile of the harmonic generation process within the implemented PhC cavity designs. The FDTD technique is well-suited for simulating wave propagation in optical structures through its sequential computational scheme. A nontrivial aspect of the modeling pertains to the inclusion of the nonlinear response of the material such that nonlinear effects can be reproduced. For instance, a nonlinear material model may be introduced where nominal  $\chi^{(2)}$  and  $\chi^{(3)}$  values are incorporated in the susceptibility definition, and consequently, harmonic terms appear in the frequency response. However, besides the simulation becoming more computationally complex, the accuracy is reduced by the dispersion model in use, and the tensorial nature of the nonlinear susceptibility is unaccounted for.

We rely instead on narrowband simulations considering the desired nonlinear process near the frequency of one of the participating fields, and the nonlinear coupling is handled externally. The interest here is to model the frequency upconversion process, so the frequency is fixed around that of the harmonic, and nonlinear polarization terms oscillating at the same frequency are directly injected into the model, based on pre-computed and normalized values. This approach involves more computational steps, however, it eventually yields more accurate and consistent simulation results.

We consider here specifically the case of a resonant GaN PhC cavity, where the fundamental mode exhibits a relatively high Q-factor ( $>10^4$ ) such that in the transverse PhC plane the field is mostly confined near the

semiconductor slab. An initial FDTD simulation identifies the resonance spectrum, after which the profile of the fundamental mode is retrieved. The mode profile is then normalized by a factor of  $\int_{-\infty}^{\infty} \varepsilon(\mathbf{r}) |\mathbf{E}(\mathbf{r})|^2 d^3\mathbf{r}$ , which should be valid for the case of localized modes. The nonlinear polarization in wurtzite GaN is then computed using the vector field components, in accordance with equation (5.4.2) for SHG, and the following equations for THG, considering degenerate input modes:

$$P_x^{(3\omega)} = \frac{\varepsilon_0}{4} \left( \chi_{xxxx}^{(3)} E_x^{(\omega)^3} + \chi_{xxyy}^{(3)} E_x^{(\omega)} E_y^{(\omega)^2} \right) \quad (5.5.1)$$

$$P_y^{(3\omega)} = \frac{\varepsilon_0}{4} \left( \chi_{yyyy}^{(3)} E_y^{(\omega)^3} + \chi_{yyxx}^{(3)} E_y^{(\omega)} E_x^{(\omega)^2} \right) \quad (5.5.2)$$

where  $\chi_{xxyy}^{(3)} = \chi_{yyxx}^{(3)} = \frac{1}{3} \chi_{xxxx}^{(3)} = \frac{1}{3} \chi_{yyyy}^{(3)}$  [40].

It should be noted that the expressions for the polarization equations are specific to  $C_{6v}$  point-group symmetry crystals. The spatial profile of the computed second- and third-order nonlinear polarization components is shown in Fig. 5.5.1. Next, the nonlinear polarization is introduced as a source term in the FDTD cavity model, and the excitation is driven at the SHG/ THG frequency.

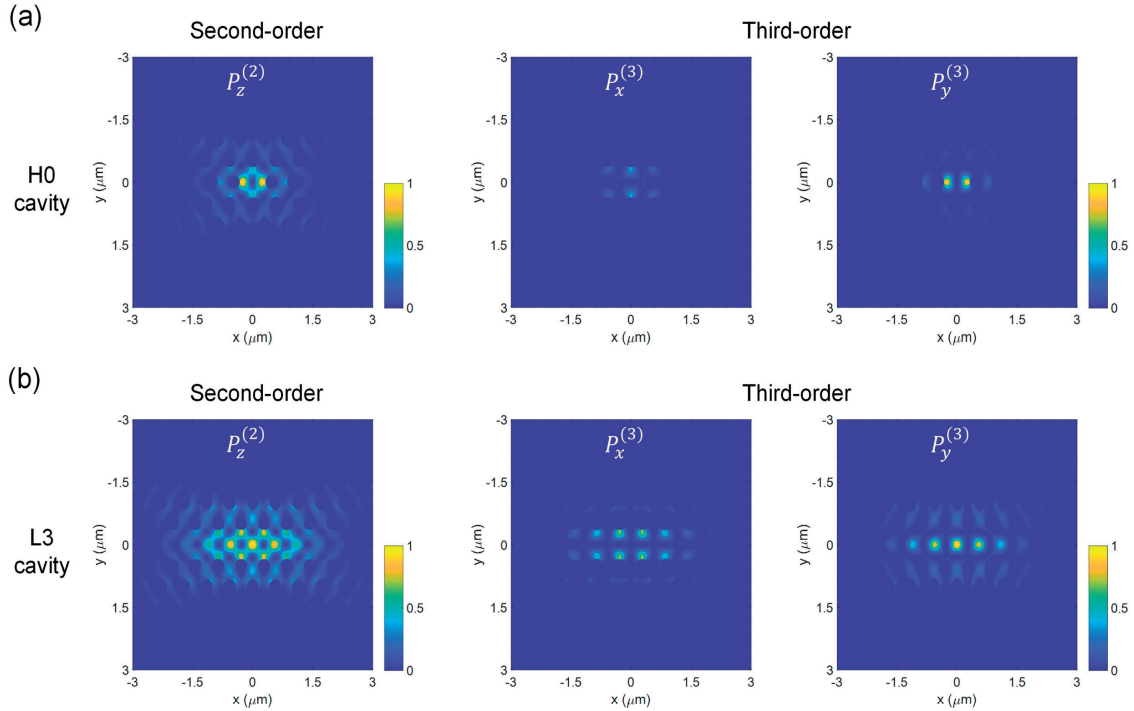


Fig. 5.5.1 Second- and third-order nonlinear polarization profile at the  $z=0$  plane of the (a) H0 and (b) L3 cavities.

### 5.5.2 Results and Comparison with Experimentation

For the simulation of the harmonic signals, we account for an L3 cavity design that is resonant at a wavelength of 1550 nm. Considering the waveguide geometry of the semiconductor slab, vertical confinement of the GaN layer supports two TM modes at the second harmonic frequency, and thus the TM-polarized SHG signal will naturally couple to propagating modes. At the frequency of the third harmonic, three TE modes are supported. Since the

surrounding triangular PhC lattice does not exhibit any higher-frequency bandgaps, the harmonic signals are not confined and can propagate in the layer. The upconverted light is generated through the nonlinear polarization sources located in cavity region, and according to the k-vector of the photons, light can either couple to Bloch modes of the PhC, radiative modes, or simply interact with the lattice. The lattice interaction involves primarily multiple reflection and scattering off the lattice hole interface, and the PhC becomes effectively a scattering medium for light of shorter wavelengths.

To reproduce the spatial profile of the harmonic fields, the time-averaged Poynting vector was computed from the near-field of the emission at the harmonic frequency above the semiconductor slab, and it was subsequently convoluted with a point-spread function corresponding to a microscope objective of NA=0.8, to mimic the collection and imaging configuration which was used. The results of the simulation are displayed in Fig. 5.5.2 for the L3 cavity design for both SHG and THG. The far-field emission profiles (without filtering) are shown alongside. A good correspondence can be seen when comparing the theoretical and experimental profiles of SHG in Fig. 5.5.2a. As predicted, the simulated SHG emission is found to constitute both radiative and propagative contributions. The propagating component is found to primarily follow the  $\Gamma K$  direction of the PhC lattice, creating a crossed-shaped profile, which was seen with both L3 and H0 cavities. The majority of the energy is coupled to propagating modes, however, strong scattering occurs as the modes travel outward, and they eventually decay.

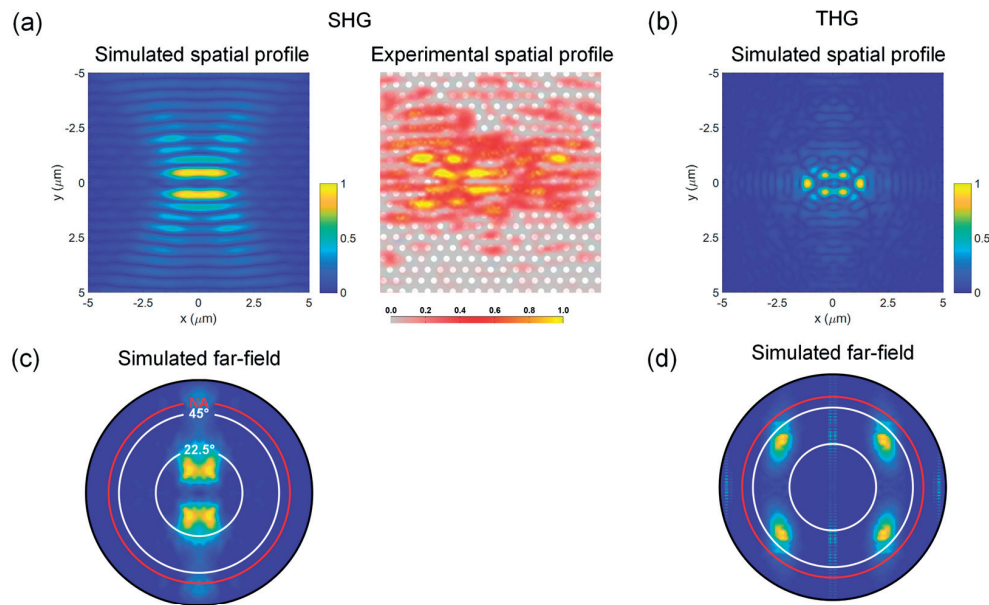


Fig. 5.5.2 (a) Simulated SHG profile (time-averaged Poynting vector) of an L3 cavity excited near  $\lambda=1550$  nm (considering NA=0.8), and the experimentally acquired SHG intensity profile (at the same scale) next to it for comparison. (b) Simulated THG profile for the same L3 cavity. The simulated far-field emission profiles for (c) SHG and (d) THG are displayed underneath. The circles correspond to emission angles of 22.5°, 45°, and numerical aperture (NA)=0.8.

Since the harmonic signal propagates in the layer, in-plane extraction could be feasible by surrounding the PhC lattice by optical microstructures that would serve that purpose. The power distribution of the SHG signal was quantified as a function of propagation distance in the PhC lattice, and the results are displayed in Fig. 5.5.3. The fundamental mode Q-factor is additionally plotted as a function of PhC cell width for different injector sizes to identify the minimal lattice size necessary to achieve the desired nonlinear conversion enhancement factor. The absorption of SHG by the GaN layer remains sufficiently low near  $\lambda=775$  nm at this length scale and is therefore neglected.



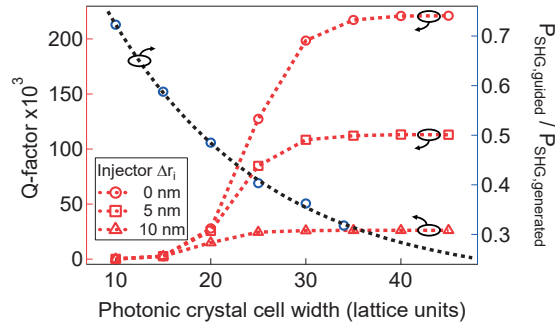


Fig. 5.5.3 Dependence of the radiation of the SHG signal and cavity Q-factor on the PhC lattice size in an L3 cavity operating near  $\lambda=1550$  nm, plotted for injector hole radius variation ( $\Delta r_i$ ) of 0, 5, and 10 nm.

It can be observed that the radiative decay of SHG follows an exponentially decaying curve as a function of propagation length. Nearly 50% of the power is lost within 20 lattice unit cells. If medium-sized injectors are to be used ( $\Delta r_i=5$  nm), the cavity Q-factor converges to the theoretical value within 30 unit cells, and the remaining guided power constitutes 36% of the total generated signal. Thus, the PhC lattice can be terminated and surrounded by a layer that serves to collect/guide the remaining light. Should the experimental Q-factors be limited by a given loss channel, the lattice size can be reduced further to retain a higher ratio of guided SHG.

## 5.6 Summary

In this chapter, the design and characterization of GaN PhC cavities operating near  $\lambda=1300$  nm and  $\lambda=1550$  nm was presented. The cavities featured injectors that assisted with the enhancement of free-space light coupling. Record-high Q-factor values for GaN cavities were achieved, reaching up to  $4.4 \times 10^4$ . Furthermore, resonance-enhanced SHG and THG were demonstrated under continuous-wave operation with excitation power as low as a few  $\mu\text{W}$  injected into the cavities. By utilizing cavities with optimal figure-of-merit, record SHG conversion efficiency in GaN was obtained, of up to  $2.4 \times 10^{-3} \text{ W}^{-1}$ . The generated harmonic signals were modeled and analyzed through FDTD, demonstrating the feasibility of employing such cavities as integrated, coherent light source.



# 6. Wideband Slow Light in Silicon Photonic Crystal Coupled-Cavity Waveguides

## 6.1 Introduction

*Slow light* is a term used to refer to electromagnetic waves that propagate in a medium with a group velocity that is significantly lower than the speed of light in vacuum, typically by more than one order of magnitude. The interest in well-controlled slow light systems arises on one hand from the need for on-chip buffering of light, for both classical signals and delicate quantum states, e.g. flying qubits. On the other hand, it arises from the desire for the enhancement of light-matter interaction in confined geometries, whether for improving the efficiency of nonlinear processes or for the control of the phase of light.

In this chapter we present the development of a PhC-based slow light device with large bandwidth and the highest group-index bandwidth product value achieved to-date [156], based on a coupled-cavity waveguide (CCW) design [12]. The device operates linearly in the optical telecom range (C/L-band) near  $\lambda=1550$  nm and exhibits negligible group velocity dispersion. Fabrication of the PhCs was carried out using standard silicon-on-insulator fabrication technology. Cavity chains comprising up to 800 cavities have been realized, which are capable of delaying light in Si by up to 70 ps over a bandwidth of 18.5 nm, with an average group index ( $n_g$ ) of 41. Device characterization was performed using an end-fire coupling configuration, while employing Fourier-space imaging to probe the dispersive behavior of light along the PhC CCW. The group velocity of light is extracted with good accuracy from the experimental dispersion, which is further matched with transmission and surface emission measurements to identify light propagation regimes and evidence the onset of diffusive light transport. Micro-Raman spectroscopic mapping of the structures is carried out to confirm the efficacy of the anti-buckling scheme and highlight its influence on slow light propagation.

### 6.1.1 Brief Overview of Slow Light Schemes

There are two primary approaches that have been utilized so far for slowing down the speed of light. The first makes use of a material resonance, whereby the optical response near an absorption (or gain) frequency line exhibits a strongly dispersive character (derived from the Kramers-Kronig relation), which increases the group index dramatically over a narrow frequency range. To overcome high losses that accompany any transmission around the absorption line, methods such as electromagnetically-induced transparency [157] and coherent population oscillation [158], [159], in the case of a saturable absorber, have been taken advantage of. Despite the ability to bring down the group velocity of light by a factor in excess of six orders of magnitude, the material resonance approach is restricted to the spectral range where the resonances are located, and furthermore, often relies on condensates or quasi-particles that require cooling to cryogenic temperatures, thereby limiting its use for practical applications.

A second more synthetic approach is based on dispersion-band engineering, where waveguiding structures are employed. Photonic crystals in particular have become highly-effective design entities. Waveguides in PhCs can be formed by introducing a defect volume to a PhC lattice, such as with line-defects (W1 or W3) for example. Guided modes exhibit non-trivial dispersion relations, which emerge as a consequence of mode hybridization. By manipulating the lattice, the dispersion relation can be altered in such a manner to control the velocity of light within

the bandwidth of operation. W1 waveguides in particular have been thoroughly investigated for slow light behavior near the band edge.

A common method, likewise based on dispersion band-engineering, is to utilize a set of microcavities that are coupled (via evanescent-field coupling for instance) in such a way that their intrinsic states form a supermode. This is effectively a waveguiding structure, and the supermode consequently exhibits characteristic dispersion properties which allow for the delay of light along the propagation direction. By implementing such a scheme using photonic crystals, one can synthesize the optical response of the material-of-choice through band engineering to obtain the desired dispersion, within the degrees of freedom that are provided by the design parameters. Since the slow-down factor, i.e. the ratio of the phase velocity to the group velocity of light, in this approach emerges from a wavelength- (or larger) scale interaction rather than atomic (in comparison to the material resonance approach), it is greatly advantageous in terms of tunability. Photonic crystals in particular are naturally scale-invariant allowing to freely—within the fabrication capacity—select the operational wavelength, and moreover, a much wider bandwidth can be accommodated when compared to the former approach. This is crucial for applications envisioning pulse propagation or high-bandwidth communication.

The characteristic figure-of-merit (FOM) of any slow light device is the delay-bandwidth product (DBP) which gives an indication of the throughput capacity of the channel. A similarly-formulated definition is the group-index bandwidth product ( $\text{GBP} = \frac{n_g \Delta \omega}{\omega}$ ), which tends to be more commonly used when assessing slow light in PhCs since it eliminates the device length dependence. From the definition of group velocity  $v_g = \frac{d\omega}{dk}$ , it can be deduced that the bandwidth of a PhC system scales with the momentum spread defined by its lattice pitch. There is a fundamental limitation however on the DBP in any reciprocal structure, which originates from the time delay-frequency relationship of a resonant system [160], [161]:  $\Delta t \Delta \nu \sim 1$ . There have been recent reports that specify mechanisms for overcoming the DBP limit by breaking Lorentz reciprocity. A non-reciprocal response in a waveguide can be achieved through schemes based on the application of magnetic fields [161], the introduction of a temporal modulation of the refractive index/ cavity resonance [162], [163], or optomechanical coupling [164], [165]. However, for static non-dissipative systems the DBP limit holds, which justifies the need for design optimization.

### 6.1.2 Implementation of Slow Light in Photonic Crystals

Early demonstrations of slow light in photonic crystals were primarily focused on W1 waveguides, where it has been theoretically predicted that the group index of light can be brought to extremely large values, approaching infinity, as the wave vector nears the vicinity of the band edge. This however was soon found not to be the case in practice through early demonstrations by Notomi et. al [166], which revealed technical limitations on the achievable slow-down factor. Varying implementations of the W1 waveguide have emerged, which attempted through band engineering to mitigate the strong GVD, which is characteristic of W1 waveguides. At the origin of the dispersive behavior in W1 waveguides is the cross-coupling of index-guided and bandgap-guided modes [16]. Dispersion compensation schemes, which utilize chirped PhCs have been also introduced to tackle this issue, the most successful of which is based on a coupled W1 waveguide-pair [167].

CCWs comprising well-studied PhC defect cavities have also emerged to compete with the W1-based approach. Cavity chains of up to 400 cavities have been demonstrated to confirm the feasibility of building such devices on Si [168]. Compared to a W1 waveguide, coupled-cavity systems offer more flexibility in terms of design and the ability to engineer the dispersion. A W1 waveguide can be similarly viewed as a strongly-coupled defect waveguide, with the unit cell length corresponding to the PhC lattice constant, i.e. the minimum achievable pitch in a PhC lattice. The bandwidth as a result is typically wide (within the limits of the operational range near the band edge), yet at the expense of a lower average group index than in the well-separated and more weakly-coupled CCWs.

When designing a slow light system, there is a set of important performance parameters to be considered such as bandwidth, average group index, and losses, through which a generalized FOM can be formulated according to the application. The definition of the operational bandwidth is not necessarily specified in terms of the 3dB-attenuation window, but may also be described by other parameters such as deviation of the slow-down factor from the nominal average value for instance. The primary FOM as mentioned earlier is the GBP. Nevertheless, the defined FOM should not be the single assessment criterion as it may not be the most critical aspect for certain applications. The group velocity dispersion ( $GVD = \frac{d^2\omega}{dk^2}$ ) value across the bandwidth is as equally as important, particularly for pulsed operation. The loss figure is another rather important parameter for consideration, if not accounted for by the bandwidth definition. The loss is most suitably expressed normalized with respect to the incurred delay time (dB/ns) rather than propagation length (dB/mm), i.e. the transmission intensity will be proportional to  $e^{-L\frac{\alpha n_g}{c}}$ , where  $\alpha$  is the attenuation (per unit time) and  $c$  is the speed of light in vacuum. This allows for more consistent comparison between devices of different design implementation that feature varying slow-down factors.

Several applications have been shown to benefit from the employment of slow light whether through the enhancement of gain [169], frequency upconversion [9], or photon-pair generation [170]–[172] in a photonic crystal waveguide platform. The majority of state-of-the-art photonic crystal (PhC)-based slow light devices which have been presented so far are unoptimized and suffer primarily from limited bandwidth. Other shortcomings include significant group velocity dispersion and non-flat transmission. This hinders their potential use for pulse propagation, with setbacks including pulse distortion [173] and generation of echoes. An ideal slow-light PhC device therefore should eliminate the aforementioned issues while maintaining an ideal FOM, which pushes the performance parameters to their theoretical/ technical limits.

## 6.2 Design

The investigated CCW design has been proposed by M. Minkov et al. [12], based on the coupling of L3 defect cavities. A similar approach based on the coupling of L3 cavities has been previously investigated by J. Jágerská et al. [103], utilizing a  $\Gamma$ K in-line propagation configuration. Band formation was then demonstrated by acquiring the dispersion of a set of coupled cavities and progressively increasing the chain length. The design studied herein improves on previous implementations with respect to the optimization of the figure-of-merit, namely the GBP. First, the bandwidth is maximized by increasing the momentum span of the unit cell. This is achieved by stacking L3 cavities along the PhC  $\Gamma$ M direction, resulting in an effective periodicity of  $a\sqrt{3}$ , where  $a$  is the PhC lattice constant. A staggered geometry is utilized, which gives freedom over the control of cavity-neighbor coupling without significantly disturbing the cavity modes. By making use of an automated optimization method [37], optimal geometric design parameters are found which maximize the target functions including GBP and radiative losses.

### 6.2.1 Theoretical Formulation: First Principles Approach

A system of coupled photonic resonators can be modeled in analogy to electron wave functions using a tight-binding formalism [14], commonly applied in solid-state physics for bandstructure computations. Such treatment originates from molecular orbit theory, where the wave function of a molecule can be computed as a linear combination of elementary atomic orbitals, which form a basis set for the computation. When an orbital belonging to an isolated atom (analogous here to a resonant state of a defect microcavity) is brought in close proximity to one or more identical atomic systems such as to attain wave function overlap, the resultant Hamiltonian of the system leads to the creation of  $N$  discrete states stemming from the  $N$  coupled atomic orbitals (depicted in Fig. 6.2.1).

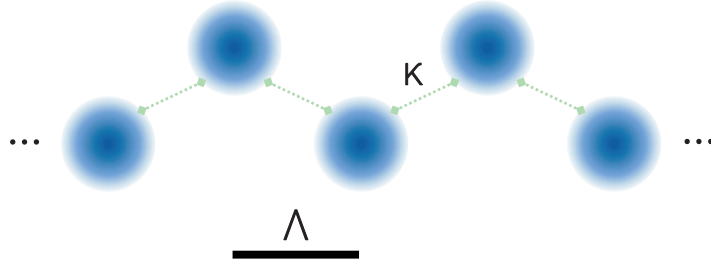


Fig. 6.2.1 Tight-binding picture of a system of coupled atomic orbitals, where  $k$  indicates the first-neighbor coupling strength and  $\Lambda$  the periodicity along the forward direction.

Taking the elementary case of two coupled identical orbitals, the result of the hybridization following the coupling of degenerate states would be the formation of a bonding ground state and an anti-bonding excited state, as shown in Fig. 6.2.2. Based on the above analogy, it is therefore common to refer to a system of coupled PhC cavities as *photonic molecules*, and in optics, these hybridized states are often labelled as *supermodes*. An important point is that in a photonic system, it does not strictly follow that a bonding state must occupy the ground state as will be discussed in section 6.2.2.

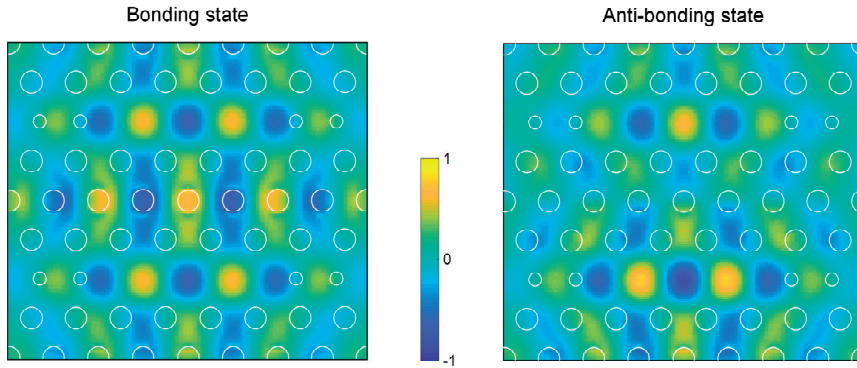


Fig. 6.2.2 Mode profile ( $E_y$  component) of the bonding ground state and anti-bonding excited state of a PhC molecule, composed of two modified L3 cavities coupled along the  $\Gamma M$  direction.

Furthermore, it has been shown that through a tight-binding analysis, similar to that used for a quantum-well superlattice model [174], the dispersion of a PhC coupled cavity system can be extracted by analyzing the fundamental eigenstates of the constituent cavities. This is done by accounting for the field overlap using the dielectric perturbation according to the transfer (T), overlap (R), and shift (S) integrals [174], [175]. The analysis here is extended to the case of multiple neighbor coupling, which is necessary when the cavity separation to neighbors beyond the first is not sufficiently large to neglect higher-order coupling (derivation and definitions are found in Appendix B). We show that the dispersion equates to:

$$E(k) = E + \frac{S + 2 \sum_m T_m \cos(mkL)}{1 + 2 \sum_m R_m \cos(mkL)} \tag{6.2.1}$$

where  $m$  is the cavity neighbor index, and  $L$  is the cavity-cavity separation. We account here for the coupling of a single eigenstate and assume that the cavity sits in a symmetric potential. The above expression can be approximated by the following equation:

$$\omega(k) \approx \omega_0 + \kappa_1 \cos(kL) + \kappa_2 \cos(2kL) \quad (6.2.2)$$

where  $\omega_0$  is the resonant frequency of the isolated cavity,  $\kappa_i$  is the phenomenological coupling strength, and accounting in this equation for the first two neighbors. The tight-binding approximation provides a very intuitive model that can accurately depict the response of a system of coupled oscillators. The expression conveys fundamental insight into how the bandwidth and group index (the latter inversely proportional to the dispersion slope) are directly influenced by the cavity coupling strength, as well as the inverse relationship that both figures have relative to one another.

### 6.2.2 Cavity Coupling Strength and Implemented Design

It has been shown that the coupling strength between two neighboring PhC cavities in a vertical  $\Gamma M$  configuration can be continuously tuned between positive and negative values [176], [177], confirming that degeneracy is supported and that an anti-bonding ground state can indeed exist. At the origin of this effect is the interference between the modes of the two coupled cavities at the barrier site. Thus, the inter-cavity coupling strength can be controlled by altering the barrier's dielectric permittivity distribution, and this is commonly carried out by changing the native PhC hole radii at the barrier site. Fig. 6.2.3 displays the coupling strength between two L3 cavities for the aforementioned vertical  $\Gamma M$  configuration and for a diagonal coupling configuration.

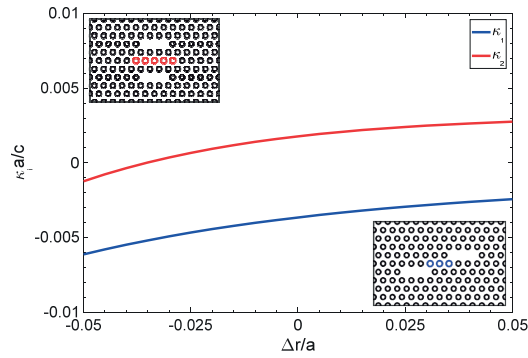


Fig. 6.2.3 Coupling strength for two L3 cavities in a diagonal (blue) and vertical  $\Gamma M$  (red) coupling configurations ( $\kappa_1$  and  $\kappa_2$  respectively). (coupling strength data from [12])

The design implemented by M. Minkov et al. [12], displayed in Fig. 6.2.4, constitutes two L3 defect cavities within a single unit cell in a Si slab, which are aligned in a staggered geometry. While the unit cell features a pitch of  $2\sqrt{3}a$  (for a lattice constant  $a=400$  nm), the effective period along the propagation direction is  $L = \sqrt{3}a$  due to the symmetry of the cavities within the unit cell around the vertical propagation axis. The design makes use of two separate hole-barriers to control the coupling between the first neighbor (PhC hole barrier in blue) and second neighbor (PhC hole barrier in red) cavities. The configuration of the first-neighbor barrier hole radius ( $\Delta r_1$ ) primarily dictates the slow light properties, while that of the second-neighbor barrier hole radius ( $\Delta r_2$ ) fine-tunes the response since it allows for the suppression of the coupling between the second-neighbor cavities, which are in close proximity due to the compactness of the unit cell design.

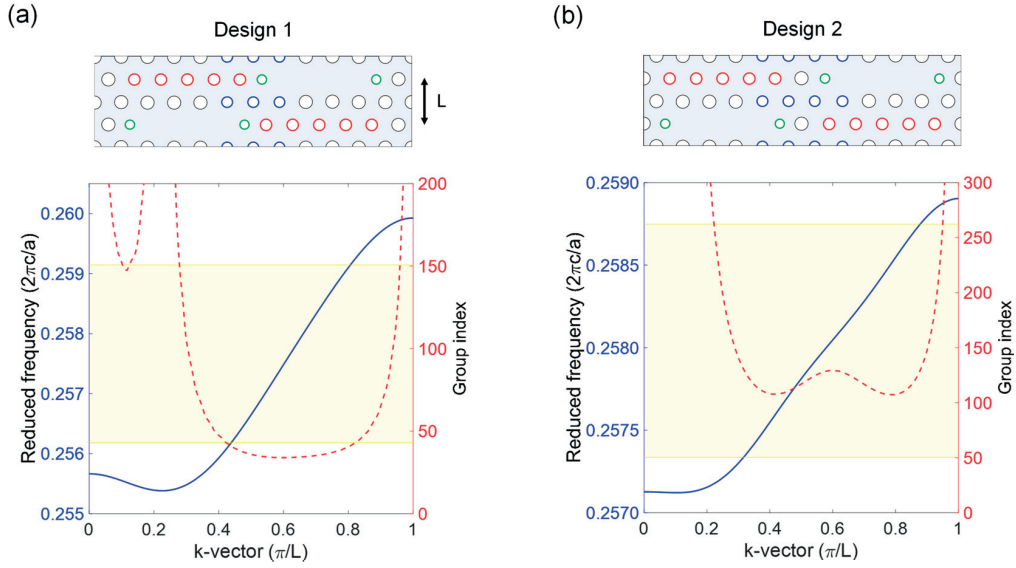


Fig. 6.2.4 A schematic illustration of CCW (a) design 1 and (b) design 2 along with their GME-computed dispersion curve and group index. The first-neighbor barrier holes are indicated in blue, while the second-neighbor barrier holes are indicated in red. The inner L3 cavity side-holes which are further adjusted in size and position are shown in green. (dispersion data from [12])

An optimization algorithm for the CCW was implemented with the GBP figure-of-merit as the target objective function. In addition to the barrier hole radii, the position ( $\Delta x$ ) and radius ( $\Delta r_3$ ) of the inner L3 cavity side holes (green PhC holes in Fig. 6.2.4) were selected as optimization parameters. The latter holes were chosen in order to cap the *radiative* losses of the device at 50 dB/ns within the operational bandwidth. This is a reasonable value given that the CCW operates above the light line [178], [179]. The bandwidth was defined in terms of the 10% deviation range from a center  $n_g$  value (chosen in such a way to maximize the bandwidth), which here is deemed a more relevant criterion than the attenuation. Multiple designs were obtained from the optimization runs, which provided a varying extent of compromise between group index, bandwidth, and group velocity dispersion.

The focus here will be on two particular designs of interest, both of which feature exceptionally high GBP. The first design exhibits one of the largest bandwidth values amongst slow-light devices, while the second design offers an average group index beyond 100. They will henceforth be referred to as designs 1 and 2 respectively. The parameters of both designs, which operate around  $\lambda=1550$  nm, are listed in Table 6.2.1. Compared to the first design, the second one exhibits a lateral single lattice-unit offset between the staggered cavities, resulting in a weaker first-neighbor coupling strength, and ergo, slower light propagation. This comes naturally at the expense of narrower bandwidth as can be seen in Fig. 6.2.4.

Table 6.2.1 Parameters for CCW designs 1 and 2, for operation near  $\lambda=1550$  nm.

Design	$\Delta x$ (nm)	$\Delta r_1$ (nm)	$\Delta r_2$ (nm)	$\Delta r_3$ (nm)	Bandwidth (nm)	Average Group Index	GBP
1	66	-15	-11	-30	18.0	37	0.43
2	88	-2	-14	-41	8.8	116	0.66



### 6.2.3 Light Coupling Scheme

In order to achieve effective light injection into the CCWs, one must take into consideration the energy density mismatch as light transitions into the slow light regime. This goes beyond the typical mode-matching analysis. In a lossless non-magnetic medium, the energy transport velocity  $v_E$  becomes equivalent to the group velocity  $v_g$  [180], and the energy flow rate in an optical system can be expressed by  $\langle \mathcal{S} \rangle = \langle u \rangle v_g$ , where  $\mathcal{S}$  is the Poynting vector, and  $u$  is the energy density of the field. A reduction of the group velocity, while conserving electromagnetic field energy, implies an energy density build-up in order to maintain the same energy flow. From an impedance matching point-of-view, this results in hampered power transfer, which is manifested in the reflection of light at the interface, which becomes more significant as the group index contrast of the transition rises. It is therefore expected that despite having perfect modal matching, coupling to a slow light system may still be lacking. This problem has been thoroughly tackled in literature, particularly for W1 waveguides, where solutions have been proposed such as adiabatic power transfer [181], [182] or the introduction of intermediate fast-taper transition sections [183]. Furthermore, it has been proposed that through the excitation of evanescent [184] or surface modes [185], more efficient coupling to slow light can be achieved, even when exciting the system through high- $v_g$  waveguides.

In CCW-based slow light systems, evanescent coupling is primarily relied on for the excitation of CCW modes given the difficulty in achieving appreciable mode matching to cavity resonance profiles of many PhC cavity geometries. Either an in-line or out-of-line configuration is employed [186], typically exciting the CCW from a W1 waveguide. An over-coupling regime is expected with the in-line configuration, where the W1-CCW coupling rate exceeds the CCW intrinsic loss rate. This results in enhanced transmission but with reduced CCW state lifetimes. Due to the staggered geometry of the implemented CCW design, which is oriented along the  $\Gamma M$  direction, an out-of-line coupling scheme was chosen. The W1.x waveguide is oriented at  $90^\circ$  relative to the propagation axis of the CCW, delivering light to the first cavity of the chain, as shown in Fig. 6.2.5 (b). This configuration reduces the CCW-W1 coupling rate, such that it operates near the critically-coupled regime for sufficiently long CCWs, given that the CCW-W1 coupling rate also depends on the photon decay rate of the CCW. The x value of the W1.x waveguide was selected to be 115 and 087 for designs 1 and 2 respectively to have the entire bandwidth of the CCW overlap with the linear dispersion region of the index-guided W1 even mode. The W1 waveguide is therefore in the fast-light regime of operation at a group index of approximately 20, which ensures transmission through the W1 waveguide while reducing the energy flow mismatch from the preceding strip waveguides to the CCW.

The aforementioned W1.x waveguides were interfaced by an adiabatically tapered Si strip waveguide on insulator. The termination of the interface between the PhC and the strip waveguide was chosen in such a way to reduce reflections that likely originate from surface state localization, as suggested in [185]. An inverse SU8 tapered waveguide was added for spot-size conversion, linking the strip Si waveguide to the chip facet, where its cross-section was chosen to match the beam profile of the coupling lensed optical fiber.

The devices were fabricated at the Cornell Nanoscale Science & Technology Facility (CNF) by Y. Lai. Electron-beam lithography was carried out using a 100 keV beam to pattern the ZEP-520A resist (positive-tone) layer, which was spun beforehand on a Si-on-insulator (SOI) wafer (220 nm Si layer on  $3 \mu\text{m SiO}_2$ ). After resist development, inductively-coupled plasma etching of the Si layer was conducted using fluorine-based chemistry to transfer the mask pattern. SU8 spot-size converters were then patterned using UV photolithography, guided by pre-deposited alignment markers. The PhC membrane was finally released by buffered-HF etching of  $\text{SiO}_2$ , after protecting the SU8 waveguides with photoresist. SEM micrographs of PhC-strip waveguide interface and the W1 coupling to the CCW are shown in Fig. 6.2.5.

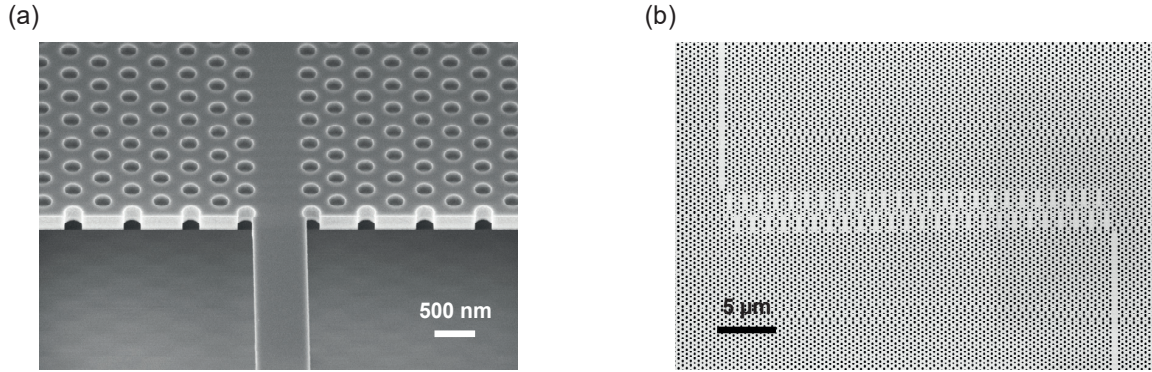


Fig. 6.2.5 SEM micrographs of the (a) PhC W1.x waveguide-strip waveguide interface, and (b) a CCW consisting of 50 cavities coupled to W1.x waveguides. (SEM micrographs acquired by Y. Lai)

Apodization refers to the process of introducing a windowing function to the cavity coupling strength such as to attain a gradual phase transition towards the end of a CCW, which helps eliminate oscillations that would otherwise be present in the transmission band [187]. This is carried out in a similar manner to filter design [188]. Apodization of cavity coupling was not considered for the terminations of the CCW, primarily due to the fabrication tolerance that is necessary for coupling control in a PhC platform, which approaches near-nm accuracy in hole radii. This is at the limit of the current electron-beam lithography resolution, which allows for 1 nm stepping with  $\approx 5$  nm beam spot size. A more feasible approach for apodization is based on cavity displacement, which can be implemented with CCWs featuring an in-line coupling configuration. The incorporation of apodized CCW terminations however is expected to reduce the ripple effect in the transmission response near the edge of the band, which arises due to interference in accordance with the accumulated phase.

### 6.3 Experimental Characterization

We have relied on a frequency-domain end-fire based configuration for the characterization of the CCW devices, in combination with real/ Fourier-space imaging microscopy. Both the transmission and radiative emission are captured simultaneously from the sample during a frequency sweep. Real and Fourier-space detection however are not carried out simultaneously and must be done in successive scans. Reconstructing the dispersion from Fourier-space acquisitions allows for the accurate measurement of slow light properties including the group index. It possesses a great advantage over interferometric and time-of-flight techniques in its ability to provide a local probe. The obtained results were verified through analysis of Fabry-Perot interference in the waveguide, originating from interface reflections.

#### 6.3.1 Fourier-Space Imaging

Out-of-plane emission from coupled PhC cavities can be related to the wave vector of the supported propagating mode through momentum conservation at the silicon-air interface:  $k_z = k \cos \phi$ . Thus, by measuring the far-field radiative angle  $\phi$ , and with knowledge of the wave vector  $k$ , the in-plane Bloch wave vector  $k_z$  of the mode is determined. Following that, the dispersion relation of the CCW can be reconstructed by scanning the input laser wavelength and analyzing the acquired far-field patterns. In k-space, the emission pattern is integrated along the axis perpendicular to the effective propagation wave vector.

A schematic of the experimental setup that was used to carry out Fourier-space imaging is shown in Fig. 6.3.1. The sample is excited in an end-fire coupling configuration through a lensed optical fiber. The polarization of the tunable laser source is controlled before injection via a polarization control unit. The sample is placed at the focal plane of a

high numerical aperture objective (Leica 100x, NA=0.9), which collects the radiated light. A spatial filter is placed at the conjugate image plane to select the region-of-interest out of the objective's field-of-view and to suppress unwanted stray scattering. The filtered image is then transformed using a set of lenses, which finally focus it onto the near-IR camera. The k-space resolution at the array detector, considering the lens system and the microscope objective (field-of-view  $\approx 250 \mu\text{m}$ ) is  $0.05 \mu\text{m}^{-1}$ . The filtered field-of-view was chosen to be larger than  $25 \mu\text{m}$  along each axis to avoid deteriorating the k-space resolution beyond the detector pixel limit. An extended description of the experimental setup and characterization technique can be found in section 4.3.

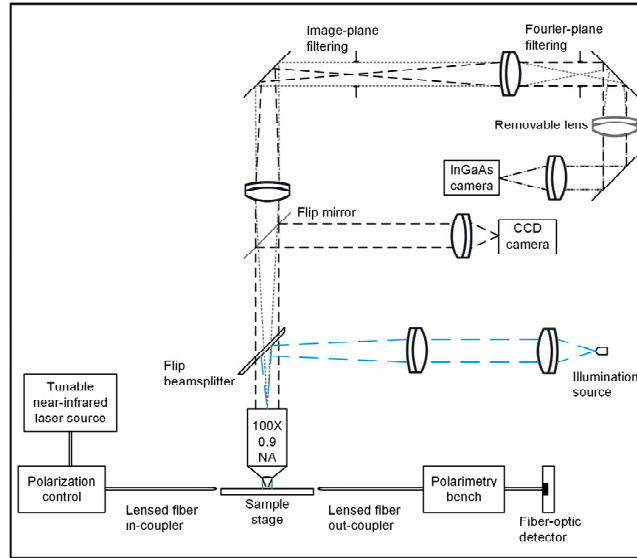


Fig. 6.3.1 Schematic illustration of the Fourier-space imaging setup.

## 6.3.2 CCW Dispersion

### 6.3.2.1 Experimental Acquisition

The acquired experimental dispersion of a 50-cavity CCW for design 1 is shown in Fig. 6.3.2, alongside the simultaneously captured transmission spectrum. The probe region was selected to be at the center of the device, corresponding to an area containing approximately 36 cavities. It can be seen that the experimental dispersion matches the profile of the theoretical dispersion lines predicted by the GME (and similarly the FDTD) computations. The experimental Brillouin zone boundary is well-defined in k-space, which follows from the near-nm accuracy of the structural patterning which is obtained through electron-beam lithography. With regard to operational bandwidth, the experimental range is found to be marginally narrower than theory, which can be attributed to slight deviations in the inter-cavity coupling strength due to limitations on the etch-dependent control of PhC hole sizes. This implies that for the same Brillouin zone extent, the dispersion lines are “flatter”, exhibiting slightly slower light as a consequence.

Although end-fire excitation favors injection into the forward propagation direction, both the forward and backward propagating modes of the CCW are observed in the acquired dispersion, the latter due to the presence of multiple scattering events, which increase as the group index of the mode rises. Both modes appear mirrored about the symmetry axis ( $k_x=0$ ) and are folded at the first Brillouin zone boundary ( $k_x=\pm\pi/2L$ ). The detected intensity is in proportion to their respective radiative contribution, given that the CCW modes extend above the light line. The forward propagating mode ( $\frac{d\omega}{dk} > 0$ ) is clearly seen to dominate the transport channel, especially in the central constant  $n_g$  (i.e. constant slope) range of the bandwidth, where the CCW operates in the dispersive regime [107]. This can be deduced from the well-defined dispersion, combined with the relatively flat transmission profile.

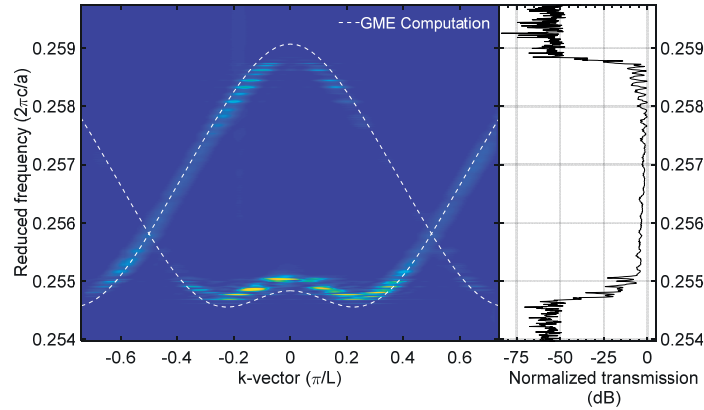


Fig. 6.3.2 Experimental dispersion of a 50-cavity CCW of design 1 with an overlay of the GME computation, along with the measured normalized transmission.

A quasi-continuous dispersion relation can be traced through the experimental data, whose shape is determined by the collective spectral response of the constituent cavities. The inherent discretization of states due to the finite cavity number is apparent, especially with the shorter CCWs. This is the case with the presented 50-cavity chain here, since the CCW design utilizes a broad bandwidth span relative to the linewidth of the formed states. In comparison to an isolated cavity, the spectral linewidth of the states can vary between approximately 8–66 pm, according to the location of the  $k$ -vector within the Brillouin zone [189]. Individual peaks are discernible, particularly near the edge of the band where radiative scattering losses are pronounced. The states in that region are also well-spaced out along the  $k$ -axis due to the band curvature, and their visibility is enhanced by the Fabry-Perot interference. Following the tight-binding formalism,  $n$  states are expected to be observed for an  $n$ -cavity system.

Moving towards the edge of the band,  $n_g$  gradually rises and scattering into the backward propagating mode becomes progressively significant due to disorder-induced scattering. It has been observed that when the group index exceeds a value of approximately 50, the light momentum linewidth ( $\Delta k$ )—which is naturally governed by the finite-sample size and attenuation [106]—begins to increasingly broaden, signaling the onset of diffusive light transport. Subsequent localization in the photonic crystal lattice occurs towards higher  $n_g$  values.

The transmission curve of the device clearly outlines the operational range of the device and confirms the obtained dispersion. It should be noted that the transmission measurement does not showcase the pure CCW response, but rather incorporates the modulation introduced by the various interfaces, including the frequency-dependent coupling at the W1-CCW interface. The spectral oscillations within the operational bandwidth were characterized with a root-mean square (RMS) intensity fluctuation of 1.3 dB and peak-to-peak intensity variation value of 5 dB.

There are several physical effects that cause the observed intensity fluctuations, and it is important to make a clear distinction between each contribution. At the origin of the intensity ripple is the discrete nature of the CCW device, i.e. overlap of finite constituent states. It is present throughout the bandwidth, especially for the relatively short CCW chains. The CCW length dependence will be elaborated on in the following section. It is seen however that despite the size of the 50-cavity CCW, the experimental RMS intensity fluctuation can be as low as 0.11 dB over a 1 nm wavelength range. Stronger oscillations in transmission that are found near the edge of the bandwidth emerge from interference effects due to the lack of apodization. The CCW terminations act effectively as mirrors due to the diminishing CCW-W1 coupling rate when  $n_g$  rises, and Fabry-Perot interference peaks appear with increasing contrast towards the edge of the transmission band. They have been clearly observed through imaging of the CCW modes in that frequency range (refer to section 6.3.4). Moreover, there are disorder-induced effects such as multiple scattering, which scale with the light slow-down factor and become increasingly significant as the CCW chain is

elongated. This can be thought of in analogy to a resonant tunneling process, where the transmission probability deteriorates and transport is hindered due to the detuning of intermediate linking states.

### 6.3.2.2 Tight-Binding Fit and Slow-Light Parameter Extraction

An advantage of the Fourier-space imaging technique is the ability to directly measure the dispersion of the device under investigation. This rids the measurement from the uncertainty associated with alternative approaches. For example, when CCW states are extracted from the frequency peaks of the transmission signal [186], an equally-spaced  $k$ -grid is typically assumed for the CCW according to the tight-binding approximation. For the current measurements, we implement an algorithm to first separate the set of propagating CCW modes of the acquisition, seen in Fig. 6.3.3, then carry out state sampling via frequency weighing of the amplitude maxima, to extract the dispersion points. We do not sample single discrete frequency states, but rather a dispersion function  $\omega(k)$  that is discretized by the  $k$ -space resolution. The result is shown in Fig. 6.3.3 for the 50-cavity CCW of design 1. Since this method relies on mode radiation, the dispersion curve is very well retrieved for the case of the forward propagating mode, where most of the energy is coupled, as opposed to the backward propagating mode, which only appears when  $n_g$  rises over a certain threshold. As light enters the diffusive regime [107], it becomes progressively difficult to identify truly dispersive behavior of light transport. The radiation appears smeared along the  $k$ -axis at this point onwards as the theoretical group index progressively goes towards infinity (in theory).

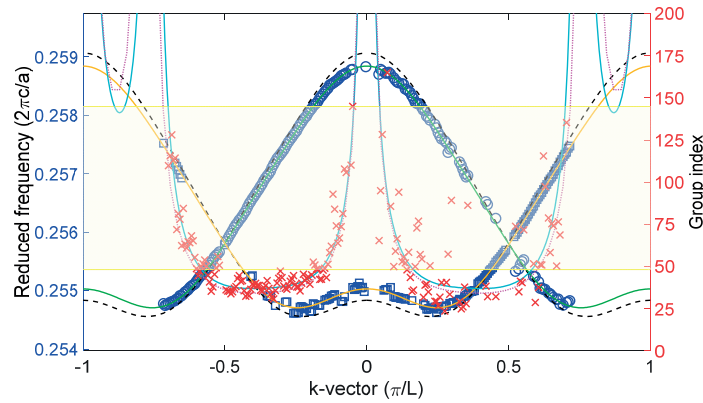


Fig. 6.3.3 The extracted experimental dispersion points (blue circles and squares) and tight-binding fit (green and orange line) of CCW design 1, for two diffraction orders of the CCW modes, along with the theoretical GME computation (dashed black line). Concerning a single diffraction order (blue circles), the group index is plotted for: direct numerical differentiation of the experimental points (red crosses), derivation from the tight-binding fit (cyan line), and derivation from the theoretical GME dispersion (dotted magenta line). The operational bandwidth is highlighted in yellow, as per the aforementioned  $n_g$  10% deviation definition.

A tight-binding fit was applied, accounting for near-neighbor coupling up to the second order, according to the following expression:

$$v_{reduced}(k) = v_0 + \kappa_1 \cos(k \cdot \sqrt{3} a) + \kappa_2 \cos(k \cdot 2 \cdot \sqrt{3} a) \quad (6.3.1)$$

According to the theoretical derivation mentioned in section 6.2.1, the above expression is an approximation to the ab-initio tight-binding equation. The coupling parameters here do not bear true physical significance, but only give an indication of the neighbor perturbation. More importantly, the fit enables the extraction of the group index with higher confidence. For the investigated device, the ratio of the near-neighbor coupling  $\frac{\kappa_2}{\kappa_1}$  was deduced to be 0.28.

It is noteworthy that  $\kappa_1$  has a positive sign, which suggests bonding character based on the employed sign convention. An interesting observation is that the staggered cavity configuration does indeed weaken the

second-neighbor coupling relative to the first-neighbor, but not entirely, such that it still influences the slow-light characteristics.

We carried out numerical differentiation of the extracted dispersion points based on a fit to a second-order Lagrange interpolating polynomial, in order to get a direct measure of the group index. The results shown in Fig. 6.3.3 are plotted as a function of the dispersion k-vector, specific to a single diffraction order that is indicated by the blue set of circles. The strong short-scale fluctuation in the group index values is only an artifact of the numerical differentiation process. To retrieve the exact values of the group index, it is more suitable to do that through the experimental dispersion tight-binding fit, which has been used thenceforth. For comparison, the curve is plotted alongside the group index that is computed from the theoretical GME simulation. The numerically derived group index points appear to follow the group index curve of the experimental tight-binding fit better than the theoretical curve. As predicted from the initial comparative observation of the dispersion curves, the experimental group index is indeed higher on average relative to the theoretical computations.

The operational bandwidth—as per the aforementioned 10%  $n_g$  deviation definition (refer to section 6.2.2)—can now be identified and is highlighted on the figure. For the 50-cavity device, it is found to be 17 nm, with an average group index of 41, yielding an experimental GBP of 0.45. This is to be compared to the predicted bandwidth of 18.0 nm at an average group index of 37 (GBP=0.43), which was obtained through theoretical computations. As mentioned earlier, the target theoretical value in terms of the bandwidth can be reached with finer control over PhC hole etching. The device was finally able to achieve one of the highest demonstrated GBP values to-date. The 50-cavity chain however was found to be a sub-optimal device length in terms of the slow-light properties, as will be discussed in the next section.

Spectral analysis of the transmission signal was carried out to further confirm the group index values which were obtained through Fourier-space imaging. Fabry-Perot oscillations appear in the transmission signal as a result of interference, when semi-reflecting interfaces are present within the device such that a low-finesse “cavity” is formed. The free spectral range indicates the optical path length, which is influenced by group index of light. Therefore, through knowledge of the existing interfaces (to identify the physical length  $l_{cavity}$ ), the group index can be retrieved using:  $n_g = \frac{\lambda^2}{2\Delta\lambda l_{cavity}}$ . With the current sample design, the strongest reflections originate at the CCW-W1 interface. Fourier-transform analysis was carried out on the transmission spectrum of the 50-cavity CCW, using a Gaussian spectral window centered on and covering the bandwidth. The extracted group index value was found to be  $39.9 \pm 1.8$ , within 3% of the k-space extracted value, thereby confirming the validity of the previous results. While spectral fluctuations of the group index may occur [190], such fine deviations cannot be deduced directly through either Fabry-Perot residual-reflection method or the dispersion curve, unless in the case of the latter, there is a sufficient number of CCW states to sample the bandwidth at the desired spectral resolution. A fine spectral characterization technique relying on referenced interferometry is necessary.

Concerning CCW design 2, which features a theoretical average  $n_g$  of 116, the fabricated devices could not adequately reproduce the simulated optical response for several reasons. First, this design is not as robust as design 1 with respect to deviations from nominal design values. Off the design wavelength, the dispersion of CCW design 2 was found to exhibit strong distortion, particularly around the inflection points of the dispersion. The deviation in  $n_g$  over the nominal bandwidth range reached up to 15%. Despite that, a group index of 102 was still obtained over a limited bandwidth of 2 nm. The highest measured propagative  $n_g$  value was 125, and the corresponding attenuation length was measured to be  $\approx 100 \mu\text{m}$ .

### 6.3.3 Length Dependence and Losses

Theoretical formulation of CCWs assumes infinite coupled-cavity chains. In realistic implementations, finite-size effects come into play, amongst which state discretization is particularly pronounced, as with the previously displayed 50-cavity CCW measurement. It is desirable to elongate the CCW length in practice for various reasons depending on the application, whether to prolong the signal delay time or to expand the light-matter interaction volume. Intuitively, it is expected that the longer the formed CCW chain, the closer that its response would resemble the theoretical Bloch-boundary device.

The CCW slow-light properties with respect to device length have been investigated for the first design using state-of-the-art fabrication. CCW chains comprising 50, 100, 200, 400, and 800 cavities were successfully realized. Based on the attained optical response throughout the development process, no attempts for longer devices have been made, as it will be shown that we are close to the limits imposed by disorder. A comparison of the transmission response of the devices is shown in Fig. 6.3.4. The reduced frequency axis of each device has been offset, such that the dispersion is frequency aligned for all devices. This is in accordance to the measured frequency offset of each device relative to the theoretical design. A vertical line on the graph should therefore run through the same  $n_g$  value for all the device plots. While the transmission signals do exhibit high peak-to-peak fluctuation values, the computed RMS fluctuation is rather reasonable, particularly when considering a 1 nm transmission window.

It is immediately noticeable that transmission characteristics of the CCW deteriorate with increasing device length. Firstly, the transmission window begins to shrink significantly as the cavity length is doubled beyond 200 cavities. Both ends of the bandwidth are affected, yet more considerably on the low-frequency side due to the profile of the dispersion in that range. In the presence of disorder-induced scattering, the device length becomes effectively a cut-off filter for light that possesses a group index value exceeding a certain limit. According to the nature and degree of disorder, each  $n_g$  value will possess a characteristic decay length, beyond which negligible transmission is expected. Based on the  $n_g$  values that were derived from the CCW dispersion, it can be inferred that the decay length for  $n_g \approx 65$  is on the order of  $\approx 550 \mu\text{m}$ . Since there is also a reduction of the CCW-W1 coupling rate ( $\tau_{CCW-W1}^{-1}$ ) near the edge of the bandwidth (due to the rising  $n_g$ ), besides  $\tau_{CCW-W1}^{-1}$  being inversely proportional to the device length [186], it follows that the transmission ceases with the longer CCWs as  $\tau_{CCW-W1}^{-1}$  drops below the cavity-cavity coupling rate. This effect progressively increases in extent from the edges of the bandwidth inwards as the cavity chain is elongated.

Secondly, the flatness of the transmission degrades with increasing CCW length, in terms of the appearance of additional fluctuations with increasing intensity contrast. This is a direct consequence of the presence of disorder in the PhC lattice. It has been proposed through a simplified disorder model [191] that such dips in transmission emerge due to disorder-induced multiple scattering. It can be inferred from the measurements that in a PhC waveguide configuration relying on a resonant tunneling mechanism for light transport, the impact of disorder is cumulative with device length. The RMS values for the transmission fluctuation which are plotted in Fig. 6.3.4 (b) indeed confirm this statement, and an exponential dependence on the device length is apparent. It was measured to be  $4.9 \times 10^{-3}$  dB/cavity across the bandwidth.

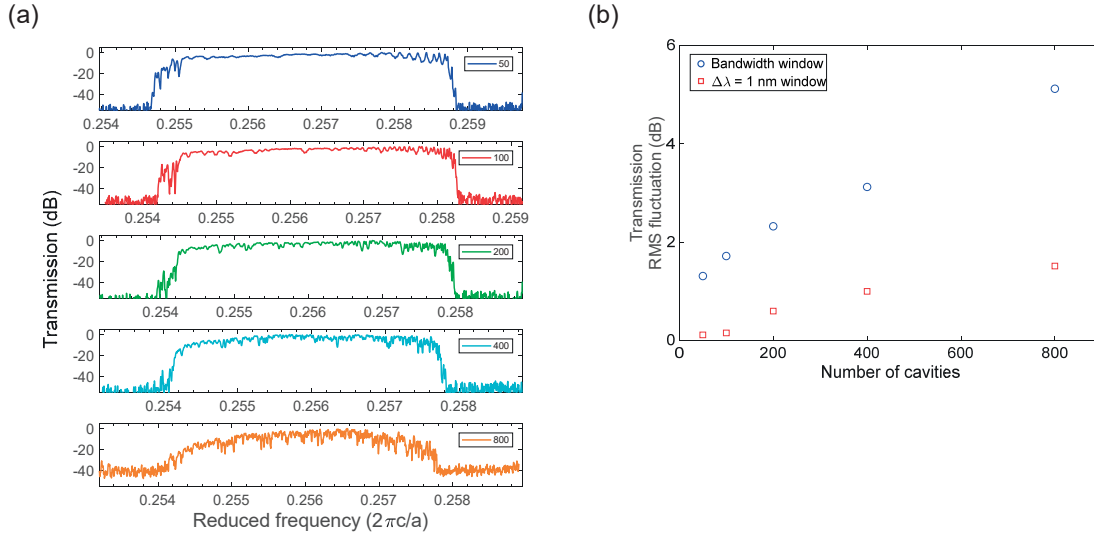


Fig. 6.3.4 (a) CCW transmission for CCW chains comprising 50, 100, 200, 400, and 800 cavities. The reduced frequency axes have been aligned on the figure such that the dispersion points of all devices are matching. (b) Transmission characteristics as a function of device length displaying the bandwidth RMS fluctuation and the lowest  $\Delta\lambda=1$  nm-window RMS fluctuation near the center of the band.

To further analyze the losses, the spatial dependence of the radiation was measured for the 800-cavity CCW by collecting the scattered light along the waveguide for different frequencies across the bandwidth. The attenuation was assumed to follow the Beer-Lambert law, that is to say that light is travelling in the dispersive regime with an insignificant multiple scattering contribution and sufficiently weak intensity as to not provoke a nonlinear material response. The validity of such an assumption has been questioned by Patterson et. al. in view of the influence of disorder-induced scattering, since the decaying light does not necessarily escape the system and may contribute to signal transmission [192]. The analysis that they carried out using a disorder model that utilized incoherent ensemble averaging shows that considerable deviation from the Beer-Lambert law occurs for long waveguides (exceeding 1 mm in length), while operating at  $n_g$  values beyond 40. These values do not invalidate our assumption, however, a more rigorous model accounting for interference effects may still be necessary to elucidate the scattering behavior.

The plots in Fig. 6.3.5 (a) display light attenuation through the 800-cavity CCW at the center ( $a=0.2560$ ) and edge ( $0.2542$ ) of the bandwidth. The long-scale modulation in intensity that is seen in the emission of a CCW is typically due to Fabry-Perot interference, while shorter-scale intensity variations may originate either from disorder or the presence of defects. Moreover, local variations of the refractive index can cause minor frequency shifts of the system's local dispersion response, which in turn may result in peaks or dips in emission intensity. An exponential fit can be extracted from the attenuation of the devices, which indicates a 56 dB/ns loss value at the center of the bandwidth, compared to 102 dB/ns at the low-frequency edge. While such frequency dependence is expected since the CCW mode becomes increasingly radiative at lower frequencies, the experimental losses are found to surpass the theoretical values by up to a factor of  $\approx 3.5$  (at  $a=0.2560$ ). The computed theoretical losses however only account for out-of-plane emission, which goes according to the radiative Bloch components in the light cone, in combination with the isolated cavity emission profile [179], [189]. Disorder-induced scattering and absorption losses on the other hand are not included in the calculation.



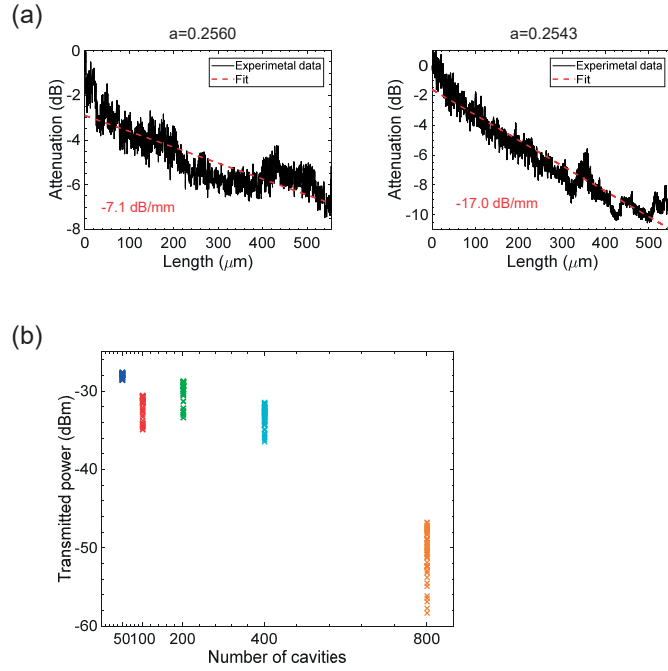


Fig. 6.3.5 (a) Attenuation of the 800-cavity CCW at the center ( $a/\lambda=0.2560$ ) and just past the edge ( $a/\lambda=0.2543$ ) of the bandwidth window, obtained from the integrated emission of an 800-cavity CCW. The attenuation corresponds to a loss rate of 56 dB/ns and 102 dB/ns, respectively for a derived group index of 38 and 50 (respectively). (b) Scatter plot of the transmitted power as a function of the number of cavities in a CCW, over a 1 nm window.

There is an indication for length-dependent scaling of the loss rate when analyzing the transmitted power through the devices of varying CCW length, located on the same chip. Fig. 6.3.5 (b) shows a scatter plot of the transmitted power over a 1 nm window near the center of the bandwidth, as a function of CCW length. Such variation can be directly explained by the reduction of the CCW-W1 coupling rate such that the transmitted power drops in accordance to  $T = \left| \frac{Q_{mode}}{Q_{coupling}} \right|^2$  [186], while taking into account the dependence of the intrinsic CCW decay rate. More detailed measurements are necessary for statistical relevance to quantify the exact dependence. Based on previous observation of scaling of transmission fluctuation with CCW length due to disorder, a length-dependent disorder contribution towards losses cannot be ruled out, especially when the device length is comparable to or larger than the localization length of light.

According to the measurements that were carried out, the optimal device length was found to be that of the 200-cavity CCW. It was able to achieve both the widest bandwidth and the highest average group index, at 17.4 nm and 41.7 respectively, achieving a record-high GBP value of 0.47. A device at this length is impacted by disorder, however, the effects are not as extreme as with the longer implemented devices. When it comes to transmission flatness, intensity fluctuations remain below 3 dB (RMS) throughout the bandwidth, which is less than a two-fold increase compared to the 50-cavity CCW. The attenuation losses are further estimated to be lower than 30 dB/ns near the center of the bandwidth. This value is less than a two-fold increase compared to the theoretical value. Such results are particularly motivating, as they confirm that we can currently achieve relatively long-scale PhC devices with performance comparable to ideal theoretical models.

### 6.3.4 Discrete State Analysis, Disorder, and Light Localization

In many implementations, slow-light PhC devices are often found to exhibit varying performance to that obtained through computational models, albeit the use of state-of-the-art fabrication. Besides finite-size effects, disorder has

a strong influence on the optical response as observed in many PhC applications. In slow light systems in general, the contribution of disorder is amplified by the slow-down factor, which in this case provides undesirable enhancement of light-matter interaction. This ultimately limits the lowest achievable group velocity in any device. More specifically with regard to coupled-cavity systems, the scale of disorder may be sufficient to disturb local coupling on the unit-cell scale, which is the essence of the functionality of the waveguiding scheme. Furthermore, under certain disorder realizations, Anderson localization of light may take place [1], [2], [193]. The identification of the physical limitations that are imposed by disorder is thus crucial for any practical use of PhC slow light systems.

The ability to achieve a continuous dispersion, setting disorder and coupling-induced effects aside, relies primarily on the ability to occupy the dispersion curve with overlapping propagative states. The condition on the required number of states can be derived from the continuity conditions of both momentum and frequency, following the tight-binding model to simplify the analysis. Considering first continuity in momentum, the wave vector spacing ( $\Delta k$ ) can be expressed as  $\Delta k = \frac{\pi}{(N+1)\Lambda}$ , assuming a finite structure of  $N$  states and spatial periodicity  $\Lambda$ . The minimal wave vector linewidth is dictated by the modal extent:  $\delta k \geq \frac{2\pi}{(N-1)\Lambda}$  and is additionally broadened by attenuation. Given that  $\delta k$  always exceeds  $\Delta k$ , one finds that the continuity relation is always fulfilled along the  $k$ -axis. Assessing next the continuity in frequency, the state frequency spacing can be expressed as:

$$\Delta\omega = \frac{c}{n_g} \Delta k = \frac{c}{n_g} \frac{\pi}{(N+1)\Lambda} \quad (6.3.2)$$

The state linewidth ( $\delta\omega$ ) is given by the state Q-factor:  $\delta\omega = \frac{\omega}{Q}$ , which besides the intrinsic lifetime also accounts for linewidth broadening due to coupling. The dispersion response becomes continuous when  $\delta\omega \geq \Delta\omega$ , thus formulating the requirement on the number of states:

$$N + 1 \geq \frac{1}{\delta\omega} \frac{c}{n_g} \frac{\pi}{\Lambda} \quad (6.3.3)$$

Care should be taken to account for the frequency dependence of the Q-factor and the group velocity dispersion. Amongst the displayed devices in Fig. 6.3.6, the 800-cavity CCW is nearest to reaching this criterion. Another more subtle requirement that practically comes into play is the levelling of the state energy densities such that a flat dispersion band is formed.

The influence of both finite-size and disorder-induced effects is pronounced when comparing the response of CCWs of varying length. The dispersion profile of the CCW coalesces when elongating the cavity chain as expected, with a proportional number of states being created, which narrow down the inter-state frequency gaps. However, as the number of coupled cavities increases, the individual elemental states are found to become spectrally finer. It comes as a consequence of the reduced coupling with the W1 waveguide when the CCW is elongated, such that the coupled cavity states will exhibit a decay rate that is closer to their natural linewidth. The response gradually transitions towards the intrinsic periodic boundary value. This is in combination with disorder-induced rise in the coupled cavity state lifetime as the CCW length exceeds the localization length. This is evident in Fig. 6.3.6, which compares the dispersion of the forward propagating mode near the edge of the bandwidth for increasing CCW device length, for up to 800 cavities. The dispersion was spatially acquired at the beginning of the CCWs, near the CCW-W1 waveguide coupling point. The Q-factors of the individual states of the forward propagating mode are extracted through collective-state fitting, and they are found to gradually shift closer to the theoretical values of a periodic-boundary CCW, which vary between  $\approx 0.25$ – $1.94 \times 10^5$  in the same frequency range. Furthermore, the expected rise in the state Q-factors with increasing  $n_g$  towards the edge of the bandwidth is observed for all CCW lengths.

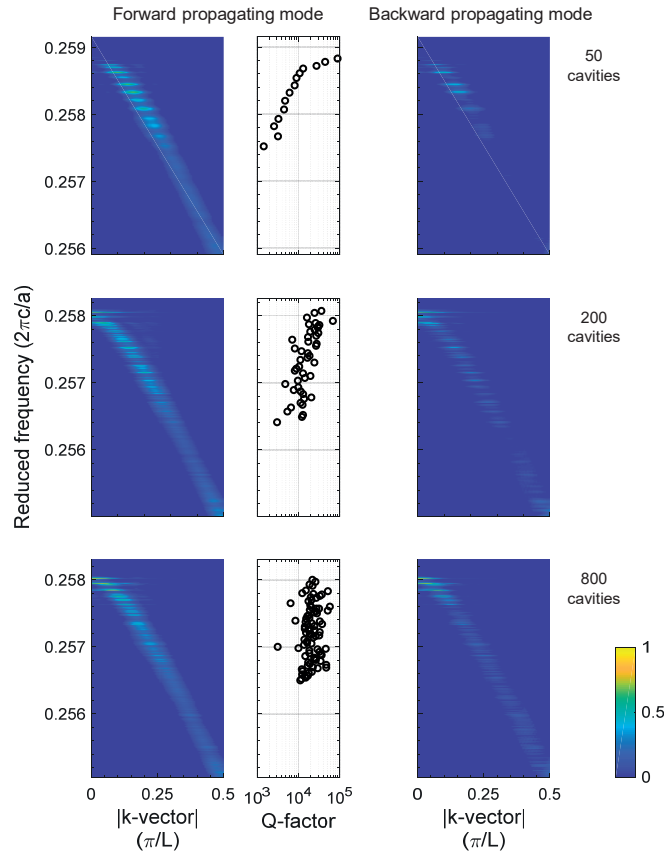


Fig. 6.3.6 Evolution of the dispersion of forward and backward propagating modes of CCW design 1 as a function of cavity length, measured near the beginning of the CCW. The extracted Q-factors of individual states are displayed for the forward propagating mode.

In k-space, the dispersion of forward and backward propagating modes of a CCW can be clearly distinguished. Light does not naturally couple to backward propagating modes beyond the coupling interface, unless mediated by an elastic scattering process, presented by the medium. A measure of the backscattered signal acts as a gauge for the degree of disorder and density of defects in a medium. When the CCW length is relatively short, up to 100 cavities, backscattering was found to become significant only at high group index values exceeding  $\approx 65$  which exist outside the operational bandwidth. This can be observed in Fig. 6.3.6, which displays the modes under a normalized intensity scale. A gradual rise in the intensity of the back-scattered signal occurs in relation with the group index (cross-reference Fig. 6.3.3), up to the point where it becomes comparable to that of the forward propagating mode, near the localization limit of light. The longer the CCW chain, the more significant the scattering into the backward propagating mode becomes and at lower group index values. For the disorder figure present in a PhC lattice, a localization length can be defined at a given group index value. The length of the device relative to the localization length determines the transport regime of light, whether ballistic if the device length is much shorter, or diffusive when both lengths are comparable. The latter case features multiple scattering events which couple the propagative mode to both the radiative loss channel as well as the backward propagating mode. The propagating mode can sense the disorder potential along an extended region of the cavity chain, which is confirmed by the measurement at hand since the probe is local and positioned near the CCW input.

The dependence of scattering in slow light systems on the group velocity has been a subject of debate in the photonic crystals community. It is known that radiative loss into the continuum goes according to the local density of states, which should naturally scale with the group index. It has been proposed by Hughes et. al. [194] that backscattering scales in proportion to  $n_g^2$ , which can be deduced by accounting additionally for the local density of states of the backscattering modes. It should be understood that this is an estimate which is based on a second-order Born approximation. We take the advantage here of the ability to separate both forward and backward modes in order to extract their respective group index dependence.

We analyzed the scattering dependence of the slow light modes for the implemented lengths of the cavities near the high-frequency edge of the bandwidth to sample the slow-down factor dependence. The opposite end of the bandwidth could not be treated similarly due to the mode degeneracy. The plot in Fig. 6.3.7 displays the normalized scattering intensity for the 800-cavity CCW as a function of propagation index for the forward and backward propagating modes of the CCW. The intensity points were retrieved from individual analysis of the discrete CCW states. A fit to the data points reveals a power dependence of 1.2 and 2.4 for the forward and backward propagating modes respectively with respect to  $n_g$ . The  $n_g$  power scaling here is found to be very close to the predicted theoretical model. However, deviations from the model are expected due to: the frequency dependence of scattering behavior as a result of varying Bloch mode profiles which will sample disorder differently, the dependence of light-cone radiation loss on frequency (as discussed earlier), and the onset of multiple scattering. Fabry-Perot interference and the accuracy of group index extraction introduce additional uncertainties to the data, however, the trends remain valid. It was found that the  $n_g$  power dependence revolves around the same aforementioned theoretical values with the shorter CCWs. The power dependence appears to gradually rise with CCW length, and the impact of disorder. The power ratio of the backward-to-forward propagating mode however remains to be approximately two in all cases.

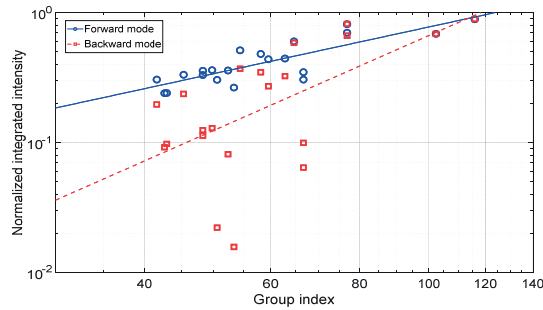


Fig. 6.3.7 Integrated intensity of forward and backward propagating modes as a function of group index for an 800-cavity CCW.

To examine the light decay and localization behavior of the CCW as a function of propagation distance, the dispersion of an 800-cavity device was acquired at the beginning, center, and end of the device. The probed regions are displayed in Fig. 6.3.8. Near the input, the entire dispersion curve of the CCW can be reconstructed, as light is coupled to and scattered from almost all existing CCW states. Localized states appear as well, but only within a typically short distance which is specified by their localization/ decay length. The attenuation of the CCW mode is clearly illustrated in Fig. 6.3.8 (a) for the mode which is seen propagating from left to right. Long-range interference oscillations faintly appear in the spatial profile as well. The effect of group index-dependent decay is evident at both frequency ends of the dispersion curve in the figure. At the high-frequency end for instance, the group index limit at the center of the CCW is 78, beyond which light does not propagate. This value drops to 64 near the end of the CCW, where the transmission of the device at the corresponding frequency is found to be negligible. A similar effect is present at the opposite end of the bandwidth, yet due to the higher intrinsic radiation loss at longer wavelengths, the cut-off group index values are comparably lower at the same site.

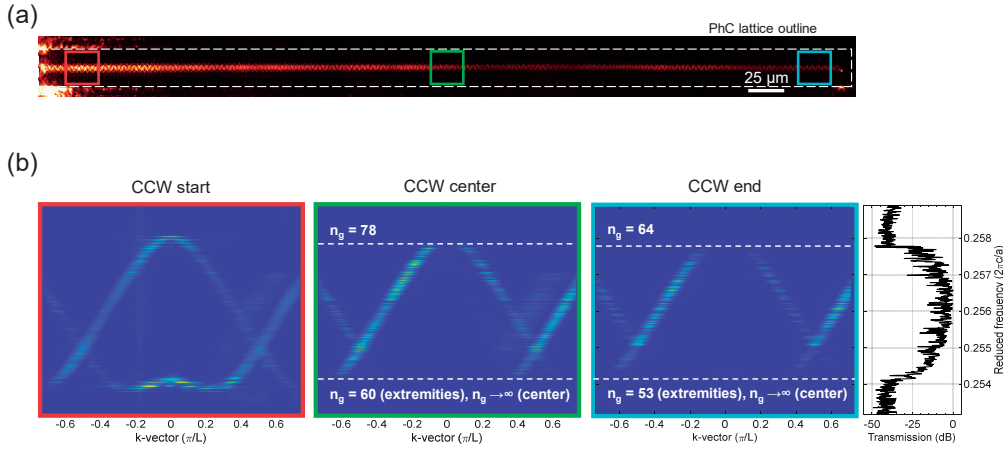


Fig. 6.3.8 (a) Light propagation through an 800-cavity CCW near the center of the bandwidth ( $a/\lambda=0.2564$ ). An outline of the PhC lattice is marked with the dashed white line. The squares at the start (red), center (green), and end (cyan) of the CCW indicate the regions probed by the dispersion measurement shown in (b), which are plotted along with the transmission of the device.

As mentioned earlier, Fabry-Perot oscillations are present due to residual reflection at the CCW-W1 interface and increase in contrast near the edge of the bandwidth as the reflectivity rises. The propagating CCW mode forms a standing-wave pattern that is pinned at the CCW-W1 boundary, and the standing wave pattern approximately satisfies the following equation:  $\sin(k_z z) = 0$ , such that the node positions are located at  $z = m \frac{\pi}{k_z}$ , where  $m$  is an integer and  $k_z$  is the effective propagation k-vector along the CCW axis. This is assuming that zero phase shift is incurred at the boundaries, and the optical medium is uniform along the entire structure. The oscillations are evident near the high-frequency end of the transmission signal, as well as in the real-space mode-profile, which is shown in Fig. 6.3.9 for the 50-cavity CCW. The sequence of patterns is shown up to  $m = 4$ , and by computing the  $k_z$  value one finds that it agrees with the tight-binding dispersion fit to within 5%. The Fabry-Perot oscillations at the opposite end of the bandwidth are not observed, since for the low  $k_z$  values (which produce large observable oscillation periods) the corresponding group index is beyond the cut-off, in addition to the degeneracy of the CCW mode within that frequency range.

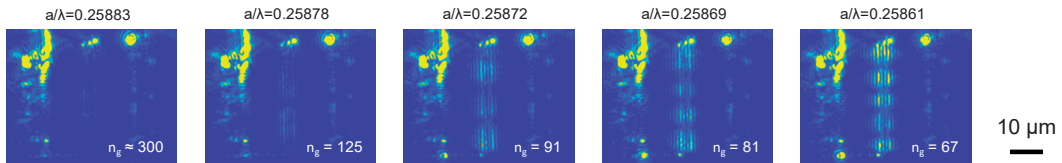


Fig. 6.3.9 Mode profile of a 50-cavity CCW for decreasing frequency from left to right, near the high frequency edge of the bandwidth, displaying Fabry-Perot interference patterns.

Localization of light occurs when the mean free-path of photons is significantly reduced relative to the sample length such that diffusive light transport comes to a halt. The localization regime, when not engineered intentionally, emerges due to disorder and defects in the medium such that multiple scattering of light takes place, eventually forming a closed path. The notion of light localization that is induced in a strongly disordered medium has been introduced by P. Anderson [193] in 1958. A binding definition for a localized state since then does not exist, however, there are particular signatures which have been observed to correlate with light localization. For instance, light transmission deviates from the standard linear attenuation model, and follows a near-quadratic dependence at the localization transition, and an exponential dependence beyond that [195]. In the presence of absorption however,

such statistics will no longer be valid. Furthermore, by the nature of the photonic crystal slabs, localization occurs in the transverse lattice plane, yet the light cone remains a leakage channel. Thus, the temporal extent of localization is limited regardless of the localization strength.

## 6.4 Structural Characterization

Introducing significant time delay into an optical system, beyond a few ps, necessitates slow-light waveguide structures that are extended in space, which measure typically  $10^{-4}$ – $10^{-2}$  m long in the case of PhC CCWs. We have been able to demonstrate a system comprising a record-high number of coupled cavities (at the time of publication), with a chain of 800 cavities that measures approximately 550  $\mu\text{m}$  in length. Achieving a functional device on that length scale necessitates fine control over cavity resonances from end-to-end, which translates physically into a strict requirement on the uniformity of the semiconductor layer, both in terms of thickness and optical properties, combined with precise patterning of the photonic crystal. With regard to patterning, state-of-the-art fabrication tools were used, and proximity effect correction has been accounted for to compensate for deviations in the target pattern exposure dose across the device. As for the layer uniformity of the SOI wafers, the thickness of Si was measured, and the thickness variation was found to be within 1 nm over 10 mm of length. The uniformity of the optical properties is the remaining factor and is indeed the challenging aspect of realizing the devices, especially in SOI layers.

SOI layers that are produced using the smart cut process are known to possess a non-negligible amount of residual stress [196]. The stress is generated due to the difference in thermal expansion coefficients between Si and  $\text{SiO}_2$ , following the thermal bonding step during wafer fabrication. When intact, the top Si layer exhibits tensile strain, while the opposite is true for the underlying  $\text{SiO}_2$  layer. Once the sacrificial  $\text{SiO}_2$  layer is wet-etched during the fabrication of the PhCs to suspend the Si membrane, compressive stress is generated in the suspended Si region with a profile that is increasing in magnitude away from the suspension edges [197]. When stress in the layer exceeds the critical buckling stress ( $\sigma_{\text{critical}}$ ), warping or buckling of the membrane occurs [198]. The threshold given by  $\sigma_{\text{critical}}$  scales with the inverse square of the length of the structure, and therefore, longer slabs are more prone to the effect. Buckling can be problematic for the fabrication of optical microstructures since the effective refractive index of the medium will be altered by the strain-induced bandgap variation and the photoelastic effect in general. Moreover, in the case of PhCs, the bending of the membrane tends to distort the PhC lattice, altering the lattice constant and hole size/ ellipticity, thereby reshaping the Brillouin zone in reciprocal space [199].

Buckling has been found to be a critical factor in the development of Si CCWs, directly influencing the optical response of the devices, whereby the measured bandwidth of the CCWs was notably reduced. Structurally, the profile of the layer deformation was observed through AFM and microscopic interferometry scans of Si CCW membranes that lacked suspension, the latter measurement displayed in Fig. 6.4.1 (c). Differential-interference contrast microscopy clearly reveals the buckling profile in the devices as shown in Fig. 6.4.1 (b), since this microscopy configuration is particularly sensitive to the optical path. Due to the dimensions of the implemented CCWs, the bending radius is higher along the propagation direction compared to that along the transverse axis, and it expectedly increases with the CCW length. The strongest deflection of the membrane however is found to occur near the edges of the suspension, which also happens to be where the W1-CCW light-injection point is located. The valley of the downward buckling is reached within a distance of approximately 25  $\mu\text{m}$  from the suspension edge, beyond which the PhC membrane remains relatively flat. The furthest downward deflection point that was observed in the membranes, relative to the surrounding bulk, was approximately 1  $\mu\text{m}$  away.

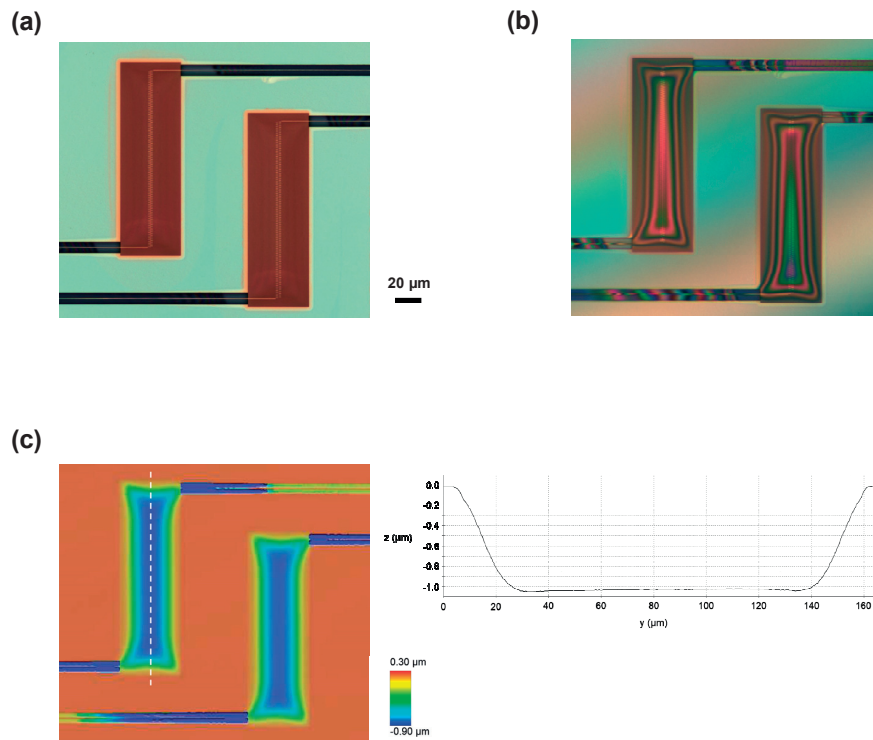


Fig. 6.4.1 (a) Bright-field microscopy image of suspended 200-cavity CCWs without nanotether support. (b) Differential-interference contrast microscopy image of the CCWs. (c) Interferometry-reconstructed depth profile of the CCWs. The lateral depth profile is displayed in the inset as indicated by the dashed line in the image.

The introduction of support nanotethers serves to alleviate the effects of residual stress in the suspended Si membrane. First, the device is isolated from bulk such that it is only contacted by support clamps, as displayed in Fig. 6.4.2. Second, the linking nanotethers function to accommodate the stress in the layer to prevent out-of-plane deflection of the PhC membrane. The reduced stiffness of the nanotethers has the capacity to relieve the stress in the layer through elastic deformation [198]. The implemented design was capable of limiting the deflection of the Si membrane to within 30 nm along the extent of the 200-cavity CCW, as shown in Fig. 6.4.2 (b).

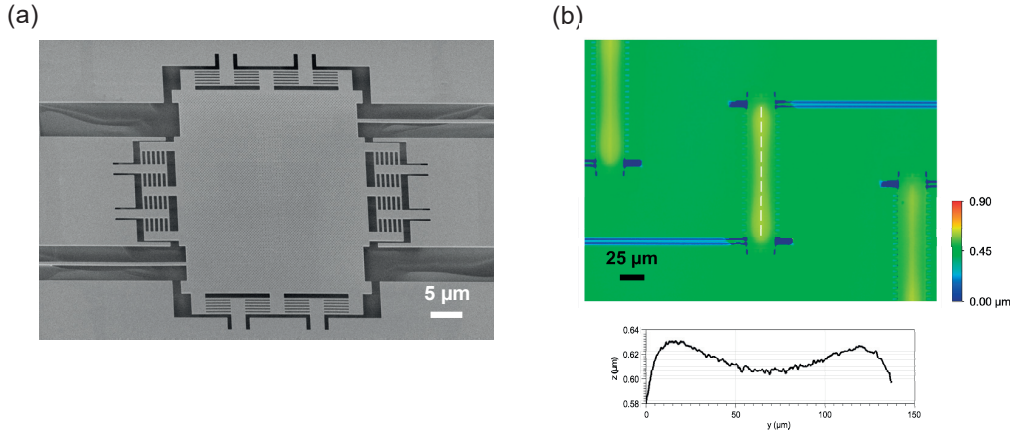


Fig. 6.4.2 (a) SEM micrograph displaying an oblique view of a 50-cavity CCW with the implemented support nanotethers. (b) Depth profile of a 200-cavity CCW reconstructed using interferometric optical microscopy. The height profile of the membrane along the white dashed line is displayed in the inset. (SEM micrograph acquired by Y. Lai)

### 6.4.1 Buckling-Induced Effects

In the presence of buckling in the Si layer, the dispersion response of the CCW becomes spatially non-uniform due to variation of the structural and optical properties of the PhC layer as a function of distance, along the propagation axis. This has been clearly observed through spatially-dependent Fourier-space imaging of the cavities in a device without nanotether support. Fig. 6.4.3 shows the acquired dispersion curves for an 800-cavity CCW, which were captured at near-equidistant spans along the propagation axis, in sequence from the entrance to the exit of the CCW. The dispersion curve is seen to red-shift in wavelength between the beginning and center of the device up to a value of 3.5 nm, before blue-shifting towards the end of the device back to a value close to that measured near the injection-point. The measured dispersion shift is stronger at the end-point acquisition ( $\Delta\lambda=-4.5$  nm) compared to the beginning ( $\Delta\lambda=-3.5$  nm) since the acquisition window at the end of the device was chosen to be closer to the suspension edge, where the compressive stress is higher. The stress profile is not necessarily symmetric with respect to the center of the device, as conveyed through the dispersion measurements here. This is due to inherent stress variations in the wafer and the nature of the wet-etching membrane release process.

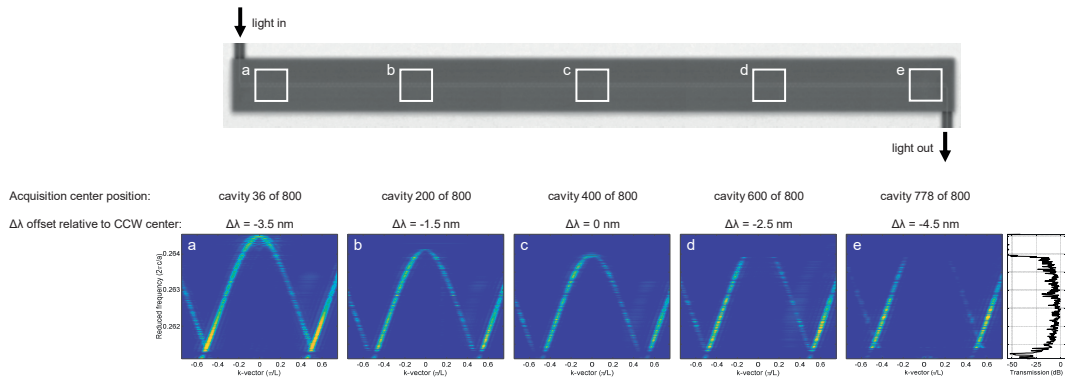


Fig. 6.4.3 Dispersion acquisition carried out on an 800-cavity CCW at five approximately equidistant locations along the CCW, centered around cavity number 36, 200, 400, 600, and 778, respectively, starting from the light injection point.

Looking at Fig. 6.4.3, the dispersion acquired near the out-coupling point of the CCW naturally matches the transmission spectrum, since the CCW operates above the light-line. By comparison with the dispersion at the injection point, CCW states near the high-frequency end are non-existent. A gradually rising attenuation is observed



from the center-frequency towards the high-frequency end as well. The behavior of light propagation in the device can be understood by tracing the frequency response along the device length. Light that is injected near the high-frequency end (at  $a/\lambda=0.2645$ ) is immediately localized/ scattered at the input of the CCW. At slightly lower frequency values (e.g.  $a/\lambda=0.2640$ ), light is coupled to a propagative mode at the input, yet as it travels through the CCW it experiences the aforementioned red-shifting of the dispersion, which imposes a progressive slow down on its group velocity as it moves towards the center of the device. It follows that the light wave will attenuate, primarily via scattering, according to the group index, as described in section 6.3.4. Since light (at  $a/\lambda=0.2640$ ) will approach the theoretical  $n_g=\infty$  point at the center of the CCW, it will attenuate entirely and consequently does not appear in the transmission spectrum either. An almost symmetric response can be seen from the center of the CCW towards the end, where the group velocity of light returns to its original value.

The effect of buckling-induced dispersion shifting is apparent on the transmission of the device. It leads to an additional cut-off region in the theoretical operation range of the CCW. The extent of the cut-off window scales with the magnitude of the dispersion translation, in addition to the degree of attenuation, and ergo, with the length of the device. Therefore, achieving extended CCW chains beyond  $10^{-4}$  m in length relies on the ability to produce uniform layers that can maintain their optical and structural properties.

An interesting proposition emerging out of the buckling observations pertains to the intentional modulation of the refractive index profile along a CCW, whether through deformation of the CCW membrane or by other means of refractive index control of Si, passively or actively, in such a manner to impose the desired dispersion on propagating light signals. For instance, an adiabatic transition of light towards the slow light regime can be achieved, possibly reducing the dominant scattering losses. Additionally, having spatial control over slow-light properties enables one to select the regions of interest along the waveguide where light-matter enhancement is desired, e.g. where emitters such as vacancy centers/ quantum dots are located or where nonlinear material is deposited. Other potential time-domain applications include: light pulse trapping, mediating pulse-pulse interactions, and pulse shaping in reduced geometries.

#### 6.4.2 Raman Spectroscopy

Micro-Raman spectroscopy measurements were carried out in order to assess the strain state of the fabricated structures. The Stokes shift of the longitudinal optical (LO) phonon mode of Si conveys the local stress value within the optically probed volume of the membrane, which is naturally diffraction limited when employing far-field excitation and detection. The sample was excited with a polarized laser beam at a wavelength of 532 nm, focused by a 100 $\times$ , 0.9 NA microscope objective down to a spot size with radius  $\approx$  360 nm. The scattered light was collected without polarization selection using a confocal detection configuration that employed an 1800 lines/mm grating, which provided a spectral resolution of 1.1  $\text{cm}^{-1}$ . The spectral peak position of the Raman shift was extracted with an accuracy of more than ten-fold beyond the spectral resolution limit through least squares fitting to a Lorentzian function [200], which is characteristic of the phonon line.

Spatial scans were performed to map the Raman scattering spectrum along the regions of interest. A step size of 500 nm was used, and each point was captured by averaging multiple runs with an integration time of 2 seconds each. The collected signal from the PhCs was notably higher than the surrounding bulk, which improved the fit accuracy of the Raman peak. The standard deviation of the measured Raman shift in the PhC region was 0.033  $\text{cm}^{-1}$  and 0.064  $\text{cm}^{-1}$  for the unsupported and supported CCW membranes, respectively.

The plot in Fig. 6.4.4 displays the acquired line scans along the length of a 200-cavity CCW (in the direction of the mode propagation), for each of the unsupported and supported CCW designs. The extracted Raman shift is seen to exhibit a pronounced spatial dependence for the unsupported membrane, within the PhC extent. Buckling is evidenced by the presence of tensile stress at the center of the membrane. This region would otherwise be under high compressive stress following membrane release [197], before the critical buckling stress that triggers the failure

state is reached. The Raman shift is found to translate by up to  $0.18 \text{ cm}^{-1}$  (corresponding to a stress variation of approximately 45 MPa) at the end of the membrane relative to the center. The increasing compressive stress towards the end of the suspended membrane indeed correlates with the observed spatial buckling profile obtained through the optical interferometric profilometry measurement.

In contrast, the Raman shift is found to be nearly constant along the length of the supported membrane, and the shift value matches that of a stress-free Si layer. This gives a clear indication that the stress profile is even along the entire CCW, and consequently the refractive index of the layer is uniform as well. It can be deduced that the stress that is normally present in the unsupported membrane has been accommodated by the supporting nanotethers of the improved design, which limits the out-of-plane deformation of the PhC slab to just a few nm.

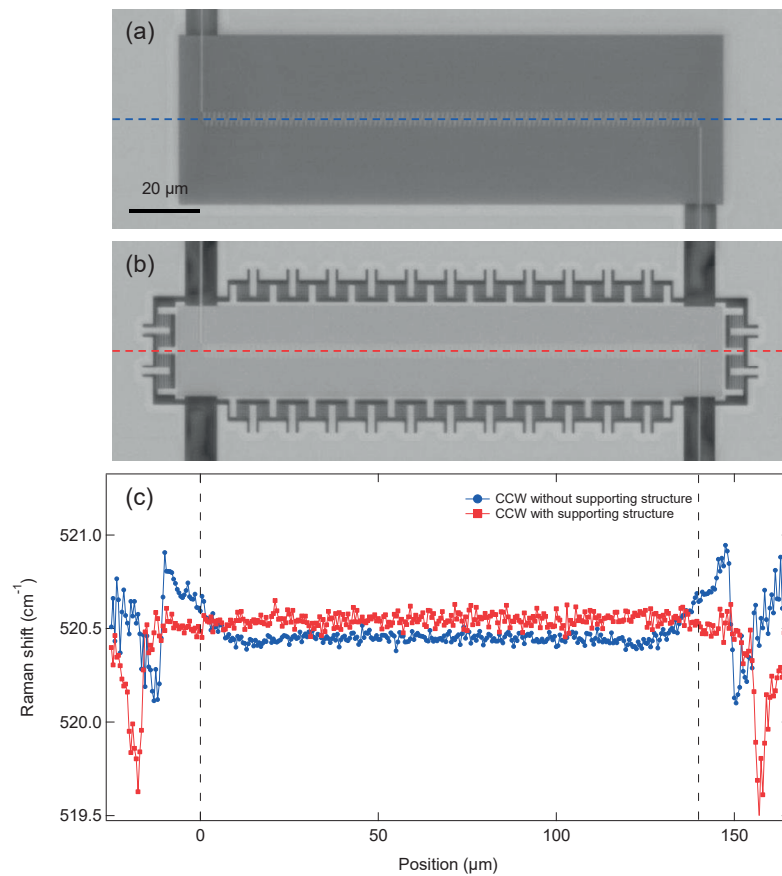


Fig. 6.4.4 Bright-field microscopy image of a 200-cavity CCW (a) without and (b) with nanotether support. (c) The corresponding Raman shift scans of the Si LO phonon along the propagation direction of the CCWs, indicated by a dashed line in (a) and (b). The dashed black line in (c) marks the extent of the CCW.

We carried out GME simulations to investigate the influence of the refractive index changes in the Si slab on the dispersion of the CCW, which is displayed in Fig. 6.4.5. In order to reach a spectral red shift of 5 nm at the employed design wavelength, which is typically observed in buckled CCW membranes, a refractive index change of  $1.2 \times 10^{-2}$  within the Si slab is necessary. Considering the stress variation of 45 MPa between the beginning and the center of a buckled membrane, one can extract the corresponding bandgap change in Si by accounting for the phonon deformation potential [201] and the stiffness tensor of Si [202], assuming biaxial tensile stress and an elastic response. The bandgap of Si is reduced as a result. Based on experimental strain-bandgap measurements in Si [203],

the bandgap change is estimated to be approximately 3 meV for the measured stress variation, and consequently, the refractive index change is deduced to be  $5 \times 10^{-4}$ . While the increasing refractive index value of Si towards the center of the CCW does resemble the trend of the simulated dispersion shift, the magnitude of the refractive index change is insufficiently small to solely reproduce it. It is therefore expected that alternative effects that originate from the PhC hole shape deformation or CCW proximity to the Si substrate, both induced by buckling, do primarily influence the dispersion dependence. The former is more likely to be the case as simulations indicate approximately a  $\Delta\lambda = 4$  nm shift per nm variation of the lattice constant, which is a feasible deformation value for the PhC lattice. Furthermore, the membrane-substrate separation with downward buckling was measured to be greater than  $2 \mu\text{m}$ , greatly reducing the interaction volume between the evanescent wave of the mode and the substrate.

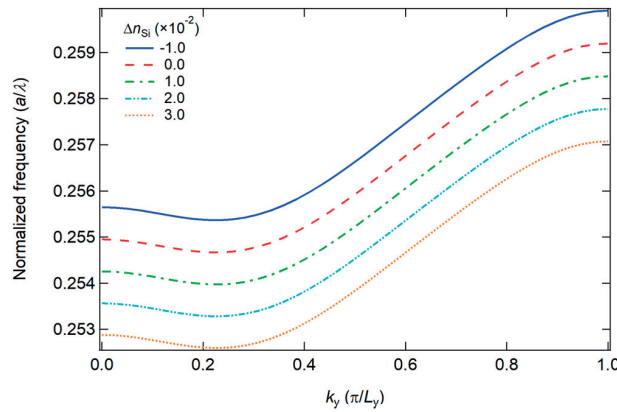


Fig. 6.4.5 GME simulation of the CCW dispersion as a function of change in the refractive index of the Si layer ( $\Delta n_{\text{Si}}$ ). The unmodified Si refractive index is considered to be 3.47 at the wavelength range of operation.

## 6.5 Summary

In this chapter, Si slow light devices based on a PhC coupled-cavity design were developed, and CCW chains of up to 800 cavities have been successfully realized. Amongst the existing slow light implementations, the presented devices achieved a record-high value for GBP, of up to 0.47. Fourier-space imaging was utilized for the characterization of the CCWs, assisting with the extraction of slow-light properties with high accuracy and spatial selectivity. Furthermore, light propagation regimes in the CCWs were identified, and the influence of both finite-size effects and disorder on slow light propagation was clarified. This helped identify the ideal device length as well as limitations on extended CCWs for state-of-the-art fabrication. Finally, the influence of membrane buckling on slow light propagation was elucidated through Raman spectroscopy of the layers, demonstrating how the operational bandwidth can be recovered in a homogeneous Si layer.



## 7. Conclusion and Outlook

The objective of this thesis was to explore applications of light confinement and nonlinear light-matter interaction in semiconductors that are suited for integrated optical circuits. Wide bandgap semiconductors, specifically III-nitrides, have been regarded as a promising material, especially for applications targeting nonlinear optical processes. A particular motivation has been to build a platform on Si which can bring all the outstanding properties of III-nitride semiconductors to the more widely adopted Si technology. The exploration of light-matter enhancement mechanisms was in line with our objective, whether by light confinement or slow light in optimized PhC geometries. The enhancement that is brought about due to the aforementioned mechanisms can reach several orders of magnitude, helping trigger certain optical processes which are primarily nonlinear in nature. Other linear optical functionalities may as well benefit from the field enhancement such as sensing for instance. This would contribute to the development of high-efficiency, compact, and low-power optical circuits.

Towards our objective, we have developed a fabrication process for III-nitride layers on Si, in a refined approach, which helped produce optical micro- and nanostructures of high quality in the semiconductor material. The primary limiting factors in the optical performance of the layers pertained to the properties introduced by the crystal growth technique. One of the main setbacks has been the high residual stress values emerging from heteroepitaxy, in excess of 1 GPa. This was successfully resolved through a combination of platform design and adapted fabrication. In comparison to earlier implementation [204] which suffered from crack formation, collapsing waveguides, and high scattering losses. The produced optical devices featured high stability without any notable degradation. This is combined with the record-low loss values obtained in suspended GaN membranes for both waveguides and microcavities. Another setback has been the inhomogeneity of the GaN on Si layer, added to the relatively high roughness of the AlN buffer-GaN interface. This issue is inherent to the implemented growth technique, and may be resolved in the future by advancing the growth methods. An existing alternative involves growing high-quality GaN on doped sacrificial III-nitride layers, and subsequently performing selective photo-electrochemical etching.

In the effort to develop optical devices, an experimental setup was designed and constructed to assist with the characterization of both near-IR and visible range integrated devices. The setup design is based on an end-fire coupling configuration suited for integrated optical circuits, which additionally supports far-field excitation. It features Fourier-space imaging capabilities that can be simultaneously operated in the near-IR and visible wavelength range. The Fourier-space imaging technique is particularly advantageous for the characterization of optical waveguides due to its effectiveness in directly acquiring and reconstructing the dispersion of optical structures. It has been successfully implemented within the scope of this thesis for the characterization of slow light PhC waveguides.

PhC cavities were first targeted for testing the efficacy of the developed GaN on Si platform. We have chosen to implement optimized PhC cavity designs to showcase the achievable light confinement in wide bandgap semiconductors, of moderate refractive index. Another objective was to investigate the nonlinear material response under enhanced light-matter interaction. The devices were successfully fabricated and characterized, yielding record-high Q-factor values for GaN cavities across the near-IR range, from  $\lambda=1300$  nm to 1550 nm. While the cavity Q-factors were more than an order of magnitude below the figures achievable in Si, the primary advantage was the transparency of the medium at shorter wavelengths. This has been the motivation for targeting frequency upconversion in the GaN layers. The optical confinement introduced by the cavities was sufficiently high to induce second- and third-order nonlinear processes under continuous-wave operation. Third harmonic generation was detected in GaN for the first time under continuous-wave operation. Moreover, the enhancement factors resulted

in the highest achievable conversion efficiency for second harmonic generation in GaN. The results are particularly promising as they indeed confirm that GaN can be employed for various on-chip nonlinear applications.

It is expected in the coming years that wide bandgap semiconductors will contribute greatly to integrated optical networks. The feasibility of building high quality devices in III-nitrides on Si has been demonstrated throughout this thesis. With further advance in growth technology, GaN- and AlN-based integrated optical circuits can reach the point of market transfer and adoption, as they are already contributing significantly to light-emitting devices. Concerning applications of nonlinear optics, the demonstrated second-order nonlinearity in GaN can be exploited for applications in classical and quantum optics, including parametric spontaneous down-conversion for the generation of non-classical light. A microring-based mechanism has been shown to achieve photon-pair generation at MHz rates [205], utilizing sputtered AlN layers. A PhC cavity-based design featuring dual resonance can contribute greatly to the enhancement factors needed to efficiently generate such a process. By utilizing epitaxial layers, frequency conversion can be attained from integrated quantum emitters such as quantum dots or color centers. Furthermore, the third-order order nonlinearity in III-nitrides can provide for a range of nonlinear processes including the generation of optical frequency combs, which on an integrated platform can find applications in metrology, sensing, and communication.

We have additionally pursued integrated light-matter enhancement approaches through the study of slow light. Given that slow light is particularly susceptible to disorder, we have opted for Si, the most mature technology amongst semiconductors. An optimized photonic crystal slow light waveguide design was implemented, based on a coupled-cavity scheme. Theoretically, the design offered unprecedented values for performance parameters, namely bandwidth and group index-bandwidth product, in slow light PhC devices. The experimental development was assisted by the Fourier-space imaging characterization technique, which enabled the successful realization of the theoretical designs, leading to the demonstration of the largest group index-bandwidth product values in slow light devices to date. In addition to that, a record number of coupled cavities was achieved creating waveguides that extend beyond 500  $\mu\text{m}$ .

The reconstructed dispersion maps of the devices, through Fourier-space imaging, served to study slow light properties in the presence of disorder. This was combined with a length dependence study to identify finite-size effects, since the behavior of a coupled-cavity system is known to follow a tight-binding description. Deviation from the ideal theoretical response was analyzed and attributed to disorder-induced effects, with notable contribution to scattering loss channels. Such losses have been found to severely limit the propagation extent of slow light, especially towards higher slow-down factors. Light propagation regimes were identified, confirming that the pre-selected slow-down factor for the implemented devices indeed falls within the dispersive regime. The obtained results serve to identify current limitations on the implementation of slow light devices, in view of the disorder figure imposed by the existing fabrication technology.

The obtained results on slow light in Si are particularly motivating as they demonstrate the potential of design optimization for building devices with superior performance. The extent of slow light propagation is certainly limited by physical mechanisms. On a positive note however, such mechanisms emerge from a fabrication-induced effect, that is disorder, which will progressively scale down with future advances in fabrication. Approaches based on topological protection, presenting immunity to backscattering in unidirectional waveguides [206], are currently being pursued to overcome this obstacle, in the meantime. Concerning the physical limit on the achievable delay-bandwidth product in static systems, breaking Lorentz reciprocity offers an alternative approach, which may be implemented in the future through dynamic time modulation or the application of magnetic fields for instance [161]. The obtained slow-down factor in the devices is nevertheless appreciable, features a high group-index bandwidth product, and extends over the length of a few hundred microns, which is sufficient for many

## 7. Conclusion and Outlook

---

applications including slow-light enhanced frequency conversion [9], slow-light based interferometers [207], as well as for pulse compression [208] and temporal soliton formation [209].





# Appendix A: Perturbation Theory Derivation of the Nonlinear Coupling Coefficient

The following derivation is based on coupled-mode theory presented in [42], and cavity analysis in [44]. It is known through perturbation theory that to the first-order, the frequency shift due to a perturbation ( $\Delta V$ ) applied to a wavefunction ( $\psi$ ) can be expressed as [42]:

$$\Delta\omega \approx \frac{\langle\psi|V|\psi\rangle}{\langle\psi|\psi\rangle} \quad (A.1)$$

Carrying the above expression on to optical systems, the perturbation of a mode frequency  $\Delta\omega$  due a perturbation in the electric permittivity  $\Delta\varepsilon$ , to the first order, is given by [16]:

$$\Delta\omega \approx -\frac{\omega}{2} \frac{\int_{-\infty}^{\infty} \Delta\varepsilon |\mathbf{E}|^2 d^3\mathbf{r}}{\int_{-\infty}^{\infty} \varepsilon |\mathbf{E}|^2 d^3\mathbf{r}} \quad (A.2)$$

In a similar sense to the quantum mechanical approach, such approximation is only valid in the limit of weak perturbation, i.e.  $\frac{|\Delta\varepsilon|}{\varepsilon} \ll 1$ . The definition of dielectric permittivity perturbation may as well be extended to higher order susceptibility terms, *i.e.* nonlinear contributions, since the magnitude of the perturbation satisfies the aforementioned condition. The frequency perturbation can then be expressed as:

$$\Delta\omega \approx -\frac{\omega}{2} \frac{\int_{-\infty}^{\infty} \mathbf{E}^* \cdot \Delta\mathbf{P} d^3\mathbf{r}}{\int_{-\infty}^{\infty} \varepsilon |\mathbf{E}|^2 d^3\mathbf{r}} \quad (A.3)$$

Considering a polarization perturbation due to the second-order nonlinearity:

$$\Delta\mathbf{P} = \mathbf{P}^{(2)} = \varepsilon_0 \chi_{ijk}^{(2)} E_j E_k \quad (A.4)$$

To adapt the perturbation expression to the coupled mode equations, an amplitude time dependence is introduced to the fields. This is valid through the slowly-varying envelope approximation, where each field is multiplied by a factor of  $\frac{a_n(t)}{\sqrt{\int_{-\infty}^{\infty} \varepsilon |\mathbf{E}|^2 d^3\mathbf{r}}}$ , consisting of a slowly-varying amplitude  $a_n(t)$  and a normalization factor for the mode in the denominator. For a total field comprising two oscillating frequency components  $\omega_0$  and  $\omega_1$ , where  $\omega_1 = 2\omega_0$ , the frequency perturbations can be computed (at their respective frequencies), considering conservation of energy constraints and applying the rotating-wave approximation:

$$\Delta\omega_0 \approx -\frac{\omega_0}{4} \frac{\int_{-\infty}^{\infty} \sum_{ijk} \varepsilon_0 \chi_{ijk}^{(2)} E_{0i}^* (E_{1j} E_{0k}^* + E_{0j}^* E_{1k}) d^3\mathbf{r} a_0^* a_0 a_1}{\left( \int_{-\infty}^{\infty} \varepsilon |\mathbf{E}_0|^2 d^3\mathbf{r} \right) \left( \int_{-\infty}^{\infty} \varepsilon |\mathbf{E}_0|^2 d^3\mathbf{r} \right) \left( \sqrt{\int_{-\infty}^{\infty} \varepsilon |\mathbf{E}_1|^2 d^3\mathbf{r}} \right)} \quad (\text{A.5})$$

$$\Delta\omega_1 \approx -\frac{\omega_1}{4} \frac{\int_{-\infty}^{\infty} \sum_{ijk} \varepsilon_0 \chi_{ijk}^{(2)} E_{1i}^* (E_{0j} E_{0k}) d^3\mathbf{r} a_1^* a_0 a_0}{\left( \int_{-\infty}^{\infty} \varepsilon |\mathbf{E}_1|^2 d^3\mathbf{r} \right) \left( \int_{-\infty}^{\infty} \varepsilon |\mathbf{E}_0|^2 d^3\mathbf{r} \right) \left( \sqrt{\int_{-\infty}^{\infty} \varepsilon |\mathbf{E}_1|^2 d^3\mathbf{r}} \right)} \quad (\text{A.6})$$

The above frequency perturbations are then introduced to the unperturbed coupled mode equations (2.3.12) and (2.3.13), where the second-order nonlinear coupling coefficients are deduced to be:

$$\beta_{\chi^{(2)},PDC} = \frac{1}{4} \frac{\int_{-\infty}^{\infty} \sum_{ijk} \varepsilon_0 \chi_{ijk}^{(2)} (E_{0i}^* E_{1j} E_{0k}^* + E_{0i}^* E_{0j}^* E_{1k}) d^3\mathbf{r}}{\left( \int_{-\infty}^{\infty} \varepsilon |\mathbf{E}_0|^2 d^3\mathbf{r} \right) \left( \sqrt{\int_{-\infty}^{\infty} \varepsilon |\mathbf{E}_1|^2 d^3\mathbf{r}} \right)} \quad (\text{A.7})$$

$$\beta_{\chi^{(2)},SHG} = \frac{1}{4} \frac{\int_{-\infty}^{\infty} \sum_{ijk} \varepsilon_0 \chi_{ijk}^{(2)} E_{1i}^* E_{0j} E_{0k} d^3\mathbf{r}}{\left( \int_{-\infty}^{\infty} \varepsilon |\mathbf{E}_0|^2 d^3\mathbf{r} \right) \left( \sqrt{\int_{-\infty}^{\infty} \varepsilon |\mathbf{E}_1|^2 d^3\mathbf{r}} \right)} \quad (\text{A.8})$$

# Appendix B: Derivation of the Coupled-Cavity Waveguide Dispersion According to the Tight-Binding Model

The dispersion of the CCW can be derived using the tight-binding model, starting with the time-independent Schrödinger equation. The analysis of an optical mode of a CCW system is carried out in analogy to the case of an electron in a superlattice potential, as described in [174], where the Hamiltonian operator is given by:

$$\hat{H} = \frac{\hat{p}^2}{2m} + V_\infty + \sum_n \Delta V_n(r) \quad (B.1)$$

Here, the potential energy of the system is described by a background potential ( $V_\infty$ ) and a contribution of each potential well in the lattice through the  $\Delta V_n(r)$  term. The time-independent Schrödinger equation for the electron wavefunction ( $\psi$ ) is then:

$$\hat{H}|\psi\rangle = \mathcal{E}|\psi\rangle \quad (B.2)$$

In the case of CCWs, the analogous optical-field analysis implies that the electron wavefunction is replaced by the magnetic field of the optical mode. The equivalent of the background potential is the native PhC lattice dielectric modulation ( $\Delta\epsilon_{PhC}$ ), while the dielectric modulation of each of the cavities in the system ( $\Delta\epsilon_{cavity}$ ) is representative of the quantum-well potential energy modulation in a superlattice. The dielectric modulation operators naturally take on a different form, which is derived from the master equation in section 2.1.2:

$$\hat{\Theta}_{PhC} = \nabla \times \left( \frac{1}{\epsilon_{PhC}} \nabla \times \right) \quad (B.3)$$

$$\hat{\Theta}_{cavity} = \nabla \times \left( \frac{1}{\epsilon_{cavity}} \nabla \times \right) \quad (B.4)$$

The CCW state can be expressed as a superposition of the single-cavity states, through the amplitude of the magnetic field ( $\mathbf{H}$ ):

$$|\mathbf{H}\rangle = \sum_n c_n |\mathbf{H}_n\rangle \quad (B.5)$$

where  $n$  is the cavity index and accounting for only a single cavity mode.

The equivalent to the time-independent Schrödinger equation can then be expressed by the following eigenvalue equation for the magnetic field:

$$\widehat{\Theta}|\mathbf{H}\rangle = \mathcal{E}|\mathbf{H}\rangle \quad (\text{B.6})$$

$$\widehat{\Theta}_{PhC}|\mathbf{H}\rangle + \sum_m \widehat{\Theta}_{cavity}|\mathbf{H}\rangle = \mathcal{E}|\mathbf{H}\rangle \quad (\text{B.7})$$

Substituting with equation (B.5), and projecting on a single-cavity mode  $|\mathbf{H}_i\rangle$ :

$$\langle \mathbf{H}_i | \widehat{\Theta}_{PhC} + \sum_m \widehat{\Theta}_{cavity, m} | \sum_n c_n \mathbf{H}_n \rangle = \mathcal{E} \langle \mathbf{H}_i | \sum_n c_n \mathbf{H}_n \rangle \quad (\text{B.8})$$

Accounting for first- and second-neighbor interactions ( $i = \pm 1, \pm 2$ ), the eigenvalue equation can be expressed as:

$$\begin{aligned} & c_i \left(\frac{\omega}{c}\right)^2 + c_{i-1} \left(\frac{\omega}{c}\right)^2 R_1^- + c_{i+1} \left(\frac{\omega}{c}\right)^2 R_1^+ + c_{i-2} \left(\frac{\omega}{c}\right)^2 R_2^- + c_{i+2} \left(\frac{\omega}{c}\right)^2 R_2^+ \\ & + c_i S + c_{i-1} T_1^- + c_{i+1} T_1^+ + c_{i-2} T_2^- + c_{i+2} T_2^+ \\ & = \mathcal{E} [c_i + c_{i-1} R_1^- + c_{i+1} R_1^+ + c_{i-2} R_2^- + c_{i+2} R_2^+] \end{aligned} \quad (\text{B.9})$$

where the overlap ( $R_m^\pm$ ), shift ( $S$ ), and transfer ( $T_m^\pm$ ) integrals are defined as:

$$R_1^\mp = \langle \mathbf{H}_i | \mathbf{H}_{i\mp 1} \rangle \quad (\text{B.10})$$

$$R_2^\mp = \langle \mathbf{H}_i | \mathbf{H}_{i\mp 2} \rangle \quad (\text{B.11})$$

$$S = \langle \mathbf{H}_i | \widehat{\Theta}_{cavity, m-1} + \widehat{\Theta}_{cavity, m+1} + \widehat{\Theta}_{cavity, m-2} + \widehat{\Theta}_{cavity, m+2} | \mathbf{H}_i \rangle \quad (\text{B.12})$$

$$T_1^\mp = \langle \mathbf{H}_i | \widehat{\Theta}_{cavity, m\mp 1} + \widehat{\Theta}_{cavity, m\mp 2} | \mathbf{H}_{i\mp 1} \rangle \quad (\text{B.13})$$

$$T_2^\mp = \langle \mathbf{H}_i | \widehat{\Theta}_{cavity, m\mp 1} + \widehat{\Theta}_{cavity, m\mp 2} | \mathbf{H}_{i\mp 2} \rangle \quad (\text{B.14})$$

The eigenvalue equation can be reduced to:

$$\begin{aligned} & c_i (E + S) + c_{i-1} (E R_1^- + T_1^-) + c_{i+1} (E R_1^+ + T_1^+) + c_{i-2} (E R_2^- + T_2^-) \\ & + c_{i+2} (E R_2^+ + T_2^+) \\ & = \mathcal{E} [c_i + c_{i-1} R_1^- + c_{i+1} R_1^+ + c_{i-2} R_2^- + c_{i+2} R_2^+] \end{aligned} \quad (\text{B.15})$$

where  $E = \left(\frac{\omega}{c}\right)^2$

By virtue of the CCW periodicity  $\widehat{\Theta}_{cavity}(\mathbf{r}) = \widehat{\Theta}_{cavity, m}(\mathbf{r} + m \cdot \mathbf{L})$ , the magnetic field is likewise periodic  $\mathbf{H}(\mathbf{r}) = \mathbf{H}(\mathbf{r} + m \cdot \mathbf{L})$ , where  $L$  is the cavity separation distance. We can then invoke Bloch's theorem and substitute in the eigenvalue equation:

$$\begin{aligned}
 c_0[E + S + e^{-ikL}(ER_1^- + T_1^-) + e^{ikL}(ER_1^+ + T_1^+) + e^{-2ikL}(ER_2^- + T_2^-) \\
 + e^{2ikL}(ER_2^+ + T_2^+)] \\
 = c_0\mathcal{E}[1 + e^{-ikL}R_1^- + e^{ikL}R_1^+ + e^{-2ikL}R_2^- + e^{2ikL}R_2^+] \quad (B.16)
 \end{aligned}$$

For an eigenstate in a symmetric potential,  $R_m^- = R_m^+ = R_m$  and  $T_m^- = T_m^+ = T_m$ , and the above expression simplifies to:

$$\begin{aligned}
 E + S + 2ER_1 \cos(kL) + 2ER_2 \cos(2 \cdot kL) + 2T_1 \cos(kL) + 2T_2 \cos(2 \cdot kL) \\
 = \mathcal{E}[1 + 2R_1 \cos(kL) + 2R_2 \cos(2 \cdot kL)] \quad (B.17)
 \end{aligned}$$

The dispersive energy relation, accounting for two-neighbor coupling, can therefore be stated as:

$$\mathcal{E}(k) = E + \frac{S + 2T_1 \cos(kL) + 2T_2 \cos(2 \cdot kL)}{1 + 2R_1 \cos(kL) + 2R_2 \cos(2 \cdot kL)} \quad (B.18)$$

This statement can be generalized to m-neighbor coupling, where the S, T, and R integrals are adjusted accordingly:

$$\mathcal{E}(k) = E + \frac{S + 2 \sum_m T_m \cos(mkL)}{1 + 2 \sum_m R_m \cos(mkL)} \quad (B.19)$$



# Bibliography

- [1] S. John, "Strong localization of photons in certain disordered dielectric superlattices," *Phys. Rev. Lett.*, vol. 58, no. 23, 1987.
- [2] S. John, "Electromagnetic absorption in a disordered medium near a photon mobility edge," *Phys. Rev. Lett.*, vol. 53, no. 22, pp. 2169–2172, 1984.
- [3] E. Yablonovitch, "Inhibited spontaneous emission in solid-state physics and electronics," *Phys. Rev. Lett.*, vol. 58, no. 20, pp. 2059–2062, 1987.
- [4] T. Yoshle *et al.*, "Vacuum Rabi splitting with a single quantum dot in a photonic crystal nanocavity," *Nature*, vol. 432, no. 7014, pp. 200–203, 2004.
- [5] M. Boroditsky, R. Vrijen, T. F. Krauss, R. Coccioli, R. Bhat, and E. Yablonovitch, "Spontaneous emission extraction and Purcell enhancement from thin-film 2-D photonic crystals," *J. Light. Technol.*, vol. 17, no. 11, pp. 2096–2112, 1999.
- [6] H. Altug, D. Englund, and J. Vučković, "Ultrafast photonic crystal nanocavity laser," *Nat. Phys.*, vol. 2, no. 7, pp. 484–488, 2006.
- [7] Y. Terada, K. Kondo, R. Abe, and T. Baba, "Full C-band Si photonic crystal waveguide modulator," *Opt. Lett.*, vol. 42, no. 24, p. 5110, 2017.
- [8] G. Shambat *et al.*, "Single-cell photonic nanocavity probes," *Nano Lett.*, vol. 13, no. 11, pp. 4999–5005, 2013.
- [9] B. Corcoran *et al.*, "Green light emission in silicon through slow-light enhanced third-harmonic generation in photonic-crystal waveguides," *Nat. Photonics*, vol. 3, no. 4, pp. 206–210, 2009.
- [10] K. Nozaki *et al.*, "Sub-femtojoule all-optical switching using a photonic-crystal nanocavity," *Nat. Photonics*, vol. 4, no. 7, pp. 477–483, 2010.
- [11] T. Tanabe, M. Notomi, E. Kuramochi, A. Shinya, and H. Taniyama, "Trapping and delaying photons for one nanosecond in an ultrasmall high-Q photonic-crystal nanocavity," *Nat. Photonics*, vol. 1, no. 1, pp. 49–52, 2007.
- [12] M. Minkov and V. Savona, "Wide-band slow light in compact photonic crystal coupled-cavity waveguides," *Optica*, vol. 2, no. 7, pp. 631–634, 2015.
- [13] R. Shankar, *Principles of Quantum Mechanics*, Second. Boston, MA: Springer US, 1994.
- [14] C. Kittel, *Introduction to Solid State Physics*, 8th ed. Wiley, 2004.
- [15] L. C. Andreani and D. Gerace, "Photonic-crystal slabs with a triangular lattice of triangular holes investigated using a guided-mode expansion method," *Phys. Rev. B - Condens. Matter Mater. Phys.*, vol. 73, pp. 1–16, 2006.
- [16] J. D. Joannopoulos, S. G. Johnson, J. N. Winn, and R. D. Meade, *Photonic Crystals: Molding the Flow of Light*, Second. Princeton University Press, 2008.
- [17] Z. Zhang and M. Qiu, "Small-volume waveguide-section high Q microcavities in 2D photonic crystal slabs," *Opt. Express*, vol. 12, no. 17, pp. 3988–3995, 2004.
- [18] H. Y. Ryu, M. Notomi, and Y. H. Lee, "High-quality-factor and small-mode-volume hexapole modes in photonic-crystal-slab nanocavities," *Appl. Phys. Lett.*, vol. 83, no. 21, pp. 4294–4296, 2003.
- [19] Y. Akahane, T. Asano, B. Song, and S. Noda, "High-Q photonic nanocavity in a two-dimensional photonic crystal," *Nature*, vol. 425, no. 6961, pp. 944–947, Oct. 2003.
- [20] M. Notomi, A. Shinya, S. Mitsugi, E. Kuramochi, and H. Ryu, "Waveguides, resonators and their coupled

- elements in photonic crystal slabs," *Opt. Express*, vol. 12, no. 8, p. 1551, 2004.
- [21] E. Kuramochi, M. Notomi, S. Mitsugi, A. Shinya, T. Tanabe, and T. Watanabe, "Ultra-high-Q photonic crystal nanocavities realized by the local width modulation of a line defect," *Appl. Phys. Lett.*, vol. 88, no. 4, p. 41112, 2006.
- [22] B.-S. Song, S. Noda, T. Asano, and Y. Akahane, "Ultra-high-Q photonic double-heterostructure nanocavity," *Nat. Mater.*, vol. 4, no. 3, pp. 207–210, 2005.
- [23] Y. Tanaka, T. Asano, and S. Noda, "Design of photonic crystal nanocavity with Q-factor of  $\sim 10^9$ ," *J. Light. Technol.*, vol. 26, no. 11, pp. 1532–1539, 2008.
- [24] J. S. Foresi *et al.*, "Photonic-bandgap microcavities in optical waveguides," *Nature*, vol. 390, no. 6656, pp. 143–145, 1997.
- [25] P. B. Deotare, M. W. McCutcheon, I. W. Frank, M. Khan, and M. Lončar, "High quality factor photonic crystal nanobeam cavities," *Appl. Phys. Lett.*, vol. 94, no. 12, pp. 10–13, 2009.
- [26] E. M. Purcell, "Spontaneous emission probabilities at radio frequencies," *Phys. Rev.*, vol. 69, pp. 674–674, 1946.
- [27] H. J. Kimble, "Strong interactions of single atoms and photons in cavity QED," *Phys. Scr.*, vol. T76, no. 1, p. 127, 1998.
- [28] L. Collot, V. Lefèvre-Seguin, M. Brune, J. M. Raimond, and S. Haroche, "Very high-Q whispering-gallery mode resonances observed on fused silica microspheres," *Europhys. Lett.*, vol. 23, no. 5, pp. 327–334, 1993.
- [29] P. T. Kristensen, C. Van Vlack, and S. Hughes, "Generalized effective mode volume for leaky optical cavities," *Opt. Lett.*, vol. 37, no. 10, p. 1649, 2012.
- [30] H. Aoki, "Critical behaviour of extended states in disordered systems," *J. Phys. C Solid State Phys.*, vol. 16, no. 6, 1983.
- [31] M. Schreiber, "Fractal character of eigenstates in weakly disordered three-dimensional systems," *Phys. Rev. B*, vol. 31, no. 9, pp. 6146–6149, 1985.
- [32] R. C. Powell, *Symmetry, Group Theory, and the Physical Properties of Crystals*, vol. 824. New York, NY: Springer New York, 2010.
- [33] S. G. Johnson, S. Fan, A. Mekis, and J. D. Joannopoulos, "Multipole-cancellation mechanism for high-Q cavities in the absence of a complete photonic band gap," *Appl. Phys. Lett.*, vol. 78, no. 22, p. 3388, 2001.
- [34] J. Geremia, J. Williams, and H. Mabuchi, "Inverse-problem approach to designing photonic crystals for cavity QED experiments," *Phys. Rev. E*, vol. 66, no. 6, p. 66606, 2002.
- [35] D. Englund, I. Fushman, and J. Vucković, "General recipe for designing photonic crystal cavities," *Opt. Express*, vol. 13, no. 16, pp. 5961–5975, 2005.
- [36] T. Nakamura, Y. Takahashi, Y. Tanaka, T. Asano, and S. Noda, "Improvement in the quality factors for photonic crystal nanocavities via visualization of the leaky components," *Opt. Express*, vol. 24, no. 9, p. 9541, 2016.
- [37] M. Minkov and V. Savona, "Automated optimization of photonic crystal slab cavities," *Sci. Rep.*, vol. 4, p. 5124, 2014.
- [38] R. W. Boyd, *Nonlinear Optics*, Third. Burlington: Academic Press, 2008.
- [39] D. A. B. Miller, *Quantum Mechanics for Scientists and Engineers*. Cambridge: Cambridge University Press, 2008.
- [40] E. G. Sauter, *Nonlinear Optics*. New York: Wiley, 1996.
- [41] S. Mukamel, *Principles of Nonlinear Optical Spectroscopy*. New York: Oxford University Press, 1995.
- [42] H. A. Haus, *Waves and Fields in Optoelectronics*. New Jersey: Prentice Hall, 1984.



- [43] S. Fan, W. Suh, and J. D. Joannopoulos, "Temporal coupled-mode theory for the Fano resonance in optical resonators," *J. Opt. Soc. Am. A*, vol. 20, no. 3, pp. 569–572, 2003.
- [44] A. Rodriguez, M. Soljacic, J. D. Joannopoulos, and S. G. Johnson, "Chi<sub>2</sub> and chi<sub>3</sub> harmonic generation at a critical power in inhomogeneous doubly resonant cavities," *Opt. Express*, vol. 15, no. 12, p. 7303, 2007.
- [45] K. Rivoire, Z. Lin, F. Hatami, W. T. Masselink, and J. Vucković, "Second harmonic generation in gallium phosphide photonic crystal nanocavities with ultralow continuous wave pump power," *Opt. Express*, vol. 17, no. 25, pp. 22609–15, 2009.
- [46] M. Galli *et al.*, "Low-power continuous-wave generation of visible harmonics in silicon photonic crystal nanocavities," *Opt. Express*, vol. 18, no. 25, pp. 26613–24, 2010.
- [47] D. Néel *et al.*, "AlN photonic crystal nanocavities realized by epitaxial conformal growth on nanopatterned silicon substrate," *Appl. Phys. Lett.*, vol. 98, no. 26, p. 261106, 2011.
- [48] Y. A. Vlasov, X. Z. Bo, J. C. Sturm, and D. J. Norris, "On-chip natural assembly of silicon photonic bandgap crystals," *Nature*, vol. 414, no. 6861, pp. 289–293, 2001.
- [49] K. Aoki *et al.*, "Microassembly of semiconductor three-dimensional photonic crystals," *Nat. Mater.*, vol. 2, no. 2, pp. 117–121, 2003.
- [50] M. Campbell, D. N. Sharp, M. T. Harrison, R. G. Denning, and A. J. Turberfield, "Fabrication of photonic crystals for the visible spectrum by holographic lithography," *Nature*, vol. 404, no. 6773, pp. 53–56, Mar. 2000.
- [51] D.-H. Kim *et al.*, "Enhanced light extraction from GaN-based light-emitting diodes with holographically generated two-dimensional photonic crystal patterns," *Appl. Phys. Lett.*, vol. 87, no. 20, p. 203508, 2005.
- [52] M. Qi *et al.*, "A three-dimensional optical photonic crystal with designed point defects," *Nature*, vol. 429, no. 6991, pp. 538–542, Jun. 2004.
- [53] G. Subramania, Q. Li, Y.-J. Lee, J. J. Figiel, G. T. Wang, and A. J. Fischer, "Gallium nitride based logpile photonic crystals," *Nano Lett.*, vol. 11, no. 11, pp. 4591–6, 2011.
- [54] E. C. Nelson *et al.*, "Epitaxial growth of three-dimensionally architected optoelectronic devices," *Nat. Mater.*, vol. 10, no. 9, pp. 676–81, 2011.
- [55] J. Lee *et al.*, "Dry etching of GaN and related materials: comparison of techniques," *IEEE J. Sel. Top. Quantum Electron.*, vol. 4, no. 3, pp. 557–562, 1998.
- [56] D. Zhuang and J. H. Edgar, "Wet etching of GaN, AlN, and SiC: a review," *Mater. Sci. Eng. R Reports*, vol. 48, no. 1, pp. 1–46, 2005.
- [57] S. Sergent, M. Arita, S. Kako, S. Iwamoto, and Y. Arakawa, "High-Q (>5000) AlN nanobeam photonic crystal cavity embedding GaN quantum dots," *Appl. Phys. Lett.*, vol. 100, no. 12, p. 121103, 2012.
- [58] E. D. Haberer, R. Sharma, A. R. Stonas, S. Nakamura, S. P. Denbaars, and E. L. Hu, "Removal of thick (>100 nm) InGa<sub>N</sub> layers for optical devices using band-gap-selective photoelectrochemical etching," *Appl. Phys. Lett.*, vol. 85, no. 5, pp. 762–764, 2004.
- [59] S. Sergent, M. Arita, S. Kako, K. Tanabe, S. Iwamoto, and Y. Arakawa, "High-Q AlN photonic crystal nanobeam cavities fabricated by layer transfer," *Appl. Phys. Lett.*, vol. 101, no. 10, p. 101106, 2012.
- [60] J. W. Chung, E. L. Piner, and T. Palacios, "N-face GaN/AlGa<sub>N</sub> HEMTs fabricated through layer transfer technology," *IEEE Electron Device Lett.*, vol. 30, no. 2, pp. 113–116, 2009.
- [61] J. W. Chung, J. Lee, E. L. Piner, and T. Palacios, "Seamless on-wafer integration of GaN HEMTs and Si(100) MOSFETs," in *IEEE Electron Device Letters*, 2009, vol. 30, no. 10, pp. 155–156.
- [62] T. K. Zywiets, J. Neugebauer, and M. Scheffler, "The adsorption of oxygen at GaN surfaces," *Appl. Phys. Lett.*, vol. 74, no. 12, pp. 1695–1697, 1999.
- [63] T. Hashizume, R. Nakasaki, S. Ootomo, S. Oyama, and H. Hasegawa, "Surface characterization of GaN and

- AlGaIn layers grown by MOVPE," *Mater. Sci. Eng. B*, vol. 80, pp. 309–312, 2001.
- [64] Y. Ooka, T. Tetsumoto, A. Fushimi, W. Yoshiki, and T. Tanabe, "CMOS compatible high-Q photonic crystal nanocavity fabricated with photolithography on silicon photonic platform," *Sci. Rep.*, vol. 5, no. 1, p. 11312, Sep. 2015.
- [65] A. N. Hattori *et al.*, "Chemical etchant dependence of surface structure and morphology on GaN(0001) substrates," *Surf. Sci.*, vol. 604, no. 15–16, pp. 1247–1253, 2010.
- [66] T. G. G. Maffei, M. C. Simmonds, S. A. Clark, F. Peiro, P. Haines, and P. J. Parbrook, "Influence of premetallization surface treatment on the formation of Schottky Au-nGaIn contacts," *J. Appl. Phys.*, vol. 92, no. 6, pp. 3179–3186, 2002.
- [67] G. Dhanaraj, K. Byrappa, V. Prasad, and M. Dudley, Eds., *Springer Handbook of Crystal Growth*. Berlin, Heidelberg: Springer Berlin Heidelberg, 2010.
- [68] D. Ehrentraut, E. Meissner, and M. Bockowski, Eds., *Technology of Gallium Nitride Crystal Growth*, vol. 133. Berlin, Heidelberg: Springer Berlin Heidelberg, 2010.
- [69] A. Watanabe, T. Takeuchi, K. Hirose, H. Amano, K. Hiramatsu, and I. Akasaki, "The growth of single crystalline GaIn on a Si substrate using AlN as an intermediate layer," *J. Cryst. Growth*, vol. 128, no. 1–4, pp. 391–396, 1993.
- [70] B. Krishnan *et al.*, "Growth of Al<sub>x</sub>Ga<sub>1-x</sub>In structures on 8 in. Si (111) substrates," *Sensors Mater.*, vol. 25, no. 3, pp. 205–217, 2013.
- [71] H. Morkoç, *Handbook of Nitride Semiconductors and Devices*. Weinheim, Germany: Wiley-VCH Verlag GmbH & Co. KGaA, 2008.
- [72] U. Bergmann, V. Reimer, and B. Atakan, "An experimental study of the reactions of trimethylgallium with ammonia and water over a wide temperature range," *Phys. Chem. Chem. Phys.*, vol. 1, no. 24, p. 5593, 1999.
- [73] G. A. Slack, L. J. Schowalter, D. Morelli, and J. A. Freitas, "Some effects of oxygen impurities on AlN and GaIn," *J. Cryst. Growth*, vol. 246, no. 3–4, pp. 287–298, 2002.
- [74] Z. C. Feng, *III-Nitride Semiconductor Materials*. London: Imperial College Press, 2006.
- [75] P. Rai-Choudhury, *Handbook of Microlithography, Micromachining, and Microfabrication. Volume 1: Microlithography*. SPIE PRESS, 1997.
- [76] R. Sproull, R. Lyon, and S. Trimmer, "The Caltech intermediate form for LSI layout description," Palo Alto, California, 1980.
- [77] E. Soe, B. K. Choi, and O. Kim, "Determination of proximity effect parameters and the shape bias parameter in electron beam lithography," *Microelectron. Eng.*, vol. 53, no. 1, pp. 305–308, 2000.
- [78] N. Unal, M. D. B. Charlton, Y. Wang, U. Waizmann, T. Reindl, and U. Hofmann, "Easy to adapt electron beam proximity effect correction parameter calibration based on visual inspection of a 'Best Dose Sensor,'" *Microelectron. Eng.*, vol. 88, no. 8, pp. 2158–2162, 2011.
- [79] M. Kohler, *Etching in Microsystem Technology*. Weinheim, Germany: Wiley-VCH Verlag GmbH, 1999.
- [80] J. Topolancik, F. Vollmer, R. Ilic, and M. Crescimanno, "Out-of-plane scattering from vertically asymmetric photonic crystal slab waveguides with in-plane disorder," *Opt. Express*, vol. 17, no. 15, pp. 12470–12480, 2009.
- [81] K. Nojiri, *Dry Etching Technology for Semiconductors*. Cham: Springer International Publishing, 2015.
- [82] I.-W. Feng, W. Zhao, J. Li, J. Lin, H. Jiang, and J. Zavada, "Correlation between the optical loss and crystalline quality in erbium-doped GaIn optical waveguides," *Appl. Opt.*, vol. 52, no. 22, pp. 5426–5429, 2013.
- [83] J. Kyeong Jeong *et al.*, "Buffer-layer-free growth of high-quality epitaxial GaIn films on 4H-SiC substrate by metal-organic chemical vapor deposition," *J. Cryst. Growth*, vol. 276, pp. 407–414, 2005.
- [84] E. Smecca *et al.*, "AlN texturing and piezoelectricity on flexible substrates for sensor applications," *Appl. Phys.*

- Lett.*, vol. 106, no. 23, p. 232903, 2015.
- [85] S. Schröder, A. Duparré, L. Coriand, A. Tünnermann, D. H. Penalver, and J. E. Harvey, "Modeling of light scattering in different regimes of surface roughness," *Opt. Express*, vol. 19, no. 10, p. 9820, 2011.
- [86] F. Tabataba-Vakili *et al.*, "Q factor limitation at short wavelength (around 300 nm) in III-nitride-on-silicon photonic crystal cavities," *Appl. Phys. Lett.*, vol. 111, no. 13, p. 131103, 2017.
- [87] D. L. Rode, V. R. Gaddam, and J. H. Yi, "Subnanometer surface roughness of dc magnetron sputtered Al films," *J. Appl. Phys.*, vol. 102, no. 2, 2007.
- [88] G. Zalczar, D. S. M. Drecam, and S. R. Sim, "Spectroscopic on transparent ellipsometry substrates near the Brewster angle," *Physica A*, vol. 2132, pp. 2132–2134, 1992.
- [89] S. Pezzagna, J. Brault, M. Leroux, J. Massies, and M. De Micheli, "Refractive indices and elasto-optic coefficients of GaN studied by optical waveguiding," *J. Appl. Phys.*, vol. 103, no. 12, pp. 1–8, 2008.
- [90] M. Miyoshi, A. Watanabe, and T. Egawa, "Modeling of the wafer bow in GaN-on-Si epiwafers employing GaN/AlN multilayer buffer structures," *Semicond. Sci. Technol.*, vol. 31, no. 10, 2016.
- [91] R. J. Yim, W M And Paff, "Thermal expansion of AlN, sapphire, and silicon," *J. Appl. Phys.*, vol. 45, no. 3, pp. 1456–1457, 1974.
- [92] M. Leszczynski *et al.*, "Lattice parameters of gallium nitride," *Appl. Phys. Lett.*, vol. 69, no. 1, pp. 73–75, 1996.
- [93] M. Tanaka, S. Nakahata, K. Sogabe, H. Nakata, and M. Tobioka, "Morphology and X-ray diffraction peak widths of aluminum nitride single crystals prepared by the sublimation method," *Japanese J. Appl. Physics, Part 2 Lett.*, vol. 36, no. 8B, 1997.
- [94] Y. Okada and Y. Tokumaru, "Precise determination of lattice-parameter and thermal-expansion coefficient of silicon between 300 K and 1500 K," *J. Appl. Phys.*, vol. 56, no. 2, pp. 314–320, 1984.
- [95] H. Iwanaga, A. Kunishige, and S. Takeuchi, "Anisotropic thermal expansion in wurtzite-type crystals," *J. Mater. Sci.*, vol. 35, no. 10, pp. 2451–2454, 2000.
- [96] J. H. Parker Jr., D. W. Feldman, and M. Ashkin, "Raman scattering by silicon and germanium," *Phys. Rev.*, vol. 155, no. 3, p. 712, 1967.
- [97] V. Y. Davydov *et al.*, "Phonon dispersion and Raman scattering in hexagonal GaN and AlN," *Phys. Rev. B*, vol. 58, no. 19, pp. 12899–12907, 1998.
- [98] G. Callsen *et al.*, "Phonon pressure coefficients and deformation potentials of wurtzite AlN determined by uniaxial pressure-dependent Raman measurements," *Phys. Rev. B - Condens. Matter Mater. Phys.*, vol. 90, no. 20, pp. 1–9, 2014.
- [99] E. Anastassakis, A. Cantarero, and M. Cardona, "Piezo-Raman measurements and anharmonic parameters in silicon and diamond," *Phys. Rev. B*, vol. 41, no. 11, pp. 7529–7535, 1990.
- [100] F. Demangeot, J. Frandon, P. Baules, F. Natali, F. Semond, and J. Massies, "Phonon deformation potentials in hexagonal GaN," *Phys. Rev. B - Condens. Matter Mater. Phys.*, vol. 69, no. 15, pp. 1–5, 2004.
- [101] R. Loudon, "The Raman effect in crystals," *Advances in Physics*, vol. 13, no. 52, pp. 423–482, 1964.
- [102] S. Tripathy, V. K. X. Lin, S. Vicknesh, and S. J. Chua, "Micro-Raman probing of residual stress in freestanding GaN-based micromechanical structures fabricated by a dry release technique," *J. Appl. Phys.*, vol. 101, no. 6, pp. 1–4, 2007.
- [103] J. Jágerská, "Dispersion properties of photonic crystals and silicon nanostructures investigated by Fourier-space imaging," *École polytechnique fédérale de Lausanne EPFL*, 2011.
- [104] N. Le Thomas, R. Houdré, M. V. Kotlyar, D. O'Brien, and T. F. Krauss, "Exploring light propagating in photonic crystals with Fourier optics," *J. Opt. Soc. Am. B*, vol. 24, no. 12, p. 2964, 2007.
- [105] N. Le Thomas, R. Houdré, L. H. Frandsen, J. Fage-Pedersen, A. V. Lavrinenko, and P. I. Borel, "Grating-assisted superresolution of slow waves in Fourier space," *Phys. Rev. B - Condens. Matter Mater. Phys.*, vol. 76, no. 3,

- pp. 1–5, 2007.
- [106] N. Le Thomas, V. Zabelin, R. Houdré, M. V. Kotlyar, and T. F. Krauss, “Influence of residual disorder on the anticrossing of Bloch modes probed in k space,” *Phys. Rev. B*, vol. 78, no. 12, p. 125301, Sep. 2008.
  - [107] N. Le Thomas *et al.*, “Light transport regimes in slow light photonic crystal waveguides,” *Phys. Rev. B*, vol. 80, no. 12, p. 125332, 2009.
  - [108] M. Notomi, E. Kuramochi, and T. Tanabe, “Large-scale arrays of ultrahigh-Q coupled nanocavities: supplementary information,” *Nat. Photonics*, vol. 2, no. 12, pp. 741–747, 2008.
  - [109] S. A. Schulz, J. Upham, L. O’Faolain, and R. W. Boyd, “Photonic crystal slow light waveguides in a kagome lattice,” *Opt. Lett.*, vol. 42, no. 16, p. 3243, 2017.
  - [110] U. Fano, “Effects of configuration interaction on intensities and phase shifts,” *Phys. Rev.*, vol. 124, no. 6, pp. 1866–1878, 1961.
  - [111] M. Galli, S. L. Portalupi, M. Belotti, L. C. Andreani, L. O’Faolain, and T. F. Krauss, “Light scattering and Fano resonances in high-Q photonic crystal nanocavities,” *Appl. Phys. Lett.*, vol. 94, no. 7, p. 71101, 2009.
  - [112] U. Dharanipathy *et al.*, “Near-infrared characterization of gallium nitride photonic-crystal waveguides and cavities,” *Opt. Lett.*, vol. 37, no. 22, pp. 4588–90, 2012.
  - [113] I. Roland *et al.*, “Near-infrared gallium nitride two-dimensional photonic crystal platform on silicon,” *Appl. Phys. Lett.*, vol. 105, no. 1, p. 11104, 2014.
  - [114] U. P. Dharanipathy, M. Minkov, M. Tonin, V. Savona, and R. Houdré, “High-Q silicon photonic crystal cavity for enhanced optical nonlinearities,” *Appl. Phys. Lett.*, vol. 105, no. 10, 2014.
  - [115] S. Buckley, M. Radulaski, K. Biermann, and J. Vučković, “Second harmonic generation in photonic crystal cavities in (111)-oriented GaAs - Supplementary Material,” *Appl. Phys. Lett.*, vol. 103, no. 111, 2013.
  - [116] P. Seidler, K. Lister, U. Drechsler, J. Hofrichter, and T. Stöferle, “Slotted photonic crystal nanobeam cavity with an ultrahigh quality factor-to-mode volume ratio,” *Opt. Express*, vol. 21, no. 26, pp. 32468–83, 2013.
  - [117] T. Araki *et al.*, “Radio-frequency plasma-excited molecular beam epitaxy growth of GaN on graphene/Si(100) substrates,” *Appl. Phys. Express*, vol. 7, no. 100, p. 71001, 2014.
  - [118] N. A. Sanford *et al.*, “Measurement of second order susceptibilities of GaN and AlGaIn,” *J. Appl. Phys.*, vol. 97, pp. 1–13, 2005.
  - [119] M. Abe *et al.*, “Accurate measurement of quadratic nonlinear-optical coefficients of zinc oxide,” *J. Opt. Soc. Am. B*, vol. 29, no. 9, p. 2392, 2012.
  - [120] J. E. Sipe, D. J. Moss, and H. M. Vandriel, “Phenomenological theory of optical 2nd-harmonic and 3rd-harmonic generation from cubic centrosymmetric crystals,” *Phys. Rev. B Condens. Matter Mater. Phys.*, vol. 35, no. 3, pp. 1129–1141, 1987.
  - [121] M. Cazzanelli *et al.*, “Second-harmonic generation in silicon waveguides strained by silicon nitride,” *Nat. Mater.*, vol. 11, no. 2, pp. 148–154, 2011.
  - [122] M. Wächter *et al.*, “Optical generation of terahertz and second-harmonic light in plasma-activated silicon nanophotonic structures,” *Appl. Phys. Lett.*, vol. 97, no. 16, 2010.
  - [123] C. Matheisen *et al.*, “Electro-optic light modulation and THz generation in locally plasma-activated silicon nanophotonic devices,” *Opt. Express*, vol. 22, no. 5, pp. 5252–5259, 2014.
  - [124] E. Timurdogan, C. V. Poulton, M. J. Byrd, and M. R. Watts, “Electric field-induced second-order nonlinear optical effects in silicon waveguides,” *Nat. Photonics*, vol. 11, no. 3, pp. 200–206, 2017.
  - [125] R. A. Hill, A. Knoesen, and M. A. Mortazavi, “Corona poling of nonlinear polymer thin films for electro-optic modulators,” *Appl. Phys. Lett.*, vol. 65, no. 14, pp. 1733–1735, 1994.
  - [126] K. Wang *et al.*, “Broadband ultrafast nonlinear absorption and nonlinear refraction of layered molybdenum dichalcogenide semiconductors,” *Nanoscale*, vol. 6, no. 18, pp. 10530–10535, 2014.

- [127] D. E. Chang, V. Vuletić, and M. D. Lukin, "Quantum nonlinear optics — photon by photon," *Nat. Photonics*, vol. 8, no. 9, pp. 685–694, Sep. 2014.
- [128] V. Pacebutas, A. Stalnionis, A. Krotkus, M. Leszczynski, P. Perlin, and T. Suski, "Nonlinear optical characterization of single-crystalline GaN by z-scan technique," *Smart Opt. Inorg. Struct. Devices*, vol. 4318, no. 370, pp. 135–139, 2001.
- [129] Y. Fujii, S. Yoshida, S. Misawa, S. Maekawa, and T. Sakudo, "Nonlinear optical susceptibilities of AlN film," *Appl. Phys. Lett.*, vol. 31, no. 12, p. 815, 1977.
- [130] D. Blanc, A. M. Bouchoux, C. Plumereau, A. Cachard, and J. F. Roux, "Phase-matched frequency doubling in an aluminum nitride waveguide with a tunable laser source," *Appl. Phys. Lett.*, vol. 659, no. 1995, p. 659, 1995.
- [131] G. T. Kiehne, G. K. L. Wong, and J. B. Ketterson, "Optical second-harmonic generation in sputter-deposited AlN films," *J. Appl. Phys.*, vol. 84, no. 11, pp. 5922–5927, Dec. 1998.
- [132] A. S. Barker and M. Illegems, "Infrared lattice vibrations and free-electron dispersion in GaN," *Phys. Rev. B*, vol. 7, no. 2, pp. 743–750, 1973.
- [133] J. Pastrňák and L. Roskovcová, "Refraction index measurements on AlN single crystals," *Phys. status solidi*, vol. 14, no. 1, pp. K5–K8, 1966.
- [134] M. Stegmaier and W. H. P. Pernice, "Mode control and mode conversion in nonlinear aluminum nitride waveguides," *Opt. Express*, vol. 21, no. 22, p. 26742, 2013.
- [135] P. M. Lundquist *et al.*, "Ultraviolet second harmonic generation in radio-frequency sputter-deposited aluminum nitride thin films," *Appl. Phys. Lett.*, vol. 65, no. 9, pp. 1085–1087, 1994.
- [136] H. Haag *et al.*, "Degenerate four-wave mixing experiments on GaN in the quasistationary regime," *Appl. Phys. Lett.*, vol. 74, no. 10, pp. 1436–1438, 1999.
- [137] J. Miragliotta and D. K. Wickenden, "Optical third-harmonic studies of the dispersion in  $\chi(3)$  for gallium nitride thin films on sapphire," *Phys. Rev. B*, vol. 50, no. 20, pp. 960–964, 1994.
- [138] C. K. Sun *et al.*, "Large near resonance third order nonlinearity in GaN," *Opt. Quantum Electron.*, vol. 32, pp. 619–640, 2000.
- [139] H. Chen *et al.*, "Characterizations of nonlinear optical properties on GaN crystals in polar, nonpolar, and semipolar orientations," *Appl. Phys. Lett.*, vol. 110, no. 18, p. 181110, 2017.
- [140] M. Zhao, C.-H. Xu, W.-J. Hu, W.-J. Wang, L.-W. Guo, and X.-L. Chen, "Observation of two-photon absorption and nonlinear refraction in AlN," *Chinese Phys. Lett.*, vol. 33, no. 10, p. 104201, 2016.
- [141] A. L. Fehrembach, S. Enoch, and A. Sentenac, "Highly directive light sources using two-dimensional photonic crystal slabs," *Appl. Phys. Lett.*, vol. 79, no. 26, pp. 4280–4282, 2001.
- [142] N.-V.-Q. Tran, S. Combríé, and A. De Rossi, "Directive emission from high-Q photonic crystal cavities through band folding," *Phys. Rev. B*, vol. 79, no. 4, p. 41101, 2009.
- [143] M. W. McCutcheon *et al.*, "Resonant scattering and second-harmonic spectroscopy of planar photonic crystal microcavities," *Appl. Phys. Lett.*, vol. 87, no. 22, p. 221110, Nov. 2005.
- [144] N. Vico Triviño *et al.*, "Gallium nitride L3 photonic crystal cavities with an average quality factor of 16 900 in the near infrared," *Appl. Phys. Lett.*, vol. 105, no. 23, 2014.
- [145] M. Minkov, U. P. Dharanipathy, R. Houdré, and V. Savona, "Statistics of the disorder-induced losses of high-Q photonic crystal cavities," *Opt. Express*, vol. 21, no. 23, pp. 28233–45, 2013.
- [146] A. Stolz *et al.*, "Optical waveguide loss minimized into gallium nitride based structures grown by metal organic vapor phase epitaxy," *Appl. Phys. Lett.*, vol. 98, no. 16, pp. 41–44, 2011.
- [147] O. Ambacher, W. Rieger, P. Ansmann, H. Angerer, T. D. Moustakas, and M. Stutzmann, "Sub-bandgap absorption of gallium nitride determined by photothermal deflection spectroscopy," *Solid State Commun.*,

- vol. 97, no. 5, pp. 365–370, 1996.
- [148] M. S. Mohamed *et al.*, “Efficient continuous-wave nonlinear frequency conversion in high-Q gallium nitride photonic crystal cavities on Silicon,” *APL Photonics*, vol. 2, no. 3, p. 31301, Sep. 2016.
- [149] A. W. Bruch, C. Xiong, B. Leung, M. Poot, J. Han, and H. X. Tang, “Broadband nanophotonic waveguides and resonators based on epitaxial GaN thin films,” *Appl. Phys. Lett.*, vol. 107, no. 14, p. 141113, 2015.
- [150] H. Hagino, Y. Takahashi, Y. Tanaka, T. Asano, and S. Noda, “Effects of fluctuation in air hole radii and positions on optical characteristics in photonic crystal heterostructure nanocavities,” *Phys. Rev. B*, vol. 79, no. 8, p. 85112, 2009.
- [151] T. Asano, B. Song, and S. Noda, “Analysis of the experimental Q factors ( $\sim 1$  million) of photonic crystal nanocavities,” *Opt. Express*, vol. 14, no. 5, pp. 1996–2002, 2006.
- [152] S. Yamada *et al.*, “Second-harmonic generation in a silicon-carbide-based photonic crystal nanocavity,” *Opt. Lett.*, vol. 39, no. 7, pp. 1768–71, 2014.
- [153] Y. Zeng *et al.*, “Resonant second harmonic generation in a gallium nitride two-dimensional photonic crystal on silicon,” *Appl. Phys. Lett.*, vol. 106, no. 8, p. 81105, 2015.
- [154] C. Xiong *et al.*, “Integrated GaN photonic circuits on silicon (100) for second harmonic generation,” *Opt. Express*, vol. 19, no. 11, pp. 10462–70, 2011.
- [155] I. Roland *et al.*, “Phase-matched second harmonic generation with on-chip GaN-on-Si microdisks,” *Sci. Rep.*, vol. 6, no. 1, p. 34191, 2016.
- [156] Y. Lai *et al.*, “Ultra-wide-band slow light in photonic crystal coupled-cavity waveguides,” *arXiv: 1706.09625*, 2017.
- [157] L. V. Hau, S. E. Harris, Z. Dutton, and C. H. Behroozi, “Light speed reduction to 17 metres per second in an ultracold atomic gas,” *Nature*, vol. 397, no. 6720, pp. 594–598, 1999.
- [158] M. S. Bigelow, N. N. Lepeshkin, and R. W. Boyd, “Observation of ultraslow light propagation in a ruby crystal at room temperature,” *Phys. Rev. Lett.*, vol. 90, no. 11, p. 4, 2003.
- [159] P.-C. Ku *et al.*, “Slow light in semiconductor quantum wells,” *Opt. Lett.*, vol. 29, no. 19, pp. 2291–3, 2004.
- [160] D. Miller, “Fundamental limit to delay-bandwidth product in one-dimensional linear optical structures,” in *Integrated Photonics and Nanophotonics Research and Applications*, *OSA Technical Digest*, 2007, p. SMB1.
- [161] K. L. Tsakmakidis *et al.*, “Breaking Lorentz reciprocity to overcome the time-bandwidth limit in physics and engineering,” *Science (80-. )*, vol. 356, no. 6344, pp. 1260–1264, 2017.
- [162] K. Fang, Z. Yu, and S. Fan, “Photonic Aharonov-Bohm effect based on dynamic modulation,” *Phys. Rev. Lett.*, vol. 108, no. 15, pp. 1–5, 2012.
- [163] K. Fang, Z. Yu, and S. Fan, “Realizing effective magnetic field for photons by controlling the phase of dynamic modulation,” *Nat. Photonics*, vol. 6, no. 11, pp. 782–787, 2012.
- [164] M. Hafezi and P. Rabl, “Optomechanically induced non-reciprocity in microring resonators,” *Opt. Express*, vol. 20, no. 2005, pp. 7672–7684, 2012.
- [165] J. Kim, M. C. Kuzyk, K. Han, H. Wang, and G. Bahl, “Non-reciprocal Brillouin scattering induced transparency,” *Nat. Phys.*, vol. 11, no. 3, pp. 275–280, 2015.
- [166] M. Notomi, K. Yamada, A. Shinya, J. Takahashi, C. Takahashi, and I. Yokohama, “Extremely large group-velocity dispersion of line-defect waveguides in photonic crystal slabs,” *Phys. Rev. Lett.*, vol. 87, no. 25, p. 253902, Nov. 2001.
- [167] D. Mori and T. Baba, “Wideband and low dispersion slow light by chirped photonic crystal coupled waveguide,” *Opt. Express*, vol. 13, no. 23, pp. 9398–9408, 2005.
- [168] N. Matsuda, E. Kuramochi, H. Takesue, and M. Notomi, “Dispersion and light transport characteristics of large-scale photonic-crystal coupled nanocavity arrays,” *Opt. Lett.*, vol. 39, no. 8, p. 2290, Apr. 2014.

- [169] S. Ek, P. Lunnemann, Y. Chen, E. Semenova, K. Yvind, and J. Mork, "Slow-light-enhanced gain in active photonic crystal waveguides," *Nat. Commun.*, vol. 5, p. 5039, 2014.
- [170] C. Xiong *et al.*, "Slow-light enhanced correlated photon pair generation in a silicon photonic crystal waveguide," *Opt. Lett.*, vol. 36, no. 17, p. 3413, 2011.
- [171] N. Matsuda, H. Takesue, K. Shimizu, Y. Tokura, E. Kuramochi, and M. Notomi, "Slow light enhanced correlated photon pair generation in photonic-crystal coupled-resonator optical waveguides," *Opt. Express*, vol. 21, no. 7, p. 8596, 2013.
- [172] J. He *et al.*, "Degenerate photon-pair generation in an ultracompact silicon photonic crystal waveguide," *Opt. Lett.*, vol. 39, no. 12, p. 3575, 2014.
- [173] R. J. P. Engelen *et al.*, "The effect of higher-order dispersion on slow light propagation in photonic crystal waveguides," *Opt. Express*, vol. 14, no. 4, pp. 1658–72, 2006.
- [174] D. Leuenberger, "Ab initio tight-binding approach to photonic-crystal based coupled cavity waveguides," *J. Appl. Phys.*, vol. 95, no. 3, p. 806, 2004.
- [175] A. Yariv, Y. Xu, R. K. Lee, and A. Scherer, "Coupled-resonator optical waveguide: a proposal and analysis," *Opt. Lett.*, vol. 24, no. 11, pp. 711–713, 1999.
- [176] N. Caselli *et al.*, "Antibonding ground state in photonic crystal molecules," *Phys. Rev. B - Condens. Matter Mater. Phys.*, vol. 86, no. 3, pp. 4–7, 2012.
- [177] S. Haddadi *et al.*, "Photonic molecules: tailoring the coupling strength and sign," *Opt. Express*, vol. 22, no. 10, p. 12359, 2014.
- [178] D. O'Brien, M. D. Settle, T. Karle, A. Michaeli, M. Salib, and T. F. Krauss, "Coupled photonic crystal heterostructure nanocavities," *Opt. Express*, vol. 15, no. 3, pp. 1228–1233, 2007.
- [179] J. Jágerská, H. Zhang, N. Le Thomas, and R. Houdré, "Radiation loss of photonic crystal coupled-cavity waveguides," *Appl. Phys. Lett.*, vol. 95, no. 11, pp. 1–4, 2009.
- [180] P. Yeh, "Electromagnetic propagation in birefringent layered media," *J. Opt. Soc. Am.*, vol. 69, no. 5, p. 742, 1979.
- [181] S. G. Johnson, P. Bienstman, M. A. Skorobogatiy, M. Ibanescu, E. Lidorikis, and J. D. Joannopoulos, "Adiabatic theorem and continuous coupled-mode theory for efficient taper transitions in photonic crystals," *Phys. Rev. E - Stat. Nonlinear, Soft Matter Phys.*, vol. 66, no. 6, pp. 1–15, 2002.
- [182] P. Pottier, M. Gnan, and R. M. De La Rue, "Efficient coupling into slow-light photonic crystal channel guides using photonic crystal tapers," *Opt. Express*, vol. 15, no. 11, pp. 6569–75, 2007.
- [183] J. P. Hugonin, P. Lalanne, T. P. White, and T. F. Krauss, "Coupling into slow-mode photonic crystal waveguides," *Opt. Lett.*, vol. 32, no. 18, p. 2638, 2007.
- [184] C. Martijn de Sterke, K. B. Dossou, T. P. White, L. C. Botten, and R. C. McPhedran, "Efficient coupling into slow light photonic crystal waveguide without transition region: role of evanescent modes," *Opt. Express*, vol. 17, no. 20, pp. 17338–17343, 2009.
- [185] Y. A. Vlasov and S. J. McNab, "Coupling into the slow light mode in slab-type photonic crystal waveguides," *Opt. Lett.*, vol. 31, no. 1, p. 50, 2006.
- [186] M. Notomi, E. Kuramochi, and T. Tanabe, "Large-scale arrays of ultrahigh-Q coupled nanocavities," *Nat. Photonics*, vol. 2, no. 12, pp. 741–747, 2008.
- [187] M. Sumetsky and B. Eggleton, "Modeling and optimization of complex photonic resonant cavity circuits," *Opt. Express*, vol. 11, no. 4, pp. 381–391, 2003.
- [188] J. Capmany, P. Muñoz, J. D. Domenech, and M. a Muriel, "Apodized coupled resonator waveguides," *Opt. Express*, vol. 15, no. 16, pp. 10196–10206, 2007.
- [189] M. L. Povinelli and S. Fan, "Radiation loss of coupled-resonator waveguides in photonic-crystal slabs," *Appl.*

- Phys. Lett.*, vol. 89, no. 19, 2006.
- [190] R. Sarkissian and J. O'Brien, "Group index oscillations in photonic crystal waveguides," *Appl. Phys. Lett.*, vol. 105, no. 12, p. 121102, 2014.
- [191] S. Mazoyer *et al.*, "Statistical fluctuations of transmission in slow light photonic-crystal waveguides," *Opt. Express*, vol. 18, no. 14, pp. 14654–14663, 2010.
- [192] M. Patterson *et al.*, "Disorder-induced incoherent scattering losses in photonic crystal waveguides: Bloch mode reshaping, multiple scattering, and breakdown of the Beer-Lambert law," *Phys. Rev. B - Condens. Matter Mater. Phys.*, vol. 80, no. 19, pp. 1–6, 2009.
- [193] P. W. Anderson, "Absence of diffusion in certain random lattices," *Phys. Rev.*, vol. 109, no. 5, pp. 1492–1505, 1958.
- [194] S. Hughes, L. Ramunno, J. F. Young, and J. E. Sipe, "Extrinsic optical scattering loss in photonic crystal waveguides: Role of fabrication disorder and photon group velocity," *Phys. Rev. Lett.*, vol. 94, no. 3, pp. 1–4, 2005.
- [195] D. S. Wiersma, P. Bartolini, A. Lagendijk, and R. Righini, "Localization of light in a disordered medium," *Nature*, vol. 390, no. 6661, pp. 671–673, 1997.
- [196] M. Bruel, B. Aspar, and A. J. Auberton-Hervé, "Smart-cut: A new silicon on insulator material technology based on hydrogen implantation and wafer bonding," *Japanese J. Appl. Physics, Part 1*, vol. 36, no. 3B, pp. 1636–1641, 1997.
- [197] D. Yamashita, Y. Takahashi, T. Asano, and S. Noda, "Raman shift and strain effect in high-Q photonic crystal silicon nanocavity," *Opt. Express*, vol. 23, no. 4, p. 3951, 2015.
- [198] E. Iwase *et al.*, "Control of buckling in large micromembranes using engineered support structures," *J. Micromechanics Microengineering*, vol. 22, no. 6, p. 65028, 2012.
- [199] X. Xu *et al.*, "Flexible single-crystal silicon nanomembrane photonic crystal cavity," *ACS Nano*, vol. 8, no. 12, pp. 12265–12271, 2014.
- [200] S. Fukura, T. Mizukami, S. Odake, and H. Kagi, "Factors determining the stability, resolution, and precision of a conventional raman spectrometer," *Appl. Spectrosc.*, vol. 60, no. 8, pp. 946–950, 2006.
- [201] C. G. Van de Walle, "Band lineups and deformation potentials in the model-solid theory," *Phys. Rev. B*, vol. 39, no. 3, pp. 1871–1883, 1989.
- [202] E. Anastassakis, A. Pinczuk, E. Burstein, F. H. Pollak, and M. Cardona, "Effect of static uniaxial stress on the Raman spectrum of silicon," *Solid State Commun.*, vol. 88, no. 11–12, pp. 1053–1058, 1993.
- [203] J. Cai, Y. Ishikawa, and K. Wada, "Strain induced bandgap and refractive index variation of silicon," *Opt. Express*, vol. 21, no. 6, pp. 7162–70, 2013.
- [204] N. Vico Triviño, U. Dharanipathy, J. F. Carlin, Z. Diao, R. Houdré, and N. Grandjean, "Integrated photonics on silicon with wide bandgap GaN semiconductor," *Appl. Phys. Lett.*, vol. 102, no. 8, pp. 3–6, 2013.
- [205] X. Guo, C. Zou, C. Schuck, H. Jung, R. Cheng, and H. X. Tang, "Parametric down-conversion photon-pair source on a nanophotonic chip," *Light Sci. Appl.*, vol. 6, no. 5, p. e16249, 2016.
- [206] L. Lu, J. D. Joannopoulos, and M. Soljačić, "Topological photonics," *Nat. Photonics*, vol. 8, no. 11, pp. 821–829, 2014.
- [207] T. Baba, H. C. Nguyen, N. Yazawa, Y. Terada, S. Hashimoto, and T. Watanabe, "Slow-light Mach-Zehnder modulators based on Si photonic crystals," *Sci. Technol. Adv. Mater.*, vol. 15, no. 2, p. 24602, 2014.
- [208] K. Kondo, N. Ishikura, T. Tamura, and T. Baba, "Temporal pulse compression by dynamic slow-light tuning in photonic-crystal waveguides," *Phys. Rev. A - At. Mol. Opt. Phys.*, vol. 91, no. 2, pp. 1–5, 2015.
- [209] P. Colman, C. Husko, S. Combré, I. Sagnes, C. W. Wong, and A. De Rossi, "Temporal solitons and pulse compression in photonic crystal waveguides," *Nat. Photonics*, vol. 4, no. 12, pp. 862–868, 2010.



# Table of Symbols and Acronyms

<b>Symbol/ Acronym</b>	<b>Correspondence</b>
<b>E-beam</b>	Electron beam
<b>CCD</b>	Charge-coupled device
<b>FEM</b>	Finite-element method
<b>FIB</b>	Focused-ion beam
<b>FDTD</b>	Finite-difference time domain
<b>FOM</b>	Figure of merit
<b>FWHM</b>	Full width at half maximum
<b>GBP</b>	Group index bandwidth product
<b>GME</b>	Guided-mode expansion
<b>ICP-RIE</b>	Inductively coupled plasma reactive-ion etching
<b>IR</b>	Infrared
<b>MBE</b>	Molecular beam epitaxy
<b>MOCVD</b>	Metalorganic chemical vapor deposition
<b>NA</b>	Numerical aperture
<b>PhC</b>	Photonic crystal
<b>Q</b>	Quality (factor)
<b>RMS</b>	Root mean square
<b>SEM</b>	Scanning electron microscope
<b>SOI</b>	Silicon-on-insulator
<b>TE</b>	Transverse electric
<b>TM</b>	Transverse magnetic



# Mohamed Sabry Abdel-Aliem Mohamed

mohsabry@outlook.com  
Av. du Tir-Fédéral, Ecublens - Switzerland

## EDUCATION

- 2010 – 2012** M.Sc. Optics & Photonics,  
Karlsruhe School of Optics & Photonics,  
**Karlsruhe Institute of Technology** – Germany
- M.Sc. Physics,  
**Université d'Aix-Marseille** – France
- M.Sc. Photonics Engineering,  
**Universitat de Barcelona, Universitat Politècnica de Catalunya,  
Universitat Autònoma de Barcelona, & ICFO** – Spain
- 2005 – 2010** B.Sc. Electronics Engineering *with Honors*,  
Faculty of Information Engineering and Technology,  
**German University in Cairo** – Egypt

## ACADEMIC POSITIONS

- Feb 2014 – Current** Doctoral assistant at **EPFL** – Switzerland  
Photonic Crystals group, Prof. Romuald Houdré
- Investigating light confinement and nonlinear light-matter interaction in semiconductor photonic crystals
- Mar 2013 – Sep 2013** CNRS visiting researcher at **Institut Fresnel** – France  
Mosaic group, Hervé Rigneault and Guillaume Baffou
- Investigating plasmon-assisted micro/nano-scale heat-pattern generation and non-invasive temperature probing
- Aug 2011 – Sep 2011** Intern at **Institut für Mikrostrukturtechnik, KIT** – Germany  
Biophotonic Sensors group, PD Dr.-Ing. Timo Mappes
- Developing an imaging and beam-shaping setup for the characterization of optical microresonators

## PERSONAL DETAILS

Date of Birth: 2<sup>nd</sup> of September, 1988  
Place of Birth: Texas, U.S.A.  
Nationality: American/ Egyptian